INVESTIGATING FLAME-BASED SYNTHESIS OF CARBON NANOTUBES AND

METAL-OXIDE NANOWIRES

By

FUSHENG XU

A Dissertation submitted to the

Graduate School-New Brunswick

Rutgers, The State University of New Jersey

in partial fulfillment of the requirements

for the degree of

Doctor of Philosophy

Graduate Program in Mechanical and Aerospace Engineering

written under the direction of

Professor Stephen D. Tse

and approved by

_____

_____

_____

_____

New Brunswick, New Jersey

October 2007

ABSTRACT OF THE DISSERTATION

Investigating Flame-based Synthesis of Carbon Nanotubes and Metal-oxide Nanowires

By FUSHENG XU

Dissertation Director:
Professor Stephen D. Tse

The synthesis of carbon nanotubes (CNTs) and metal-oxide nanowires (e.g. ZnO, $WO_{2.9}$) are examined experimentally by inserting probes into various flame geometries at atmospheric pressure. The main probed-flame configurations are the inverse co-flow diffusion flame (IDF) and the counter-flow diffusion flame (CDF), which are compared with each other to assess the translatability of local synthesis conditions in producing the same growth attributes and morphologies. The CDF is characterized using laser-based spontaneous Raman spectroscopy (SRS), and validated with simulations using detailed chemical kinetics and transport. SRS is used to measure local conditions in the 2-D axisymmetric IDF. Properties of the as-synthesized nanostructures are determined by field-emission scanning electron microscopy (FESEM), high-resolution transmission electron microscopy (TEM), energy dispersive X-ray spectroscopy (EDXS), and resonance Raman spectroscopy (RRS).

Various morphologies of CNTs are grown catalytically on metal-alloy substrates of different compositions (i.e., Fe, Fe/Cr, Ni/Cu, Ni/Ti, Ni/Cr, Ni/Cr/Fe), as well as on metal-oxide solid solutions (i.e. $NiAl_2O_4$, $CoAl_2O_4$ and $ZnFe_2O_4$). Vertically well-aligned multi-walled CNTs (MWNTs) with uniform diameters are obtained from Ni/Cr/Fe and

Ni/Ti alloys. CNTs produced from $ZnFe_2O_4$ substrates are found to be a mixture of MWNTs and single-walled carbon nanotubes (SWNTs) with at least 30% SWNTs by number. Effects of local gas-phase temperature, substrate temperature, carbon-based precursor species concentrations, and substrate voltage bias on CNT formation, diameter, growth rate, yield, density, and morphology are investigated.

Aligned single-crystal tungsten oxide nanowires with diameters of 20-50nm are grown directly from tungsten substrates at high rates, with local gas-phase temperature and chemical species specified at the substrate for self-synthesis. Voltage bias is shown to dramatically alter the morphologies of the as-synthesized WO_x nanomaterial. Single-crystalline ZnO nanowires are grown directly on zinc-plated steel substrates at high rates with no catalysts. Larger-diameter (>100nm) nanowires are produced at higher temperatures; while smaller-diameter (25-40nm) nanowires are produced at lower temperatures, and only on the fuel side of the reaction zone. Reactions with H_2O appear to be the dominant route for nanowire synthesis. Nanoribbons and other nanowire-based morphologies are also found and discussed.

Preface

All the spontaneous Raman spectroscopy measurements in this dissertation are performed

by Mr. Xiaofei Liu who is listed as an author for the papers related to this work.

Much of content in Chapters 6, 7, 9 and 11 is verbatim from the published and

submitted corresponding papers[1,2,3,4], and I have obtained permission from the

co-authors.

Reference

[1]Xu F., Liu X., and Tse S.D., Synthesis of Carbon Nanotubes on Metal Alloy Substrates with Voltage Bias in Methane Inverse Diffusion Flames, *Carbon,* 44(3): 570-577, 2006

[2]Xu F., Zhao H., and Tse S.D., Carbon Nanotube Synthesis on Catalytic Metal Alloys in Methane/Air Counterflow Diffusion Flames, *Proceedings of the Combustion Institute,* 31(2): 1839-1847, 2006

[3]Xu, F., Liu, X., Tse, S.D., Cosandey, F., and Kear, B.H., Flame Synthesis of Zinc Oxide Nanowires, submitted to *Chemical Physics Letters,* 2007.

[4]Xu F., Tse S.D., Al-Sharab J.F., and Kear B.H., Flame Synthesis of Aligned Tungsten Oxide Nanowires, *Applied Physics Letters*, 88: 243115, 2006

Table of Contents

List of tables

List of illustrations

xvi

Chapter 1

Introduction

One-dimensional (1D) nanostructures such as tubes, rods, wires, and ribbons are generally defined as structures having a characteristic dimension less than 100nm and a high length-to-diameter aspect ratio[1]. Such structures have triggered significant research attention in recent years, due to their many unique properties and potential applications, which are superior to their bulk counterparts. These properties are intrinsically associated with their low dimensionality and quantum confinement effects[1], making them suitable as building blocks for future electronics and photonics[2,3,4], as well as for biological applications[5]. They are also expected to play an important role as both interconnects and functional units in fabricating electronic, optoelectronic, electrochemical, and electromechanical nanodevices[1,6,7].

Although various approaches have been employed to fabricate 1D nanostructures, flame synthesis is investigated in this work due to its unique advantages of high growth rate, controllability, and processing continuity. At the same time, the inherent gradients allow for examination of a large parameter space, providing the local conditions, i.e. temperature and chemical species, conducive for carbon nanotube (CNT) and metal-oxide nanowire growth.

This dissertation focuses on investigating the growth of 1D nanostructures in flame configurations in order to better understand the fundamental mechanisms. Specifically, the investigated 1D nanostructures include CNTs and metal-oxide nanowires (i.e. ZnO,

$WO_{2.9}$, Fe_2O_3/Fe_3O_4, CuO/Cu_2O). Reviews of these 1D nanostructures in terms of their properties and synthesis are given in Chapter 2.

In this chapter, the motivation and objectives of this work are presented, along with strategies and innovations. Ensuing, an overview of the thesis is given, which includes experimental methods, computations, and major findings. Finally, highlights of the work are summarized followed by the content outlines of each chapter.

1.1 Motivation and objective

1D nanostructures have been successfully fabricated using various techniques such as arc discharge (AD), laser ablation (LA), chemical vapor deposition (CVD), and molecular beam epitaxy (MBE). However, these techniques are often energy intensive (e.g. CVD and LA), are characterized by batch-to-batch inconsistencies (e.g. AD and LA), or require expensive vacuum equipment (e.g. AD, CVD and MBE). Moreover, they are not readily or economically scalable for large-scale applications. In contrast, flame synthesis can be a cost effective technique with a demonstrated history of scalability (e.g. commercial production of titania, silica, carbon black, etc.). Flame synthesis features energy-efficiency (by providing both heat and chemical reagents), large parameter space (by offering examination of key affecting factors in a single flame), high growth rate (by operating at atmospheric pressure), controllability (by adjusting flame stoichiometries and velocities), and processing continuity (by maintaining a constant flow process). As a result, flames can be tuned to specify the local temperature and chemical species concentrations that are optimal for CNT and metal-oxide nanowire growth.

In this work, we focus on two flame configurations, namely the inverse diffusion flame (IDF) and the counter-flow diffusion flame (CDF). An IDF features a large parameter space, due to its 2-D geometry. Moreover, the carbon-related growth species generated in IDFs can be much greater in concentration than that practically achieved in pre-mixed flames, which should enhance the yield of CNTs. At the same time, IDFs separate soot formation processes from oxidation processes more effectively, and also tend to soot less than normal diffusion flames (NDFs). The soot formation processes would compete with CNT formation routes, as well as contaminate metal-oxide nanowires. The quasi-one-dimensionality of the CDF allows for simulation involving detailed chemistry and transport, which can be verified by gas-phase spontaneous Raman spectroscopy (SRS). By designing a flame through simulation and then by investigating the local conditions for materials synthesis, a CDF provides facile examination of the appropriate variables.

As a first step towards large-scale synthesis, CNT and metal-oxide nanowire synthesis in flames need to be explored. We investigate effects of various parameters (i.e. local gas-phase temperature, gas-phase species concentrations, substrate temperature, catalyst composition, and substrate voltages bias) on the growth properties (i.e. quantity, alignment, diameter, length, and morphology).

Theoretically, the local growth conditions of 1D nanostructures should be "universal," independent of the specific flame configuration, or even gas-phase synthesis method. This motivates us to compare different flame configurations. Particularly, we investigate the growth of CNTs and ZnO in IDFs and CDFs, where the local conditions are the same, despite geometrical differences.

Therefore, the objective of this work is to increase fundamental understanding of the mechanisms of CNT and metal-oxide nanowire formation using flame synthesis. It will be shown that the crystallography, microstructure, and characteristics of organic and non-organic nanomaterials produced in well-defined flames can be correlated to local-gas conditions and properties of the substrate.

The primary research components are to:

(a) Conduct experiments in aerodynamically simple flow fields, mainly IDFs and CDFs, to characterize the effects of fuel composition, flame temperature, oxygen concentration, strain rate, and other controllable process parameters on nano-tube/rod/wire properties;

(b) Investigate the influence of the nature as well as the content of the transition metal component (Ni, Fe, and Co) in metal alloys and spinel solid solutions on the CNTs formed;

(c) Perform direct synthesis of metal-oxide nanowires on/from metal substrates in oxidizing zones of the flame structure;

(d) Probe the influence of electric fields to control nano-tube/rod/wire purity, morphology, alignment, and growth rate;

(e) Measure the local conditions in the flames using laser-based diagnostics, with comparisons to simulations using detailed chemistry and transport.

(f) Characterize the as-synthesized nanomaterial properties using field emission scanning electron microscopy (FESEM), high-resolution transmission electron microscopy (HRTEM), and energy dispersive X-ray spectroscopy (EDXS), and correlate them to the local gas-phase conditions.

1.2 Strategies and innovations in this work

The IDF, which is formed by flowing oxidizer in the center of a jet with fuel co-flowing on the outside, can be especially advantageous in synthesizing CNTs. A net effect of the configuration is that post-flame species are largely comprised of pyrolysis vapors that have not passed through the oxidation zone. Consequently, the hydrocarbon and pyrolysis species generated can be much greater in concentration than that practically achieved in premixed flames (PFs). By using diffusion flames (burning stoichiometrically), flame-speed and cellular stabilization problems related to PFs are also avoided.

Despite the large-parameter-space advantages provided by the large gradients in the IDF, they also smear the resolution of local conditions when probed. The 1-D CDF, established by oppositely impinging oxidizer and fuel flows, is only characterized by gradients in the axial direction. Thus, a radially inserted probe defines a single local growth condition. Moreover, the quasi-one-dimensionality of the CDF offers a simple and well-defined flame geometry allowing for meaningful comparisons between precise experimental probing and detailed computational simulations, facilitating deduction of controlling mechanisms.

Since the hydrocarbon fuel not only provides the source of process heat but also the carbon-based growth reagents to make CNTs, we specifically investigate methane/air systems, thus exploring the possibility of using natural gas in atmospheric air to economically synthesize large quantities of CNTs.

In order to achieve high-purity yields, we probe CNT synthesis in soot-free regions of the flow field where C-related species (i.e. CO and C_2) concentrations are still high.

Since soot formation is a rate process, subject to residence-time considerations, the aerodynamic straining implicit in CDFs becomes beneficial. Because growth from acetylene into a phenyl ring occurs relatively slowly in comparison to ring-growth reactions, it may be possible to produce CNTs in an acetylene-rich flame without a lot of soot byproduct.

For metal-oxide nanowire production, flame synthesis can be a robust process with high growth rates needing no catalysts or vacuum systems. Flames inherently provide for (i) an elevated enthalpy source to bring metal substrate atoms into the gas phase, (ii) the gas-phase chemical species (e.g. O_2, H_2O, CO_2) to produce the requisite oxide, and (iii) a favorable temperature gradient (from a cooler substrate to a hotter gas-phase) for condensation-based growth of the nanowires.

Additionally, electrical force fields can be used to improve uniformity and productivity. Several works[8,9,10,11,12,13,14] in CVD and plasma CNT synthesis systems have reported successful electromagnetic-field application to control CNT coiling, alignment, and growth rate. However, despite the promise of electric field control and its elucidated feasibility, only the recent work of Merchan-Merchan *et al*[15] (and this work) has examined its application in flame synthesis of CNTs. Both Ref. 15 and our work (as will be seen) show that CNT alignment and growth rates can be enhanced under electric fields.

We tailor our IDFs and CDFs such that the local growth conditions probed are similar. Optimal local conditions for CNT and metal-oxide nanowires synthesis should be translatable, and such comparisons allow for assessment of the role of spatial gradients

in temperature and species in affecting morphologies and growth rates of CNT and metal-oxide nanowires.

1.3 Overview
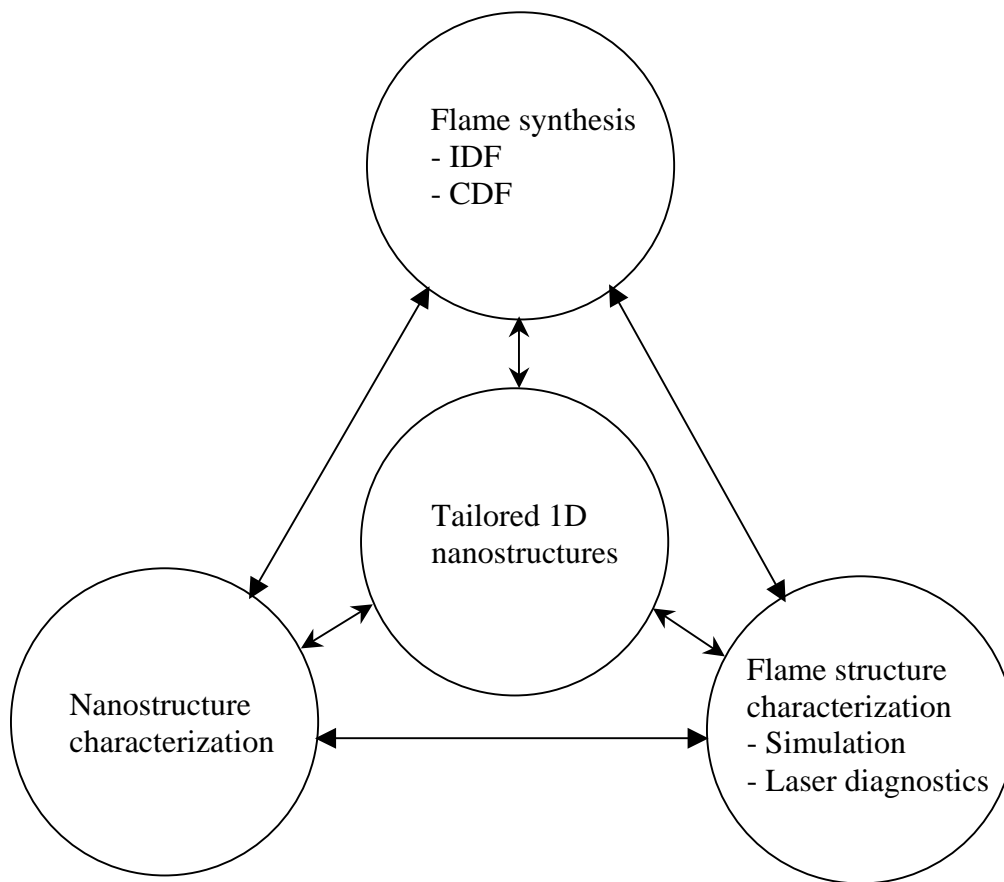
Figure 1.1 The flowchart of this work

The flowchart of the investigative strategy employed in this work is illustrated in Figure1.1, where the ultimate goal is to produce tailored 1D nanostructures. A number of flame configurations are utilized and compared, including PFs, NDFs, IDFs, and CDFs. The flame structures of CDFs are computed using detailed chemical kinetics (GRI-Mech

1.2) and molecular transport, and then probed with SRS to map gas-phase temperature and major growth-involved species concentrations, along the axial centerline. By comparing the simulation and measurements, the nature of the material processing flow field can be revealed. The flame structures of IDFs are measured by SRS as well, including the gas-phase temperatures and concentrations of major species (i.e. N_2, H_2, CO, C_2H_2, O_2, and H_2O) at specific locations of CNT and ZnO growth. Temperatures within the flame structures (IDFs and CDFs) are also measured using a 125 µm Pt/Pt–10%Rh thermocouple (S-type) coated with silica to assess the actual substrate temperatures, which are expected to differ from gas-phase temperatures due to radiative effects and conductive losses along the probe lengths.

Various morphologies of MWNTs are produced catalytically on metal-alloy substrates with different compositions (i.e., Fe, Fe/Cr, Ni/Cu, Ni/Ti, Ni/Cr, Ni/Cr/Fe) in both IDFs and CDFs. Vertically well-aligned MWNTs with uniform diameters from Ni/Cr/Fe and Ni/Ti alloys are obtained, and special-structured CNTs such as regularly coiled CNTs, large bending CNTs, and Y-junction CNTs are observed. CNTs are also grown by *in-situ* reduction of metal-oxide solid spinel solutions (i.e. $NiAl_2O_4$, $CoAl_2O_4$ and $ZnFe_2O_4$) serving as catalytic substrate in the CDFs. It should be noted that CNTs produced from $ZnFe_2O_4$ are found to be composed of at least 30% SWNTs. Effects of other parameters on CNT growth are also studied, including local gas-phase temperature, carbon-based precursor species (e.g. CO, C_2H_2) concentrations, and substrate voltages bias. Our results show that voltage bias on the substrate is conducive to forming aligned CNTs, as well as enhancing their growth rates as compared to grounded conditions. As

will be seen, the variation of the aforementioned parameters strongly affects CNT formation, diameter, growth rate, yield, and morphology.

Experimental analyses evince the feasibility of producing 1D metal oxide nanostructures from flames. In this work we fabricated 1D metal oxide nanostructures in flames directly from substrates, including nanostructures of zinc oxide, tungsten oxide, iron oxide, and copper oxide.

Aligned single-crystal $WO_{2.9}$ nanowires are grown on the oxidizer side in CDFs directly from tungsten substrates. The nanowires have diameters of 20-50nm, lengths > 10µm, coverage density of 10^9-$10^{10}cm^{-2}$, and growth rates > 1µm/min. Tungsten oxide nanowires are also produced on the fuel side of CDFs, but exhibit decreased yield and lack of vertical alignment. Applying voltage to the substrate results in a change of morphology for the tungsten oxide nanostructures.

Various ZnO nanostructures (i.e. nanowires, nanorods, nanoribbons, and complex hierarchal structures) are sythesized in both IDFs and CDFs, on Zn-plated steel substrates. ZnO nanomaterials from both the fuel side and the oxidizer side are examined and compared, revealing that H_2O plays a major role and that the growth direction of nanowires from the fuel side can be different from that from the oxidizer side. Preliminary results of nanowries of iron oxide and copper oxide are obtained in CDFs.

By comparing the growth conditions of CNTs in IDFs and CDFs, local synthesis conditions for CNTs in the flame environment are extracted. Conditions for similar growth in IDFs and CDFs for ZnO nanostructure synthesis are found to coincide, revealing that local conditions for CNT and ZnO growth and their corresponding morphologies can be reasonably translated between different configurations.

1.4 Outline of this dissertation

Chapter 2 gives a background of the 1D nanostructures synthesized in this work, as well as a review of different synthesis methods. Chapter 3 describes the detailed experimental setup, diagnostics, and methods. Chapter 4 the addresses experimental characterization of the employed flame structures and compares them with simulations. Chapter 5 presents CNT results from PFs and NDFs, and compares them with works from others. Chapter 6 investigates CNT growth from IDFs on catalytic metal alloy substrates. Chapter 7 examines CNT growth from quasi-1-D CDFs on catalytic metal alloys. Chapter 8 presents CNT synthesis from metal-oxide spinel substrates in CDFs. Chapter 9 examines the nanorods/wires/ribbons of ZnO produced in the IDF. Chapter 10 examines these ZnO nanostructures produced in the 1-D CDF. Chapter 11 investigates tungsten oxide nanowires produced in CDFs. Finally, Chapter 12 offers some concluding remarks and suggestions for future work. Appendix 1 gives some preliminary results for iron oxide and copper oxide nanowire formation. Appendix 2 lists GRI Mech 1.2, the optimized chemical kinetic mechanism for natural gas combustion.

Reference

[1] Xia Y.N., Yang P.D., Sun Y.G., Wu Y.Y., Mayers B., Gates B., Yin Y.D., Kim F., and Yan H.Q., One-dimentional nanostructures: synthesis, characterization, and applications, *Adv. Mater.,* 15: 353, 2003

[2] Appell D., Wired for success*, Nature,* 419:553, 2002

[3] Samuelson L., Self-forming nanoscale devices, *Mater. Today,* 6:22, 2003

[4] Duan X.F., Huang Y., Cui Y., Wang J., and Lieber C.M., Indium phosphide nanowires as building blocks for nanoscale electronic and optoelectronic devices, *Nature*, 409:66, 2001

[5] Cui Y., Wei Q., Park H., and Lieber C.M., Nanowire nanosensors for highly sensitive and selective detection of biological and chemical species, *Science*, 293: 1289, 2001

[6] Wang Z.L., Characterizing the structure and properties of individual wire-like nanoentities, *Adv. Mater.,* 12:1295, 2000

[7] Hu J., Odom T.W., and Lieber C.M., Chemistry and physics in one dimension: synthesis and properties of nanowires and nanotubes, *Acc. Chem. Res.*, 32:435, 1999

[8]Kuzuya C., Kohda M., Hishikawa Y., Motojima S., Preparation of carbon micro-coils with the application of outer and inner electromagnetic fields and bias voltage, *Carbon*, 40:1991–2001, 2002

[9]Avigal Y., Kalish R., Growth of aligned carbon nanotubes by biasing during growth, *Appl Phys Lett* , 78(16):2291–3, 2001

[10]Srivastava A.K., Srivastava O.N., Curious aligned of carbon nanotubes under applied electric field, *Carbon,* 39:201–6, 2001

[11]Lee K.H., Cho J.M., Sigmund W., Control of growth orientation for carbon nanotubes, *Appl Phys Lett*, 82(3): 448–50, 2003

[12]Ant U, Yiming L, Hongjie D. Electric-field-aligned growth of singlewalled carbon nanotubes on surfaces. Appl Phys Lett 2002;81(18):3464–6.

[13]Colbert D.T., Smalley R.E., Electric effects in nanotube growth*, Carbon,* 33(7): 921–4, 1995

[14]Srivastava A., Srivastava A.K., Srivastava O.N., Effect of external electric field on the growth of nanotubules, *Appl Phys Lett,* , 72(14):1685–7, 1998

[15]Merchan-Merchan W., Saveliev A.V., Kennedy L.A., High-rate flame synthesis of vertically aligned carbon nanotubes using electric field control, *Carbon,* 42:599–608, 2004

Chapter 2

Literature Review

Over the past decade, much effort has been made targeting research related to 1-D nanostructures. Research on carbon nanotubes (CNTs) has been conducted extensively since its discovery in 1991. Fabrication of CNTs has made a lot of progress in terms of yield, alignment, and patterned-growth. Many properties of CNTs have been investigated, for which applications have been explored. In the late 90's, nanowires (e.g. SiC, Si, and ZnO) and inorganic nanotubes gained much research interest. In this chapter, a review of the 1D nanostructures examined in this dissertation is presented, namely CNTs and metal-oxide nanowires of zinc oxide, tungsten oxide, iron oxide, and copper oxide. Gas-phase synthesis methods are presented, along with a review of flame synthesis.

2.1 An overall introduction to gas-phase synthesis of 1D nanostructures

Gas-phase processes are generally purer than liquid-based processes. Even the most ultra-pure water contains traces of minerals that can be detrimental to the final properties of nanostructured materials. Impurities seem to be avoidable only in vacuum and gas-phase systems. Moreover, liquid-based techniques are usually a batch process.

For the synthesis of CNTs and metal-oxide nanowires, gas phase processes generally utilized include arc discharge (AD), laser ablation (LA), physical vapor deposition (PVD), and chemical vapor deposition (CVD). A precursor vapor is usually generated

first, which is then transported from a high temperature zone to low temperature zone. A substrate (with or without catalyst pre-deposited) is placed in the downstream low temperature zone. When the precursor vapor sweeps past the substrate, part of the vapor diffuses to and deposits on the substrate where CNT or metal-oxide nanowires nucleate and grow.

2.2 CNT background and its gas phase synthesis

The credit for the discovery of CNT remains in debate[1], especially for MWNTs. However, there is no doubt that the work on MWNTs was boosted by the report made by Iijima in 1991[2] showing their occurrence in the hard deposit growing at the cathode during electric arc experiments intended to produce fullerenes[1].

2.2.1 Molecular Structure of CNTs

CNTs belong to the architecture of sp^2-bonded carbon, where topological defects can create unique, closed shell structures out of planar graphite sheets[3]. As indicated in Figure 2.1, there are two types of CNTs, i.e. SWNT and MWNT. A SWNT can be visualized by simply rolling up a graphite sheet into a seamless cylinder and capping each end with half of a fullerene molecule. A MWNT can be considered as a collection of SWNTs forming concentric cylinders with a common central hollow, and a spacing between the layers that is ~0.34nm (close to that of the interlayer distance in graphite) (Figs.2.1 (b) and (c)).
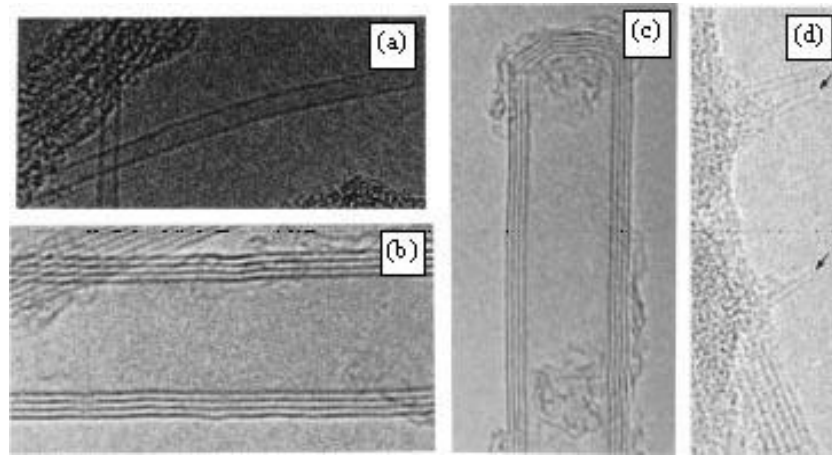
Figure 2.1 High-resolution transmission electron microscopy images of typical SWNT (a) and MWNT (b). Closed nanotube tips are also shown in panel (c) (MWNT tips) and panel (d) (SWNT tip, shown by arrows). The inner space corresponds to the diameter of the inner hollow in the tube. The separation between the closely spaced fringes in the MWNT ((b), (c)) is 0.34 nm, close to the spacing between graphite planes. The diameter of the SWNT ((a), (d)) is ~1.2 nm. Every layer in the image (fringe) corresponds to the edges of each cylinder in the nanotube assembly (Figure from reference 3).

An important structural characteristic of a CNT is its chirality, which strongly determines its properties. The rolling up of graphene sheets into cylinders can be done in several ways, such that in a general nanotube structure, on the curved surface of the tube, the hexagonal arrays of carbon atoms wind around in a chiral fashion, introducing chirality to the structure[3]. This is schematically illustrated in Figure 2.2. The chiral vector is defined on the hexagonal lattice as $C_h = n\bar{a}_1 + m\bar{a}_2$, where $\bar{a}_1$ and $\bar{a}_2$ are unit vectors; and n and m are integers. The chiral angle, θ, is measured between C_h and $\bar{a}_1$. To form the nanotube, imagine that this cell (Fig.2.2 (a)) is rolled up so that O meets A and B meets B', and the two ends are capped with half of a fullerene molecule[4,5]. The chiral vector OA thus forms the circumference of the nanotube's circular cross-section, and different values of n and m lead to different nanotube structures (Fig.2.2 (b)).

There are two special structures called armchair nanotube and zigzag nanotube. Armchair nanotubes are formed when $n = m$ and the chiral angle is 30° (Fig.2.3 (a)).

Zigzag nanotubes correspond to $(n, 0)$ or $(0, m)$ and have a chiral angle of 0° (Fig.2.3 (b)). All other nanotubes, with general (n, m) values and chiral angles between 0° and 30°, are known as chiral nanotubes (Fig.2.3(c)).
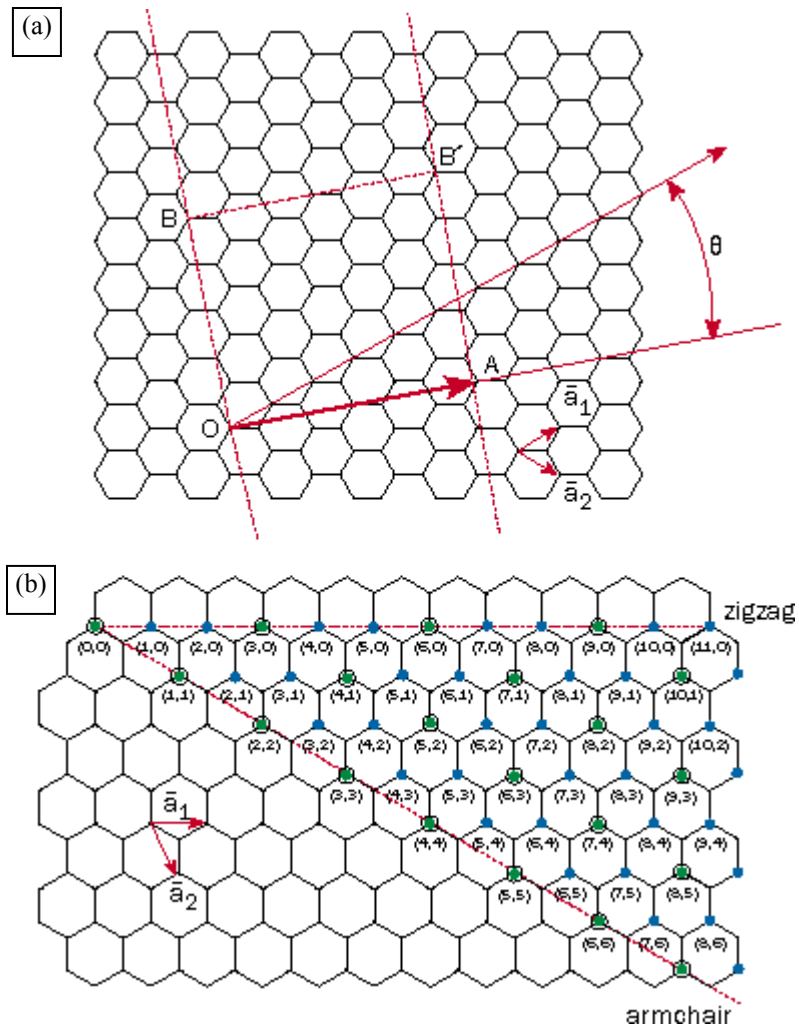
Figure 2.2 Schematic diagrams show (a) the winding procedure to form the nanotube cylinder from a planar graphene sheet, and (b) all possible structures of SWNTs can be created from chiral vectors with different (n,m) (Figure from references 4 and 5).

The diameter of a SWNT, d_t, is found to be: $d_t = (\sqrt{3}/\pi)a_{c-c}(m^2 + mn + n^2)^{1/2}$,

where a_{c-c} is the distance between neighbouring carbon atoms in the flat sheet. In turn,

the chiral angle is given by $\tan^{-1}(\sqrt{3}n/(2m+n))$[4,5].
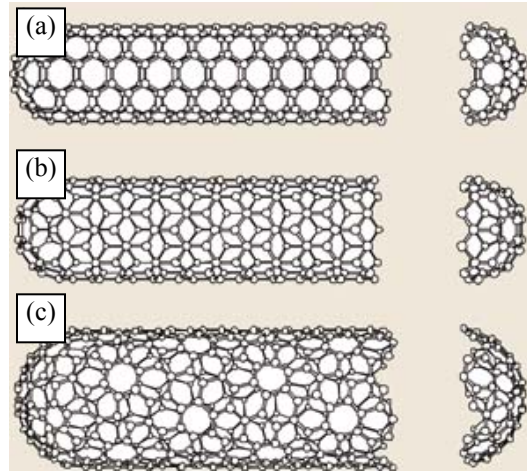
Figure 2.3 SWNTs with different chiralities. The structural differences can be identified from the open ends of the tubes, (a) armchair structure, (b) zigzag structure, (c) general chiral structure (Figure from reference 5).

2.2.2 Properties of CNT

CNTs, with fascinating nanostructures, are expected to exhibit many remarkable properties. These properties are determined mainly by their diameter, length, and chirality. According to theory, nanotubes can either be metallic (green circles in Fig.2.2 (b)) or semiconducting (blue circles in Fig.2.2 (b)), depending on their chirality.

2.2.2.1 Mechanical properties

CNTs are considered to be one of the strongest and stiffest materials known, in terms of tensile strength and elastic modulus, respectively. This results from the covalent sp^2 bonds formed between the individual carbon atoms. A tensile strength of 63 GPa has

been measured from a MWNT [6], much higher than that of high-carbon steel (approximately 1.2 GPa). The elastic modulus (Young's modulus) of a CNT has been found to be on the order of 1 TPa[7]. Additionally, CNTs have low density for a solid, 1.3-1.4 g/cm³[8], such that its specific strength of up to 48,462 kN·m/kg, compared to high-carbon steel's 154 kN·m/k*g,* is the best of known materials. However, CNTs are not nearly as strong under compression. Due to their hollow structure and high aspect ratio, they tend to undergo buckling when placed under compressive, torsional, or bending stress.

2.2.2.2 Thermal properties

All nanotubes are expected to be very good thermal conductors along the tube length, exhibiting a property known as "ballistic conduction." They are also good insulators lateral to the tube axis. An unusually high value of SWNT thermal conductivity, ~6600 W/mK, was tested for an isolated (10, 10) nanotube at room temperature[9], comparable to the thermal conductivity of a hypothetical isolated graphene monolayer or diamond[9,10]. The temperature stability of CNTs is estimated to be up to 2800 $^{\circ}$C in vacuum and about 750 $^{\circ}$C in air[8].

2.2.2.3 Electronic properties

The extraordinary electronic properties of CNTs are due to the quantum confinement of electrons normal to the nanotube axis. Because of this quantum confinement, electrons can only transport along the nanotube axis, and so their wavevectors point in this direction[4,5]. In general, a SWNT will be metallic when *n* - *m* = 3*i*, where *i* is an integer;

otherwise the nanotube is a semiconductor. All armchair nanotubes ($n=m$) are metallic, as are one-third of all possible zigzag nanotubes. Theoretically, metallic nanotubes can have an electrical current density more than 1,000 times greater than metals such as silver and copper[9].

2.2.2.4 Chemical properties

The enhanced chemical reactivity of CNTs, compared to their graphite counterparts, is due to the curvature induced $\sigma - \pi$ hybridization on the surface that alters the energy band dispersion close to the Fermi energy[3], as well as the presence of large numbers of topological defects (e.g., bond rotational defects or pairs of 5-7 rings)[11]. Furthermore, the cap ends of nanotubes have been shown to be more reactive than the sidewalls[12]. When the tubes are oxidized, the tube ends are etched away, resulting in open tubes. The presence of pentagonal defects at the ends and the extra dimensional curvature (and strain) caused by these defects are responsible for this enhanced tip reactivity. The average Mulliken population (charge density) at a pentagon is 3-4 times larger than at a graphene hexagon in both planar and tubular structures[3]. Therefore, covalent chemical modification of either sidewalls or cap ends becomes possible.

2.2.3 Potential applications of CNT

The many unique properties of CNT can lead to numerous potential applications. Some extensively studied applications are reviewed.

2.2.3.1 CNT-based composites

With remarkable mechanical strength, elasticity and low density, CNTs can be used as fillers to create composites with high strength, low weight, and excellent performance[13]. The primary concern associated with CNT-reinforced composites is in forming a strong interface between the nanotubes and the matrix such that the load can be effectively transferred between them. This is because it is likely that individual nanotube layers may slide with respect to each other in nanotube aggregates during stress transfer, due to the weak intertubular bonding in MWNT and SWNT ropes[3]. In this regard, the load transfer in compression could be better than in tension[14], which suggests that under tension, only the outer layers of the nanotubes are loaded, whereas in compression, load is transferred to all the layers.

2.2.3.2 Production and storage of energy

Due to their small dimensions, smooth surface topology and high surface specificity, CNTs have been found to be superior in electron transfer reactions[15,16]. It has been predicted that CNTs can store a liquid or a gas in the inner hollow either using gas phase adsorption (physisorption) through a capillary effect or using electrochemical storage (chemisorption). However, the experiments on hydrogen storage in nanotube samples have not been conclusive or reproducible.

2.2.3.3 Electronic devices

CNT-based film field emitters have been domonstrated[17]. A CNT film can, with threshold voltages of a few tens of volts, emit electrons at current densities of a few

hundred mA/cm^2. The nanotube electron source remains stable over several hours of field emission and is stable in air[3]. These CNT film field emitters could find their applications in flat panel displays, gas discharge tubes in telecom networks, and electron guns for electron microscopes. Field-effect transistors have been fabricated using either a single SWNT or CNT films[18,19]. Recently a transistor-like structure was reported only using a Y-branched carbon nanotube, making an overall CNT-based nanoelectronic architecture more complete and feasible[20].

2.2.3.4 Sensors and nanoprobes

Individual MWNTs or SWNTs have been used as a nanoprobe, by attaching a CNT to the end of an AFM or STM tip, for imaging[21]. Due to extremely small sizes, good conductivity, and high mechanical strength, these CNT-based nanoprobes can enhance imaging resolution compared to conventional Si or metal tips. Also, due to their high elasticity, the tips do not suffer from crashes on contact with the substrate, as any impact should cause buckling in the nanotube structure that is reversible[3].

2.2.4 CNT synthesis

2.2.4.1 CNT growth mechanism

The growth mechanism of CNTs is not exactly known, and there remains no consensus. More than one mechanism might be involved in the formation of CNTs. One of the most accepted mechanisms[22,23] (known as Baker mechanism[24]) is proposed as follows (Fig. 2.4). Catalytic nanoparticles from transitional metal/metal alloys (e.g. Fe, Ni, and Co) are assumed to be spherical or pear-shaped that are either floating or supported on a

substrate. The catalytic decomposition of the carbon precursor molecules (e.g. CH_4, CO, C_2) will take place on only one half of the nanoparticle surfaces (this is the lower curvature side for the pear shaped particles). The released carbon atoms diffuse into the nanoparticles along the concentration gradient and precipitate in solid carbon form on the opposite half around and below the bisecting diameter, when carbon supersaturation occurs upon reaching the carbon solubility limit in the nanoparticle at a given temperature[25]. The specific physical form (e.g. MWNT, SWNT, amorphous carbon and particle-encapsulated graphite cell) of the precipitated solid carbon depends on several factors, including catalyst particle size[26] and precipitation rate[27]. When the precipitation rate is in equilibrium with or less than the carbon diffusion rate, graphitic layers are formed surrounding the catalytic nanoparticles resulting in the thermodynamically most stable carbon forms[27]. When the carbon diffusion rate exceeds the precipitation rate, amorphous carbon growth may result. Only when the precipitation rate is larger than the carbon diffusion rate can CNTs growth occur[27]. Generally only catalytic nanoparticles that are sufficiently small (<20nm) are active for CNT nucleation and growth, with the tube diameter corresponding to that of the catalytic nanoparticle. That a nanoparticle of larger size tends to precipitate carbon forms other than CNTs is likely due to a diffusion rate greater than the precipitation rate, where the larger nanoparticle takes a longer time to reach the carbon supersaturation. From the point of view of minimizing energy, it would be energetically more costly for a larger nanoparticle to form a CNT than to precipitate other carbon forms[28]. In terms of CNT growth, however, solid carbons do not precipitate from the apex of the hemisphere, which accounts for the hollow core that is characteristic of CNTs. The tubule formation is due to solid-state atom diffusion at high

temperatures. Energetically, the tubule formation is attributed to the exceptionally low surface energy of the (0002) plane of graphite[29]. The tube is elongated by incorporating carbon into the graphitic lattice when more deposited carbon either diffuses into or over the surface of the catalytic nanoparticle of the particle[30]. A slow graphitization of CNT walls also happens during CNT elongation. The graphitization likely results from the annealing process that was observed in real time in a high resolution transmission electron microscope[29]. For supported catalysts, CNTs can form either by "extrusion" (also known as base growth), in which CNTs grow upward from the nanoparticles that remain attached to the substrate, or the nanoparticles detach and situate at the head of the growing CNT (known as tip-growth[31]).
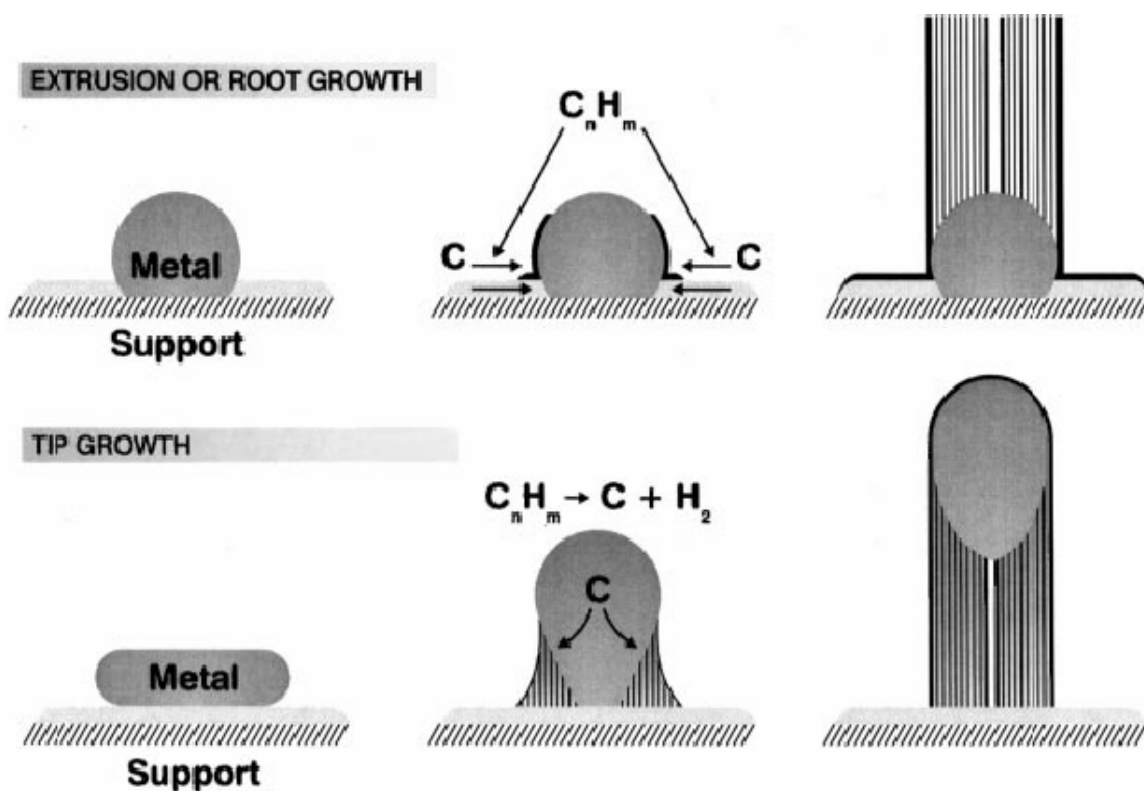
Figure 2.4 Schematic diagram of a possible growth mechanism of CNTs based on catalysts (Figure from reference 27).

Another often talked-about growth mechanism is the so-called yarmulke mechanism (Yiddish for skull cap)[28]. The key characteristic of this mechanism lies in CNT nucleation. When carbon precursor molecules (e.g. hydrocarbon) hit the surface of a catalytic nanoparticle (e.g. Fe, Ni, and Co), they stick to the nanoparticle and one of the hydrogen-carbon bonds can be catalytically broken, with the hydrogen going and leaving carbon behind. The carbon atoms bond to the nanoparticle, allowing the carbon atoms to effectively dissolve. These dissolved carbon atoms can diffuse into the particle and wander around. They can make and break bonds with metal atoms within the nanoparticle. They can also make and break bonds with each other[32]. Once carbon atoms become supersaturated in the nanoparticle, the overall circumstance would energetically favor linking the carbons together in the form of a hexagonal sheet that conforms to the curvature of the particle[32]. The "yarmulke mechanism" is such called because it resembles a little skullcap. In the case of nanoparticles supported on a substrate, the carbon "yarmulke" goes about half way around and then lifts off, with the particle remaining at the root[32]. The tube then starts growing longer by inserting newly arriving carbons into the tube network. In the case of floating catalytic nanoparticles, the strain of the carbon sheet trying to curve around the nanoparticle is so high that often it only makes a little half cap before beginning to make a tube[32]. In terms of MWNT, a second yarmulke can form underneath the first with a space roughly close to the interlayer spacing of graphite (~0.34nm)[28]. As additional yarmulkes grow, one beneath the other, older yarmulkes are forced to lift up such that a MWNT is formed, whose open end remains chemisorbed to the catalytic particle. But as the strain resulting from increasing curvature of new walls becomes too large, nucleation of new inner walls will

stop. This might explain why the inner diameters of MWNTs are rarely smaller than 3 nm[28]. In this mechanism, the diameters of CNTs are also associated with the nanoparticle size. Again the larger particles are inactive for CNT growth.

It is worth discussing carbon monoxide (CO) among the many carbon precursors. CO is a carbon precursor used often in CNT synthesis[27,33,34,35,36]. Solid carbon can be produced by CO self-disproportionation (known as the Boudouard reaction):

$$CO^{(g)} + CO^{(g)} \rightarrow C^{(s)} + CO_2^{(g)} \tag{2.1}$$
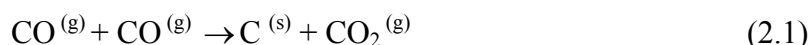
which occurs catalytically on the surface of the nanoparticle[36]. This reaction is exothermal and reversed at high temperature[27]. Unlike pyrolysis of hydrocarbon precursors, the CO disproportionation route is clean and simple making it an ideal choice for CNT synthesis. Hydrocarbon precursors readily undergo complex self-pyrolysis at temperatures higher than 800-900 °C[28]. However, thermodynamic calculations show that unsaturated hydrocarbons (e.g. C_2H_2 and C_2H_4) can decompose favorably (by the reaction $C_xH_y \rightarrow xC + 1/2yH_2$) at a low temperature (200 °C), resulting from easily disrupted π-bonds in their structure[25]. The pyrolysis of hydrocarbons can make the carbon feeding rate much greater than the tube growth rate, resulting in substantial amorphous overcoating[28]. Subsequent processing steps would be needed to remove the overcoating, which would complicate efforts to scale up production[36]. Also the pyrolysis of hydrocarbons can deactivate catalysts by accumulating amorphous carbon on the catalyst surface[25]. CO does not suffer this problem, making it an ideal precursor to produce high quality CNTs. Figure 2.5 presents thermodynamic data on the CO disproportionation reaction. As can been seen, the effective CO disproportionation reaction is limited to a temperature range of 520–800°C at normal pressure[25]. The reaction becomes inhibited

when temperatures are higher than about 900°C (CO and CO_2 equilibrium composition is 97% and 3%, respectively)[27]. But this limitation can be overcome by increasing the CO pressure, shifting the effective CO disproportionation reaction temperature range to higher temperatures[27]. This attempt has been made to increase the SWNT production yield by increasing the CO pressure[35,36]. The increase in the yield of CNTs in a CO system can also be achieved by hydrogen addition according to the reaction[34]:

$$CO^{(g)} + H_2^{(g)} \leftrightarrow H_2O^{(g)} + C^{(s)} \tag{2.2}$$
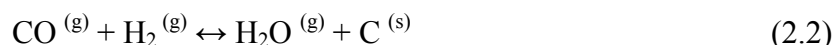
Nevertheless, CO disproportionation is much slower than hydrocarbon thermal decomposition at a given temperature and pressure[36]. Addition of a small amount of hydrocarbon (e.g. methane) helps increase the yield of clean CNTs, while a large amount of methane produces CNTs with significant amorphous overcoating[36].
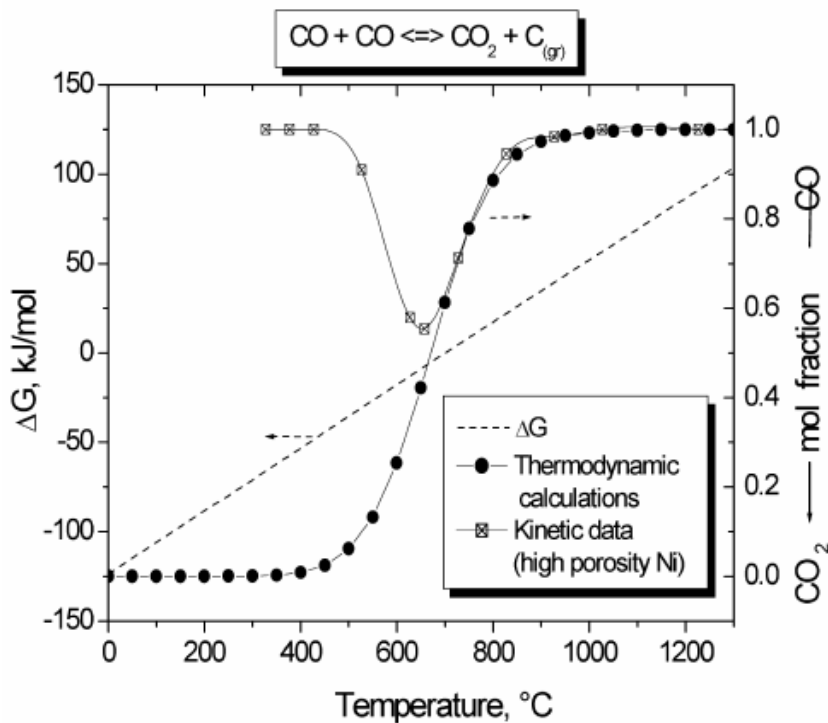
Figure 2.5 Thermodynamic data for CO disproportionation: free energy change, ΔG, and equilibrium concentration of CO in the gaseous phase. Kinetic data: CO concentration after disproportionation on the surface of a high-porosity nickel catalyst (Figure from reference 27).

In the following section, brief introductions to synthesis approaches are given for arc discharge, laser ablation, and chemical vapor deposition. Flame synthesis will be explained in detail in a later.

2.2.4.2 Arc discharge

Sumio Iijima[2] reported MWNTs by using the arc discharge technique in 1991. This technique usually uses two graphite electrodes (with or without catalysts) separated by an appropriate distance in a low-pressure chamber that is filled with noble gases (usually argon/helium)[37]. One of the electrodes is vaporized when a high temperature discharge is created between the two electrodes by a high direct current. The vaporized carbon deposits, and CNTs form on the other electrode and on the chamber wall. This technique generally produces a mixture of CNTs, amorphous carbon, fullerenes and other carbonaceous products, and the CNTs need to be separated from this mixture.

Nonetheless, it is possible to selectively produce SWNTs or MWNTs depending on the exact method. To grow SWNTs, metal catalysts, such as Fe, Co, or Ni are usually doped into the anode. The quantity and quality of as-obtained SWNTs are determined by various parameters, including the metal concentration, inert gas pressure, gas type, electric current, and system geometry. The diameter of SWNTs generally ranges from 1.2 to 1.4 nm. If both electrodes are pure graphite without metal catalysts doped, the primary products are MWNTs. The inner diameter of as-prepared MWNTs is typically in the range of 1-3 nm with an outer diameter of approximately 10nm.

2.2.4.3 Laser ablation

Smalley's group at Rice University reported the synthesis of SWNTs by laser ablation in 1995[38]. In the laser ablation technique, a pulsed or continuous laser is used to vaporize a graphite target[39] or a volume of carbon-containing feedstock gas (CH_4 or CO)[31] at a low pressure. The vaporized species is then transferred, and CNTs-containing products are deposited on a collector. Laser ablation is almost similar to arc discharge in terms of the optimum background gas and catalyst mix. This might be due to the same mechanism in both systems[31]. Uniform SWNTs can be formed using metal catalysts (e.g. Fe, Ni, and Co) in laser ablation. SWNTs are usually self-assembled to be "ropes" by van der Waals forces. The size of the SWNTs ranges from 1-2 nm with a narrower size distribution than SWNTs produced by arc-discharge.

2.2.4.4 Chemical vapor deposition

Chemical vapor deposition (CVD) synthesis is the most explored technique. In general, carbon precursors in the gas phase (e.g. CH_4, CO, C_2H_2) at elevated temperatures are swept into a furnace or a chamber which houses a substrate coated with transition metal catalysts. When the gas precursors diffuse to the substrate, the precursors catalytically decompose on the heated substrate and then CNTs grow on the substrate. This technique was demonstrated to have a good control over alignment[40,41], diameter, growth rate, as well as positional control on nanometer scale[42]. The characteristic temperature for CVD is usually between 650–900 ºC[41,42,43,44]. Different specific techniques for CNT synthesis with CVD have been developed, such as plasma enhanced CVD, thermal chemical CVD, alcohol catalytic CVD, vapor phase growth, aero gel-supported CVD, and laser assisted

CVD[31]. Generally, there are two ways to prepare catalysts for CNT growth in CVD techniques. On way is to support catalysts on a substrate. The catalysts are generally first sputtered onto a substrate. The nanosized catalytic metal particles are then formed using either chemical etching or thermal annealing. When a catalytic metal film is supported on a substrate, the thickness of the catalytic film can determine the diameter range of the CNTs[31]. Metal-oxide solid solutions are also used to prepare catalytic nanoparticles. Fresh nanoparticles can be produced upon the reduction (e.g. by hydrogen) of metal-oxide solutions, and dispersed on the surface of the reduced matrix. Another way is to prepare catalysts in the gas phase. One example is to use ferrocene $(Fe(CO)_5)$ as the catalyst precursor [45]. Ferrocene is vaporized, decomposed, and condensed into Fe nanoparticles. These nanoparticles are introduced into the synthesis system by carrier gas such that CNTs can form. The temperatures for CNT production by CVD generally range from 650–900 ^oC[46,47]. Various MWNTs and SWNTs can be prepared by CVD depending on the specific techniques and the experimental conditions.

2.2.4.5 Summary of the three synthesis methods

Table 2.1 Summary of some characteristics of arc discharge, laser ablation, and chemical vapor deposition[31].

	Arc discharge	Laser ablation	Chemical vapor deposition
Typical CNT yield	30 to 90%	up to 70%	20 to 100 %
SWNT	Short tubes with diameters of 0.6 - 1.4 nm	Long bundles of tubes (5-20 microns), with individual diameter from 1-2 nm.	Long tubes with diameters ranging from 0.6-4 nm
MWNT	Short tubes with inner diameter of 1-3 nm and outer diameter of approximately 10 nm	Not very much interest in this technique, as it is too expensive, but MWNT synthesis is possible.	Long tubes with diameter ranging from 10-240 nm
Advantages	Can easily produce SWNTs and MWNTs. SWNTs have few structural defects; MWNTs without catalyst, not too expensive, open air synthesis possible	Primarily SWNTs, with good diameter control and few defects. The reaction product is quite pure.	Easier to scale up to industrial production; long length, simple process, SWNT diameter controllable, quite pure
Disadvantages	Tubes tend to be short with random sizes and directions; often needs a lot of purification	Costly technique, because it requires expensive lasers and high power requirement, but is improving	CNTs are usually MWNTs and often riddled with defects

2.3 Backgrounds of metal-oxide nanowires and their gas-phase synthesis

2.3.1 ZnO structure, properties, and applications

Nanostuctured ZnO materials have received much attention due to their distinguished performance in electronics, optics, and photonics. Since the 1960s, synthesis of ZnO thin films has been an active field due to their applications as sensors, transducers, and catalysts[48].

At ambient conditions, the thermodynamically stable phase is wurtzite ZnO having a hexagonal unit cell with lattice parameters a = 0.3296nm and c = 0.52065nm. The structure can be described simply as a number of alternating planes composed of tetrahedrally coordinated O^{2-} and Zn^{2+} ions, stacked alternately along the c-axis[48]. The tetrahedral coordination in ZnO leads to a noncentral symmetric structure that consequently results in strong piezoelectric and pyroelectric properties. These properties could find their applications in mechanical actuactors and piezoelectric sensors.

In addition, ZnO can be used for short wavelength optoelectronic applications due to its wide band-gap (3.37 eV). The high exciton binding energy (60 meV) in the ZnO crystal can ensure efficient excitonic emission at room temperature, and room temperature ultraviolet (UV) luminescence has been reported in disordered nanoparticles and thin films[48]. ZnO is also transparent to visible light and can be made highly conductive by doping. Furthermore, ZnO is bio-safe and biocompatible, making it useful for biomedical applications without coating[49].

Intensive research has been focused on fabricating ZnO nanostructures and in correlating their morphologies with their size-related optical and electrical properties[50,51]. Various kinds of ZnO nanostructures have been realized, such as nanorods, nanowires,

nanobelts, nanotubes, nanohelixes, seamless nanorings, polyhedral cages, and nanocombs[49,52], as seen in Fig. 2.6.
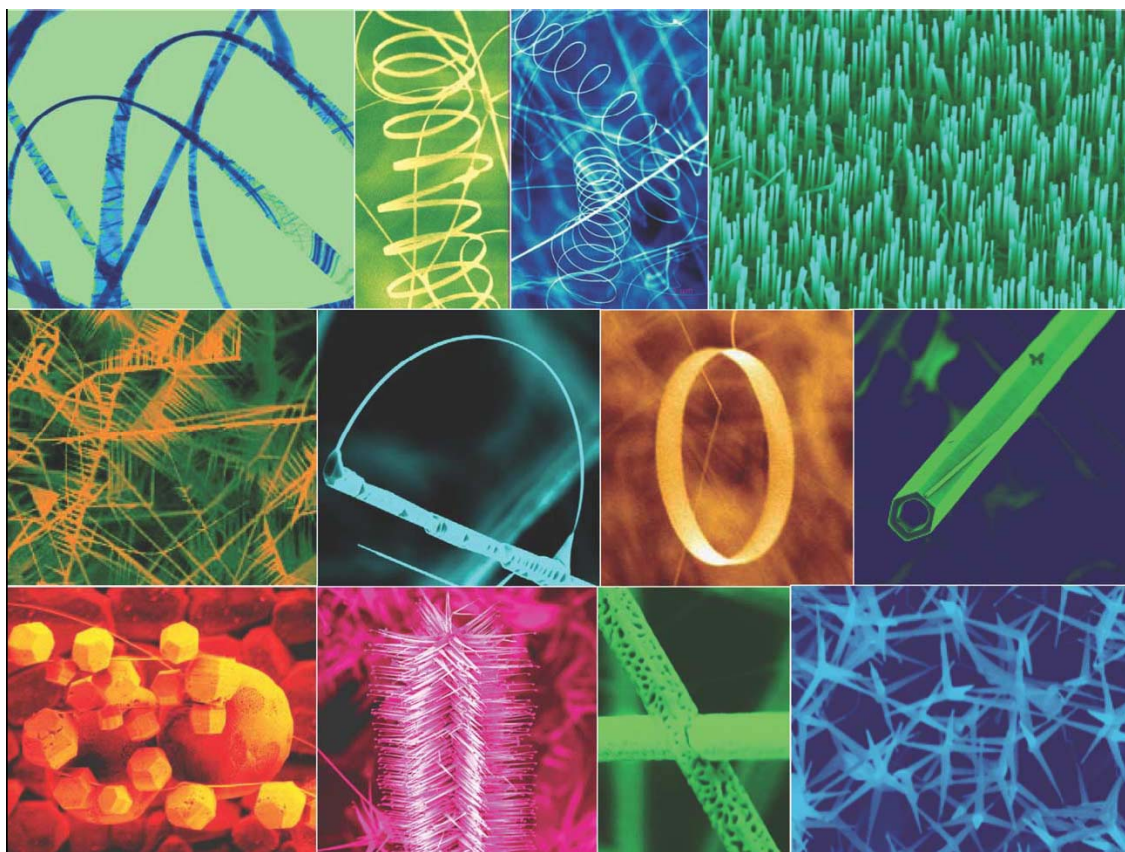
Figure 2.6 A collection of nanostructures of ZnO synthesized under controlled conditions by thermal evaporation of solid powders (Figure from reference 49).

2.3.2 Tungsten oxide structure, properties, and applications

Tungsten oxides have been intensively studied for a long period of time due to their promising physical properties (e.g. n-type semiconductor and photocatalyst) and applications (e.g. gas sensors for the determination of NO_2 and hydrogen) in chemistry[53]. Tungsten oxide can exhibit different crystal structures, such as cubic and monoclinic WO_3, tetragonal $WO_{2.9}$, and monoclinic $W_{18}O_{49}$. WO_3 has been used to construct electrochromic windows, optical devices, and gas sensors. The oxygen reduced sub-

stoichiometric tungsten oxides also display promising physical and chemical properties, such as the superconductivity of WO_{3-x} plate-like sheet particles and the catalytic activity of WO_2 crystal[54].

Recently, nanostructured tungsten oxide materials have attracted considerable attention due to their unique properties, compared those of their bulk counterparts, such as eletrochromic [55], gaschromic [56], and optochromic [57] properties. Based on these properties, devices such as information display, gas sensor, smart window, have been fabricated. Among the nanosized tungsten oxides, one-dimensional nanorod and nanowire are especially interesting, and various approaches, such as the vapor transport method[58] and the wet chemical method[59], have been reported with successful fabrication.

2.3. 3 Iron oxide and copper oxide properties and applications

Iron oxides are widely used as semiconductor, recording material, and photocatalyst[60]. Hematite (a-Fe_2O_3), the most stable form of iron oxide under ambient conditions, has received considerable attention as a solar energy conversion material due to its excellent properties, such as a small bandgap (2.1 eV), high resistivity to corrosion, and low cost[61]. Recent research has shown that the high aspect ratio of magnetic nanowires can produce a larger magnetic moment than that observed in particles of the same volume, providing significant benefits in numerous applications. One-dimensional nanostructures of magnetite (Fe_3O_4), hematite (α -Fe_2O_3), and $\varepsilon - Fe_2O_3$ also provide ideal theoretical systems for fundamental studies of electron spin and magnetic behavior of materials near quantum levels[62].

Copper oxide is a p-type semiconductor, and it is useful for the preparation of organic catalysts. Applications of copper oxides have recently been extended to gas sensors[63]. Cuprous oxide (Cu_2O) is a nonstoichiometric p-type semiconductor with a bandgap of 2.0 eV and recently has been proposed as a photocatalytic material for splitting water into H_2 and O_2 via visible light irradiation[64]. CuO is a p-type semiconductor with a band gap of 1.2 eV commonly studied for its photoconductive properties[65].

The synthesis of these materials is given as preliminary results in Appendix 1.

2.3.4 Gas phase synthesis of metal-oxide nanowires

2.3.4.1 Growth mechanism

The growth mechanisms of metal-oxide nanowires can be divided into vapor-liquid-solid (VLS) requiring a metal particle as catalyst[66] and vapor-solid (VS)[67].

Employing the vapor-solid (VS) mechanism, starting materials in a solid form of metal-oxides or metals (powder or other forms) are loaded into a synthesis tube or chamber in a vacuum environment. The starting materials are heated (e.g. electrically resistance and laser ablation) into a vapor phase. The temperatures required are different for different starting materials (usually a little bit lower than their melting points)[48]. The generated vapors in the higher temperature zone are transported by inert carrier gases (e.g. argon) to a downstream region of lower temperature where a substrate is placed. The vapors start to condense and deposit onto the substrate where nanowires nucleate and grow. Nanowires with different morphologies and diameters can be collected in different lower temperature zones[62]. At the initial stage of nucleation, the growth rates in different crystallographic planes compete against each other. A specific plane exhibiting the

fastest growth rate is usually favored leading to a preferential growth along that direction[68]. Thus a nanowire can be formed by condensing the newly incoming vapor on that specific favorable plane. The growth rate is generally determined by the surface free energy of the crystallographic plane. Crystallographic planes with relatively higher surface free energies are thermodynamically more unstable and vulnerable to attack of external molecules[68]. The surface free energy G of a specific crystallographic plane can be expressed as $G = \mu \times n$, where μ is the chemical potential of the species, and n is the atom number located on the plane[69]. The fastest growth rate usually occurs on a close-packed crystallographic plane that has a maximum number of atoms. For the VS mechanism, the supersaturation ratio of the condensing species in the gas plays a key role for nanowire growth [70, 71, 68]. To form nanowires, the supersaturation ratio of the condensing species must be kept below some critical value, above which two-dimensional or even isotropic growth occurs[68]. A low supersaturation ratio is required for anisotropic growth to form nanowires, whereas a medium supersaturation ratio leads to growth of bulk crystals. A high supersaturation ratio results in homogeneous nucleation in the vapor phase leading to powder formation[68]. As such, the local growth conditions (e.g. temperature and species concentration) can vary the critical supersaturation ratio, changing the morphologies of as-grown nanostructures.

The vapor-liquid-solid mechanism was proposed by Wagner et al[72] in 1964 when they produced single crystal Si whiskers. Generally, VLS growth for metal-oxide nanowires is composed of four main steps[73]: (1) generation and transport of growth species in vapor phase, (2) chemical reaction on the liquid catalyst droplet surface, (3) diffusion in the liquid phase, and (4) crystallization at the liquid-solid interface. Nanowires synthesized

by VLS are characterized by a metal or alloy particle located at the growth front of the wires. The particle, acting as catalyst, is maintained in the liquid phase (droplet) during the nanowire gowth, directing the nanowire growth orientation and eventually determining the nanowire diameter. In many aspects, VLS for metal-oxide nanowire growth is very similar to the process of catalytic growth of CNTs.

Many different specific fabrication techniques have been created for the gas phase synthesis of metal-oxide nanowires, such as chemical vapor deposition[74], metal-organic vapor phase epitaxy (MOVPE)[75], physical vapor deposition[76]. All these techniques are exclusively based on VS or VLS mechanism.

2.3.4.2 Physical vapor deposition

The starting materials are vaporized at an elevated temperature. The resultant vapors condense under certain conditions (e.g. temperature, pressure, and substrate properties) to produce the desired nanowires[77]. Kong *et al*[78] reported a massive production of ZnO nanowires using a physical vapor deposition approach. A powder mixture of 70% pure zinc and 30% (wt%) of pure selenium was heated in a quartz tube to 1100 °C for 10 h at a wet oxidation atmosphere (~10% O_2 plus 5% H_2, and 85% Ar) under a pressure of about 100 torr. A dark-red colored, wool-like product was collected on a water-cooled copper collector after cooling down to the room temperature. The collected products were identified as ZnO nanowires having an average diameter around 60 nm and length up to a few micrometers.

Different ZnO nanostructures can be grown by tuning the growth rates along the different growth directions[48]. There are several processing parameters such as

temperature, pressure, flow species composition, flow rate, substrate characteristics, and residence time, which can be controlled and need to be selected properly before and/or during the growth process[48]. The local temperature determines the type of product that will be obtained likely resulting from the temperature-dependent supersaturation ratio (as discussed previously for the VS growth mechanism).

2.3.4.3. Chemical vapor deposition

This technique generally involves chemical reactions on the substrate to produce nanowires. For example, Li *et al*[79] produced tungsten oxide nanowires with diameters ranging from 10 to 50 nm and lengths up to several micrometers using CVD. First, mesolamellar tungsten oxide (referred to as WO-L) with intercalated cetyltrimethylammonium (CTA+) cations was prepared through the cocondensation reaction of sodium tungstate (Na_2WO_4) and cetyltrimethylammonium bromide (CTAB) under mild hydrothermal conditions. Then the as-prepared WO-L precursor was loaded in a quartz boat and placed in the hot zone of a quartz tube furnace, where calcinations occur at 720 °C for 2 h with a pressure range from 10^{-1} to 10^{-2} atm. Ar (99.9%) was flowed into the tube to protect the medium from reacting further. After cooling down to the room temperature, tungsten oxide nanowires were finally produced. It was observed in their experiments that high argon flow rate and low temperature rising speed were favorable for the formation of tungsten oxide nanowires.

2.3.4.4 Metal-organic vapor phase epitaxy

This method employs metalorganic materials as the precursor for nanowire growth. Using this technique, Park *et al*[80] grew vertically well-aligned ZnO nanowires on Al_2O_3 (001) substrates at 400°C. Diethylzinc (DEZn) was used as Zn precursor and introduced into the MOVPE system at low-pressure, along with oxygen as reactant and argon as carrier gas. A typical growth temperature was in the range of 400–500°C, and the growth time is 1 hour with no catalysts involved. The as-obtained ZnO nanowires exhibited uniform diameter (~25nm) and length (~800nm).

2.4 Flame synthesis of 1D nanostructures

Due to the various advantages presented by flame routes mentioned in Chapter 1, the flame synthesis of 1D nanostructures, primarily CNTs, has been explored by several research groups over the last few years.

2.4.1 Flame synthesis of CNTs

A number of works have shown that flame synthesis can be exploited as a relatively inexpensive, yet robust method for growing filamentous carbon nanostructures. These works are primarily focused on premixed flames and normal diffusion flames, whereas inverse diffusion flames and counter-flow diffusion flames (as studied in this work) have been rarely researched. A premixed flame is defined as a flame where the oxidizer and fuel are completely mixed before burning (e.g. Bunsen flame). A normal diffusion flame is defined here as a flame established in a co-flow jet burner where the fuel is issued from the inner tube and the oxidizer is flowed through the outer annulus. When the fuel and oxidizer are inverted in a co-flow jet burner, an inverse diffusion flame is formed. A

counter-flow flame is established from two converging nozzle burners arranged in an opposed setup with a fixed distance, where oxidizer issued from one burner impinges onto the fuel flow issued from the other burner.

2.4.1.1 CNTs in premixed flames

Initial studies of CNTs in premixed flames began in 1994. Howard and coworkers in 1994[81] and 1995[82] reported CNT synthesis in a premixed flame under low pressure (20–97 torr), with burner gas velocity between 25 and 50 cm/s. They explored a number of different fuels and fuel/oxygen compositions (C/O ratios) including acetylene (C/O 1.06, φ=2.65), benzene (C/O 0.86–1.00, φ=2.15–2.65) and ethylene (C/O 1.07, φ=3.21), with diluent concentrations between 0% and 44 mol%. The equivalence ratio (φ) is defined as the actual fuel/oxygen ratio divided by the stoichiometric fuel/oxygen ratio corresponding to conversion of all carbon to CO_2 and all hydrogen to H_2O[83]. These flames were 'sooting' flames as soot agglomerates suspended in the flame gases were spontaneously generated. The reported CNTs ranged from 2 nm to 30 nm in size with a hollow core measuring about 1 nm to 10 nm in diameter and containing 5 to 20 shells[82]. Around the same time in 1994, Duan *et al*[84] also reported the synthesis of CNTs in a premixed flame established by mixing benzene vapor, oxygen, and argon above a water-cooled burner surface. The pressures varied from 30 to 70 torr, and the C:O ratio was 0.9. Large quantities of fullerene-rich soot were produced in the flame front, in which nanotubes were randomly distributed. All the nanotubes were identified as MWNTs with the number of walls usually higher than ten. For some tubes, the walls were up to 0.1 µm thick. Their lengths range from 0.3 to 2 µm.

Very small amounts of SWNTs were observed in 1996 by Richter *et al*[85] in an acetylene/oxygen/argon-premixed flame, and no detailed information was given. A detailed study of SWNTs in premixed flames was reported in 2000 by Diener et al[86]. The work was performed in premixed flames using different fuel gases (acetylene, ethylene, or benzene) in a low-pressure chamber (80 torr). Iron and nickel biscompounds (cyclopentadiene) were vaporized and introduced into an inert gas (argon) feed line that mixes with the fuel gas and oxygen at the burner. SWNTs were observed in acetylene and ethylene sooting flames (over equivalence ranges of 1.7–3.8) along with a few MWNTs (<5% of all CNTs), while only MWNTs were observed in benzene flames (over equivalence ratios of 1.7–3.4). These long (> 10μm) MWNTs were filled with metals exhibiting many defects. The absence of SWNTs in benzene flames was attributed to the slower dissociation rate of benzene on the nanometer-sized particles versus these for acetylene and ethylene.

Later on, Vander Wal and coworkers also conducted research on CNT (SWNT and MWNT) synthesis in premixed flames[87,88,89,90,91,92,93,94]. They usually utilized an annular burner configuration consisting of a 50 mm diameter sintered metal plate with a central tube of 11 mm diameter mounted flush with the surface of the burner plate[83,95]. A fuel-rich premixed flame was established on the outer annular section of the burner plate. Reactant gas mixtures, including metal catalyst species, were introduced through a central tube. A chimney was placed vertically in the flame gases and CNT samples were collected at the exit of the chimney. In a comparative study of CNTs synthesized in premixed flames and in a high-temperature tube furnace[88], the premixed flame used acetylene/air mixtures of equivalence ratios between 1.4 and 1.62. Two types of reactant

gas mixtures were examined (carbon monoxide/hydrogen and acetylene/hydrogen), along with iron or nickel nanoparticles. It was found that the reactant gas mixture of carbon monoxide/hydrogen generally yielded SWNTs with iron, while the acetylene/hydrogen mixture usually produced MWNTs with nickel. This observation was attributed to the susceptibility of the metal nanoparticle toward restructuring induced by adsorption of CO[96]. Iron is known to readily undergo such restructuring upon CO absorption. The restructuring enhances the reactivity of an iron nanoparticle such that it begins to catalyze SWNTs at an earlier particle growth stage (smaller diameter). Nickel does not undergo such restructuring upon CO adsorption, and thus can remain inactive toward catalyzing CNT growth from CO. In addition, they found that acetylene did not induce such restructuring towards either iron or nickel. Vander Wal and coworkers investigated a number of techniques to introduce metal catalyst particles into the aerosol-based synthesis system. In one study[89], an ultrasonic nebulizer was used to produce a fine mist of aerosol droplets from a solution of metal nitrate or ferrofluid. These droplets were entrained into a flow of inert gas or CO, where the water was removed by a dryer at 140°C, to produce an aerosol of metal nitrate particles or ferrofluid particles. SWNT growth was observed for the residence times of catalytic nanoparticles less than 100ms within the flame. In another study[90], ferrocene was used as a catalyst precursor reagent introduced via sublimation into the reactant gas mixture in the center tube. A sample holder containing ferrocene was placed within the central tube. By adjusting the height of the sample holder to vary the sublimation temperature, the mass introduction rate of ferrocene was controlled from 1 to 50 mg/min. The ferrocene vapor was entrained into the reactant gas mixtures. In contrast to the aerosol catalyst methods discussed above,

supported catalyst methods have been used in several studies of MWNT growth in premixed flames for various hydrocarbon fuels and equivalence ratios[93,94]. For example, a submonolayer film (<10 nm) of cobalt as catalyst was coated onto 304 stainless steel meshes (400 x 400 mesh with 0.0009 in. diameter wire) by physical vapor deposition (PVD). Metal islands resembling droplets were formed upon the mesh support to serve as catalyst particles. Meshes were maintained in the flame gases for 12 min, measured from the time of insertion to extraction. Samples were collected from the different height within the flame and cooled by immersion in flowing N_2 through a 1 in. diameter quartz tube to avoid air oxidation.

Height and coworker[83] studied SWNTs produced in a premixed acetylene/oxygen/15 mol% argon flame operated at a pressure 50 torr. Iron pentacarbonyl ($Fe(CO)_5$) was used as the metallic catalyst precursor, with the vapor supplied to the premixed feed gases via a temperature-controlled (4.0 ± 0.5°C) bubble saturator unit using argon as the carrier gas. The catalyst-feeding rate was adjusted by proportioning the total argon flow between the saturator and a bypass line, with typical $Fe(CO)_5$ feed concentrations of 6000 ± 500 ppm (molar). Thermophoretic sampling was conducted at various heights-above-burner (HAB). The immediate post-flame region (10–40 mm HAB) was dominated by catalyst particle formation and growth. SWNTs were observed to form after 40 mm HAB with an order of magnitude growth-rate between 10 and 100 μm per second. The as-obtained SWNTs were revealed to be bundles with individual SWNT diameters between 0.9 and 1.5 nm. Particles associated with SWNT bundles were identified as primarily Fe_2O_3. A SWNT formation 'window' was observed with formation limited to fuel equivalence ratios between 1.5 and 1.9.

2.4.1.2 CNTs in normal diffusion flames

In 2001, Yuan *et al*[97] reported the synthesis of MWNTs in a laminar co-flow methane-air diffusion flame using the catalyst-supported method. Methane (99.9% purity) was flowed through a 1.1 cm diameter stainless-steel tube, which was surrounded by a 5 cm diameter tube through which air was issued. A normal diffusion flame was established on the burner port at atmospheric pressure. A stainless-steel grid with a holding wire of 0.4 mm diameter bare Ni/Cr (60%Ni/ 26%Cr/14%Fe) was inserted horizontally into the flame at certain height and was retained for 15-30 min. The materials found on the grid contained MWNTs with diameters between 20 and 60 nm. The encapsulated nanoparticles were identifies as nickel oxides, suggesting their ability catalyze MWNT growth. The growth zone of MWNTs was found to be on the fuel side and in the post-flame region where oxygen concentration is low. Using the same setup, Yuan and coworkers[98] produced entangled and curved MWNTs from an ethylene–air diffusion flame with yield rate of 3 mg/min. These MWNTs were 10nm to 60nm in diameter. The entangled MWNTs were straightened by adding nitrogen to the flame, probably due to lowering of the flame temperature. Well-aligned MWNTs were produced on a cobalt-electrodeposited stainless steel grid placed in the nitrogen-diluted ethylene diffusion flame. These well-graphitized MWNTs were about 20 nm in diameter and 10 μm in length.

Vander Wal[99] also reported MWNTs grown on supported catalysts in a normal diffusion flame. The flame was stabilized on burner consisting of a central fuel tube (11.0 mm inner diameter) surrounded by an air co-flow. Metal nitrate as catalyst

precursor was supported on TiO_2 powder (400 mesh). The metal catalyst particle shape was found to determine the nanotube structure.

2.4.1.3 CNTs in inverse diffusion flames

Relatively little research has been conducted on the synthesis of CNTs in inverse diffusion flames. In 2004, Lee et al[100,101] reported the synthesis of MWNTs in an inverse ethylene diffusion flame using the supported catalyst techniques. The burner consisted of two concentric tubes, with 11 and 94 mm diameters, respectively. An inverse diffusion flame was established by supplying air through the central tube at a fixed rate of 0.8 l/min while flowing the mixture of ethylene and nitrogen throughn the outer tube at fixed rates of 5 and 30 l/min, respectively. The visible flame length was approximately 20 mm with mainly blue color due to the large amount of nitrogen dilution. A Pyrex glass chimney was installed to prevent ambient air from perturbing the flame. Two bare stainless steel (304) plates coated with $Ni(NO_3)_2$ (nickel nitrate, hex-hydrate) was placed at a height 10 mm above the burner and retained for 120s. MWNTs with diameters of 20–60 nm were formed on the substrate. By controlling a radial distance from the flame to the substrate the effects of temperature variation of the catalyst substrate on the formation of nanomaterials were investigated. The CNTs were found to grow in the region of 5–7 mm from the flame center along the radial direction. The gas temperature for this region ranged from 1300 to 800 K. However, nanofibres dominate the region ranging from 1000 to 800 K, and the region ranging from 1300 to 1000 K was dominated by MWNTs.

2.4.1.4 CNTs in counter-flow diffusion flames

Like the inverse diffusion flame, counter-flow diffusion flames have been relatively unexplored for CNT synthesis. In 2001, Merchan-merchan *et al*[102] reported the growth of MWNTs in a counter-flow diffusion flame without catalysts. A flame was established in a counter-flow burner consisting of two opposing streams of gases. The fuel (methane) was issued from the top nozzle and the oxidizer ($50\%O_2 50\%/N_2$ mixture) was supplied from the bottom nozzle. Co-flowing nitrogen was supplied through a cylindrical annular duct around the outer edge of the oxidizer nozzle, extinguishing the flame near the outer jacket and preventing dissipation into the environment. The quantity of obtained MWNTs was small, and the quality of the MWNTs was not given. The growth of nanotubes was proposed to be through pyrolysis of hydrocarbons resulting from an increase of radicals due to oxygen enrichment. Later in 2003, Saveliev and Merchan-merchan *et al*[103] reported a relatively large quantity of MWNTs and carbon nanofibres in the same flame by inserting a Ni-alloy probe. The 0.64-mm diameter probe with a length of 40mm was Ni-based alloy with composition 73%Ni/17%Cu/10%Fe. The catalytic probe was inserted radially through a flame-protecting shield into the yellow soot-containing region of the flame (the fuel side) and was retained for 10 min. The different positions (heights) along the flame axis were investigated, and various morphologies of MWNT and nanofibres were observed. The diversity of formed nanomaterials was attributed to the strong variation of flame properties along the flame axis including temperature, hydrocarbon and radical pool. In 2004, Merchan-merchan *et al*[104] produced vertically aligned MWNTs on the same composition catalytic probe in the same flame by means of an electric field induced from the flame. It was observed that the presence of an

electric potential provides the ability to control the nanostructure morphology and synthesis rate. A thick layer (35–40 μm) of vertically aligned MWNTs was formed on the probe surface, which exhibited uniformity and narrow distribution of nanotube diameters.

2.4.1.5 Summary of some flame geometries for CNT growth

Table 2.2 lists some reported flame types and growth conditions under which CNTs are produced.

Table 2.2 Summary of some specific flame configurations reported for CNT synthesis (reference 83)

Author	Burner configuration	Flame type	Flow 1	Flow 2	Catalyst
Vander Wal et al. [17]		Diffusion	Fuel flow: 0.15 slm C_2H_2 or C_2H_4; 1.75 slm N_2	Oxygen flow: 0 to 11 slm air (exact flow not specified in paper)	Cobaltocene
Saito et al. [12,15,18,43]		Diffusion	Fuel flow: 0.93 slm CH_4, or 0.27 slm C_2H_4	Oxygen flow: 74.2 slm	Ni-Cr-Fe wire substrate
Merchan-Merchan et al. [16]		Diffusion	Fuel flow: CH_4/C_2H_2 (flow not stated)	Oxygen flow: O_2/N_2 (Flow not stated)	None
Vander Wal et al. [26-30]		Pyrolysis 'flame' (with outer annular premix flame)	Reactant gas: CO/H_2 C_2H_2/H_2 $CO/C_2H_2/H_2$ + diluents	Annular flame: 11.0 slm air; 1.5 slm C_2H_2	Fe, Ni (evaporation [27]; colloidal [28]; metallocene [29];nebulizer [26,30])
Vander Wal et al. [31]		1st stage diffusion flame 2nd stage premixed	Reactant gas: $CO/H_2/He$ (0.25 slm ea.)+exhaust gas & ambient air	Annular flame: 11.0 slm air; 1.5 slm C_2H_2	Fe (iron nitrate on filter paper)
Vander Wal et al. [32,33]		Premixed	Fuel flow: CH_4; C_2H_2; C_2H_4; C_2H_6; C_3H_8 (flow varied to give various equiv ratios)	Oxygen flow: 1.5 slm Air	Cobalt on stainless steel mesh
Diener et al. [25]		Premixed	Fuel flow: ~3.75 slm C_2H_2, C_2H_4 and C_6H_6	Oxygen flow: O_2 + Ar (Flow not stated)	Fe, Ni (from Ferrocene, Nickelocene vapor)
Height et al. (present study)		Premixed	Fuel flow: ~1.5 slm C_2H_2	Oxygen flow: ~1.9 slm O_2 +15% Ar	Fe (from $Fe(CO)_5$ vapor)

As can be seen, most of the above-referred papers focus on premixed flames and normal jet diffusion flames. Moreover, no detailed flame structures were given such that the correspondence of the local growth conditions and CNT properties remain unclear. In addition, the derivation of a general growth condition in flame environment still remains challenging due to the lack of comparisons among flame geometries. This research work concentrates on CNT production from inverse diffusion flames and counter-flow diffusion flames. The detailed flame structures will be given computationally and experimentally to map out the relations between the local growth conditions and CNT properties. Influences of catalyst properties and external electrical application on the CNT growth in the flame environment will be intensively investigated. "Universal" growth conditions in flames will be established through comparisons between IDFs and CDFs.

2.5.2 Flame synthesis of metal –oxide nanowires

Although many techniques have emerged to fabricate 1-D nanostructures of metal-oxides, this work represents some of the first investigated flame synthesis of metal-oxide nanowires[105,106,107,108]. Recently, Height *et al*[109] reported the nanorods of ZnO made by flame spray pyrolysis, and Merchán-Merchán *et al*[110] presented flame synthesis of molybdenum oxide whiskers. Through experimental analysis, the feasibility and advantages of 1D nanostructures of metal oxide from the flame technique are presented. For the first time, this work successfully produces 1D nanostructures of metal-oxide directly from metal substrates in flames, including nanorods/wires/ribbons of ZnO, tungsten oxide nanowires, and nanowires of iron oxide and copper oxide.

Reference

[1] Monthioux M., and Kuznetsov V. L., Who should be given the credit for the discovery of carbon nanotubes?, *Carbon*, 44(9): 1621, 2006

[2] Iijima S., Helical microtubles of graphitic carbon. *Nature,* 354:56, 1991

[3] Ajayan P. M., Nanotubes from Carbon*, Chem. Rev.,* 99:1787, 1999

[4] Dresselhaus M.S., Dresselhaus G., and Eklund P.C., Science of Fullerenes and Carbon Nanotubes, *Academic Press, New York,* 1996

[5] Ebbesen T., Carbon Nanotubes: Preparation and Properties, *CRC Press, Boca Raton, Florida*, 1997

[6] Yu M.-F. et. al, Strength and breaking mechanism of multiwalled carbon nanotubes under tensile load, *Science,* 287: 637-640, 2000

[7] Forró L., et al, Electronic and mechanical properties of carbon nanotubes, in Science and Application of Nanotubes (Tomanek and Enbody, eds), Kluwer Academic/Plenum Publishers, New York, 2000

[8] Philip G. C., and Phaedon A., Nanotubes for electronics, *Scientific American,* December 2000

[9] Berber S., Kwon Y.K., and Tománek D, Unusually high thermal conductivity of carbon nanotubes, *Physical review letters,* 84(20): 4613, 2000

[10] Che J., Cağın T., and Goddard III W.A., Thermal conductivity of carbon nanotubes, *Nanotechnology,* 11:65, 2000

[11] Ebbesen, T. W., Carbon Nanotubes: Preparation and Properties, CRC Press: Boca Raton, FL, 1997.

[12] Ajayan P. M., Ebbesen T. W., Ichihashi T., Iijima S., Tanigaki K., and Hiura H., Opening carbon nanotubes with oxygen and implications for filling, *Nature,* 362:522, 1993

[13] Wagner H. D., Lourie O., Feldman Y, and Tenne R., Stress-induced fragmentation of multiwall carbon nanotubes in a polymer matrix, *Appl. Phys. Lett.,*72:188, 1998

[14] Schadler L. S, Giannaris S. C., and Ajayan P. M., Load transfer in carbon nanotube epoxy composites, *Appl. Phys. Lett.*, 73:3842,1998

[15] Che G., Lakshmi B. B., Fisher E. R., and Martin, C. R., Carbon nanotubule membranes for electrochemical energy storage and production, *Nature,* 393:346, 1998

[16] Britto P. J., Santhanam K. S. V., Alonso V., Rubio A., and Ajayan,P. M., Improved charge transfer at carbon nanotube electrodes, *Adv. Mater.,*11:154, 1998

[17] de Heer W. A., Chatelain A., Ugarte D., A Carbon nanotube field-emission electron source, *Science,* 270:1179, 1995

[18] Baughman R. H., Zakhidov A. A., and de Heer W. A., Carbon nanotubes--the route toward applications, *science,* 297:787, 2002

[19] Tans S. J., Verschueren A. R. M., and Dekker C., Room-temperature transistor based on a single carbon nanotube, *Nature*, 393:49, 1998

[20] Bandaru P.R., Daraio C., Jin S. and Rao A.M., Novel electrical switching behaviour and logic in carbon nanotube Y-junctions, *Nature: materials,* 4:663, 2005

[21] Dai H. J., Hafner J. H., Rinzler A. G., Colbert D. T., Smalley R.E., Nanotubes as nanoprobes in scanning probe microscopy, *Nature,* 384:147, 1996

[22] Yasuda A., Kawase N., and Mizutani, W., Carbon-Nanotube Formation Mechanism Based on in Situ TEM Observations, Journal *of Physical Chemistry B,* 106(51): 13294, 2002

[23] Sinnot S. B., Andrews R., Qian D., Rao A. M., Mao Z., Dickey E. C., and Derbyshire, F., Model of carbon nanotube growth through chemical vapor deposition, *Chem.Phys.Lett.*, 315:25, 1999

[24] Baker RTK, Barber MA, Harris PS, Feates FS, Waite RJ, Nucleation and growth of carbon deposits from the nickel catalyzed decomposition of acetylene, *J Catal,* 1972;26(1):51–62.

[25] Moisala A., Nasibulin A.G., and Kauppinen E.I., The role of metal nanoparticles in the catalytic production of single-walled carbon nanotubes – a review, *J. Phys.: Condens. Matter,* 15:s3011, 2003

[26] Cheung C. L., Kurtz A., Park H. and Lieber C. M., Diameter-Controlled Synthesis of Carbon Nanotubes , *J. Phys. Chem. B*, 106:2429, 2002

[27] Nasibulin A. G., Moisala A., Brown D. P. and Kauppinen E. I., Carbon nanotubes and onions from carbon monoxide using $Ni(acac)_2$ and $Cu(acac)_2$ as catalyst precursors, *Carbon,* 41:2711,2003

[28] Hongjie Dai, Andrew G. Rinzler, Pasha Nikolaev, Andreas Thess, Daniel T. Colbert,Richard E. Smalley, Single-wall nanotubes produced by metal-catalyzed disproportionation of carbon monoxide, *Chemical Physics Letters,* 260 (1996) 471-475

[29] J. Y. Huang, S. Chen, Z. F. Ren, G. Chen, and M. S. Dresselhaus, Real-Time Observation of Tubule Formation from Amorphous Carbon Nanowires under High-Bias Joule Heating, *NANO LETTERS,* 2006 Vol. 6, No. 8 1699-1705

[30] Christian P. Deck, Kenneth Vecchio, Growth mechanism of vapor phase CVD-grown multi-walled carbon nanotubes, *Carbon,* 43 (2005) 2608–2617

[31] Daenen M., de Fouw R.D., Hamers B., Janssen P.G.A., Schouteden K. and Veld M.A.J., The wondrous world of carbon nanotubes, Eindhoven University of Technology, 2003

[32] Bucky Balls, Fullerenes, and the Future: An Oral History Interview with Professor Richard E. Smalley January 22, 2000

[33] Dragos Ciuparu,* Yuan Chen, Sangyun Lim, Gary L. Haller, and Lisa Pfefferle, Uniform-Diameter Single-Walled Carbon Nanotubes Catalytically Grown in Cobalt-Incorporated MCM-41, *J. Phys. Chem. B*, Vol. 108:504-507, No. 2, 2004

[34] Bo Zheng, Chenguang Lu, Gang Gu, Alexander Makarovski,Gleb Finkelstein, and Jie Liu, Efficient CVD Growth of Single-Walled Carbon Nanotubes on Surfaces Using Carbon Monoxide Precursor, *NANO LETTERS*, 2002,Vol. 2, No. 8:895-898

[35] D.E. Resasco, W.E. Alvarez, F. Pompeo, L. Balzano, J.E. Herrera, B. Kitiyanan and A. Borgna, A scalable process for production of single-walled carbon nanotubes (SWNTs) by catalytic disproportionation of CO on a solid catalyst, *Journal of Nanoparticle Research*, 4: 131–136, 2002.

[36] Pavel Nikolaev, Michael J. Bronikowski, R. Kelley Bradley, Frank Rohmund, Daniel T. Colbert, K.A. Smith, Richard E. Smalley, Gas-phase catalytic growth of single-walled carbon nanotubes from carbon monoxide, *Chemical Physics Letters*, 313:91–97,1999

[37] Ebbesen T. W. and Ajayan P. M., Large-scale synthesis of carbon nanotubes, *Nature*, 358:220,1992

[38] Guo, T., Nikolaev, P., Thess, A., Colbert, D. T., and Smalley, R. E., Chemical Physics Letters, 243,(1,2), 1995

[39] Guo T., Nikolaev P., Thess A., Colbert D. T., and Smalley R. E., Catalytic growth of single-walled manotubes by laser vaporization. *Chemical Physics Letters*, 243:49, 1995

[40] Damnjanovic M., Milosevic I., Vukovic T., and Sredanovic R., Full symmetry, optical activity, and potentials of single-wall and multiwall nanotubes, *Physical Review B*, 60 (4): 2728, 1999

[41] Ren Z. F., Huang Z. P., Xu J. W., Wang J. H., Bush P., Siegel M. P., and Provencio P. N., Synthesis of large arrays of well-aligned carbon nanotubes on glass*, Science,* (Washington, D.C.), 282(5391): 1105, 1998

[42] Ren, Z. F., Huang, Z. P., Wang, D. Z., Wen, J. G., Xu, J. W., Wang, J. H., Calvet, L. E., Chen, J., Klemic, J. F., and Reed, M. A., Growth of a single freestanding multiwall carbon nanotube on each nanonickel dot, *Applied Physics Letters*, 75(8): 1086, 1999

[43] Yudasaka M., Kikuchi R., Matsui T., Ohki Y., Yoshimura S., and Ota E., Specific conditions for Ni catalyzed carbon nanotube growth by chemical vapor deposition, *Applied Physics Letters*, 67(17): 2477, 1995

[44] Yudasaka M., Kikuchi R., Ohki Y., Ota E., and Yoshimura S., Behavior of Ni in carbon nanotube nucleation, *Applied Physics Letters*, 70(14): 1817, 1997

[45] Lee, Cheol Jin, Lyu, Seung Chul, Kim, Hyoun Woo, Park, Chong Yun, and Yang, Cheol Woong, *Chemical Physics Letters*, 359, (1,2), 2002

[46] Ren, Z. F., Huang, Z. P., Xu, J. W., Wang, J. H., Bush, P., Siegel, M. P., and Provencio, P. N., *Science* (Washington, D.C.), 282, (5391), 1998

[47] Yudasaka, Masako, Kikuchi, Rie, Matsui, Takeo, Ohki, Yoshimasa, Yoshimura, Susumu, and Ota, Etsuro, *Applied Physics Letters*, 67, (17), 1995

[48] Wang Z.L., Zinc oxide nanostructures: growth, properties and applications, *J. Phys: Condens. Matter,*16: R829, 2004

[49] Wang Z.L., Nanostructures of zinc oxide, *Mater. Today*, 7:26, 2004

[50] Keem K, Kim H, Kim GT, Lee JS, Min B, Cho K, Sung MY, Kim S, Photocurrent in ZnO nanowires grown from Au electrodes, *Appl. Phys. Lett.* 84:4376. 2004

[51] Arnold M.S., Avouris P., Pan Z.W., Wang Z.L., Field-effect transistors based on single semiconducting oxide nanobelts*, J. Phys. Chem. B*, 107:659, 2003

[52] Park J.H., Choi H.J., Choi Y.J., Sohn S.H., Park J.G., Ultrawide ZnO nanosheets*., J. Mater. Chem,* 14:35, 2004

[53] Koltypin Y., Nikitenkob S.I., and Gedanken A., The sonochemical preparation of tungsten oxide nanoparticles, *J. Mater. Chem.,* 12:1107, 2002

[54] Liu Z., Bando Y., and Tang C., Synthesis of tungsten oxide nanowires, *Chemical Physics Letters*, 372:179, 2003

[55] Cheng W., Baudrin E., Dunn B., and Zink J., Synthesis and electrochromic properties of mesoporous tungsten oxide, *J. Mater. Chem.,* 11(1): 92, 2001

[56] Solis J.L., Saukko S., Kish L., Granqvist C.G., and Lantto V., Semiconductor gas sensors based on nanostructured tungsten oxide, *Thin solid Films,* 391:255, 2001

[57] Sayama K., Mukasa K., Abe R., Abe Y. and Arakawa H., Stoichiometric water splitting into H2 and O2 using a mixture of two different photocatalysts and an IO3–/I– shuttle redox mediator under visible light irradiation., *Chem. Commun,* 23: 2416, 2001

[58] Vaddiraju S., Chandrasekaran H., and Sunkara M.K., Vapor phase synthesis of tungsten nanowires, *J. AM. CHEM. SOC.*, 125:10792, 2003

[59] Lou X.W., and Zeng H.C., An inorganic route for controlled synthesis of $W_{18}O_{49}$ nanorods and nanofibers in solution, *Inorg. Chem.,* 42:6169, 2003

[60] Fu Y., Chen J., Zhang H., Synthesis of Fe2O3 nanowires by oxidation of iron, *Chemical Physics Letters*, 350:491, 2001

[61] Fu Y.Y., Wang R.M., Xu J., Chen J., Yan Y., Narlikar A.V., Zhang H., Synthesis of large arrays of aligned a-Fe2O3 nanowires, *Chemical Physics Letters*, 379:373, 2003

[62] Morber, J. R., Ding, Y., Haluska, M. S., Li, Y., Liu, J. P., Wang, Z. L., and Snyder, R. L., PLD-Assisted VLS Growth of Aligned Ferrite Nanorods, Nanowires, and NanobeltssSynthesis, and Properties, *J. Phys. Chem. B,* 110:21672, 2006

[63] Wang W., Zhan Y. and Wang G., One-step, solid-state reaction to the synthesis of copper oxide nanorods in the presence of a suitable surfactant, *Chem. Commun.,* 727–728, 2001

[64] Oh J., Tak Y. and Lee J., Electrodeposition of Cu2O nanowires using nanoporous alumina template, *Electrochemical and Solid-State Letters*, 7(3): C27, 2004

[65] Wang W., Varghese O.K., Ruan C., Paulose M. and Grimes C.A., Synthesis of CuO and Cu2O crystalline nanowires using Cu(OH)2 nanowire templates, *J. Mater. Res.,* 18(12): 2756, 2003

[66] Wen J.G., Lao J.Y., Wang D.Z., Kyaw T.M., Foo Y.L., Ren Z.F., Self-assembly of semiconducting oxide nanowires, nanorods, and nanoribbons, *Chem. Phys. Lett*, 372:717, 2003

[67] Hu J.Q., Quan L.., Wong N.B., Lee C.S., Lee S.T., Synthesis of uniform hexagonal prismatic ZnO whiskers, *Chem. Mater.,* 14:1216, 2002

[68] Yung-Jung Hsu and Shih-Yuan Lu, Vapor-Solid Growth of Sn Nanowires: Growth Mechanism and Superconductivity, *J. Phys. Chem. B,* 2005, 109, 4398-4403

[69] Tiller, W. A. The Science of Crystallization: Microscopic Interfacial Phenomena; *Cambridge University Press*: New York, 1991.

[70] Xia, Y.; Yang, P.; Sun, Y.; Wu, Y.; Mayers, B.; Gates, B.; Yin, Y.; Kim, F.; Yan, H. AdV. Mater. 2003, 15, 353.

[71] Sears, G. W. *Acta Metall.* 1955, 3, 361.

[72] Wagner R.S., Ellis W.C., Vapor-liquid-solid mechanism of single crystal growth, *Applied physics letters,* 4(5): 89-90, 1964

[73] Zhuo Chen and Chuanbao Caoa, Effect of size in nanowires grown by the vapor-liquid-solid mechanism, *APPLIED PHYSICS LETTERS,* 88: 143118, 2006

[74] Wang, Y.W., Zhang, L.D., Wang, G.Z., Peng, X.S., Chu, Z.Q., and Liang, C.H., "Catalytic growth of semiconducting zinc oxide nanowires and their photoluminescence properties," Journal of Crystal Growth 234:171-175 (2002).

[75] Ogata K., Maejima K., Fujita Sz., Fujita Sg., Growth mode control of ZnO toward nanorod structures or high-quality layered structures by metal-organic vapor phase epitaxy, *Journal of crystal Growth,* 248:25, 2003.

[76] Zhang Y., Wang N., Gao S., He R., Miao S., Liu J., Zhu J., and Zhang X., A simple method to synthesize nanowires, *Chem. Mater,* 14:3564, 2002

[77] Dai Zurong, Zheng Weipan and Wang Zhongling, Novel nanostructures of functional oxides synthesized by thermal evaporation, *Adv. Funct. Mater.*, 13:9-24, 2003

[78] Kong Y.C., Yu D.P., Zhang B., Fang W., and Feng S.Q., Ultraviolet-emitting ZnO nanowires synthesized by a physical vapor deposition approach, Applied physics letters, 78:407-409, 2001

[79] Xiao-Lin Li, Jun-Feng Liu, and Ya-Dong Li, Large-Scale Synthesis of Tungsten Oxide Nanowires with High aspect ratio, *Inorganic Chemistry*, 42(3): 921-924, 2003

[80] W. I. Park, D. H. Kim, S.-W. Jung, and Gyu-Chul Yia, Metalorganic vapor-phase epitaxial growth of vertically well-aligned ZnO nanorods, *Applied Physics Letters,* 80(22): 4232-4234, 2002

[81] J.B. Howard, K. Das Chowdhury and J.B. Vander Sande, Carbon shells in flames. Nature 370 6491,1994

[82] K. Das Chowdhury, J.B. Howard and J.B. Vander Sande, Fullerenic Nanostructures in Flames. J. Mater. Res. 11 2 (1996), pp. 341–347

[83] Murray J. Heighta, Jack B. Howard, Jefferson W. Testera and John B. Vander Sande, Flame synthesis of single-walled carbon nanotubes, Carbon, 42(11): 2295-2307, 2004

[84] Duan H.M, Mc Kinnon J.T. Nanoclusters produced in flames. J. Phys Chem, 98 (49): 12815-8. 1994.

[85] H. Richter, K. Hernadi, R. Caudano, A. Fonseca, H.N. Migeon, J.B. Nagy et al., Formation of nanotubes in low pressure hydrocarbon flames. Carbon 34 3 (1996), pp. 427–429

[86] M.D. Diener, N. Nichelson and J.M. Alford, Synthesis of single-walled carbon nanotubes in flames. J. Phys. Chem. B 104 41 (2000), pp. 9615–9620

[87] Vander Wal R.L., Lee J.H., Ferrocene as a precursor reagent for metal-catalyzed carbon nanotubes: competing effects*, Combust Flame* , 130:27-36, 2002

[88] R.L. Vander Wal and T.M. Ticich, Flame and furnace synthesis of single-walled and multi-walled carbon nanotubes and nanofibers. J. Phys. Chem. B 105 42 (2001), pp. 10249–10256

[89] R.L. Vander Wal and T.M. Ticich, Comparative flame and furnace synthesis of single-walled carbon nanotubes. Chem. Phy. Lett. 336 1–2 (2001), pp. 24–32.

[90] R.L. Vander Wal and L.J. Hall, Ferrocene as a precursor reagent for metal-catalyzed carbon nanotubes: competing effects. Combust. Flame 130 1/2 (2002), pp. 27–36.

[91] R.L. Vander Wal, Flame synthesis of Ni-catalyzed nanofibers. Carbon 40 12 (2002), pp. 2101–2107

[92] R.L. Vander Wal, G.M. Berger and L.J. Hall, Single-walled carbon nanotube synthesis via a multi-stage flame configuration. J. Phys. Chem. B 106 14 (2002), pp. 3564–3567

[93] R.L. Vander Wal, L.J. Hall and G.M. Berger, Optimization of flame synthesis for carbon nanotubes using supported catalyst. J. Phys. Chem. B 106 51 (2002), pp. 13122–13132

[94] Vander Wal RL, Hall LJ, Berger GM. The chemistry of premixed flame synthesis of carbon nanotubes using supported catalysts. Proceedings of the Twenty-Ninth Symposium (International) on Combustion, The Combustion Institute, 2002. p. 1079–85

[95] Vander Wal R.L., Lee J.H., Ferrocene as a precursor reagent for metal-catalyzed carbon nanotubes: competing effects*, Combust Flame* , 130:27-36, 2002

[96] Rodriquez N.M., Kim M.S., Baker R.T., J. Catal., 144:93, 1993

[97] Yuan L, Saito K, Pan C, Williams F.A., Gordon AS. Nanotubes from methane flames, *Chem Phys Lett* , 340:237-41, 2001

[98] Yuan L., Saito K., Hu W., Chen Z., Ethylene flame synthesis of well aligned multi-walled carbon nanotubes*, Chem Phys Lett,* 346:23-8, 2001

[99] Vander Wal R.L., Flame synthesis of substrate-supported metalcatalyzed carbon nanotubes, *Chem Phys Lett.,* 324:217-23, 2000

[100] Lee G.W., Jurng J., Hwang J., Synthesis of carbon nanotubes on a catalytic metal substrate by using an ethylene inverse diffusion flame, *letters to the editor/Carbon*, 42:6982-685, 2004

[101] Lee G.W., Jurng J., Hwang J., Formation of Ni-catalyzed multiwalled carbon nanotubes and nanofibres on a substrate using an ethylene inverse diffusion flame, Combust. Flame, 139: 167-175, 2004

[102] W. Merchan-Merchan, A. Saveliev, L.A. Kennedy and A. Fridman, Formation of carbon nanotubes in counter-flow, oxy-methane diffusion flames without catalysts. Chem. Phys. Lett. 354 1–2 (2002), pp. 20–24

[103] A.V. Saveliev, W. Merchan-Merchan and L.A. Kennedy, Combust. Flame 135 (2003), pp. 27–33.

[104] W. Merchan-Merchan, A.V. Saveliev and L.A. Kennedy, Carbon 42 (2004), pp. 599–608

[105] Xu F., Liu X., and Tse S.D., Synthesis of Carbon Nanotubes on Metal Alloy Substrates with Voltage Bias in Methane Inverse Diffusion Flames, *Carbon,* 44(3): 570-577, 2006

[106] Xu F., Zhao H., and Tse S.D., Carbon Nanotube Synthesis on Catalytic Metal Alloys in Methane/Air Counterflow Diffusion Flames, *Proceedings of the Combustion Institute,* 31(2): 1839-1847, 2006

[107] Xu, F., Liu, X., Tse, S.D., Cosandey, F., and Kear, B.H., Flame Synthesis of Zinc Oxide Nanowires, submitted to *Chemical Physics Letters,* 2007.

[108]Xu F., Tse S.D., Al-Sharab J.F., and Kear B.H., Flame Synthesis of Aligned Tungsten Oxide Nanowires, *Applied Physics Letters*, 88: 243115, 2006

[109]Height M.J., Mädler L. and Pratsinis S.E., Nanorods of ZnO made by flame spray pyrolysis, *Chem. Mater.*18:572-578, 2006

[110]Merchán-Merchán W., Saveliev, A.V., and Kennedy, L.A., Flame synthesis of molybdenum oxide whiskers*, Chemical Physics Letters*, 422: 72-77, 2006

Chapter 3

Experimental Setup

The synthesis experimental setups and characterization techniques of 1D nanostructures from flames are described in this chapter. Two different setups are used in this work to probe the flame synthesis of 1D nanostructures. One setup is based on a co-flow jet burner, on which premixed flames (PFs), normal diffusion flames (NDFs), and inverse diffusion flames (IDFs) are produced. Another setup is based on two opposing flow burners in which CDFs are established. The *in-situ* gas-phase diagnostic utilizes laser-based spontaneous Raman spectroscopy, which is described in Chapter 4. The characterization techniques include field-emission scanning electron microscopy (FESEM), transmission electron microscopy (TEM), energy dispersive X-ray spectrum (EDXS), and resonance Raman spectroscopy (RRS).

3.1 Setup based on a co-flow jet flow burner

This setup is mainly composed of a jet flow burner, subsystem of flow controlling and metering, and a three-way translator. The schematic diagram of this setup is shown in Fig. 3.1 and a picture of the actual setup is given in Fig. 3.2.

3.1.1 The co-flow jet flow burner

The jet flow burner (Fig. 3.1) consists of two concentric tubes. The central tube is stainless steel with a 1.22 ± 0.02 cm inner diameter, a wall thickness of 0.23 ± 0.01 mm

and a length of 70 ± 0.05 cm. This tube is placed through a concentric brass tube with an

8.9 ± 0.05 cm outer diameter, a wall thickness of 3 ± 0.01 mm, and a length of

16 ± 0.05 cm. The annular region is filled with 3 ± 0.01 mm glass beads to distribute the

gas flow, which ultimately flows through a honeycomb to produce a flat velocity profile.

The central tube is sufficiently long to produce a fully developed laminar velocity profile

at the burner exit[1]. An encompassing cylindrical quartz tube (Fig.3.2 A) prevents

ambient leakage, on which sidewall slots are machined to allow the access of a flame

igniter, sampling probe, and thermocouple.
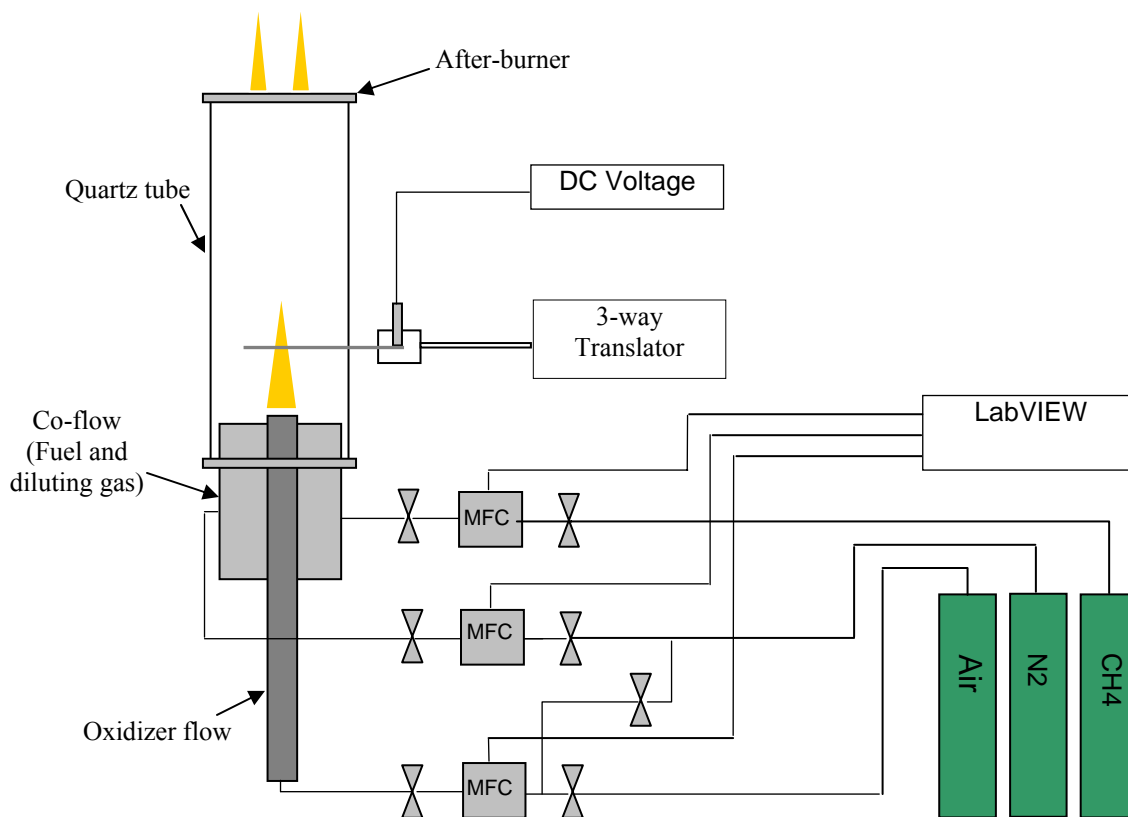
Figure 3.1 The schematic diagram (IDF) of the synthesis experimental setup based on a jet flow burner (MFC stands for mass flow controller).

When the fuel and oxidizer are mixed in the central tube before they are issued from

the central tube, a premixed flame (PF) is formed at the central tube exit surrounded by

N$_2$ flowing through the co-flow region. A normal diffusion flame can be established by flowing fuel through the central tube and issuing oxidizer through co-flow region. When fuel issues out of the co-flow region and oxidizer issues from the inner tube, an inverse diffusion flame is established, and an additional flame support afterburner at the top of the quartz tube (Fig.3.2 A) is employed as an afterburner to consume up the excess fuel. The flame heights and sampling positions are measured with a cathetometer (Fig.3.2E), and the measurement is reproducible to approximately 0.5mm.
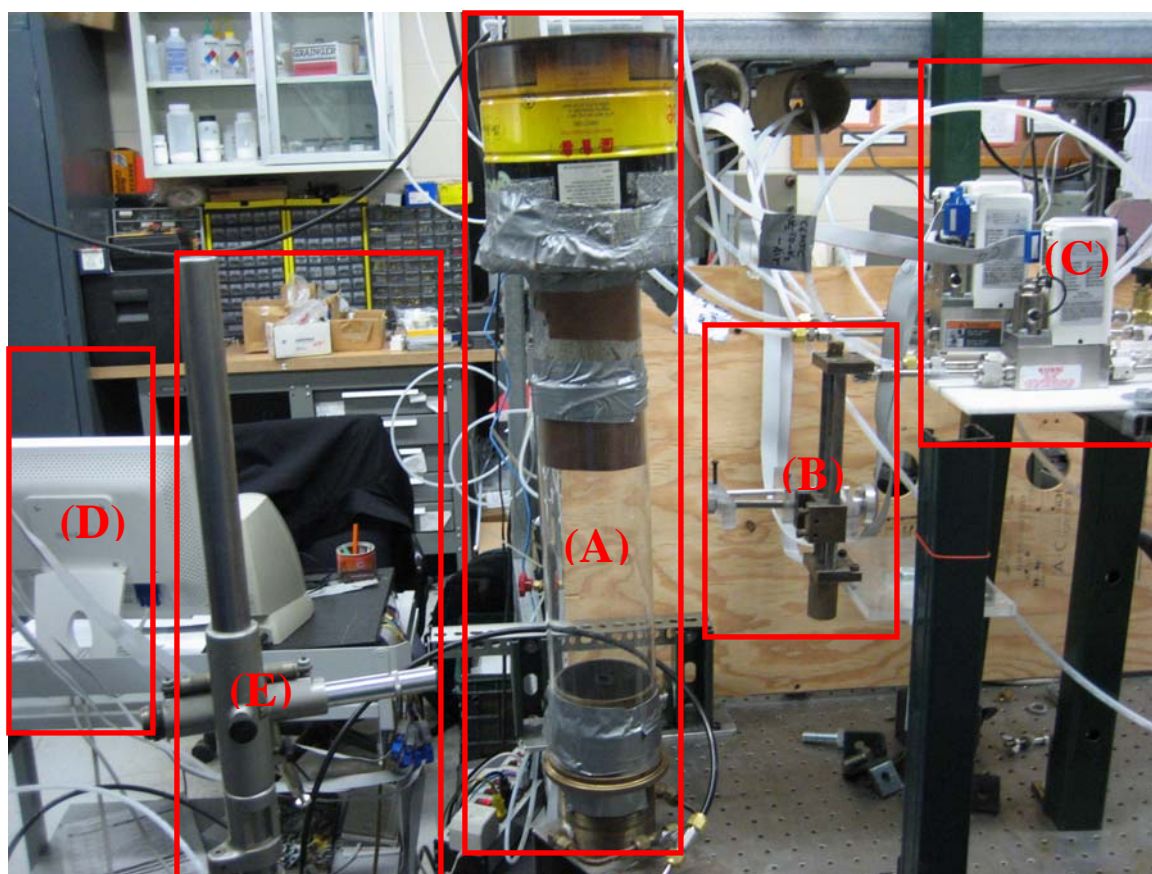
Figure 3.2. The real experimental setup of synthesis based on a jet flow burner. (A) a jet flow burner with a glass shield, (B) a 3-way translator, (C) mass flow controllers, (D) a LabVIEW program running on a computer to control the mass flow controllers, (E) a cathetometer measuring the flame hieght and the smapling position.

Additionally, the burner setup (Fig.3.2A) is easily movable, and it is very convenient to experimentally probe the flame structures by mounting the burner to a milling machine top so that it can be translated in three dimensions while keeping the excitation laser beam fixed for Raman studies.

3.1.2 Subsystem of flow controlling and metering

Mass flow controllers (MFCs) from Brooks Company (model 5850) are chosen to meter and control the gas flow rates (Fig. 3.2C). A computer program is developed from labVIEW to control the mass flow controllers through the data acquisition boards (Fig.3.2D). This can ensure the reproducibility of the flame and reduce the experimental error.

3.1.3 Three-way translator

A three-way translator (spacially resolution of 0.5mm) was designed and built as shown in Fig.3.2B, on which a sample holder is installed. Using this translator, a sampling probe can be inserted into and withdrawn from the flame structure through the sidewall slot on the glass shield. Voltage bias can be applied to the sampling probe as well (Fig.3.1).   In addition, a thermocouple can be mounted to the sample holder to measure the flame temperature profiles along the radial and vertical directions.

3.1.4 Thermocouple (TC) and its coating

To better evaluate the substrate temperatures, temperatures within flame structures are measured using a 125µm Pt/10%Rh-Pt S type thermocouple (OMEGA, Model: P10R-

005). TC junction is coated with silica to prevent catalytic oxidation on platinum-based TC in the flames. A small burner is employed to do the coating. A small premixed flame is established on the burner, and the silicon oil (Fisher scientific, Part No: NC9611089) is injected into the gas mixture by a syringe pump at a rate of 0.5 ± 0.05 ml/min. While the silicon oil is oxidizing in the flame, the TC junction is inserted into the flame. The TC junction is retained for 2 seconds in the flame, and the process is repeated 3 times. Examination under a microscope shows that the silica coating is uniform and 3 ± 0.5 μm in thickness.

3.2 Setup based on two-jet flow burners

A setup based upon two aerodynamically converging nozzle burners was designed and built. This setup mainly consists of two opposing burners, a subsystem of flow controlling and metering, a ventilation hood, water cooling lines, a cathetometer, and a three-way translator for the catalytic probe. The entire setup is mounted on a small milling machine top to make easy access for investigating the flame structures by laser diagnostics. The schematic diagram of this setup is shown in Figure3.3 and a picture of the actual setup is given in Figure 3.4.
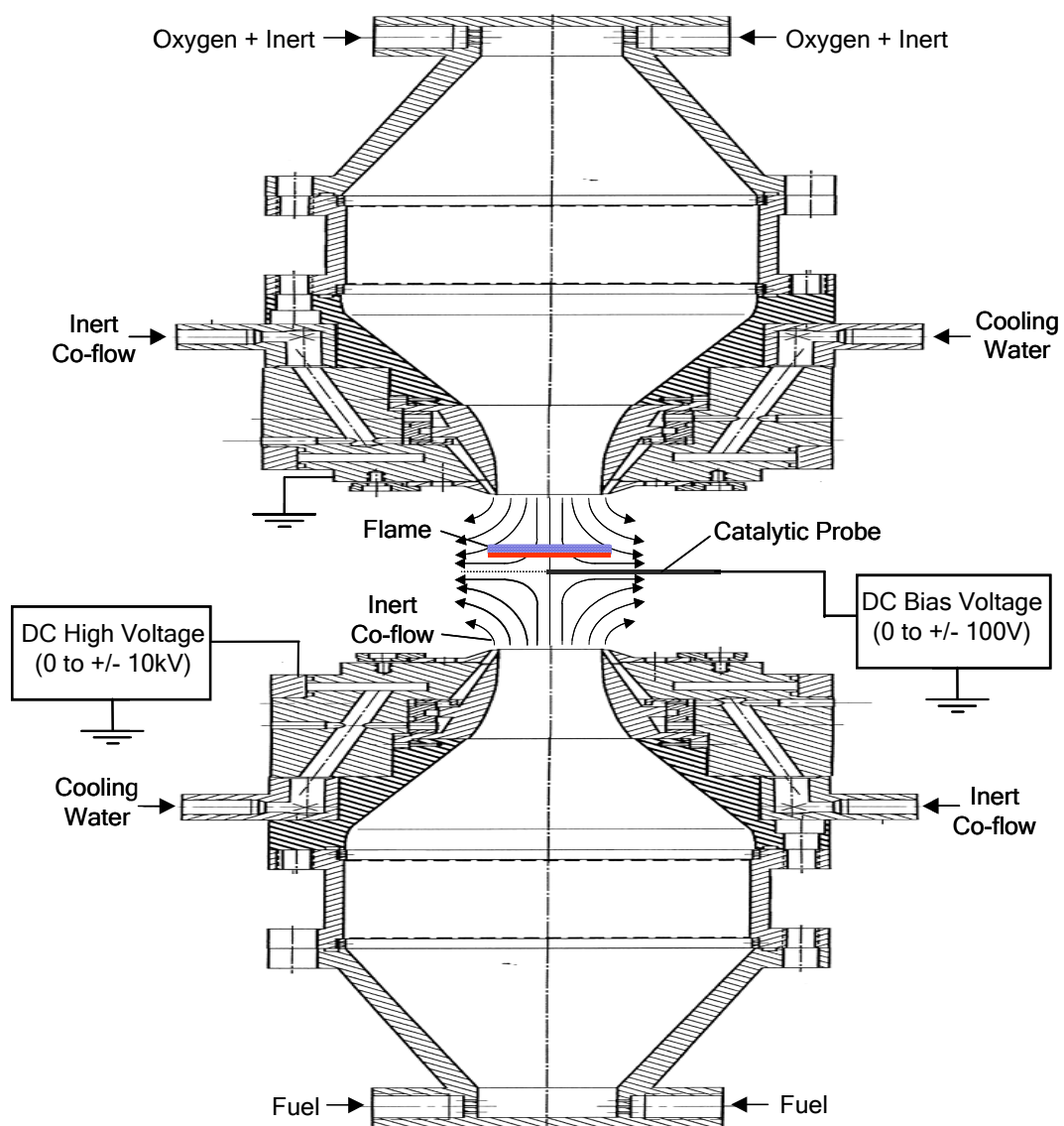
Figure 3.3 the schematic diagram of the counter-flow burners setup.
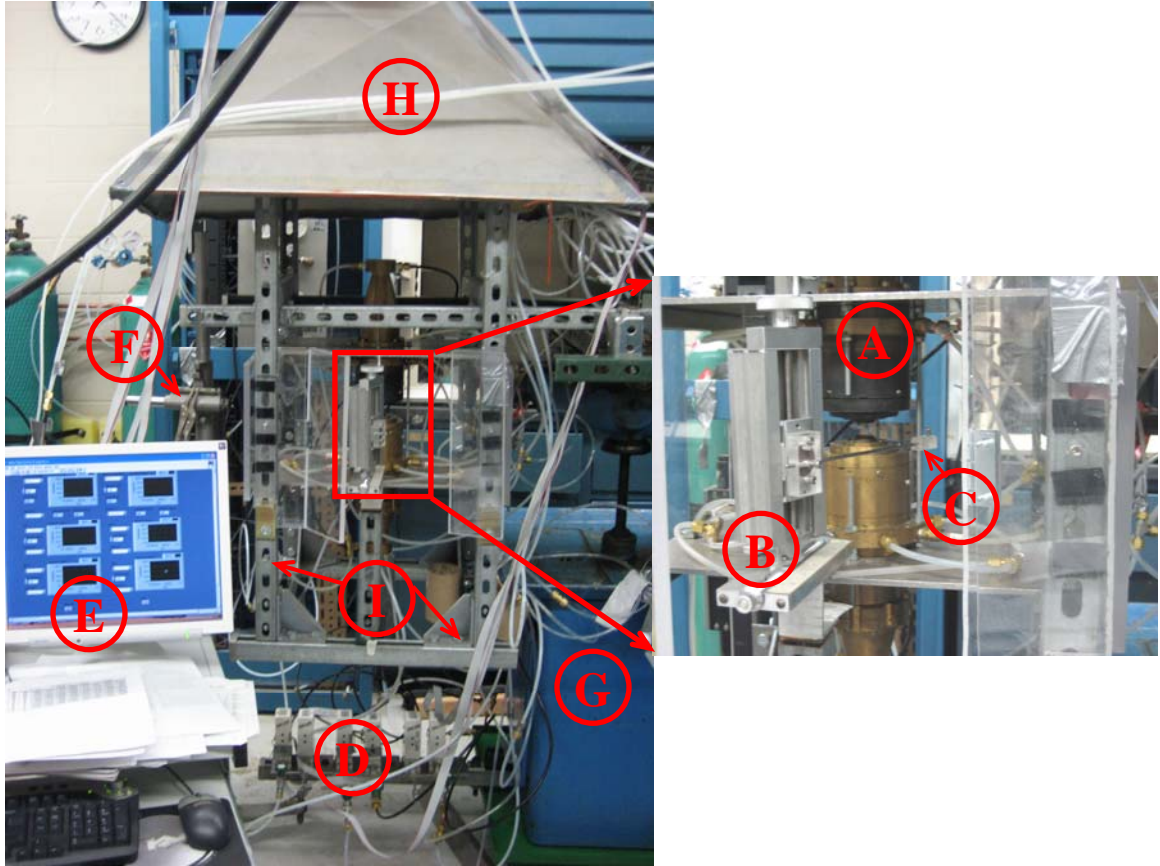
Figure 3.4. The real experimental setup based on counter-flow burners. (A) burners with water-cooling lines, (B) a 3-way translator, (C) a sampling holder, (D)mass flow controllers, (E) a LabVIEW program running on a computer to control the mass flow controllers, (F) a cathetometer measuring the flame hieght and the smapling position, (G) a small milling machine, (H) the ventilating hood, (I) UNISTRUT support.

3.2.1 the two converging-nozzle burners

The burner configuration, as shown in Fig. 3.3 and Fig. 3.4A, consists of two convergent nozzles with a 19mm exit diameter and 15mm separation distance. The exit flows have a top-hat velocity profile. Airflow as oxidizer is issued from the top burner, and nitrogen-diluted fuel flow is issued from the bottom burner, establishing a flat flame in-between (CDF). Co-flowing nitrogen eliminates oxidizer entrainment into the flame, extinguishes the outer flame, and minimizes shear instabilities. Both burners are water-cooled.

For the relative concentrations of fuel and oxidizer used in our experiments, the flame is located on the oxidizer side of the stagnation surface. The resulting flames are

monitored by a cathetometer (Gaertner scientific corporation, Serial No. 1089A) and flickering of these flames is minimal, with less than ±75μm of spatial displacement. A picture of the CDF is shown in Figure 3.5.

Figure 3.5 A CDF flame.

3.2.2 Description of other subsystems

The burner configuration is supported with a UNISTRUT frame (Fig. 3.4I), which is mounted to a small milling machine. An enclosure is built with transparent glass to protect the flame from disturbance by surroundings. At the top of the frame is located a ventilating hood to remove the excess fuel and flame gas products. The subsystem of flow controlling and metering, and the three-way translator are almost the same as those depicted in a jet flow burner based setup.

3.3 Experimental procedures

Two main flame configurations are utilized in this work: inverse diffusion flame and counter-flow diffusion flame. The experimental procedures for operating these two configurations are given below (a labVIEW program interface is illustrated in Table 3.1).

3.3.1 Experimental procedure for Inverse Diffusion Flames

(1) Place the experimental setup under a ventilation hood.

(2) Turn on the roof fan.

(3) Turn on the compressed air on the wall.

(4) Turn on the methane cylinder and the nitrogen cylinder, setting the regulator pressure for both to 20 psi.

(5) Turn on the valves immediately upstream of the mass flow controllers (MFCs): MFC1 for methane and MFC2 for air.

(6) Turn on the power for the MFCs.

(7) Open the LabVIEW program: set MFC1 at 10 L/Min. and MFC2 at 0.8 L/Min.

(8) Turn on the valve for nitrogen metered by a flow meter (Brooks Instruments, Model No.: 1110-05H1B1A, Serial No.: 7811H63094): set the flow meter at 4.2 L/Min.

(9) Click on the RUN button in the LabVIEW program to run the program.

(10) Ignite the flame, and also ignite the afterburner on top of the quartz tube to burn out the excess methane.

(11) Set up the cathetometer, and make sure that it is level.

(12) Measure the flame height.

(13) Mount the substrate to the translator; adjust its height to the investigated flame height; and insert it radially into the flame.

(14) Run the experiment for about 10 minutes.

(15) When the sample is done, withdraw it from the flame, put it on a SEM sample stub; get ready to examine it using FESEM.

(16) After all the experimental runs are finished, shut off the methane cylinder first; let the flame burn until it goes out.

(17) Shut off the nitrogen cylinder and the compressed air.

(18) Shut off all the valves.

(19) Shut off the MFC power and the LabVIEW program.

3.3.2 Experimental procedure for Counter-flow Diffusion Flames

(1) Place the experimental setup under a ventilation hood.

(2) Turn on the roof fan.

(3) Turn on the compressed air.

(4) Turn on the methane cylinder and the nitrogen cylinder, setting the regulator pressure for both to 20 psi.

(5) Turn on the cooling water.

(6) Turn on the valves immediately upstream of the mass flow controllers (MFCs).

    (a) Flame with 50% methane and 50% nigtrogen.

      MFC1: methane, set at 1.32 L/Min.

      MFC2: nitrogen for diluting methane, set at 1.32 L/Min.

      MFC3: air, set at 2.58 L/Min.

MFC4: not used for this flame, set at 0.

MFC5: nitrogen for co-flow on the fuel side, set at 2.4 L/Min.

MFC6: nitrogen for co-flow on the oxidizer side, set at 3.2 L/Min.

(b) Flame with 42% methane plus 3% acetylene and 55% nitrogen (labVIEW settings for this fame are given at the end to be an example).

MFC1: methane, set at 1.11 L/Min.

MFC2: nitrogen for diluting methane, set at 1.45 L/Min.

MFC3: air, set at 2.58 L/Min.

MFC4: acetylene, set at 0.08 L/Min.

MFC5: nitrogen for co-flow on the fuel side, set at2.4 L/Min.

MFC6: nitrogen for co-flow on the oxidizer side, set at 3.2 L/Min.

(7) Turn on the power for MFCs.

(8) Open the LabVIEW program: set MFCs at values specified in step 6.

(9) Click on the RUN button in the LabVIEW program to run the program.

(11) Ignite the flame.

(12) Set up the cathetometer, and make sure that it is level.

(13) Measure the flame height.

(14) Mount the substrate to the translator; adjust its height to the investigated flame height; and insert it radially into the flame.

(15) Run the experiment for about 10 minutes

(16) When the sample is done, withdraw it from the flame; put it on a SEM sample stub, get ready to examine it using FESEM.

(17) After all the experimental runs are finished, shut off the methane cylinder first; let the flame burn until it goes out.

(18) Shut off the nitrogen cylinder, the compressed air, and the cooling water.

(19) Shut off all the MFC valves.

(20) Shut off the MFC power and the LabVIEW program.

Table 3.1 An interface of labVIEW program for controlling the mass flow controllers.
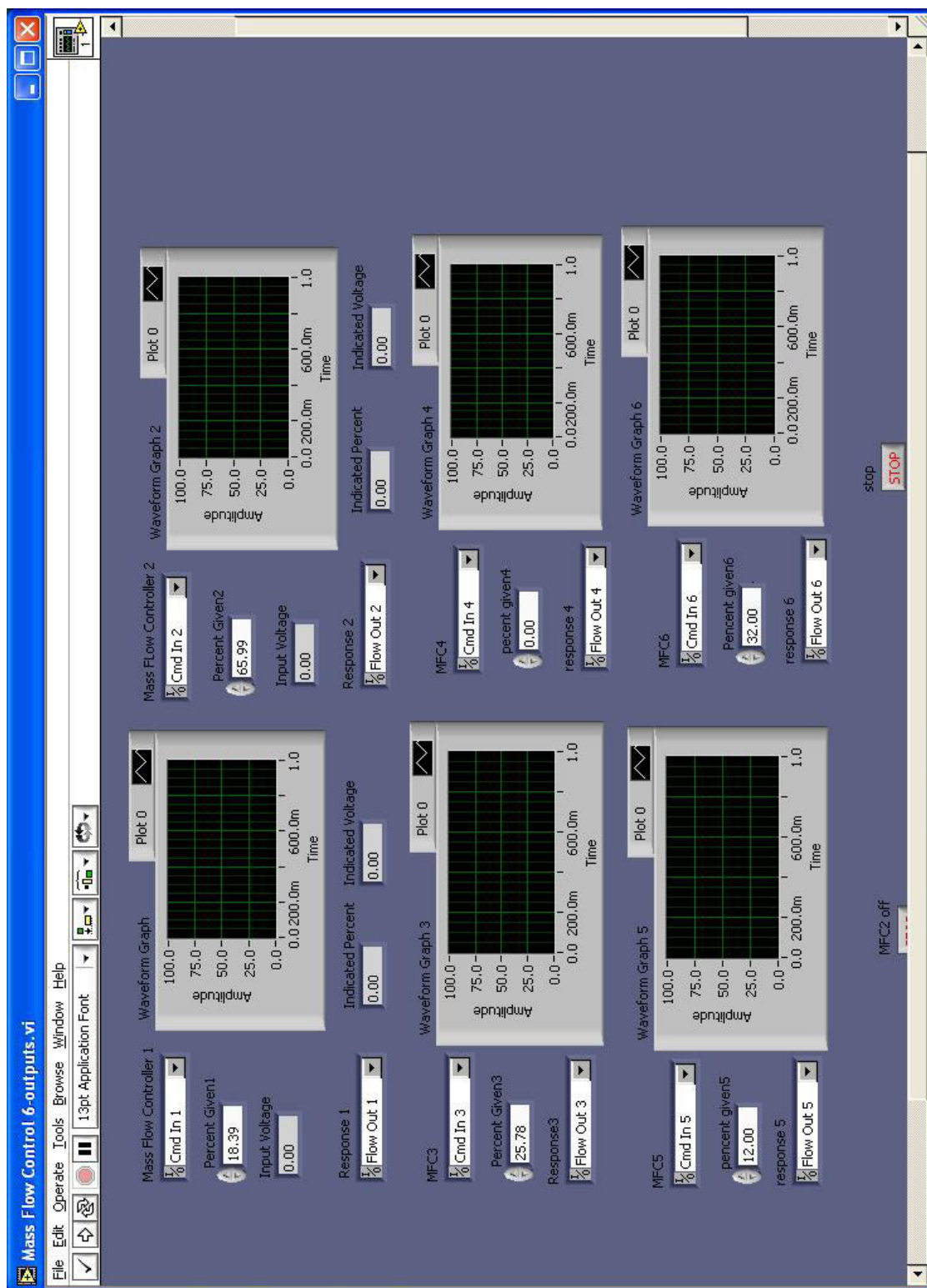
3.3.4 Information of MFCs and gases used in this work

MFCs and gases used in this work are summarized in Table 3.2 and Table 3.3 respectively.

Table 3.2 Information of MFCs used.

Name	Model No.	Flow range (L/min.)
Inverse Diffusion Flame		
MFC1	5850EME3DAMVEKC	2
MFC2	5850EME3CAL4BKC	20
Counter-flow Diffusion Flame		
MFC1	5850EMF3CAK2BKC	10
MFC2	5850EME3CAMVEKC	2
MFC3	5850EME3DAFRBKC	10
MFC4	5850EME3CAC1BKA	1
MFC5	5850EME3CAL4BKC	20
MFC6	5850EMF3CAK2BKC	10

Table 3.3 Information of gases used.

Name	Purity
Methane (CH_4)	CP grade (99%)
Acetylene (C_2H_2)	CP grade (98%)
Ethylene (C_2H_4)	CP grade (99.5%)
Nitrogen (N_2)	Extra dry grade (99.6%)
Hydrogen (H_2)	Extra dry grade (99%)

3.4 Sample preparation

All the probes tested in this work are 40 ± 1 mm long cut from their corresponding commercially obtained wires/sheets. These probes are generally cleaned for 5 ± 0.2 min in ethanol in an ultrasonic cleaner, and then are air-dried. To facilitate the identification of nanomaterial growth regions on the probe, these probes are marked at 2 ± 0.5 mm intervals at the tested end by using a razor. The tested probes in this work are given in Table 3.4.

Table 3.4 Some information about tested probes.

Name	Company	Part #
99.5% Fe	Omega	Spir-032
83% Fe / 17% Cr	A-1 wire tech, Inc.	570890
45% Ni / 55% Cu	Omega	Spir-032
56% Ni / 44% Ti	Small Parts, Inc	NW-032
80% Ni / 20% Cr	Omega	Ni80-032
60% Ni / 16% Cr / 24% Fe	Omega	Ni60-032
Zinc-galvanized steel	McMaster-Carr	8943K14
99.95%W	Small Parts, Inc	TW-032

3.5 Characterization techniques

There are many different tools to characterize the nanostructures, including *in-situ* and *ex-situ* techniques. In this work, the *ex-situ* techniques employed are FESEM, TEM, EDXS, and RRS.

3.5.1 FESEM

Scanning electron microscopy (SEM) is a basic tool for present nanotechnology, and is usually used to observe the morphologies of as-grown nanostructures, and estimate the size and yield of those nanostructures. This work uses a SEM with field emission electron source (called FESEM, LEO Zeiss Gemini 982, operated at 5 kV) to investigate the morphologies of 1D nanostructrues produced from flames, and estimate the size and yield of these structures at various magnifications ranging from 1000 to 50000. The probe with as-deposited nanomaterials is glued to a pin mount (SPI, part# 1507L) using a 9mm carbon tab (SPI, part # 5073). The pin mount is then placed in a vacuum desiccator (SPI, part#1822) for at least 12 hours.

3.5.2 TEM

TEM is performed on a TOPCON 002B ultrahigh resolution transmission electron microscope operated at 200kV in order to probe the detailed structures of the synthesized nanomaterials. Nanomaterials from flames are sonicated in methanol and then dispensed onto holey/lacey carbon coated copper grids (300 mesh, SPI, part#3630C) for TEM examination. Various magnifications are used ranging from 29k to 490K. The atomic-level structures of these 1D nanomaterials are examined using HRTEM (490K). Selected area electron diffraction (SAED) is conducted on TEM to evalutate the crystallinity and phase composition of the nanomaterials.

3.5.3 EDXS

The elemental compositions of as-prepared nanomaterials from flames are analyzed using EDXS attached to either TEM or FESEM. EDXS is conducted for nanomaterials ranging from a single nanostructure to bundles of nanostructures.

3.5.4 RRS

The "conventional" Raman scattering signal (which will be discussed in Chapter 4) is usually weak. Hundreds of bands might be shown in "conventional" Raman spectra for large molecules[2] (CNTs belong to large molecules). However, the scattering efficiency gets larger when the excitation laser frequency is tuned to match the energy between optically allowed electronic transitions (resonance) in the material[3]. Vibrational modes associated with that particular excited electronic state are greatly enhanced[2]. The enhanced signal usually overwhelms Raman signals from all of the other transitions. For instance, for CNTs, resonance with a π-π* transition enhances stretching modes of the π-bonds involved with the transition, while the other modes remain unaffected[4]. This intensity enhancement process is known as resonance Raman scattering (RRS). Usually Raman spectra are independent of the electronic structure of the material and the laser energy used to excite the Raman spectra[2]. But in RRS, the resonance Raman intensity depends on the density of electronic states (DOS) available for the optical transitions, which is very important for one-dimensional (1D) systems[2]. For single-walled CNTs (SWNTs), the transition energies depend on the diameter and chirality. As such, rich information of CNTs can be extracted from their resonance Raman spectra. In case of CNTs, tunable lasers are very important and convenient (where the wavelength can be

altered within a specific range), such that a response from a few nanotubes dominates the Raman spectrum for a particular laser excitation line. RRS is now considered as an easy and quick characterization tool for CNT samples, especially for SWNTs. The Raman spectra from CNTs are rich in information about the structure and properties of nanotubes[5]. In this work, Raman spectroscopy (performed on a Renishaw System 1000 micro-Raman spectrometer) is excited at two laser wavelengths: 633nm and 785nm, and used to detect the abundance, diameter distribution, and purity of SWNTs. The typical SWNT diameters can then be calculated from Raman spectra by using the empirical relationship $d = 248/\lambda$, where $d(nm)$ indicates the nanotube diameter and λ (cm^{-1}) is the Raman shift[6,7].

Reference

[1] Sidebotham G.W., An inverse co-flow approach to sooting laminar diffusion flames, department of mechanical and aerospace engineering, Princeton university, New Jersey, 1988

[2] Raman spectroscopy, http://en.wikipedia.org/wiki/Raman_spectroscopy

[3] Jorio A., Pimenta M.A., Souza Filho A.G., Saito R., Dresselhaus G. and Dresselhaus M.S., Characterizing carbon nanotube samples with resonance Raman scattering, *New Journal of Physics,* 5:139.1–139.17, 2003

[4] Resonance Raman spectroscopy, http://en.wikipedia.org/wiki/Resonance_Raman_spectroscopy

[5] Jorio A., Pimenta M.A., Souza Filho A.G., Saito R., Dresselhaus G. and Dresselhaus M.S., Characterizing carbon nanotube samples with resonance Raman scattering, *New Journal of Physics,* 5:139.1–139.17, 2003

[6] Saito R., Dresselhaus G. and Dresselhaus M. S., Trigonal warping effect of carbon nanotubes, *Phys. Rev. B*, 61:2981-2990, 2000

[7] Jorio A., Saito R., Hafner J. H., Lieber C. M., Hunter M., McClure T., Dresselhaus G. and Dresselhaus M. S., Structural (n, m) determination of isolated single-wall carbon nanotubes by resonant Raman scattering, *Phys Rev. Lett.,* 86:1118-1121, 2001

Chapter 4

Flame Structure Characterizations

Local temperature and growth-related species are determinative in the synthesis of 1D nanostructures. Probing these parameters is essential in controlling and optimizing the produced nanostructures and in increasing the understanding of the fundamental growth mechanisms. The establishment of correlations between these parameters, especially species, and the corresponding nanostructures is not always straightforward in synthesis systems such as electric arc discharge and laser ablations. Utilizing well-defined flame systems, however, can be advantageous for the investigation of local temperature and growth-related species through comparative modeling of the flame flow field and diagnosing through laser-based spectroscopy. At the same time, oxygen concentration distribution can be well controlled from the source to the reaction zone.

In this chapter, the simulation and experimental validation (through spontaneous Raman spectroscopy (SRS)) of flame structures of CDFs are described. Favorable comparisons between the simulation and the measurement for the well-defined 1-D configuration give confidence to the SRS measurement of flame structures of IDFs.

4.1 Flame structures of CDFs

As presented in Chapter 3, a flat flame can be formed in between when the fuel and oxidizer issued from the bottom and top burners, as they impinge at atmospheric pressure. The flame is aerodynamically well-defined, with gradients existing only in the

axial direction, and can be easily probed by SRS and compared with simulations involving detailed chemical kinetics and transport. A picture of an actual CDF is given in Fig. 4.1.
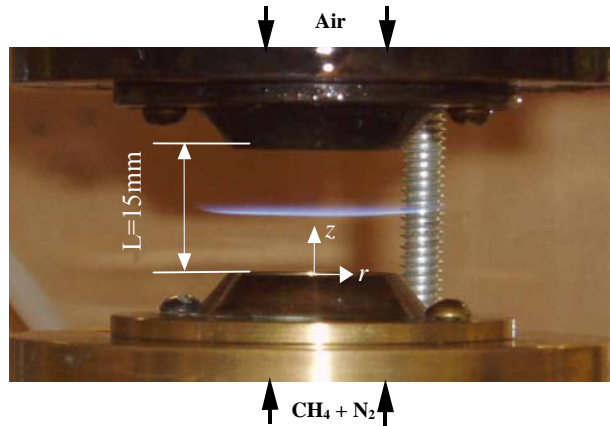
Figure 4.1 A real flame is established between the two burners.

4.1.1 Simulation of CDF
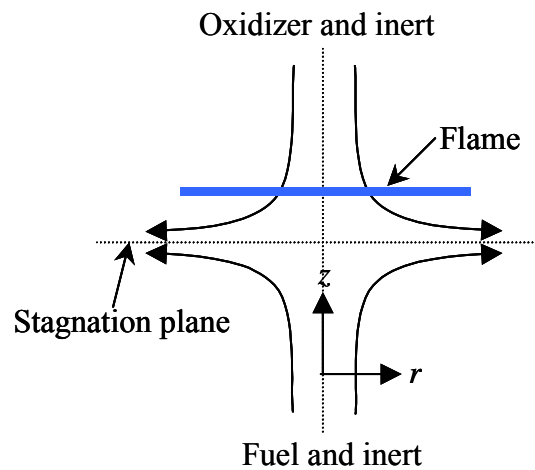
Figure 4.2 The schematic flow field with a flame established on the oxidizer side

The problem is posed as a steady stagnation flow problem where the fuel and oxidizer flows impinge against each other to form a stable stagnation surface, with a diffusion

flame established on either the oxidizer side or fuel side depending on the flow rates and gas compositions. In the case of a flame established from the oxidizer side, fuel coming out from the burner reaches the stagnation surface due to the forced convection, and then further diffuses toward the flame where the oxidization reaction occurs.

The cylindrical coordinates are introduced as in Fig.4.2, along with the schematic streamlines of flow field. Starting with the Navier-Stokes equations, a stream function is introduced in the form $\varphi = r^2 U(z)$ where $U(z)$ is the axial mass flux. By defining[1]

$$\frac{\partial \varphi}{\partial r} = r\rho u = 2rU , \qquad (4.1)$$

and

$$-\frac{\partial \varphi}{\partial z} = r\rho v = -r^2 \frac{dU}{dz} , \qquad (4.2)$$

the mass continuity equation is satisfied

$$\frac{\partial}{\partial z}(r\rho u) + \frac{\partial}{\partial r}(r\rho v) = 0 , \qquad (4.3)$$

where u is the axial velocity , v is the radial velocity, and ρ is the density of the gas mixture. From Equations (4.1) and (4.2), u depends only on z , and v varies linearly in r . The temperature T and species mass fraction Y_k are also assumed to be functions of z alone. Defining $G(z) = \frac{v}{r}$ as reduced radial velocity, Equation (4.3) becomes

$$\frac{dU}{dz} + \rho G = 0 . \qquad (4.4)$$

Introducing the above assumptions and definitions into the linear momentum equation (while neglecting buoyancy effects), the momentum equation is reduced to

$$\frac{d}{dz}(\mu\frac{dG}{dz}) - 2U\frac{dG}{dz} + J - \rho G^2 = 0, \tag{4.5}$$

where $J = \frac{1}{r}\frac{\partial p}{\partial r}$; and p is the thermodynamic pressure. Also, $\frac{dJ}{dz} = 0$, and μ is the

viscosity of the gas mixture.

With the K species included, the species equation is given as

$$2U\frac{dY_k}{dz} + \frac{d}{dz}(\rho Y_k V_k) - W_k\dot{\omega}_k = 0 \ \ (k = 1, K), \tag{4.6}$$

where V_k is the diffusion velocity of kth species, W_k is the molar weight of kth species,

and $\dot{\omega}_k$ is the molar rate of production of the kth species by chemical reaction.

The energy conservation equation is then

$$2Uc_p\frac{dT}{dz} - \frac{d}{dz}(\lambda\frac{dT}{dz}) + (\sum_{k=1}^{K}\rho Y_k V_k c_{pk})\frac{dT}{dz} + \sum_{k=1}^{K}h_k W_k\dot{\omega}_k = 0, \tag{4.7}$$

where c_p is the specific heat of the gas mixture; λ is the mixture thermal conductivity;

c_{px} is the specific heat of the kth species, and h_k is the specific molar enthalpy of the

k^{th} species.

The problem is reduced to a one-dimensional boundary problem with boundary

conditions prescribed as

$$\text{at } z = 0: \ U = \frac{\rho_0 u_0}{2}, G = 0, T = T_0, Y_k = Y_{k0}, \tag{4.8}$$

and

$$\text{at } z = L: \ U = \frac{\rho_L u_L}{2}, G = 0, T = T_L, Y_k = Y_{kL}. \tag{4.9}$$

The required thermodynamic properties (c_k, c_{pk}, h_k), the transport coefficients (λ, μ),

and the chemical production rate ($\dot{\omega}$) (which involve detailed transport and complex

chemical kinetics) are calculated using CHEMKIN[2] and TRANSPORT[3] subroutines. The flame structures are simulated using a CDF program[4], which solves for the above governing equations and boundary conditions.

The numerical calculation procedure is illustrated in Fig. 4.3. The elementary reaction mechanism (involving 177 reactions and 32 species) is given in Appendix 2 from GRI-Mech 1.2[5]. Additional reactions for CH^* chemiluminescence from Tse *et al*[6] have been included.

Figure 4.3 Relationship of the CDF Program[4] to the CHEMKIN and TRANSPORT preprocessors, and to the associated input and output files[7].

Various flame structures with different fuel compositions are computed, among which two are chosen to run the experiments for nanomaterial synthesis. One is the flame structure produced with 50% CH_4 diluted by 50% N_2 as given in Fig. 4.4, and another is shown in Fig. 4.5 with 42 % CH_4 plus 3% C_2H_2 diluted by 50% N_2. The role of addition of C_2H_2 to the fuel will be discussed in Chapter 7. In both flame structures, the flow velocity at the nozzle exit is 15 ± 0.5 cm/s and the flow overall strain rate is around 20 s^{-1}. The stagnation plane in both flames is illustrated as a dash line, showing that the flames are situated on the oxidizer side.
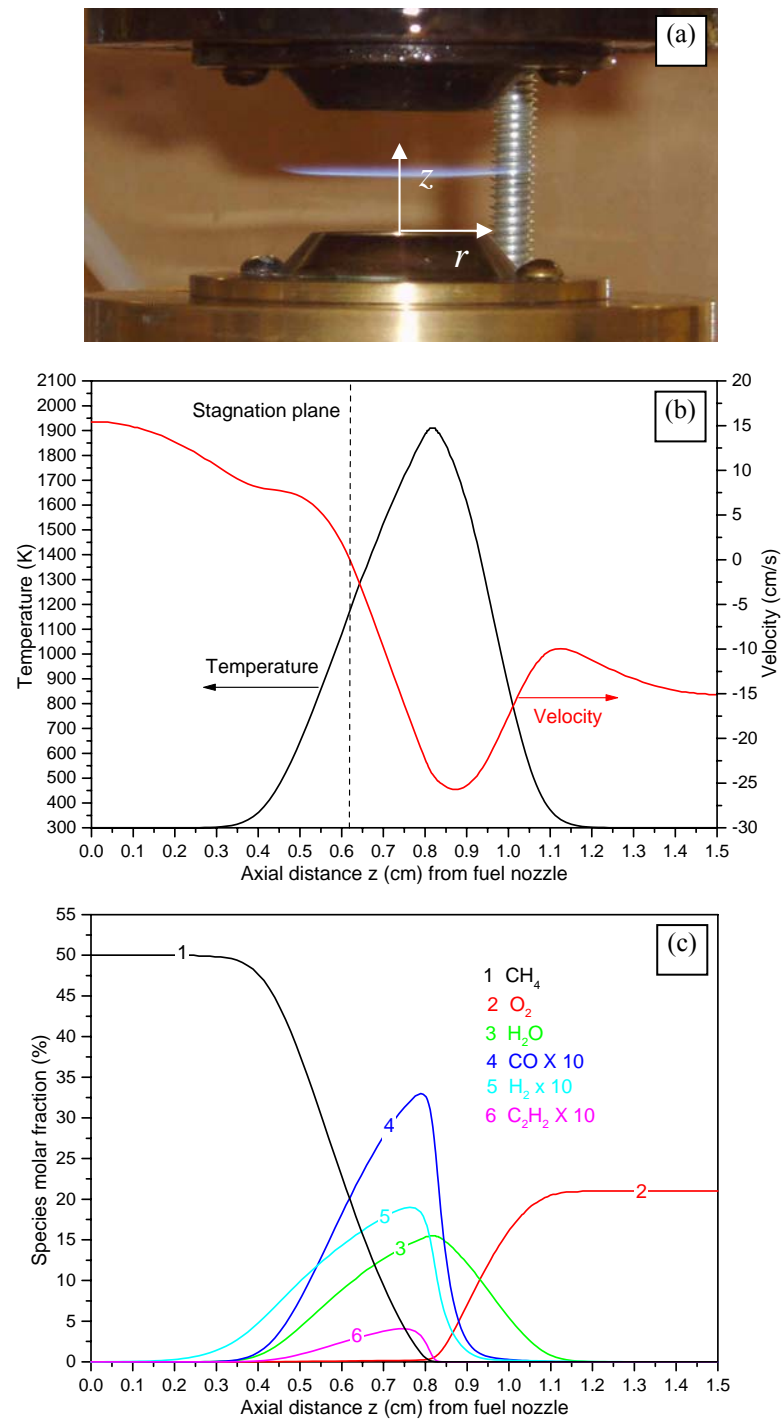
Figure 4.4 A flame structure with 50%CH$_4$ diluted by 50% N$_2$, (a) the real corresponding flame, (b) the temperature profile and velocity distribution along the axial z direction with the stagnation plane marked, (c) the profiles of major species.
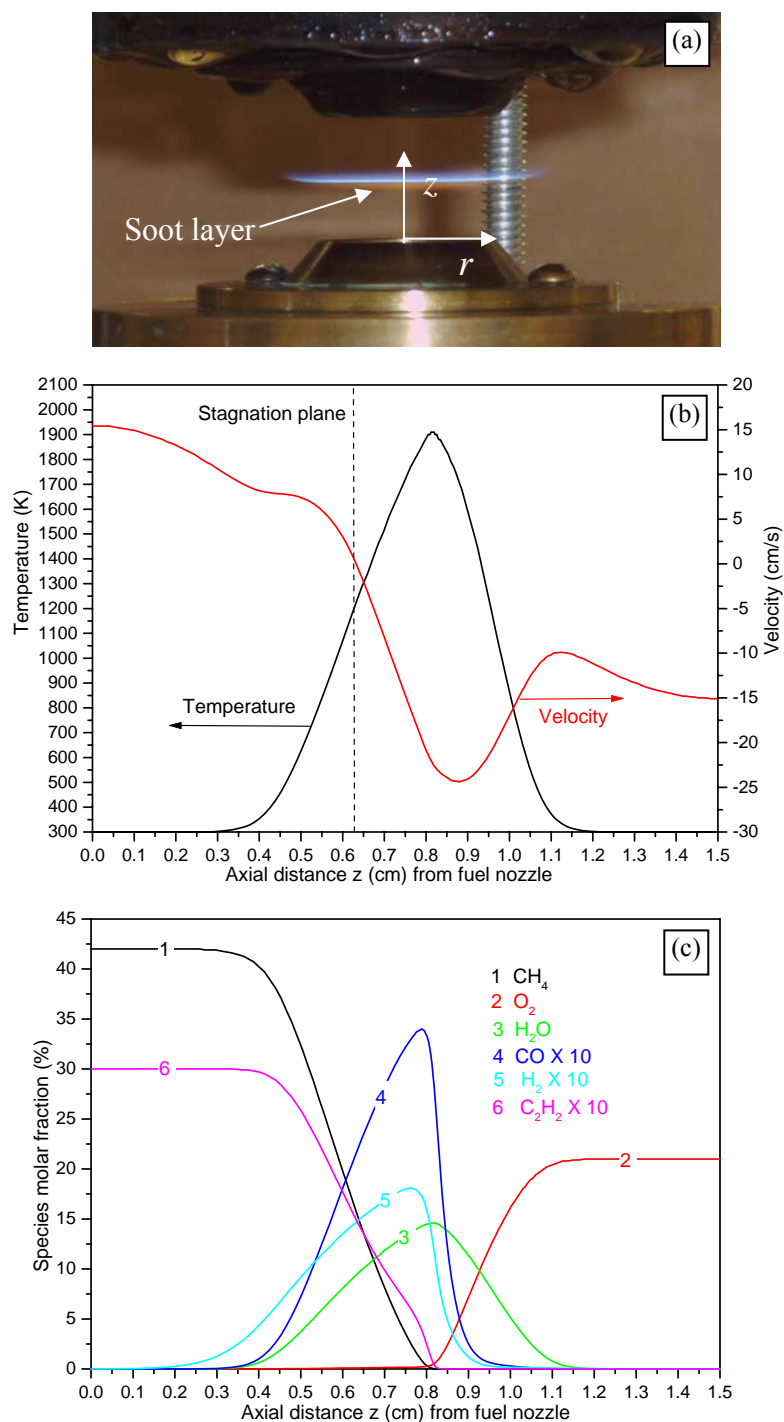
Figure 4.5 A flame structure with 50%CH$_4$ plus 3% C$_2$H$_2$ diluted by 50% N$_2$, (a) the real corresponding flame, (b) the temperature profile and velocity distribution along the axial z direction with the stagnation plane marked, (c) the profiles of major species.

4.1.2 Flame structures measured by SRS and compared with simulations

SRS is a spectroscopic technique that can be used to detect the temperature and species concentrations in the gas phase. Since vibrational information is very specific for the chemical bonds in molecules, SRS provides a fingerprint by which the molecule can be identified. The Raman effect occurs when light impinges upon a molecule and interacts with the electron cloud of the bonds of that molecule. The incident photon (light quantum) excites one of the electrons into a virtual state. For the spontaneous Raman effect, the molecule will be excited from the ground state to a virtual energy state (Fig. 4.6)[8], and then relax into a vibrational excited state, which generates Stokes Raman scattering. If the molecule was already in an elevated vibrational energy state, the Raman scattering is then called anti-Stokes Raman scattering. A molecular polarizability change, or amount of deformation of the electron cloud, with respect to the vibrational coordinate is required for the molecule to exhibit the Raman effect. The amount of the polarizability change will determine the intensity, whereas the Raman shift is equal to the vibrational level that is involved.

.
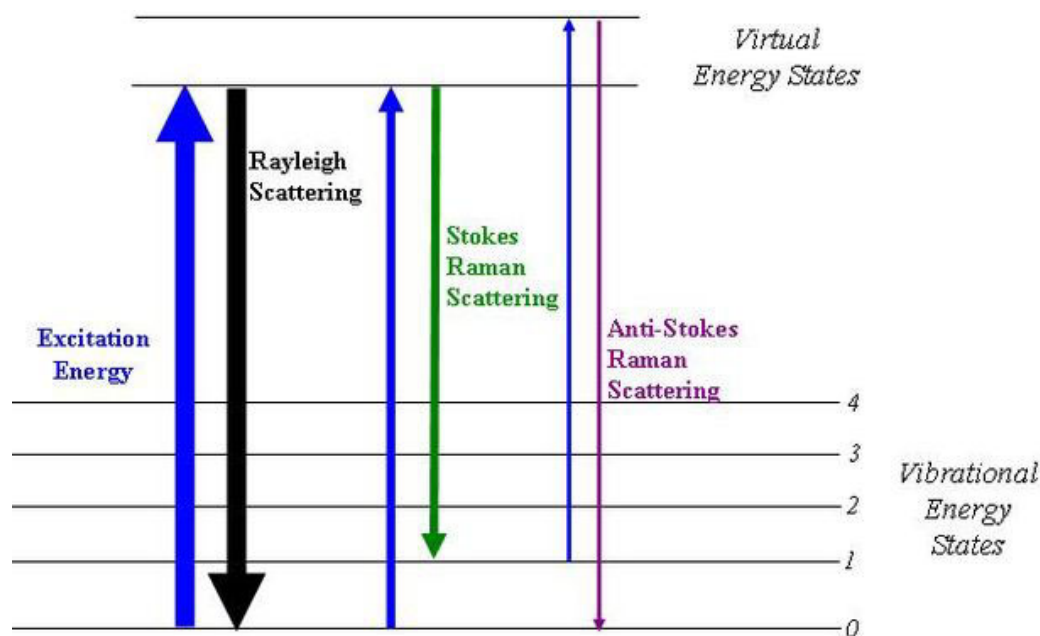
Figure 4.6 Energy level diagram showing the states involved in Raman signal. The line thickness is roughly proportional to the signal strength from the different transitions (Figure from reference 8).

We utilize SRS (setup as shown in Fig. 4.7) to measure the gas-phase temperatures and concentrations of major species at specific locations. The excitation source is a frequency-doubled (532nm) Nd:YAG laser operating at 10 Hz. The laser beam is focused into the test section with a 300mm focal-length plano-convex fused silica lens. Detection of the vibrational Stokes Q-branch Raman signal is accomplished by passing the collected light from a 100μm diameter × 100μm length measuring volume through a Raman notch filter plus a depolarizer and into a 0.5m imaging spectrometer with a 2400 groove/mm grating, with an ICCD camera as detector. The use of the pulse laser source and gated detector significantly improves the signal to noise ratio. Temperature measurements are obtained by least-squares fitting the shape of the N_2 Raman spectrum to theoretical library spectra spaced 50K apart. The uncertainty in the fitted temperature is less than ±50K, and the reproducibility of the measurements is within ±20K. Species

mole fraction profiles are determined from the strength of the Raman signal of individual species, relative to N_2. The signals used to determine the concentrations of CH_4, H_2, CO, C_2H_2, CO_2, and H_2O are collected at Raman shifts of 2915, 4160, 2145, 1980, 1388, and $3657cm^{-1}$, respectively. The interference from the O-branch of N_2 on the CO spectrum is considered and subtracted. Broadband florescence from C-related species are also subtracted. The reproducibility of the concentration measurements is usually within ±5%. The measurements of the flame structure with 50% CH_4 by SRS are shown in Fig. 4.8 and compared with simulations, evincing the accuracy of the simulations and their suitability in guiding experiments and interpreting results.
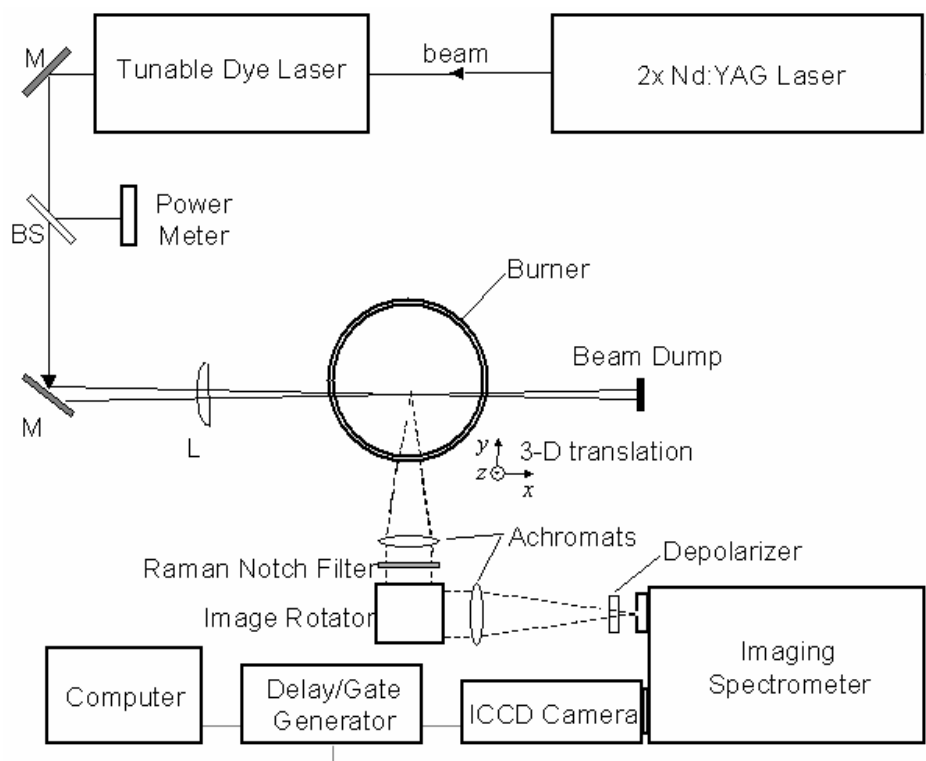
Figure 4.7 The setup of flame structure measurement by SRS
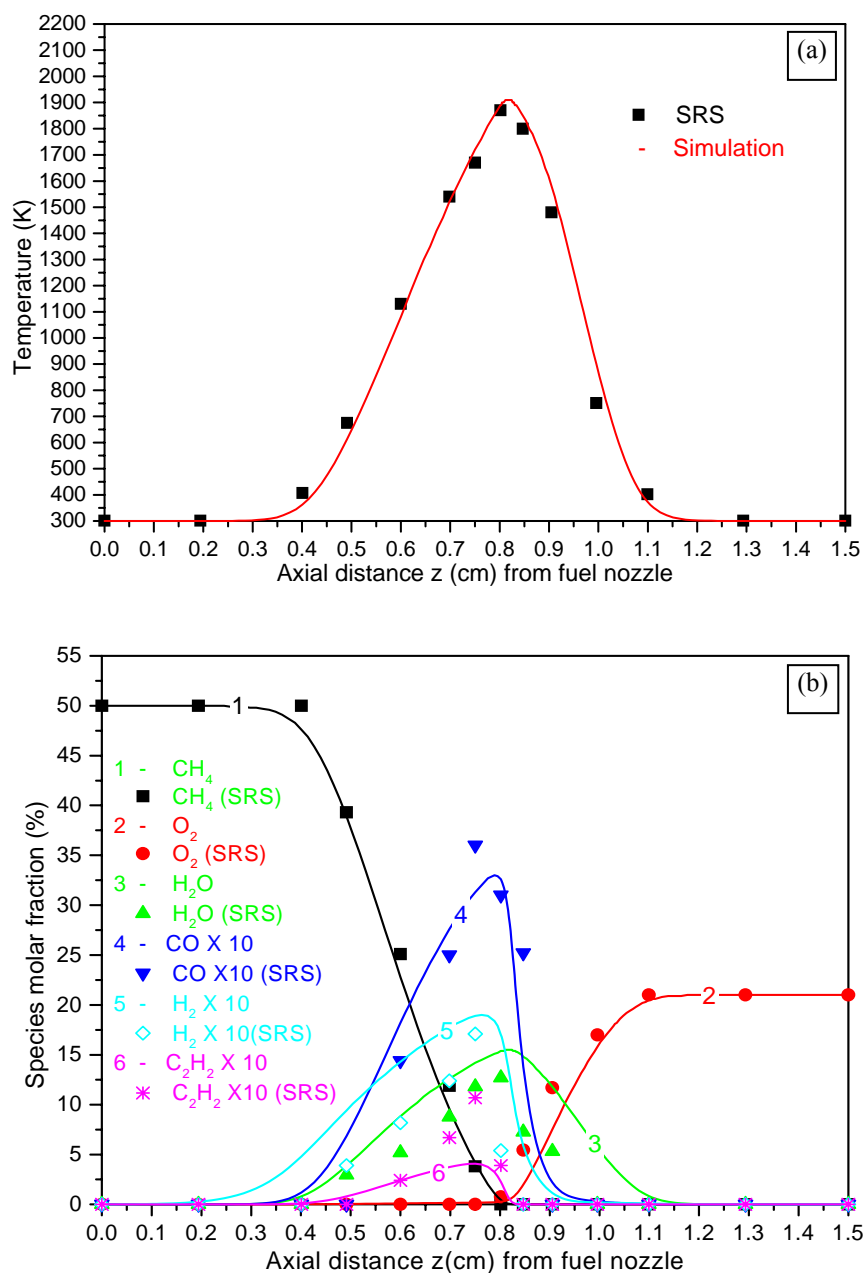
Figure 4.8 Flame structure with 50%CH$_4$ measured by SRS and compared with simulations, (a) temperature profile along the axial z direction, and (b) the molar fractions of major species along the axial z direction.

4.2 Flame structures of IDFs measured by SRS

A mixture of 10 L/min CH_4 and 4.2 L/min N_2 flows through the outer annulus, and air at 0.8 L/min flows through the center tube, so an IDF is established at the central tube exit. The visible flame is about 15mm in height with ~9mm (bluish chemiluminescence from CH*) of it at the base being from primary reaction zone and ~6mm (faint orange) of it at the top being from pyrolysis and sooting mechanisms. The actual flame is shown in Fig. 4.9, and this flame is used to explore the synthesis of CNTs and ZnO nanostructures. The temperature and major species along z and r directions are measured using the same SRS setup for CDF. Due to the sensitivity of ZnO nanostructures to growth conditions, flame structures at more points along the z and r directions are measured for the growth of ZnO nanostructures. The measured profiles of temperature and major species along the z and r directions at the specific positions using SRS are presented in Chapter 9 for the production of ZnO nanostructures, and are described in Chapter 6 for CNT synthesis. As such, to avoid duplication, they are not shown in this chapter, as they are used in the discussion of growth mechanism in those chapters.
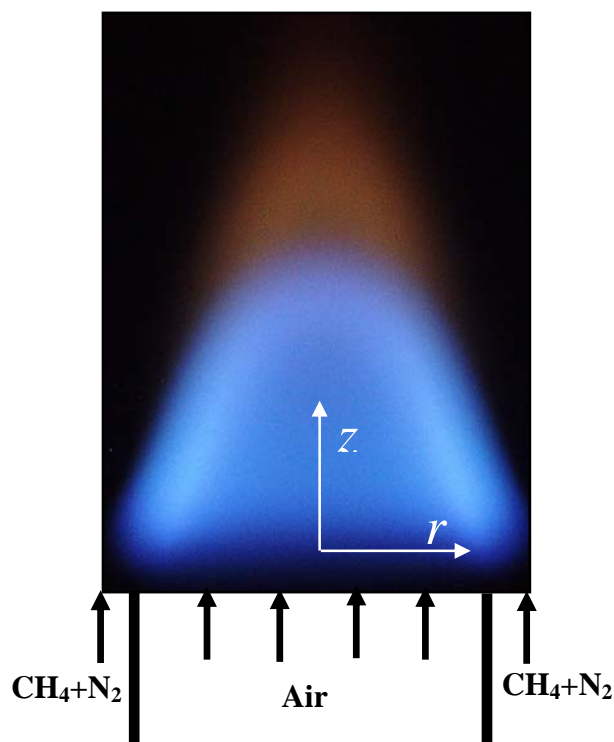
Figure 4.9 The real IDF established at the center tube exit.

4.3 Conclusions

The CDFs are simulated by a program involving detailed chemical kinetics and transport properties. SRS is employed to validate these flame structures. The measurement results are compared with the simulated results, and are in excellent agreement with the simulations. The profiles of temperature and major species for IDFs are obtained by SRS as well, but shown in Figs 6.2 and 9.2 of Chapter 6 and 9, respectively.

Reference

[1]Kee R.J., Miller J.A., Evans G.H. and Dixon-lewis G., A computational model of the structure and extinction of strained, opposed flow, premixed methane-air flames, Twenty-second symposium (international) on combustion/ the combustion institute, pp. 1479-1494, 1988

[2]Kee R.J., Rupley F.M., Meeks E., Miller J.A., CHEMKIN-III: A fortran chemical kinetics package for the analysis of gas-phase chemical and plasma kinetics, Rept. SAND96-8216, Sandia national laboratories, 1996

[3]Kee R.J., Dixon-Lewis G., Warnatz J., Coltrin M.E., Miller J.A. and Moffat H.K., A fortran computer code package for the evaluation of gas-phase, multicomponent transport properties, Rept. SAND86-8246B, Sandia national laboratories, 1998

[4]Ju Y., Guo H., Maruta K. and Liu F., On the extinction limit and flammability limit of non-adiabatic stretched methane-air premixed flames, *Journal of Fluid Mechanics*, 342:315-334, 1997

[5]Frenklach M., Wang H., Goldenberg M., Smith G.P., Golden D.M., Bowman C.T., Hanson R. K., Gardiner W. C. and Lissianski V., Gas Research Institute Topical Report 95/0058 (1995).

[6] Tse S.D., Zhe D., Sung C.J., Ju Y., and Law C.K., Microgravity burner-generated spherical diffusion flames: Expreimental and computation*, Combustion and flame*, 125: 1265-1278, 2001

[7]Kee R.J., Grcar J.F., Smooke M.D., Miller J.A. and Meeks E., PREMIX: A FORTRAN program for modeling steady laminar one-dimensional premixed flames, Reaction Design 11436 Sorrento Valley Road San Diego, CA 92121, 1998

[8]Raman spectroscopy, http://en.wikipedia.org/wiki/Raman_spectroscopy

Chapter 5

Initial Results of CNTs Grown from Premixed Flames and Normal Diffusion Flames to Compare with Works of Others

The first flame-synthesized CNTs reported in the literature were with premixed flames (PFs)[1] and normal diffusion flames (NDFs)[2]. Vander Wal[1] demonstrated the flame synthesis of SWNTs using Fe nanoparticles. Fe was found to exhibit preferential reactivity toward CO for SWNT catalysis with this reactivity being strongly dependent upon catalyst particle size within their flame conditions. Yuan *et al*[2] observed entangled MWNT formation (with a diameter range of 20-60nm) directly on Ni/Cr wires in a sooty laminar co-flow methane flame. Height and co-workers[3] used premixed co-flow flames to grow SWNTs, studying the effects of flame position and air-to-fuel ratio.

In this research, PFs and NDFs are initially examined and compared with the results of others to benchmark and validate the flame synthesis process. The various PFs and NDFs are established using the co-flow jet flow burner described in Chapter 3. Different fuels (methane, acetylene and ethylene) are investigated with different catalysts tested (iron, nickel, and cobalt). Some FESEM images of CNTs produced from these flames are given and compared with the results of others in Fig. 5.1 and Fig. 5.2.

Figure 5.1 compared our results with those reported by Yuan et al in methane[2] (CH_4) and ethylene (C_2H_4)[4] NDFs. In methane flames, a stainless steel grid with a holding Ni-

Cr wire is inserted into the flame, and the materials deposited on the Ni-Cr holding wire are examined. Our results and those by Yuan *et al*[2] are given in Fig. 5.1 (a) and (d), which show the similar morphology (entangled CNTs) and diameters. As reported by Yuan *et al*, we observe that the growth region of CNT is limited to the fuel side. Moreover, closer to the flame axis, CNT yield decreases or CNT growth stops probably due to the significant increase of carbon-containing pyrolysis products, especially polycyclic aromatic hydrocarbons (PAHs)[2]. PAHs can deactivate the catalyst required for CNT growth because PAHs are large aromatic structures with high thermodynamic stability and resistant to catalytic decomposition[5,6]. In ethylene NDFs, similar entangled CNTs are obtained using the same stainless steel grid with the same holding Ni-Cr wire, as shown in Fig. 5.1(b) (our results) and (e) (results by Yuan *et al*[4]). However, aligned CNTs are produced in a nitrogen-diluted ethylene NDF using a Co-coated stainless steel grid with the same Ni-Cr holding wires (Fig. 5.1(c) and (f) represent our result and that by Yuan *et al* respectively). Yuan *et al* attributed this alignment to the temperature decrease (from 1547 ^{o}C to 1244 ^{o}C) at the sampling position due to the nitrogen addition, which reduce the pyrolysis rate of hydrocarbon products in the flame. In addition, this alignment likely has something to do with the formation, interaction, and carbon solubility of catalytic nanoparticles resulting from the decreased temperature.
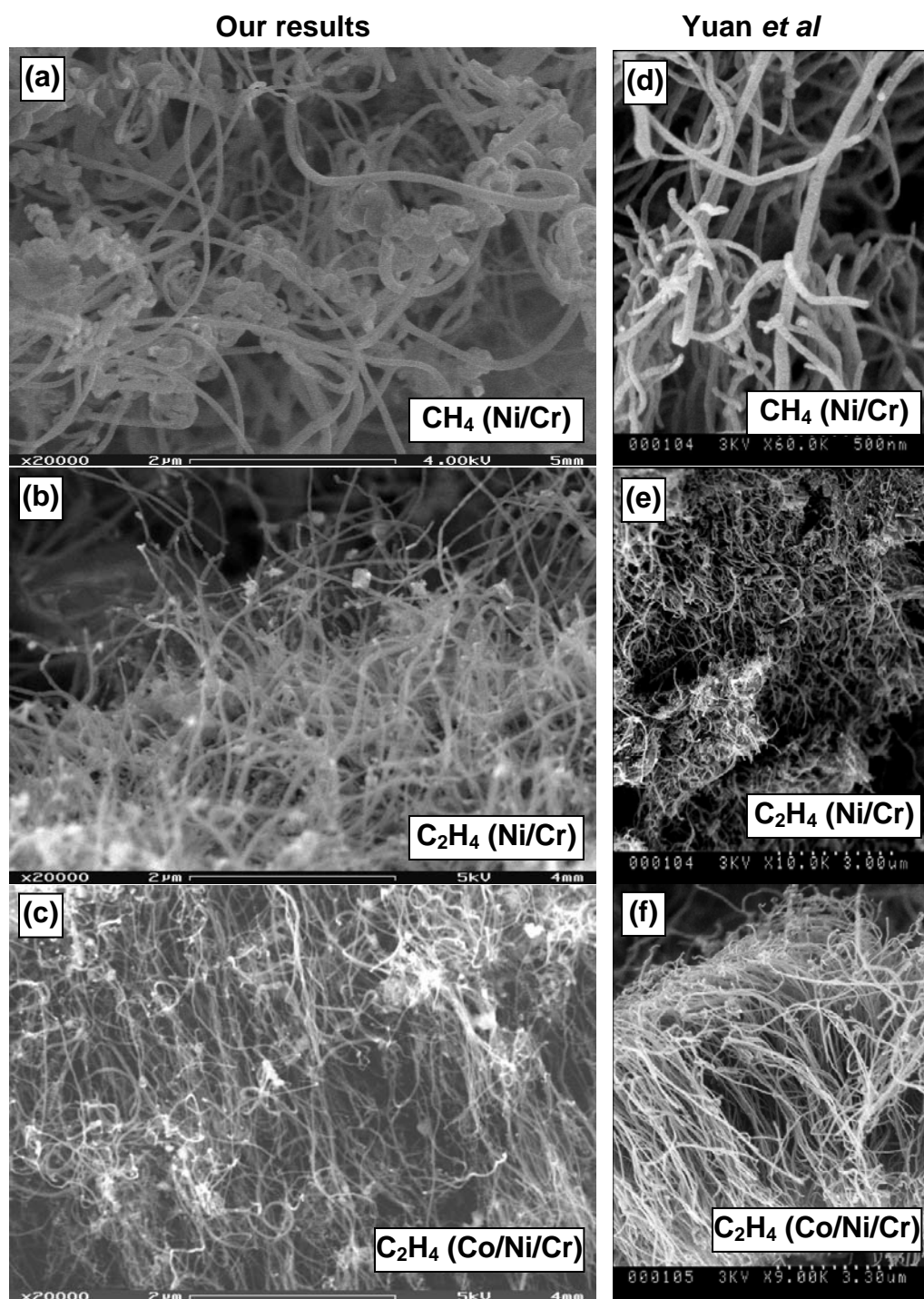
Figure 5.1 CNTs in normal diffusion flames by this work (left column) are compared with those reported by Yuan *et al* (right column, references 2 and 4).

Our CNTs (left column in Fig. 5.2) grown in premixed flames are compared with those reported by Vander Wal *et al*[7] (right column Fig. 5.2). One of the requirements for CNT synthesis is the supply of carbon source. In PFs, a fuel-rich (the equivalence ratio ϕ >1) flame is usually used to provide extra fuel as carbon source. For comparisons, we conduct some PF experiments at ϕ=1.6 (ϕ=1.62 by Vandel Wal *et al*). These groups of experiments are conducted to identify the effects of fuels and catalysts on CNT growth in PFs. Two fuels studied are ethylene (C_2H_4) and acetylene (C_2H_2), along with two forms of catalysts (Co-coated stainless steel grid and pure stainless steel grid (SS)). Our results and those by Vander Wal *et al*[7] show the similarity in terms of diameter and morphologies. The Co-coated stainless steel usually produce uniform diameter of CNTs (Figs. 5.2(a), (e), (c) and (g)) due to the size uniformity of deposited catalytic Co particles. CNTs with different diameters and morphologies usually occur using stainless steel only (Figs. 5.2(b), (f), (d) and (i)). In case of pure stainless steel grid, the required catalytic nanoparticles are formed generally through the steel surface breakup induced by the surface carbide formation, which usually create a wide range of crystal particle sizes and shapes. According to the theory that the diameter of CNT usually reflects the size of the associated catalytic nanoparticle[8], these surface-breakup-formed nanoparticle account for the varied diameters and morphologies. While the stainless steel grid is coated with Co particles, the size uniform Co particles dominate the CNT growth explaining the uniformity of CNTs. It is also observed that CNTs produced in acetylene are a little bit larger than those in ethylene. The reason is ascribed to the higher H_2 concentration in the acetylene flame[7]. H_2 facilitates carbide formation followed by surface breakup by etching

or removing surface-adsorbed carbon, thus promoting the contribution of surface-break-

formed nanoparticles in CNT growth.

Our results (ϕ =1.6) **Vander Wal *et al* (ϕ =1.62)**
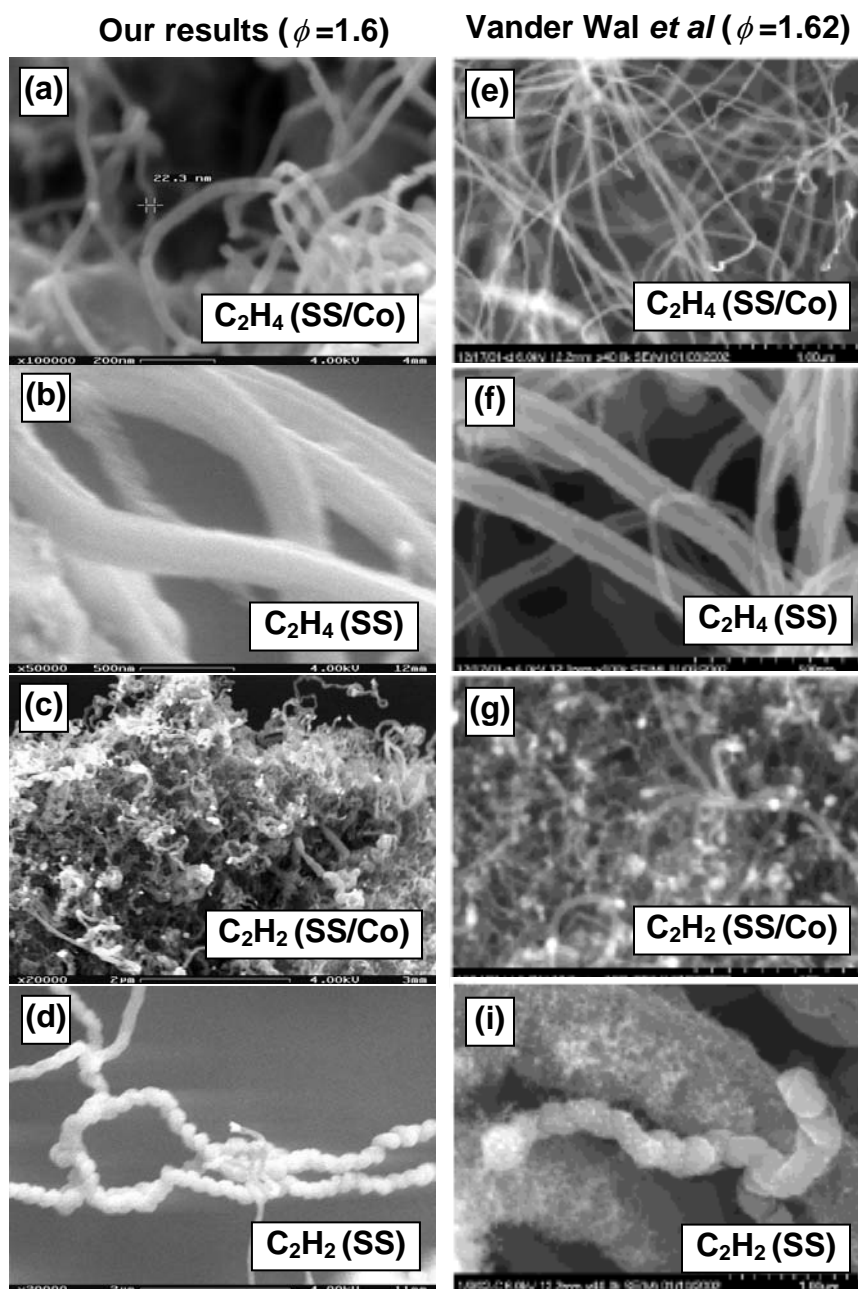
Figure 5.2 CNTs in premixed flames by this work (left column) are compared with those reported by Vander Wal *et al* (right column, from reference 7).

As seen from the above comparisons and discussions, CNT growth in flames involves several factors (e.g. temperature, chemical species, catalyst formation). These initial results validate and reproduce the results of others, aiding in identifying the range of conditions appropriate for CNT synthesis in flames. Subsequently, we examine CNT synthesis for similar ranges of local conditions (e.g. temperature), but in other strategic geometries, whereby fundamental growth conditions can be more easily identified and isolated.

Reference

[1] Vander Wal R.L., Fe-catalyzed single-walled carbon nanotube synthesis within a flame environment, *Combustion and Flame,* 130:37–47, 2002

[2] Yuan L, Saito K, Pan C, Williams FA, and Gordon AS, Nanotubes from methane flames, *Chem Phys Lett,* 340:237-41, 2001

[3] Height M.J., Howard J.B., Tester J.W., Synthesis of single-walled carbon nanotubes in a premixed acetylene/oxygen/argon flame, *Proceedings of the Third Joint Meeting of the U.S. Section of the Combustion Institute,* 2003

[4] Yuan L., Saito K., Hu W., and Chen Z., Ethylene flame synthesis of well-aligned multi-walled carbon nanotubes, *Chemical Physics Letters,* 346: 23-28, 2001

[5] Stein S., and Fahr A*., J. of Phys. Chem*., 89:3714, 1985

[6] Vander Wal R.L., Flame synthesis of substrate-supported metal-catalyzed carbon nanotubes, *Chemical Physics Letters*, 324:217-223, 2000

[7] Vander Wal R.L., Hall L.J., and Berger G.M., Optimization of flames synthesis for carbon nanotubes using supported catalyst, *J. Phys. Chem B*, 106:13122-13132, 106

[8] Moisala A., Nasibulin A.G., and Kauppinen E.I., The role of metal nanoparticles in the catalytic production of single-walled carbon nanotubes-a review*, J. Phys: Condens. Matter*, 15:S3011-S3035, 2003

Chapter 6

CNTs from Methane Inverse Diffusion Flames

6.1 Introduction

The unique flame configuration employed in this chapter is the inverse diffusion flame (IDF), where oxidizer is issued from the center jet while fuel is issued from the surrounding co-flow. The configuration was concurrently examined by Lee and co-workers[1,2]. The net effect of this geometry is that post-flame species are largely comprised of pyrolysis vapors that have not passed through the oxidation zone. As such, soot formation processes, which compete with CNT formation routes, are more effectively separated from oxidation processes in IDFs, which also tend to soot less than normal diffusion flames (NDFs)[3]. Furthermore, the hydrocarbon and pyrolysis species (rich in C_n and CO) generated can be much greater in concentration than that practically achieved in PFs. By using diffusion flames (burning stoichiometrically), flame-speed and cellular stabilization problems related to PFs can be avoided. In our setup, transition-metal alloy probes (with and without voltage bias) are inserted radially into the flame structure at various location heights to probe for conducive regions of CNT synthesis. Under favorable conditions, catalyst nanoparticles are formed, and carbon-based precursor species readily undergo dissociative adsorption and diffuse through the catalyst nanoparticles and grow into CNTs[4], with the nanoparticles either remaining attached to the substrate and situated at the base of the growing CNT or detaching from the probe and situated at the tip of the growing CNT. Since both CO and C_2 species can participate

in the growth processes of CNTs, their local concentrations must be characterized to understand the initial chemical reaction pathways and the conditions promoting their kinetic dominance. As such, local gas-phase temperatures and concentrations of precursor species are measured at those locations of direct CNT formation.

In our case, CNTs grow directly from the transition-metal alloy probes. The required catalytic nanoparticles responsible for CNT growth are formed primarily through the probe surface breakup induced by surface carbonization. Carbide induced breakup of the metal probe surface occurs often within a rich hydrocarbon-based flame. When the metal probe is inserted into the flame, carbon deposits and builds upon the surface. If the dissolved carbon reaches a concentration sufficient to form carbide phase, the resulting lattice mismatch between the carbide phase and the underlying metal creates stresses localized within the surface region[5]. Surface breakup will proceed along the weakest sections such as grain boundaries and edge dislocations where lattice stresses are concentrated, and the carbon concentration will likely be highest[5]. This formation mechanism of catalyst nanoparticles generally creates a wide variety of sizes and geometries[6,7,8,9], which are determined by various factors, such as temperature, chemical species, and carbon solubility of the metal. Different metals and metal alloys show different carbon solubilities that also vary with temperature[10]. Additionally, hydrogen can facilitate the carbide breakup process by etching or removing surface-adsorbed carbon where the rate of carbon deposition exceeds that of solvation[5]. All these parameters affect the formed nanoparticle properties such as size and yield, which will impact CNT morphologies and properties, as shown in this and other chapters.

Two other possible mechanisms for the direct formation of nanoparticles on a metal probe surface in flames are hydrogen reduction and evaporation–condensation. The inherent presence of oxygen-bearing species (e.g. OH) near the flame front on the fuel side can lead to local oxidization of the metal probe. Nanoparticles can then be formed from the oxidized metal through hydrogen reduction. When the metal probe is inserted into the flame, surface metal can evaporate. The evaporated metal might diffuse back and deposit on the probe surface where nanoparticles can be created through condensation. However, based on our studies and observations, these two mechanisms contribute little to nanoparticle formation, since oxygen-containing species are limited to a small region near the flame front that is usually not favorable for CNT growth. In the CNT growth zone, the temperature is generally much lower than the melting point of the metal probe, so very little metal vapor can be generated. Furthermore, carbon-bearing species are overwhelmingly dominant in the local flame structure such that the surface-breakup mechanism dominates for nanoparticle formation.

Additionally, the use of electrical force fields provides an advantageous tool to improve uniformity and productivity in gas-phase synthesis processes. Several works[11,12,13,14,15,16,17] in CVD and plasma CNT synthesis systems have reported successful electromagnetic-field application to control CNT coiling, alignment, and growth rate. However, despite the promise of electric field control and its elucidated feasibility, only the recent work of Merchan-Merchan *et al*[18] has examined its application in flame synthesis of CNTs. Both Ref[18] and our work (as will be seen) show that CNT alignment and growth rates can be enhanced under electric fields.

In the following sections, we will show that the variation of catalyst type, flame position (radial *r* as well as axial *z*), and voltage bias strongly influences CNT morphologies.

6.2 Experiment

The experimental setup is shown in Fig. 3.1 and Fig. 3.2. The established IDF is the same as the one presented in the Section of 4.2, with its flame structures for CNT growth measured by SRS. A picture of the IDF is given in Fig. 6.1, along with the investigated axial positions. Its flame structures as measured by SRS are plotted in Fig. 6.2, with the CNT growth regions marked. Transition-metal alloy probes with different compositions (i.e. Fe, Ni/Cu, and Ni/Cr/Fe) are inserted radially/horizontally (see Fig.6.1) into the flame structure at specific vertical positions to induce catalyst nanoparticle formation and subsequent CNT growth (Some properties of tested probes are given in table 6.1). The Fe and Ni/Cu probes are both 0.8mm in diameter; the Ni/Cr/Fe probe is 1 mm in diameter. The substrates are operated at floating potential mode (FPM), where the flame induced voltages are measured for each case, as well as grounded and with applied voltage bias. A dual-polarity power supply connected to the end of a probe maintains a given bias voltage; the burner assembly is always kept at ground potential.

Table 6.1 Catalytic metal alloys investigated

Chemical composition	Melting point (K)
99.5% Fe	1808
45% Ni / 55% Cu	1493
60% Ni / 16% Cr / 24% Fe	1623

Post-synthesis, the surfaces of the probes are imaged directly using FESEM to assess CNT morphology. After ultrasonic treatment, HRTEM characterizes individual CNTs and bundles; XEDS analyzes the included catalyst nanoparticles.
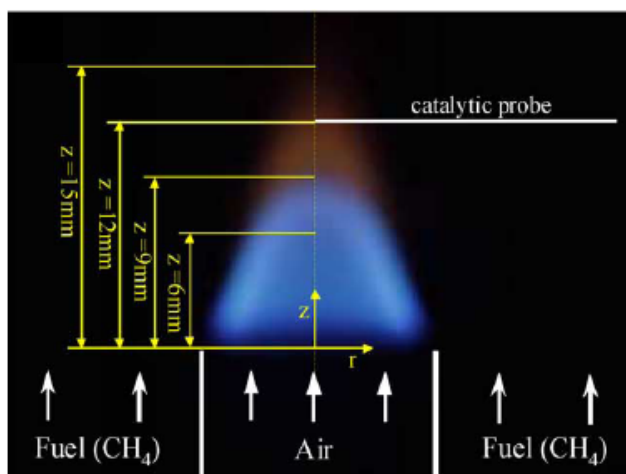
Figure 6.1 IDF with methane (CH_4) as fuel

6.3 Results and discussion

6.3.1 Effect of alloy composition and local flame conditions on morphology

Although the synthesis process is quite complex, involving both catalyst nanoparticle formation and CNT growth, under very specific conditions, the setup allows for strategic control of the many process parameters involved. We investigate the effect of different vertical (z) and radial (r) sampling positions in the IDF (see Fig. 6.1), as well as alloy

composition of the catalytic substrate, on CNT morphology. For example, at $z = 6$mm, no CNTs or fibrous nanostructures are found to have been grown on any of the probes, despite sufficient concentrations of CO and C_2H_2, as indicated by SRS measurements (Fig. 6.2(a)). Two reasons might be responsible for the absence of CNTs at this position. One is the lack of catalytic nanoparticles. With melting temperatures for Fe, Ni/Cu, and Ni/Cr/Fe as shown in Table 6.1, the temperatures (well below 1100K) may be too low (Fig.6. 2(a)) for the formation/extraction of catalytic nanoparticles on/ from the probes. Since both the carbon solubility and the carbon diffusion coefficient in a metal are temperature-dependent and decrease with decreasing temperature [19, 20] the dissolved carbon may not reach a concentration sufficient to form a carbide phase. As such no surface breakup can occur to produce the catalytic nanoparticles. Another reason could be the deactivation of catalytic nanoparticles. Even with a small amount of catalytic nanoparticles, they could be deactivated due to the formation of coking layer (e.g. amorphous carbon), resulting from a relatively faster carbon deposition rate than the carbon diffusion inside the nanoparticles at this position. Additionally, the cleaning role of hydrogen by etching away amorphous carbon is not available due to absence of hydrogen at this position[21].
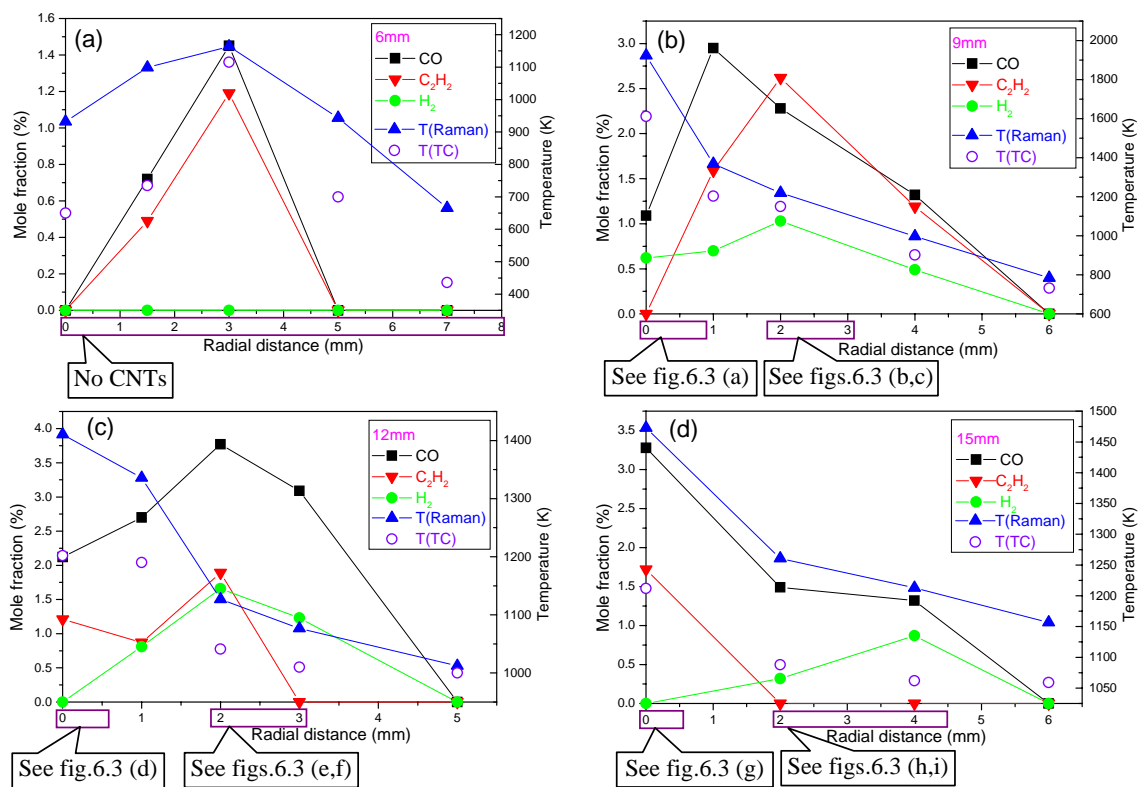
Figure 6.2 Gas-phase temperature (Raman) and species mole fraction profiles as measured by SRS, including thermocouple temperature (TC), at investigated sampling heights within the flame structure of Fig. 6.1: (a) $z = 6$mm, (b) $z = 9$mm, (c) $z = 12$mm, and (d) $z = 15$mm.

Figs. 6.3(a)–(c) show filamentous nanomaterials grown on probes of different compositions positioned at $z = 9$mm. At this height, use of the Fe probe results in micro- and nano-scale carbon fibers and tubes, as seen in Fig. 6.3(a), which are characterized by various forms along with a large distribution in diameter. The fibers tend to be coiled and very entangled. Moreover, CNTs and carbon fibers are found to grow only near the centerline of the flame. This is reasonable since the temperatures are perhaps high enough only in this region (see Fig. 6.2(b)) to form the requisite catalytic Fe nanoparticles, along with supplying sufficient concentrations of CO and C_2H_2 species to induce CNT growth. For the Ni/Cu (Fig.6. 3(b)) and Ni/Cr/Fe (Fig. 6.3(c)) probes,

CNTs, characterized by the catalyst at the tip mechanism, grow profusely in the $r = 2$–3mm region of Fig. 6.2(b). This region is located just outside the visible soot/pyrolysis regime shown in Fig. 6.1. Gas-phase temperatures around 1100K (Fig. 6.2(b)) seem sufficient to produce the Ni catalytic nanoparticles from these probes (which have much lower characteristic melting temperatures than iron), as well as support CNT growth with ample concentrations of CO and C_2H_2 available. The CNTs are dispersed evenly on the probe surface without intermixed fibers, and exhibit rather uniform diameters of around 15–20nm.

Figs. 6.3(d)–(f) manifest filamentous nanomaterials grown on the probes positioned at $z = 12$mm, which turns out to be the optimal location height for CNT growth. A Fe probe still produces micro- and nano-scale carbon fibers and tubes that tend to be coiled, entangled, and twisted, as shown in Fig. 6.3(d). These nanomaterials exhibit diverse forms with diameters more uniform than those for Fe probes at previous flame height locations; however, their diameters are much larger than those formed from the nickel-based catalysts. Nanomaterials on the iron probe are still produced near the flame centerline (Fig. 6.2(c)), where the temperature is highest. For the Ni/Cu (Fig. 6.3(e)) and Ni/Cr/Fe (Fig. 6.3(f)) probes, CNTs form in the $r = 1.75$–3.25mm region of Fig. 6.2(c), which is again outside the visible soot/pyrolysis region of Fig. 6.1. Nanomaterials harvested on the Ni/Cu probe (Fig. 6.3(e)) show little difference from those grown at the $z = 9$mm location (Fig. 6.3(b)). However, we now find that vertically well-aligned CNTs (Fig. 6.3(f)) are obtained for the Ni/Cr/ Fe probe. These CNTs are characterized by dense compactness and vertical orderliness with a uniform diameter. As revealed by TEM (Fig. 6.4(a)), the synthesized materials are MWNTs with strong graphitic structure and a

diameter of about 15nm. Fig.6. 4(b) shows the catalyst nanoparticles at the tips of a bundle of these MWNTs; and EDXS identifies the elemental composition of single catalyst nanoparticles (Fig. 6.4(c)), confirming that transition metal nanoparticles were extracted from the Ni/Cr/Fe probe. It is interesting to note that well-aligned CNTs are formed near the $r = 3.25$mm region where there is almost no C_2H_2, but plenty of CO, for the Ni-based probes. The gas-phase temperature is ~1100K and the probe temperature (estimated through the thermocouple measurement) is ~1000K.
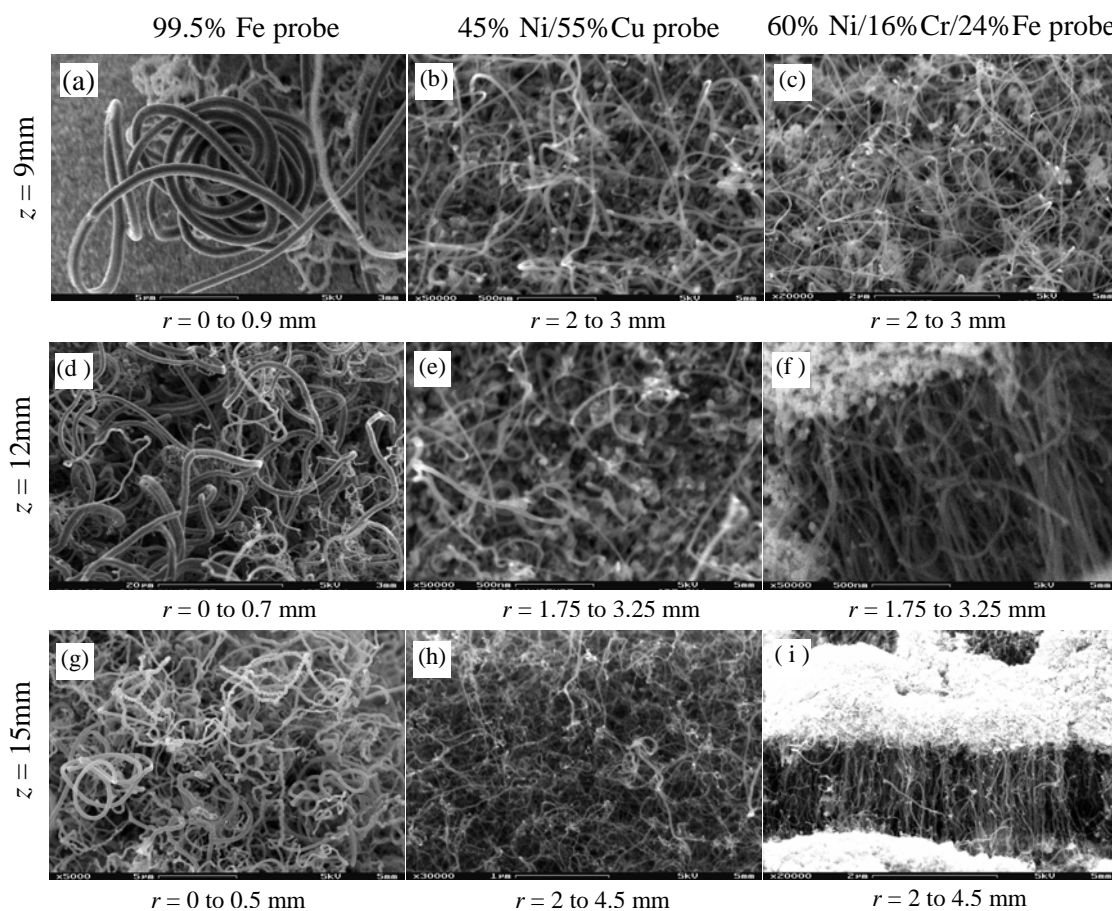
Figure6. 3 FESEM images of CNT morphology corresponding to catalytic probe composition (column) and flame sampling height (row) of Fig. 6.1. The alloy probes are operated at floating potential mode (FPM) for a 10 minute sampling duration.

Figs. 6.3(g)–(i) show nanomaterials grown on the probes positioned at $z = $ 15mm, corresponding to the location of the visible soot/pyrolysis tip (Fig. 6.1). Nano-scale tubes without intermixed microscale materials are obtained from the Fe probe (Fig. 6.3(g)), with much more uniform and smaller diameters than those grown from the same Fe probe positioned at lower heights. Nonetheless, the diameters are still much larger than those produced from nickel based catalysts of Figs. 6.3(h) and (i). The tubes are still often coiled and entangled. Again, CNTs only grow near the flame centerline (Fig. 6.2(d)). For the Ni/Cu probe at this flame height, as shown in Fig. 6.3(h), the CNTs are characterized by almost the same aspects as those of previous sample location heights, but with shorter lengths. Similarly, for the Ni/Cr/Fe probe, CNTs formed are still vertically well-aligned (Fig. 6.3(i)), but of shorter lengths as compared to those at $z = $ 12mm. The CNTs have a uniform diameter of around 15–20nm and are vertically bundled into regular patterns covering the probe surface. Notice the thick "white" layer of catalysts at the top of the CNTs. We hypothesize that, similar to the well-aligned case at $z = $ 12mm, a layer of particles of Ni–Fe–Cr–O composition are initially lifted off the surface of the probe, from which elemental transition nanoparticles are reduced which, in turn, catalyze nanotube growth. An oxide layer of Cr_2O_3 is likely formed at the probe surface that prevents additional probe material from leaving the surface. In a way, one can view the growth mechanism as conforming to the particle-at-the-base mechanism, with the outwardly-growing top "white" layer considered the "base". Again, CNTs from the Ni-based catalytic probes grow well outside the visible soot/pyrolysis region. The flatter temperature distribution and higher temperatures can perhaps explain the shorter CNT lengths and wider CNT growth regions ($r = $ 2–4.5mm of Fig. 6.2(d)), as well

as the orderly-arrayed patterns for Ni/Cr/Fe. Note that the estimated probe temperatures are at least 100K below the gas-phase temperature. It seems that CO is mainly responsible for CNT formation (Fig. 6.2(d)), as C_2H_2 is absent in these regions.
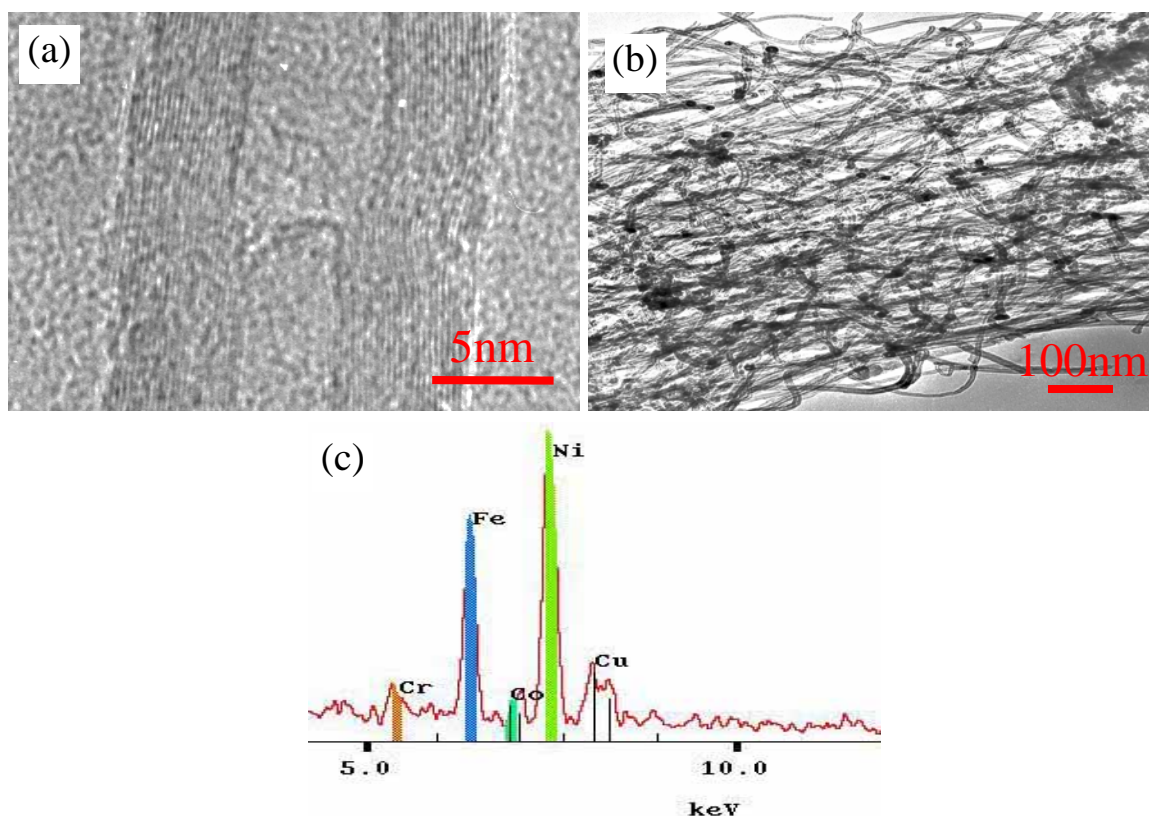
Figure 6.4 TEM images of CNTs grown from Ni/Cr/Fe probe at $z = 12$mm, along with XEDS spectrum of the catalyst nanoparticles. (a) High resolution TEM image showing well-graphitized MWNT with a hollow core. (b) Low magnification TEM image showing the catalyst particles at the CNT tips. (c) EDXS spectrum showing elemental composition of catalyst nanoparticle at tip of a MWNT.

As seen from Fig. 6.2, hydrogen is present only for probe location heights ($z = 9, 12, 15$mm) correlating to CNT synthesis. Hydrogen cannot only form sufficient concentrations of hydrocarbons, but also satisfy unfilled carbon valences at the precipitating rear facets of the metal catalyst. The catalyst metal particles can also be

obtained by selective hydrogen reduction of the alloy, and preliminary results show that hydrogen prolongs the life of the catalysts. At the same time, however, there may exist competition between etching of sp^2 carbon by H atoms and deposition of sp^2 carbon by hydrocarbon intermediates. Future studies will involve *in-situ* measurements of the H radical using laser induced fluorescence (LIF).

Compared to NDFs, an advantage of IDFs for producing CNTs is that the pyrolysis zone of the IDF is outside the oxidation zone. Thus oxidation effects on CNT formation can be avoided. Also, polycyclic aromatic hydrocarbon (PAH) formation pathways are likely altered, which can be conducive to CNT growth from supported catalysts sensitive to PAH deactivation, thereby broadening the growth range. From our studies, the diameters of deposited materials from Fe probes decrease and become fairly uniform as the location height probed in the flame is increased. As probe-location height is scanned, CNTs from Ni/Cr/Fe probes change from randomly directed growth to vertically well-aligned growth. At the tip of the visible soot region, the lengths of CNTs from all probes are much shorter than that at locations just a few millimeters below. While filamentous carbon grows on the Fe probes in the range of $r \approx 0 - 0.9$ mm (at the appropriate vertical locations in the flame), no CNT formation—only amorphous carbon and soot—was found for the Ni/Cu and Ni/Cr/Fe probes in this region. We find that Fe-based catalysts are much more likely to produce large, twisted CNTs, as shown in Fig. 6.3(a). We hypothesize that this may be due to the high Curie temperatures for Fe, which along with the presence of flame-induced magnetic fields, result in circular catalyst nanoparticle motion within the high temperature zones.

Given that optimal conditions for CNT growth are attained at $z = 12$mm for the Ni/Cr/Fe probe in terms of diameter, growth rate, and alignment, sampling time is varied to study the growth rate of CNTs under that condition. The synthesized CNTs are about 1μm in length after 5 minutes, 5 μm after 10 minutes, and 10 μm after 30 minutes. The diameters remained the same for all durations.

6.3.2 Effect of voltage bias on morphology and alignment
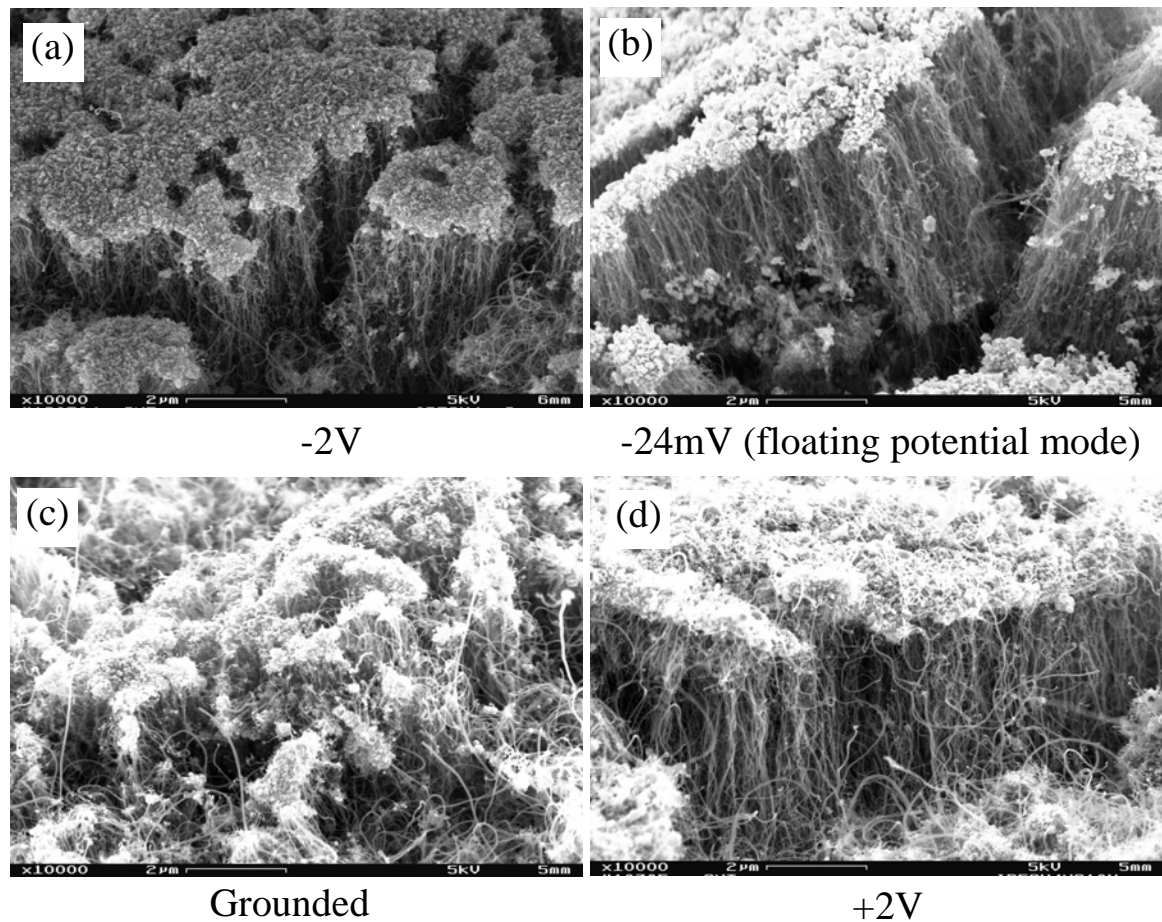
Figure 6. 5 Effect of voltage bias applied to Ni/Cr/Fe catalytic probe at $z = 12$ mm and $r = 1.75$–3.25mm (same positions as in Fig. 6.3(f)) on resulting CNT morphology.

We investigate the effect of voltage bias on the Ni/Cr/ Fe sampling probe on CNT growth. The ideas behind using electrical assistance are to electrophoretically keep soot particles and their precursors from contaminating the CNT yield, and to optimize hydrocarbon precursor delivery to the catalyst nanoparticles through chemical effects induced by transposing and re-distributing ionic species by the action of the electric fields. Our results show that voltage bias on the substrate is conducive to aligning CNTs, as well as enhancing their growth rates as compared to grounded conditions, as depicted in Figure 6.5. Again, the previously optimal condition at $z = 12$ mm and $r = 1.75$–3.25mm is examined. Both negative and positive voltages seem to improve CNT alignment and growth (with negative voltages working a bit better), which we cannot presently explain. Note that operating the probe in FPM results in negative voltages (~24 mV, as induced by flame-generated ions and electrons), and well-aligned CNTs, as seen in Fig. 6.5(b).

6.4 Concluding remarks

The robustness of flame systems to harvest various morphologies and micro-structures of CNTs is evinced in our results. The large thermal and chemical gradients characterizing flames are especially advantageous for determining CNT growth conditions in that a large parameter space of conditions can be found within a single flame. By probing a flame such as that shown in Fig. 6.1 at various heights, local flame structure conditions amenable for CNT growth are readily found. In comparison, systematic variation of parameters such as chemical species and temperature in a CVD reactor would be very time-consuming and tedious. Further utilization of advanced laser-diagnostics to

determine the local *in-situ* temperature and gas-phase chemical species concentrations for given CNT morphologies and growth rates not only reveal fundamental mechanisms, but also establish ''universal'' conditions which should be directly applicable as specific operating conditions for other methods of synthesis. It is worth noting, however, that since there is a large temperature gradient in the radial direction, the temperature and its gradient at the surface of the probes are likely to be less than those in the gas-phase (due to radiative effects and conductive losses). This in effect smears out the spatial resolution, and affects the interpretation of the conditions as local measurements, with respect to CNT growth. Moreover, since there must exist a transient period of nanoparticle formation prior to actual CNT growth, CNT formation and morphology is likely influenced by transient heating effects and spatial gradients. As such, absolute temperature and species concentrations may not be the only parameters identifying specific conditions for CNT growth in our configuration. For example, although gas-phase temperatures and CO and C_2H_2 mole fractions are comparable at locations [z = 9mm, r = 1.0 mm] and [z = 12 mm and r = 0], as seen in Figs. 6.2(b) and (c), the Fe probe inserted at the latter location is more conducive to CNT growth than at the former. More study is needed, especially of the gas/solid interactions.

As seen from our results, alloy composition strongly affects CNT morphology. We generally observe CNT growth that complies with the tip-growth mechanism. Flame structure plays an important role, producing the requisite catalytic nanoparticles, pyrolyzing the fuel into the appropriate reagents (e.g. C_2H_2 and CO) at proper concentrations and temperatures, and facilitating carbon migration diffusion through the particle and precipitation to form the CNT. Using Ni/Cr/Fe probes, we obtained vertically

well-aligned CNTs with uniform diameters of 15nm in our methane-based IDF. The smallest CNT diameters found were around 4 nm. While other works[18, 22, 23, 24, 25] employing NDFs found CNT formation to occur in the soot-laden regions of their flames, our IDF experiments have shown that optimal CNT growth occurs in regions just outside of visible soot/precursor luminescence. Nevertheless, due to the T^4 dependence of soot luminosity, particulate Rayleigh scattering should be employed in future studies to verify that soot particles are actually absent from the region.

Reference

[1]Lee G.W., Jurng J., Hwang J., Synthesis of carbon nanotubes on a catalytic metal substrate by using an ethylene inverse diffusion flame, *Letters to the Editor/Carbon,* 42:667–91, 2004

[2]Lee G.W., Jurng J., Hwang J., Formation of Ni-catalyzed multiwalled carbon nanotubes and nanofibers on a substrate using an ethylene inverse diffusion flame, *Combust Flame,* 139:167–75, 2004

[3]Sidebotham G., An inverse co-flow approach to sooting laminar diffusion flames, PhD thesis, Princeton University, Princeton NJ USA, 1988

[4]Baker R.T., *Carbon,* 27:315–23, 1989

[5]Vander Wal R.L., Hall L.J., and Berger G.M., Optimization of flames synthesis for carbon nanotubes using supported catalyst, *J. Phys. Chem. B*, 106:13122-13132, 2002

[6]Jablonski G.A., Guerts F.W., Sacco A. Jr., Biederman R.R., *Carbon*, 30:87, 1992

[7]Jablonski G.A., Guerts F.W., Sacco A. Jr., *Carbon*, 30:99, 1992

[8]Soneda Y., Makino M., Carbon, 38:475, 2000

[9]Baird T., Fryer J.R., Grant B., Carbon, 12:591, 1974

[10]Moisala A., Nasibulin A.G., and Kauppinen E.I., The role of metal nanoparticles in the catalytic production of single-walled carbon nanotubes-a review*, J. Phys: Condens. Matter*, 15:S3011-S3035, 2003

[11]Kuzuya C., Kohda M., Hishikawa Y., Motojima S., Preparation of carbon micro-coils with the application of outer and inner electromagnetic fields and bias voltage, *Carbon*, 40:1991–2001, 2002

[12]Avigal Y., Kalish R., Growth of aligned carbon nanotubes by biasing during growth, *Appl Phys Lett* , 78(16):2291–3, 2001

[13]Srivastava A.K., Srivastava O.N., Curious aligned of carbon nanotubes under applied electric field, *Carbon,* 39:201–6, 2001

[14]Lee K.H., Cho J.M., Sigmund W., Control of growth orientation for carbon nanotubes, *Appl Phys Lett*, 82(3): 448–50, 2003

[15]Ant U, Yiming L, Hongjie D. Electric-field-aligned growth of singlewalled carbon nanotubes on surfaces. Appl Phys Lett 2002;81(18): 3464–6.

[16]Colbert D.T., Smalley R.E., Electric effects in nanotube growth*, Carbon,* 33(7): 921–4, 1995

[17]Srivastava A., Srivastava A.K., Srivastava O.N., Effect of external electric field on the growth of nanotubules, *Appl Phys Lett,* , 72(14):1685–7, 1998

[18]Merchan-Merchan W., Saveliev A.V., Kennedy L.A., High-rate flame synthesis of vertically aligned carbon nanotubes using electric field control, *Carbon,* 42:599–608, 2004

[19]Arana C.P., Puri I.K., Sen S., Catalytst influence on the flame synthesis of aligned carbon nanotubes and nanofibers, *Proceedings of the Combustion Institute*, 30:2553-2560, 2005

[20] Yokoyama H., Numakura H., and Koiwa M., the solubility of and diffusion of carbon in palladium, *Acta. Mater.*, 46(8):2823-2830, 1998

[21] Vander Wal R.L., Flame synthesis of substrate-supported metal-catalyzed carbon nanotubes, *Chemical Physics Letters*, 324: 217-223, 2000

[22] Yuan L., Saito K., Pan C., Williams F.A., Gordon A.S., Nanotubes from methane flames*, Chem Phys Lett,* 340:237–41, 2001

[23] Yuan L., Saito K., Hu W., Chen Z., Ethylene flame synthesis of well aligned multi-walled carbon nanotubes*, Chem Phys Lett,*346:23–8, 2001

[24] Saveliev A., Merchan-Merchan W., Kennedy L.A., Metal catalyzed synthesis of carbon nanotubes in an opposed flow methane oxygen flame, *Combust Flame*, 135:27–33, 2003

[25] Sen S., Puri I.K., Flame synthesis of carbon nanofibers and nanofiber composites containing encapsulated metal particles, *Nanotechnology*, 15:264–8, 2004

Chapter 7

CNT Synthesis on Catalytic Metal Alloys in Methane/Air Counter-flow Diffusion Flames

7.1 Introduction

In the previous Chapter, an IDF was used to scan a large parameter space of conditions to find auspicious local conditions for CNT growth. However, the 2-D geometry presents large gradients in the radial direction, making it difficult to isolate certain conditions. The CDF is a quasi-one dimensional flame with ideally no gradient in the radial direction. As such, conditions can be sought as a function of axial position. Moreover, the simple and well-defined flame geometry allows for meaningful comparisons between precise experimental probing and detailed computational simulations, facilitating deduction of fundamental controlling mechanisms. We note that Merchan-Merchan and co-workers[1,2,3] have also utilized this geometry (only for oxygen-enriched flames). Additionally, since the hydrocarbon fuel not only provides the source of process heat but also the carbon-based growth reagents to make CNTs, we specifically investigate methane/air systems, thus exploring the possibility of using natural gas in atmospheric air to economically synthesize large quantities of CNTs. We also examine the effects of acetylene addition. Acetylene is often necessary for metal-catalyzed CNT growth since C_2 species readily undergo dissociative adsorption. Concurrently, however, the molecular path towards soot formation requires C_2 species, most notably acetylene (C_2H_2), which is essential to the formation of the first aromatic ring, benzene, enabling

subsequent polycyclic aromatic hydrocarbon (PAH) growth. PAHs can then form soot particles adulterating the yield. Moreover, PAHs (which are particularly stable thermodynamically and resistant towards catalytic dissociation[4,5]) can be detrimental to CNT growth by deactivating the metal-catalyst species. In line with the previous consideration, in order to achieve high-purity yields, we probe CNT synthesis in soot-free regions of the flow field where C-related species (i.e. CO and C_2) concentrations are still high. Since soot formation is a rate process, subject to residence-time considerations, the aerodynamic straining implicit in CDFs becomes advantageous. Because growth from acetylene into a phenyl ring occurs relatively slowly in comparison to ring-growth reactions, it may be possible to produce CNTs in an acetylene-rich flame without a lot of soot byproduct. Finally, we tailor our flames such that the local growth conditions are similar to those that we employed in Chapter 6 in synthesiation of CNTs on metal alloys in IDFs. Optimal local conditions for CNT synthesis should be "universal," as stated in Chapter 6, and such comparisons allow for assessment of the role of spatial gradients in temperature and species in affecting CNT morphologies and growth rates.

7.2 Experiments and Computations

The experimental setup employed in this chapter is as shown in Figs.3.3 and 3.4 in Chapter 3. Two specific CDFs are established, which we refer to as Flame#1 and Flame#2. Flame#1 is a non-sooty 50%CH_4/50%N_2-verus-air flame (Figure 7.1 (a)). Flame#2 is a 42%CH_4/3%C_2H_2/55%N_2-verus-air flame, with a very-thin visible soot layer adjacent to the blue flame chemiluminescence, as seen in Fig. 7.1 (b). Flame structures of these two CDFs are simulated, as shown in Figs. 4.4 and 4.5 in Chapter 4.

For the purpose of discussions, they are given again in Figs. 7.1(c) and 7.1(d) respectively (along with the regions probed). Both flames have the same characteristic peak temperature. A metal alloy probe (0.8mm) is inserted into the hydrocarbon-rich fuel side of the flow field (strategically in the stagnation region to minimize flame perturbation), thereby precipitating CNT growth via carbon migration diffusion through the catalytic nanoparticles extracted from the probe. Prior to synthesis, all metal-alloy probes are ultrasonically cleaned in ethanol and pretreated with diluted nitric acid to remove natural oxidize layers.
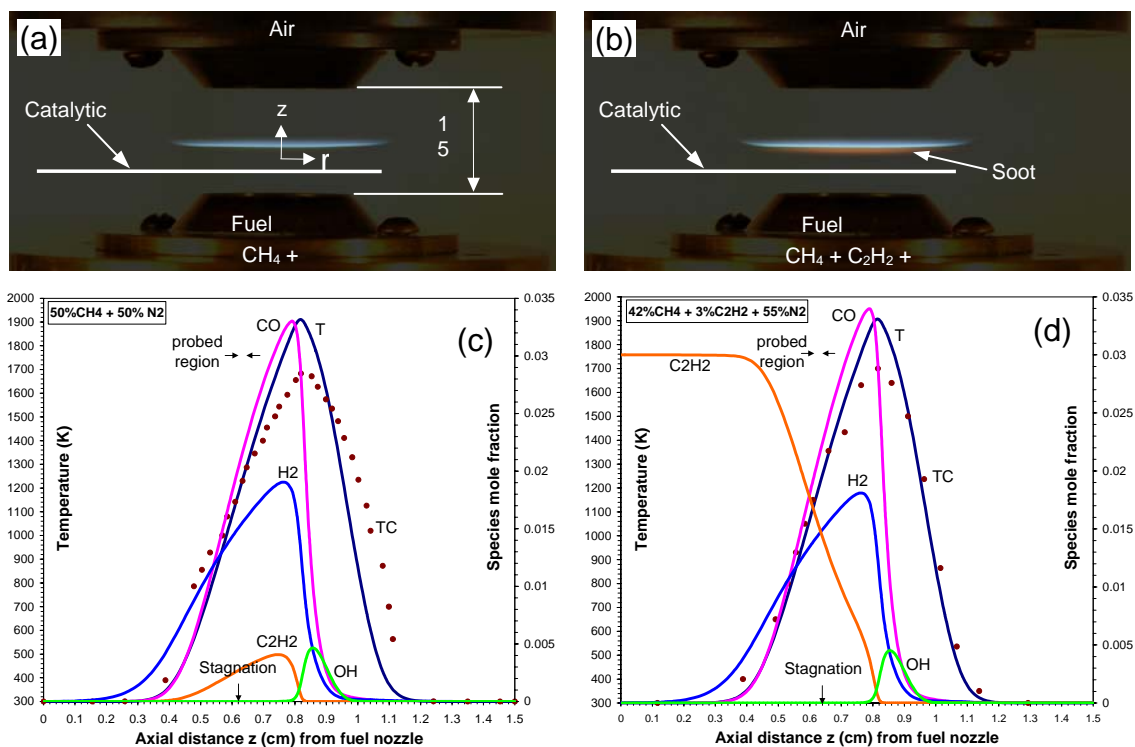
Figure 7.1 Experimental setup for (a) Flame #1, and (b) Flame #2, with visible orange soot layer. Flame structure for (c) Flame #1, and (d) Flame #2. Thermocouple measurements (TC) assess actual probe temperatures. Strain rate is 20 s^{-1}.

7.3 Results and discussions

Table 7.1 summarizes the metal-alloy substrates examined. In general, transition metals (Ni, Co, and Fe) and their alloys have been used as catalysts for CNT growth. Bimetallic catalysts, such as alloys, are known to increase the yield of CNTs[6]. Alloys show a decrease in their melting temperature and an increase in the carbon solubility as compared to single metals[7]. Since both CO and C_2 species can participate in the growth processes of CNTs, we tailor our flames such that there are sufficient concentrations of them in the regions that we probe. Flame#1 and Flame#2 mainly differ by the C_2H_2 concentrations in the region of interest, as seen in Figs.7.1(c,d). Since our synthesis process involves both catalyst nanoparticle formation and CNT growth, the temperatures in the probed region must be conducive for nanoparticle nucleation and active catalytic behavior. In this respect, hydrogen presence in the flame structure (see Figs.7.1(c,d)) is very important. Catalyst metal particles can also be obtained by selective hydrogen reduction of the alloy, and preliminary results show that hydrogen prolongs the life of the catalysts, perhaps by satisfying unfilled carbon valences at the precipitating rear facets of the metal catalyst. At the same time, however, there may exist competition between etching of sp^2 carbon by H atoms and deposition of sp^2 carbon by hydrocarbon intermediates. Consequently, we carefully assess CNT morphologies as functions of local gas-phase temperatures, concentrations of precursor species, and metal alloy compositions.

Table 7.1 Catalytic metal alloys investigated.

Chemical composition	Melting point (K)
99.5% Fe	1808
83% Fe / 17% Cr	1763
45% Ni / 55% Cu	1493
56% Ni / 44% Ti	1583
80% Ni / 20% Cr	1673
60% Ni / 16% Cr / 24% Fe	1623

Figure7.2 compares the morphologies of MWNTs synthesized on different metal alloys in Flame#1 and Flame#2. The Fe/Cr case is not shown in Fig.7.2 because no filamentous carbon grows on its surface for the flame conditions tested. As can be seen, filamentous carbon grows on 99.5% Fe, and CNTs grow on Ni-included Cr-containing alloys (i.e. Ni/Cr and Ni/Fe/Cr). Although the melting temperature of the Fe/Cr alloy is lower than that of the pure Fe metal, and nanoparticles are readily formed on the probe, Cr presence in the nanoparticles may deactivate or lower the catalytic activities of the Fe, perhaps due to the formation of stable chromium carbide (CrC). Chromium carbide formation can compete for incoming carbon, delaying the carbon saturation in nanoparticles. Moreover, once the chromium carbide is formed, its low carbon diffusivity would slow down the diffusion rate of carbon in the nanoparticles[8]. These effects may inhibit CNT nucleation in the Fe/Cr alloy. On the other hand, it seems that Ni presence in Cr-containing nanoparticles permits favorable carbon solubility (Table 7.2) and CNT precipitation at these temperatures, despite the possible formation of CrC. Taking a look at Table 7.2, we can notice that the carbon diffusivities in Ni and Fe are similar (2×10^{-11} and 1.5×10^{-11} respectively), while the carbon solubilities in Ni and Fe at their melting points are 10.7% and 20.2%, respectively. As such, carbon would be saturated earlier and precipitated sooner in Ni than in Fe[9]. Therefore, chromium carbide

formation might not be able to exert its effects to the extent that it would prevent the CNT nucleation as it may in the Fe/Cr alloy.

Table 7.2 Carbon solubility in selected transition metals[10,11,12]

Name	Melting point (T_m) (K)	Carbon solubility (%) at T_m	Carbon diffusion coefficient in metal (m^2s^{-1}) at 1273 K
Iron (Fe)	1808	20.2	1.5×10^{-11}
Cobalt (Co)	1768	13.9	1×10^{-11}
Nickel (Ni)	1726	10.7	2×10^{-11}
Copper (Cu)	1356	2×10^{-4}	Not available

We now examine the CNTs produced in Flame#1 (left-hand column of Fig.7.2). For the 99.5% Fe probe, micro- and nano-scale carbon fibers and tubes are produced, as seen in Fig.7.2 (a), which are characterized by various forms along with a large diameter and distribution (50-100nm). The fibers/tubes tend to be coiled and entangled. Also compared to other metal alloys, CNT yield from the Fe substrate is low. We next consider the three bimetallic Ni-based alloys starting with the lowest melting temperature. The Ni/Cu probe is covered with an entangled mat of CNTs of uniform diameter (~20nm), as shown in Fig.7.2(c). Randomly-directed entangled CNTs cover uniformly the surfaces of both Ni/Ti and Ni/Cr probes, as indicated in Figs.7.2 (e,g). The Ni- and Fe- containing alloy, i.e. Ni/Fe/Cr, allows for entangled growth of CNTs directed outwards from the probe surface with a layer of catalysts at the top of the CNTs. Among the Ni-containing metal alloys, Ni/Cr/Fe and Ni/Cu tend to grow CNTs of smaller diameter (~10-25nm), while Ni/Cr and Ni/Ti grow CNTs of relatively larger diameter (~20-40nm).

TEM imaging reveals that the CNTs synthesized on the alloys are MWNTs with strong graphitic structure. Figure 7.3 shows characteristics of the MWNTs produced by

the Ni/Cu alloy. Figure 7.3(a) presents a low magnification TEM image of bundles of MWNTs, some with catalyst nanoparticles at the tips and some with open tips caused by the removal of catalyst nanoparticles during ultrasonication. Figure 7.3(b) displays a HRTEM image of a helical MWNT node (as will be seen in the inset of Figure 7.6 (d)) showing that the graphitic layers are circulating around the center of the node, and there is a hollow structure at the center[13] (Formation of the node will be discussed later, and images in Ref 13 are shown in Figure 7.4 for comparison), where the spacing between the graphitic layers is ~0.34nm[13, 14, 15]. Figure 7.3(c) shows a 25nm-diameter MWNT segment with parallel graphite walls enclosing a hollow core[16].
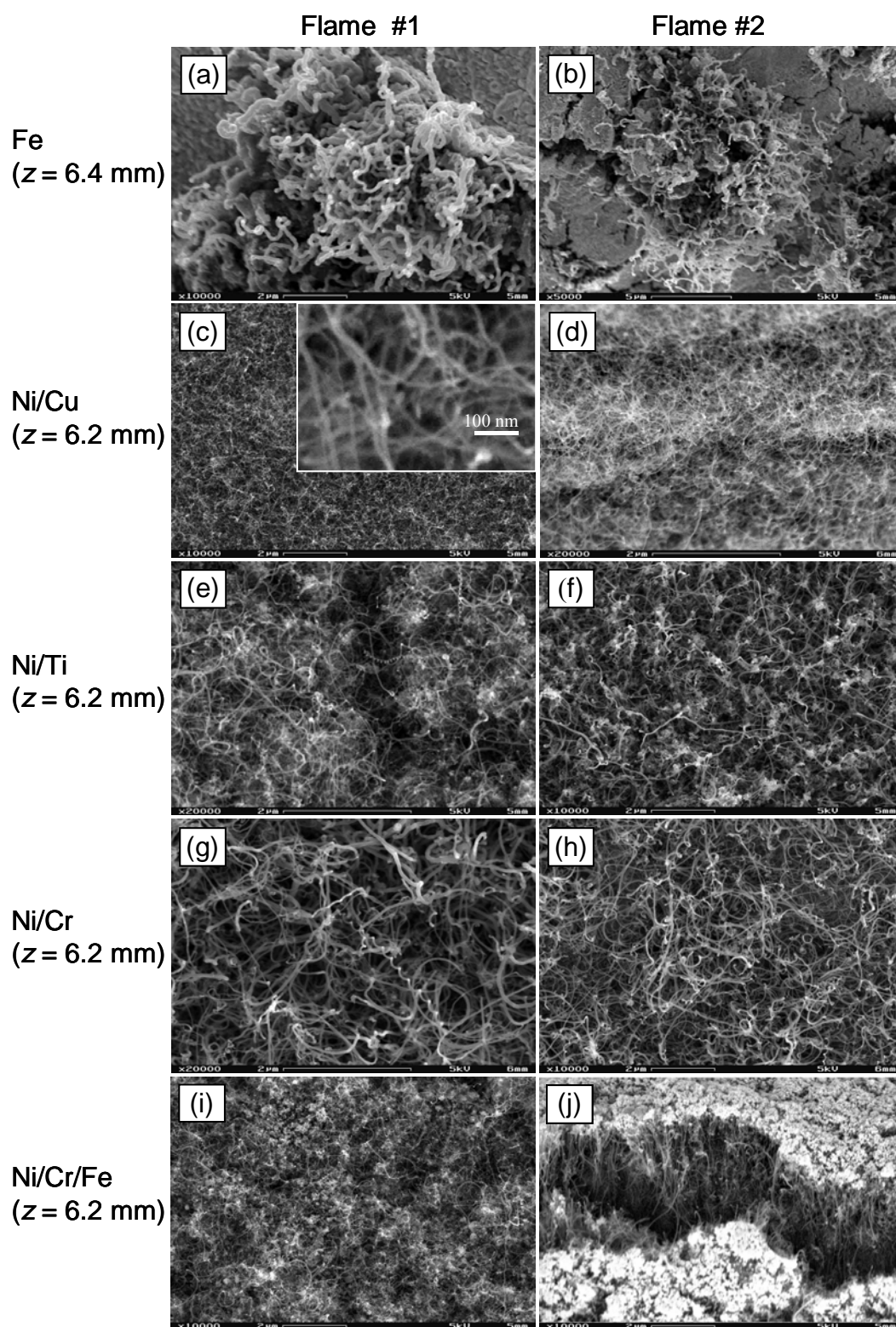
Figure7. 2 Typical FESEM images of MWNTs grown on different catalytic metal alloy probes for Flame #1 and Flame #2. The axial height *z* corresponds to distance from the fuel nozzle as shown in Fig. 7.1.
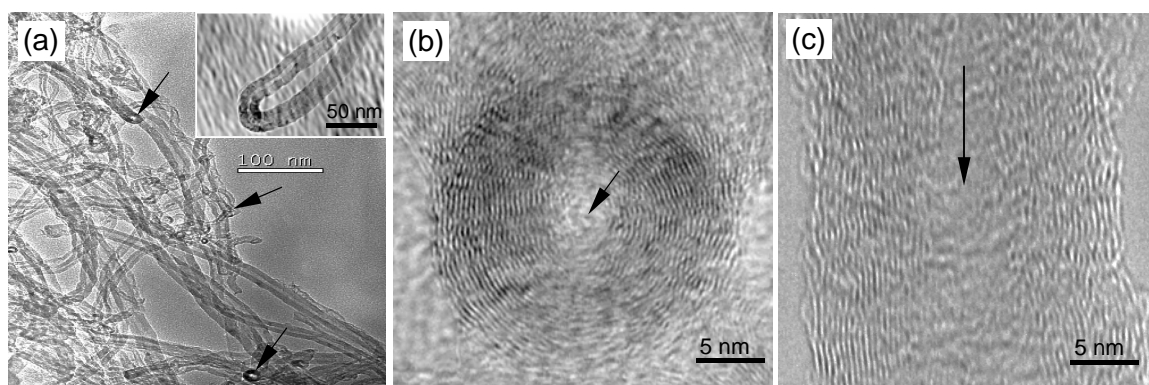
Figure 7. 3 TEM images of MWNTs grown on Ni/Cu probe inserted at z=6.2mm in Flame #1. (a) Low magnification TEM image shows MWNTs of different diameters ~10-25nm. Inset shows a high-bent CNT. Arrows show included catalyst nanoparticles. (b) HRTEM image of a helical MWNT node with a hollow structure at the node center, as indicated by arrow. (c) HRTEM image of graphitic wall layers of a MWNT with a hollow core, as indicated by the arrow.
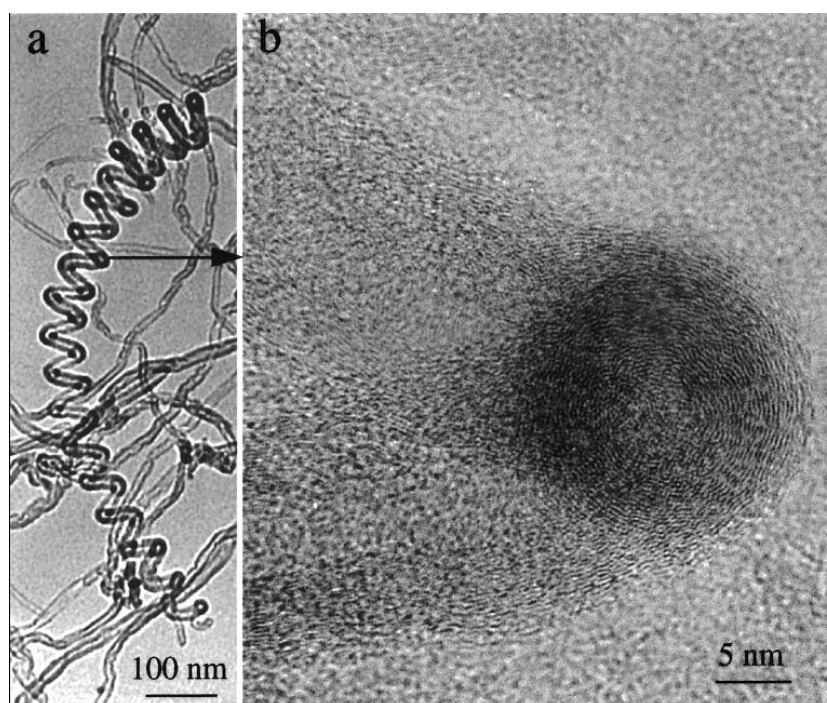
Figure 7.4 (a) Morphologies of the helical MWNTs, (b) High-resolution TEM image recorded from a node (as indicated by an arrowhead in (a)) (Figure from Ref. 13)

The effects of C_2H_2 addition to the fuel on CNT growth are displayed in the right-hand column of Fig.7.2, corresponding to Flame#2. As can be seen in Fig.7.1 (d), C_2H_2 mole fraction at the probe location is about 6 times higher for Flame#2 than Flame#1, while gas-phase temperature and CO mole fraction remain about the same. The amount of C_2H_2 addition was determined by matching the local gas-phase probe conditions (i.e. temperature, C_2H_2, CO, H_2) for Flame#2 to that measured (through SRS) for optimal CNT growth in Chapter 6 which used an IDF that resulted in vertically well-aligned CNTs for the Ni/Cr/Fe probe. Parenthetically, we note that due to the geometry differences, it was difficult to match the actual substrate probe temperature, which was about 100°C higher for the CDF than for the IDF, due to less conductive losses along the length of the probe. Nonetheless, vertically well-aligned CNTs normal to the Ni/Cr/Fe alloy surface (Fig.7.2 (j)) are obtained, showing that local conditions for CNT growth and morphology can be translated between different flame configurations of synthesis. C_2H_2 addition affects the morphology significantly for the Ni/Cr/Fe alloy, by aligning the CNTs. For the other metal alloys, the effects are more subtle, with close examination revealing that the characteristic diameters may be a bit smaller and the overall yield a bit higher, as shown in Fig.7.2, due to the increase of C-related species concentrations.

C_2H_2 addition is found to significantly affect the floating potential, as induced by flame-generated ions and electrons, on the Ni/Cr/Fe probe. For Flame#1, the floating potential is -2mV, while for Flame#2, it is -14mV. The floating potential for the IDF in Chapter 6 is -24mV; the difference in induced voltages may be due to differences in ion deposition rates from different probe temperatures. Nevertheless, the study in Chapter 6 and by others[17] has shown that such electric potentials can significantly affect CNT

alignment. Although applied potentials as small as a few tens of millivolts can develop an electric field exceeding 1000V/cm at the characteristic nanotube diameter[17], perhaps causing alignment, we do not observe alignment in the other metal alloys, even under applied voltage bias. As such, the density of catalytic nanoparticles formed is likely the key parameter, which allows for neighboring CNTs to provide vertical support for each other so that orderly growth perpendicular to the substrate occurs. Carbide induced breakup of the alloy surface to form catalyst nanoparticles responsible for CNT growth may be affected by C_2 transport to the surface, as reflected by the induced voltage. Methane is known as the most stable hydrocarbon and starts its thermal decomposition at approximately $900^{\circ}C$ [18]. The stability of hydrocarbon molecules decreases with increasing number of carbon atoms in saturated hydrocarbons (CH_4, C_2H_6 and C_3H_8)[10]. Unsaturated hydrocarbons (e.g. C_2H_2) are more reactive and unstable resulting from the more easily disrupted π-bonds in their structure. Thermodynamic calculations show that the decomposition of unsaturated hydrocarbons (through the reaction $C_xH_y \rightarrow xC + 1/2yH_2$) is already favorable at the lowest calculated temperature ($200^{\circ}C$). In fact, especially acetylene (C_2H_2) is thermodynamically unstable already at $25^{\circ}C$ [19,10]. The decomposition proceeds readily and the reaction products might undergo further reactions (e.g. decomposition and polymerization) at high temperatuures[10], explaining the presence of the sooting layer and the increased voltage potential (resulting from more ions) due to the addition of acetylene.

EDXS of a single catalyst nanoparticle at the tip of a CNT grown from a Ni/Cr/Fe probe reveals that both Fe and Ni are present. Re-inspecting the FESEM image of Fig.7.2 (j), it seems that a layer of densely packed nanoparticles of Ni-Fe-Cr composition

is uniformly lifted off the surface of the probe, catalyzing aligned nanotube growth. Interestingly, the Ni/Cr/Fe alloy is more favorable for aligned-CNT growth than is Ni/Cr (Figs.7.2 (g,h)) or Fe/Cr (which does not catalyze CNT growth at all). As such, it is possible that Ni is the active catalyst in this nanoparticle, and the presence of Fe in the alloy solution alters mixture properties such that closely-packed nanoparticle nucleation is possible. This hypothesis seems plausible given the observation that the nanoparticles at the tips of the CNTs are often larger in diameter than the CNTs themselves. Nonetheless, more study is needed.
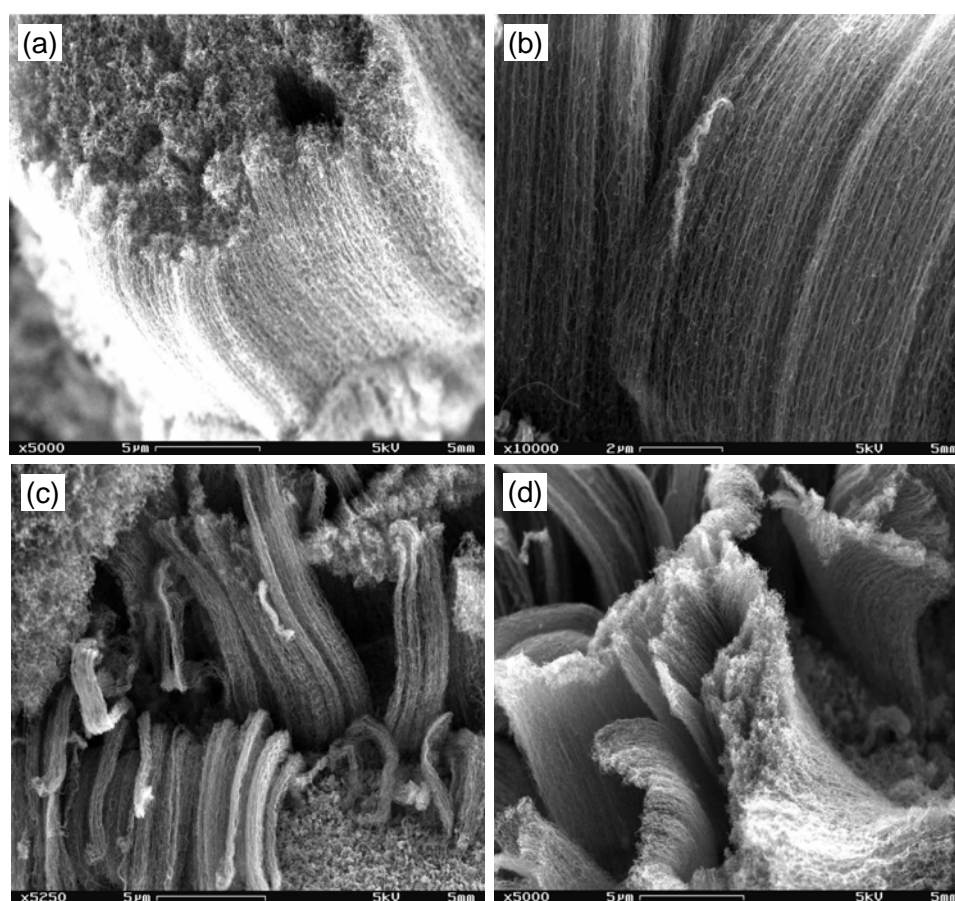
Figure7. 5 FESEM of well-aligned MWNTs grown on Ni/Ti probe inserted at z=6.2mm in Flame #2. (a) Low magnification, and (b) high magnification of vertically well-aligned MWNTs of ~10nm diameter. (c) Bundles of well-aligned MWNTs. (d) Bundled "walls" of well-aligned MWNTs.

Particularly interesting CNT-growth morphology is manifested by the Ni/Ti alloy under Flame#2 conditions. Although the majority of the surface of the probe is covered with entangled CNTs as shown in Fig.7.2 (f), selected areas display high growth rates of well-aligned MWNTs with much smaller diameter (~10nm), as shown in Figure 7.5. These MWNTs are very densely packed, much more so than those grown from the Ni/Cr/Fe alloy (Fig.7.2 (j)). For 10-minute growth duration, the MWNTs are about 20μm in length. As shown in Figs.7.5(c,d), these MWNTs are often found in bundles held tightly together by Van der Waals forces. These different morphologies of CNTs appear to sprout out of fissures on the substrate surface. In hydrocarbon-rich flames, carbide-induced breakup of the alloy surface can occur along grain boundaries and other faults due to volumetric lattice mismatch between the carbide and surrounding metal[20]. As such, non-homogeneities in the grain structure and crystallinity of the metal-alloy probe formed by the die during the drawing process may allow for densely-packed nucleation of nanoparticles in these selective sites. Among these nanoparticles, titanium carbide (TiC) might exist either in the form of nanosized TiC particles or in the form of TiC phase incorporated in the Ni nanoparticles. Unlike chromium carbide, nanoscaled TiC particles (<50nm) exhibit a sufficiently fast diffusion rate of carbon through them. CNTs formed from TiC nanoparticles have been successfully demonstrated[8]. As a result, TiC nanoparticles can increase CNT yield, while TiC phase incorporated into the Ni nanoparticles should not affect the diffusion and saturation of carbon in the Ni nanoparticles. Further, considering the relatively low carbon solubility of Ni compared to that of Fe (Table 7.2), CNTs should be precipitated out without significant growth of Ni nanoparticles, explaining the smaller CNT diameter (~10nm, Figure 7.5).

The large characteristic thermal and chemical gradients characterizing our flames are especially advantageous for determining CNT growth conditions in that a large parameter space of conditions can be easily investigated within a single flame. Metal alloys are tested at different axial locations z in Flame#1 and Flame#2. In both flames, no filamentous carbon (only amorphous carbon) deposits above $z=6.6$mm, corresponding to the fuel side where the local gas-phase temperature is 1350K, despite increasing concentrations of CO and C_2H_2. This is likely due to deactivation of the catalyst at higher temperatures, resulting from metal surface coking due to the rapid amorphous carbon deposition. The evaporation of nanoparticles at these higher temperatures might also account for the absence of CNTs. A remarkable increase in the ratio of surface atoms to internal atoms occurs as the metal particle size decreases to nanometer scale, which results in differences in various physical and chemical properties compared to the bulk material, e.g. lower melting temperatures and higher carbon solubilities in metals[10]. This is because the atoms located on the surface are electronically and coordinatively unsaturated and thus are more reactive and mobile. The melting temperature of a particle (T_c) with radius r can be approximated by

$$T_c = T_0 - \frac{2T_0}{\Delta H_{fusion} \rho_s r}[\sigma_{sl} + (1 - \frac{\rho_s}{\rho_l})\sigma_l]$$

where T_0 is the bulk melting temperature; H_{fusion} is the latent heat of fusion; ρ_s and ρ_l are the densities of solid and liquid metal, respectively; σ_{sl} is the solid–liquid interfacial energy; and σ_l is the surface energy of the liquid[10,21]. The melting temperature of metal particles smaller than approximately 100 nm can be significantly reduced from the bulk value, especially for particles below 10 nm[22].

z = 6.4 mm   z = 6.2 mm   z = 5.8 mm
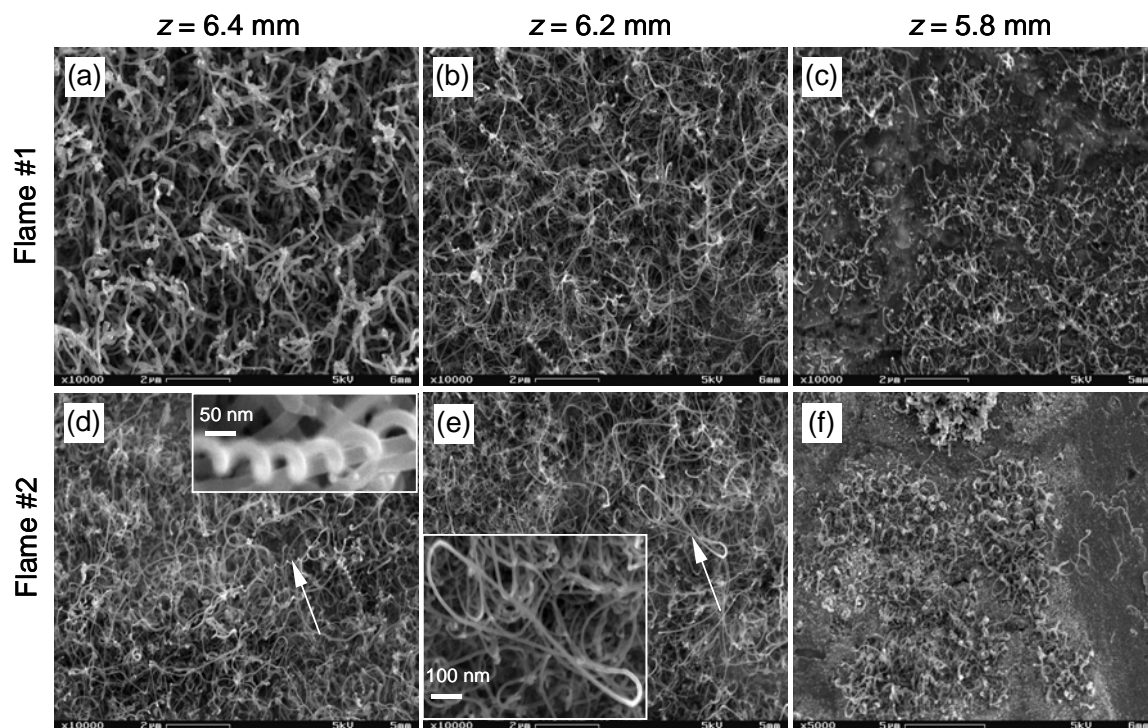
Figure 7.6 FESEM images of MWNTs grown on Ni/Cr probes inserted at different axial locations z, near the stagnation plane for Flame #1 and Flame #2. Insets show interesting structures.

Figure 7.6 shows FESEM images of MWNTs grown on Ni/Cr probes inserted at three different axial locations (near the stagnation point) in the two flames, respectively, where the gas-phase temperatures range from 1300K to 1000K with decreasing axial height. As can be seen in Figs.7.6 (a-c) for Flame#1 and Figs.7.6 (d-f) for Flame#2, there appear to be a very-slight decreases in CNT diameters, but obvious decreases in yields and lengths. The catalyst nanoparticles are active at these temperatures, and the increase in CNT diameter with axial height may be attributable to continued nanoparticle growth with increasing temperature (see Figs.7.1(c,d)). The decrease in CNT yield with decreasing axial height is attributable to reduced rates of catalytic nanoparticle formation at lower temperatures. Below z= 5.8mm in Flame#1 and Flame#2, where the local gas-phase

temperatures are ~950K, CNTs are no longer observed, despite sufficient concentrations of CO for both flames and sufficient concentrations of C_2H_2 for Flame #2. This result corresponds to lack of nanoparticle formation at these temperatures. Note from Figs.7.1 (a,b) that probe temperatures and gas-phase temperatures are approximately the same in the region of CNT formation. Similar trends are found for the other metal alloy compositions.

Finally, since the axial gradients are large in our flames, we assess the effects of probe diameter on CNT growth. Large diameter probes could experience significantly different chemical species concentrations and local gas-phase temperatures between the top and bottom surface of probe due to the large gradients. The large diameter probes could also disturb more severely the flow field, affecting the local reactions. Additionally, large diameter probes might suffer more heat loss through radiation and conduction. All these effects could impact CNT growth. As such, two different diameters (0.5mm and 0.8mm) of Fe and Ni/Ti probes are compared. The results show no discernable differences in characteristics of as-grown MWNTs. The reason may be that the probe diameter is not large enough to change CNT growth significantly. We conclude that for the characteristic probe diameters employed in this work, the CNT morphologies and characteristics obtained correlate well with local absolute conditions.

7.4 Concluding Remarks

In the present investigation, we have successfully grown CNTs on various catalytic metal alloys in non-sooting methane/air CDFs. Alloy composition strongly affects CNT morphology, along with gas-phase temperature and local C_2H_2 concentration. Vertically

well-aligned MWNTs are synthesized on Ni/Cr/Fe (~20nm diameter) and Ni/Ti (~10nm diameter), when there is sufficient C_2H_2 concentration. Notably, C_2H_2 addition affects the potential induced on the substrate.
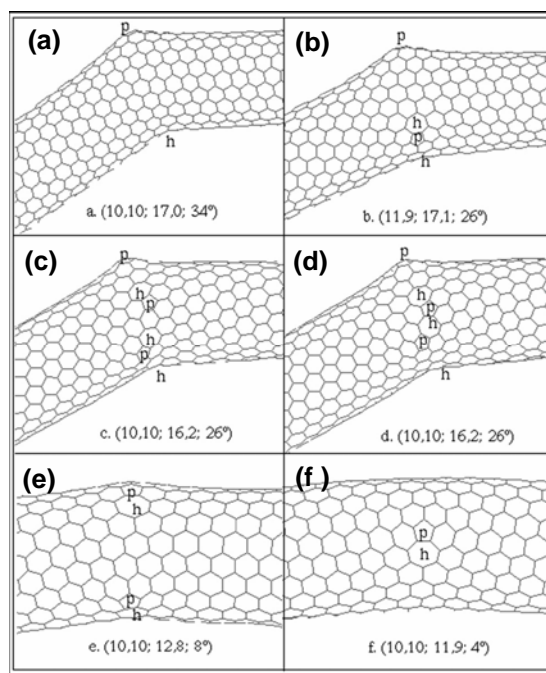
Figure 7.7 Examples of simulated SWNT bends. (a) a 34° bend has one pentagon and one heptagon in the opposite sites of the joint; (b)–(d) a 26° bend has three pentagon-heptagon defects with one in opposite sites and the other two defects (fused pentagon heptagon pairs) in different arrangements; (e) a 8° bend has two fused defects; and (f) a 4° bend has only one fused defect (Figure from reference 23).

We also observed some special structured CNTs such as coiled and highly bent CNTs, as seen in the insets of the figures (Fig. 7.6 (d) and (e)). Structurally, these types of structures result from the introduction of defects (pentagon rings and heptagon rings) into the usual network of hexagonal rings (Figure7.7)[23]. These defects are likely introduced into the hexagonal ring network due to the shape of the catalyst particle. This

explanation is based on the assumption that dissociative adsorption and carbon dissolution occur on different crystalline facets of the catalyst particle[24]. The different facets of catalyst nanoparticle could exhibit different carbon precipitation rate during the CNT growth, causing non-homogeneity of the extrusion velocity of carbon on different facets that can introduce the pentagon and heptagon rings. Comparisons with our previous work using CDFs in Chapter 6 evince that local condition (i.e. temperature and growth related chemical species) for CNT growth and morphology can be translated between different configurations of synthesis.

Reference:

[1]W. Merchan-Merchan, A. Saveliev, L.A. Kennedy, A. Fridman, Chem. Phys. Lett. 354 (2002) 20-4.

[2]W. Merchan-Merchan, A.V. Saveliev, L.A. Kennedy, Carbon 42 (2004) 599-608.

[3]Alexei V. Saveliev, Wilson Merchan-Merchan, Lawrence A. Kennedy, Combust. Flame 135 (2003) 27-33.

[4]S.E. Stein, A.J. Fahr, J. Phys. Chem. 89 (1985) 3714.

[5]R.L. Vander Wal, T.M. Ticich, V.E. Curtis, Chem. Phys. Lett. 323 (2000) 217-223.

[6]A. Moisala, A.G. Nasibulin, E.I. Kauppinen, J Physics: Cond. Mat. 15 (2003) S3011-S3035.

[7]C.P. Arana, I.K. Puri, S. Sen, Proc. Combust. Inst. 30 (2005) 2553-2560.

[8]Deck C.P., and Vecchio K., Prediction of carbon nanotube growth success by the analysis of carbon-catalyst binary phase diagrams, *Carbon*, 44:267-275, 2006

[9]C.P. Arana, I.K. Puri, S. Sen, Proc. Combust. Inst. 30 (2005) 2553-2560.

[10]Moisala A., Nasibulin A.G., and Kauppinen E.I., The role of metal nanoparticles in the catalytic production of single-walled carbon nanotubes-a review, *J. Phys: Condens. Matter*, 15:s3011-s3035, 2003

[11]Kulikov I S, Termodinamika Karbidov i Nitridov (Thermodynamics of Carbides and Nitrides) (Chelybinsk:
Metallurgija) pp 149–52, , 1988

[12]Yokoyama H, Numakura H and Koiwa M, *Acta Mater.*, 46: 2823–30, 1998

[13]Gao R., Wang Z.L., and Fan S., Kinetically controlled growth of helical and zigzag shapes of carbon nanotubes, *J. Phys. Chem. B*, 104:1227-1234, 2000

[14]Merchan-merchan W., Saveliev A.V., Kennedy L.A., Carbon nanostructures in opposed-flow methane oxy-flames, *Combustion Science and Technology*, 175:2217,2003

[15]Ajayan P. M., Nanotubes from Carbon*, Chem. Rev.,* 99:1787, 1999

[16]Vander Wal R.L., Flame synthesis of substrate-supported metal-catalyzed carbon nanotubes, *Chemical Physics Letters*, 324: 217-223, 2000

[17]W. Merchan-Merchan, A.V. Saveliev, L.A. Kennedy, Carbon 42 (2004) 599-608.

[18]Shah N, Panjala D and Huffman G P 2001 *North American Catalysis Society Mtg,* (Toronto, Canada, June 2001)

[19]P¨assler P, HefnerWandWernicke H-J 1985Ullmann's Encyclopedia of Industrial Chemistry volA1 (Weinheim:
VCH) pp 97–145

[20]R.L. Vanderwal, Comment on paper: Proc. Combust. Inst. 30 (2005) 2553-2560.

[21]Friedlander S K 2000 Smoke, Dust, and Haze 2nd edn (New York: Oxford University Press) p 407

[22]Buffat Ph and Borel J-P 1976 Phys. Rev. A 13 2287–98

[23]Han J., Anantram M.P., Jaffe R.L, Kong J., and Dai H., Observation and modeling of singe-wall carbon nanotube bend junctions, *Physical Review B*, 57(23): 14983-14989

[24]Vander Wal R.L., Hall L.J., and Berger G.M., Optimization of flames synthesis for carbon nanotubes using supported catalyst, *J. Phys. Chem B*, 106:13122-13132, 106

Chapter 8

MWNTs and SWNTs Catalytically Synthesized from Spinels in Methane/Air Counter-flow Diffusion Flames

8.1 Introduction

Among the many factors involved in carbon nanotube (CNT) synthesis, catalyst properties such as size, density, and distribution play a key role. Using catalytic chemical vapor deposition method (CCVD), Colomer *et al.*[1]explored the relationship between CNT production and different catalyst metals supported on different substrates. In their work, both isolated single-walled CNTs (SWNTs) and SWNT bundles were prepared by flowing an ethylene-nitrogen mixture (30 and 80 ml min^{-1} respectively) over different types of supported metal catalysts in a fixed-bed reactor at 1080 ^{o}C for 60 mins. Various catalytic metals (Co, Ni, Fe) and metal mixtures (Co-Fe, Ni-Co, Co-Fe, Co-Ni-Fe) supported on different supports (alumina and silica) were investigated. Although SWNTs were obtained in all cases, the authors observed that the yield differences of SWNTs depending on the nature of the metal and the type of the support. For metal catalysts, alumina support showed greater SWNT yield than fumed silica, whereas for metal mixtures, support material did not play an important role. Individual SWNTs were observed for all metals, but Co and Fe seemed to behave more actively than Ni, with some SWNT bundles also detected in the samples from Co and Fe. Fe-Co and Fe-Co-Ni mixtures supported on alumina were found to be the most effective among all the metal

mixtures, with a significant amount of SWNT bundles obtained from these two mixtures. In addition, individual SWNTs were observed to have a larger diameter (~2nm) that was considered to be associated with the size of catalytic metal particle, while each SWNT in the bundle showed a smaller diameter (~0.7nm) that was explained to be linked to the nature of the metal surface. In Colomer *et al.*'s another work[2], the authors pointed out that the choice of the support and the choice of the metals or metal mixtures seem be determinant in the synthesis of single-walled carbon nanotubes (SWNTs). As-grown SWNT samples from Fe and Fe-containing mixtures contained more MWNTs and encapsulated metal particles than did the SWNT samples from Co catalysts. The authors further reported that only catalyst particles with a size smaller than 15nm were active for growing SWNT bundles, whereas larger particles were often observed to be encapsulated by several graphitic layers. An attempt was made by Kukovecz *et al.*[3] to synthesize MWNTs using cobalt, iron, and nickel supported on different types of silica-aluminas to investigate the mechanisms governing their nanotube-producing activity. They reported that increasing the reaction temperature and the flow rate of acetylene increased the deposited carbon. The catalytic activity of metal particles was enhanced by increasing the silica in the support mixture, but this also resulted in an increase in the thickness of the CNTs.

The main difficulty is to obtain these nanometric particles at the relatively high temperature (usually higher than 600 ºC) required for the formation of CNTs. The reduction of metal-oxide solid solutions produces metal particles at a high enough temperature for hydrocarbon gas to immediately interact with them, thereby forming CNTs prior to any considerable particle growth[4]. As such, very small diameter CNTs can

be grown, with CNT diameter correlating with catalytic particle size. In contrast, materials derived from the impregnation of a substrate by a transition metal salt usually produced large carbon fibers, some of which are hollow, with only a small proportion of true CNTs[4]. Employing different oxide solid solutions (e.g. $Al_{1.8}Fe_{0.2}O_3$, $Mg_{1-x}Co_xO$), Peigney's group[5,6,7,8] has successfully produced CNTs (with high purity and high amount of SWNT bundles) and CNTs-metal-oxide nanocomposites using CCVD in a H_2-CH_4 atmosphere. They also extensively investigated the effects of various compositions of solid solutions on the growth of CNTs and nanocomposites. The decomposition of CH_4 over incipient nanoparticles prevents further particle growth resulting in a very strong proportion of SWNTs and double-walled carbon nanotubes (DWNT) compared to other carbon structures[9].

Another advantage of utilizing metal-oxide solid solutions is that the production of CNTs can be achieved by purposely selecting the composition of the metal-oxide solution, for example, using $Mg_{1-x}Co_xO$ because MgO can be easily removed from the material by a mild non-oxidative washing with HCl aqueous solution[5,10]. Additionally this route can result in direct synthesis of CNT-containing nanocomposites from which macroscopic dense ceramic-matrix composites can then be prepared by hot pressing[11]. Because most of the research on CNT-containing composites so far has dealt with polymer-matrix materials, ceramic-matrix composites have been much less investigated[12]. The significance of directly growing CNT-containing nanocomposites lies not only in the remarkable mechanical properties of CNTs, but also in their interesting electronic characteristics. Ceramics and metal-oxide nanocomposites are generally insulators. However, to avoid the electrostatic charging of an insulating matrix, an

electrical conductivity above 10^{-4} S/cm is needed, which is required to provide electrostatic discharge as well as electromagnetic radio-frequency interference protection[12]. CNT-containing nanocomposites grown directly from metal-oxide solid solutions have been shown to possess an electrical conductivity of the order of 1 S/cm, due to the percolation of the CNTs network [11,13].

Some of the drawbacks of the above-mentioned CCVD method using metal oxide solid solutions involve long processing time (up to 4h[7]), non-continuous batch processing, and high energy consumption (e.g. using H_2/CH_4 as gas supply while heating the furnace electrically). For cost-reducing large-scale applications, synthetic methods should be continuous and energy-efficient, utilizing inexpensive starting materials. In this chapter, the catalytic synthesis of CNTs (MWNTs and SWNTs) in a soot-free methane/air CDF by using catalysts elements (Ni, Co and Fe) found within metal-oxide solid solutions (i.e. $NiAl_2O_4$, $CoAl_2O_4$ and $ZnFe_2O_4$) serving as substrates is reported. The CDF geometry is chosen for the reasons given in Chapter 7 (Introduction part). An attempt is made to explore a common growth environment independent of the specific form of catalyst support by comparing alloy-supported (Chapter 7) and metal-oxide supported forms (this chapter). We not only demonstrate the successful growth of CNTs using metal-oxide solid solutions in the flame environment under atmospheric pressure, but also probe some growth parameters in order to optimize their growth. It is envisioned that our technique can be employed to directly produce CNT-metal-oxide and CNT-ceramic nanocomposite powders from which massive CNT-containing composites can be synthesized.

8.2 Experiments and Computations

8.2.1 Spinels preparation
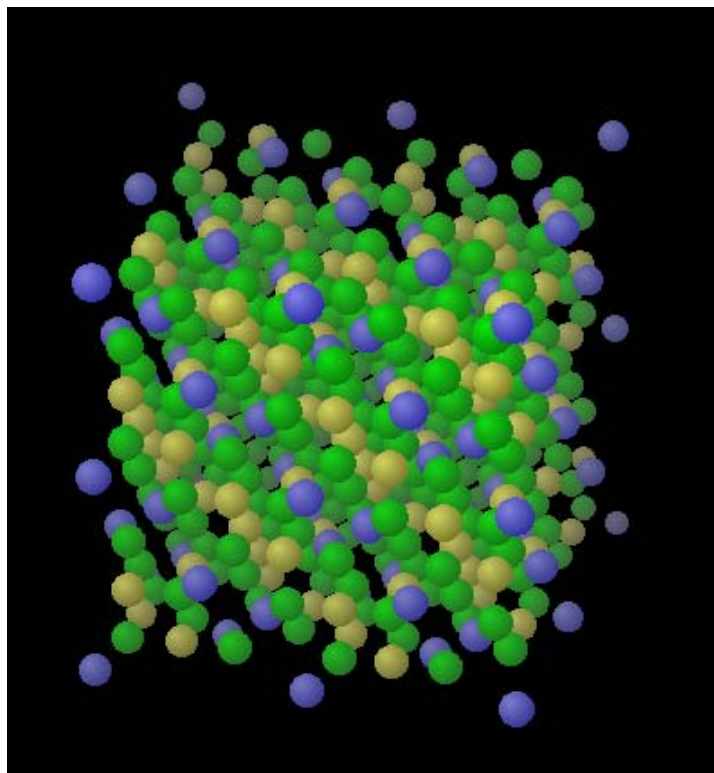
Figure 8.1 Schematic structure of Spinel having a chemical formula of AB_2O_4 where B is yellow, A is blue and O is green. It consists of a B cation in the center of an oxygen octahedron and an A cation in the center of an oxygen tetrahedron.

Spinels have a chemical formula of AB_2O_4, where a B cation is in the center of an oxygen octahedron and an A cation is in the center of an oxygen tetrahedron. Spinels have face centered cubic (FCC) oxygen sub-lattice and contain 8 molecules in the unit cell (i.e. $A_8B_{16}O_{32}$). The unit cell of so-called normal spinels (investigated in this Chapter) therefore has 32 oxygen ions, 32 octahedral holes (half filled by B) and 64 tetrahedral holes (1/8 filled by A), as shown in Fig. 8.1. As a result, the matrix nature of the oxide

solid solution allows for spatially-distinct and size-limited metal nanoparticles to form on its surface. According to the generally-accepted growth mechanism of CNTs, CNT diameter is determined by the size of the catalytic nanoparticle. Spinels are expected to give well-spaced SWNTs and MWNTs of seemingly "uniform" diameters, controllable within the 1.5 to 15nm range. The normal spinels examined in this chapter include: $NiO \cdot Al_2O_3 = NiAl_2O_4$; $CoO \cdot Al_2O_3 = CoAl_2O_4$; and $ZnO \cdot Fe_2O_3 = ZnFe_2O_4$. All spinel powders are prepared by a co-precipitation process.

8.2.1.1 Cobalt aluminate (CoAl$_2$O$_4$)

A mixture of $CoSO_4 \cdot 7H_2O$ and $Al(NO_3)_3 \cdot 9H_2O$ in a 1:2 ratio is dissolved in de-ionized water. This mixture is mixed into an alkali solution where ammonia is added simultaneously to keep the pH value of the whole solution system at 10. The solution system is stirred magnetically for 12 hours. The precipitates (the mixture of cobalt hydroxide and aluminum hydroxide) are separated from the solution with a filter, and washed with de-ionized water and ethyl alcohol. After being dried at 70 ^{o}C in air for 12 hours, the samples are heated at 950 ^{o}C in an oven for 1 hour. The obtained the $CoAl_2O_4$ solids are ground with a pestle and mortar into a fine powder.

8.2.1.2 Nickel aluminate (NiAl$_2$O$_4$)

$NiAl_2O_4$ powders are obtained and heated in the oven at 900 ^{o}C through the same procedures as in the preparation of $CoAl_2O_4$, with the exception that the starting reagent is $Ni(NO_3)_2 \cdot 6H_2O$.

8.2.1.3 Zinc ferrite (ZnFe$_2$O$_4$)

The preparation is again identical to that used for CoAl$_2$O$_4$, except that ZnCl$_2$ and FeSO$_4\cdot$7H$_2$O are used as starting reagents and heated at 1000 ^{o}C.

8.2.2 Characterizations of spinels

The as-prepared spinels are characterized by X-ray diffraction (XRD) using Cu-Kα radiation (λ=0.15418nm). Their patterns are shown in Fig. 8.2. All peaks in the second spectrum are indexed to the CoAl$_2$O$_4$ phase without impurities in the cobalt aluminate. Although all the peaks are accounted for the NiAl$_2$O$_4$ phase in the nickel aluminate solution, the peaks are a bit wider than those for the CoAl$_2$O$_4$ peaks shown in the cobalt aluminnate, which reflect the smaller crystallization size and a poorer crystallization level[7] than CoAl$_2$O$_4$ phase in the cobalt aluminate solution. For zinc ferrite, the peaks can be attributed to ZnFe$_2$O$_4$ phase, where the peaks are the sharpest showing the best crystallization level among the three solid solutions.
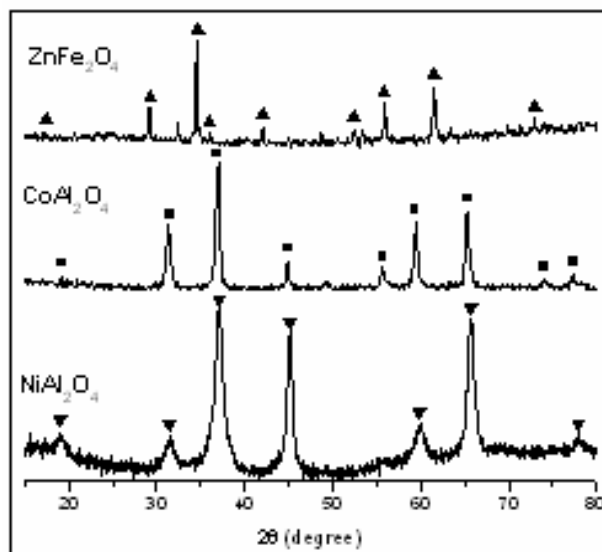
Figure 8.2 XRD patterns of as-prepared spinel solid solutions.

8.2.3 Spinels coating onto the support substrates

The as-prepared spinel powders are put into ethanol with a weight ratio of 2% spinel, and then ultrasonicated for 20 minutes to form a homogeneous suspension. This suspension is dropped onto the surface of the flat end of a spatula-shaped copper substrate with a dimension of 0.8mm wide and 0.2mm thick at the flat end. These substrates are ready to be tested for CNT growth after being dried in air.

8.2.4 Experiment
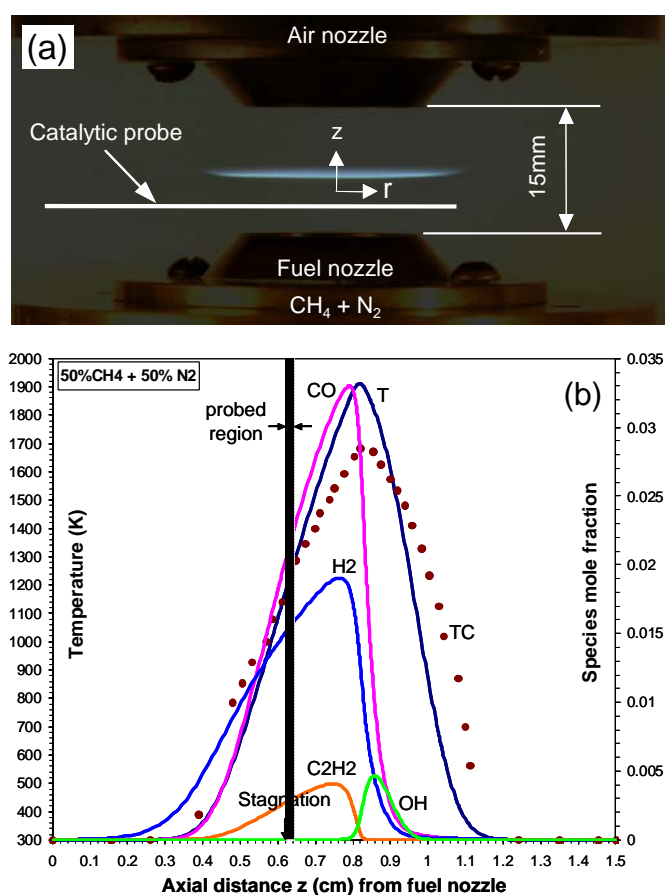
Figure 8.3 Experimental setup (a) and Flame structure (b). Thermocouple measurements (TC) assess actual probe temperatures. Strain rate is 20s^{-1} (reproduced from Chapter 7).

The experimental setup described in Chapter 7 is used. The Flame#1 in Chapter 7 is investigated and reproduced here (Fig. 8.3). A spinel-coated copper substrate is inserted into the hydrocarbon-rich fuel side of the flow field by mounting the substrate to a linear translation stage. After 10 minutes, the substrate is removed, and then a second substrate is inserted immediately. It is envisioned that a continuously fed wire may be used to produce CNTs in a continuous process. The as-grown carbon materials are investigated using FESEM to assess CNT morphology. After ultrasonic treatment, low magnification TEM and HRTEM characterize individual CNTs and bundles.

8.3 Results and discussions

8.3.1 Effects of spinel solid solutions on CNT growth

Table 8.1 Temperatures at which spinels are reduced by hydrogen[45,14,15]

Spinels	Reduction temperature by H_2
$NiAl_2O_4$	790 ^{o}C
$CoAl_2O_4$	870 ^{o}C
$ZnFe_2O_4$	650 ^{o}C

Three spinel solid solutions, $NiAl_2O_4$, $CoAl_2O_4$ and $ZnFe_2O_4$, are investigated in our experiment to assess the quality and quantity of CNTs grown from them. The catalyst nanoparticles (Ni, Co and Fe) are extracted from the metal-oxide substrate by the *in-situ* reduction from their corresponding ion states in the three corresponding spinel solid solutions with flame-generated H_2[16] and CO[17] species as reductants, as shown in Fig.8.3 (c). Table 8.1 shows the temperature of hydrogen reduction for these three metal-oxide

solutions. The prepared catalyst nanoparticles can either stay inside or attach to the surface of the reduced grains, yet only nanoparticles present on the surface of the reduced grains can catalyze CNT growth, whereas those present in the interior of the grains remain inactive[5]. Carbon precursors (e.g. CH_4, CO and C_2H_2) readily undergo dissociative adsorption over the incipient catalytic nanoparticles and diffuse on their surface or through them to grow into CNTs[18]. The nanoparticles can either remain attached to the suface and situated at the base of the growing CNT or detach from the surface and situated at the tip of the CNT.
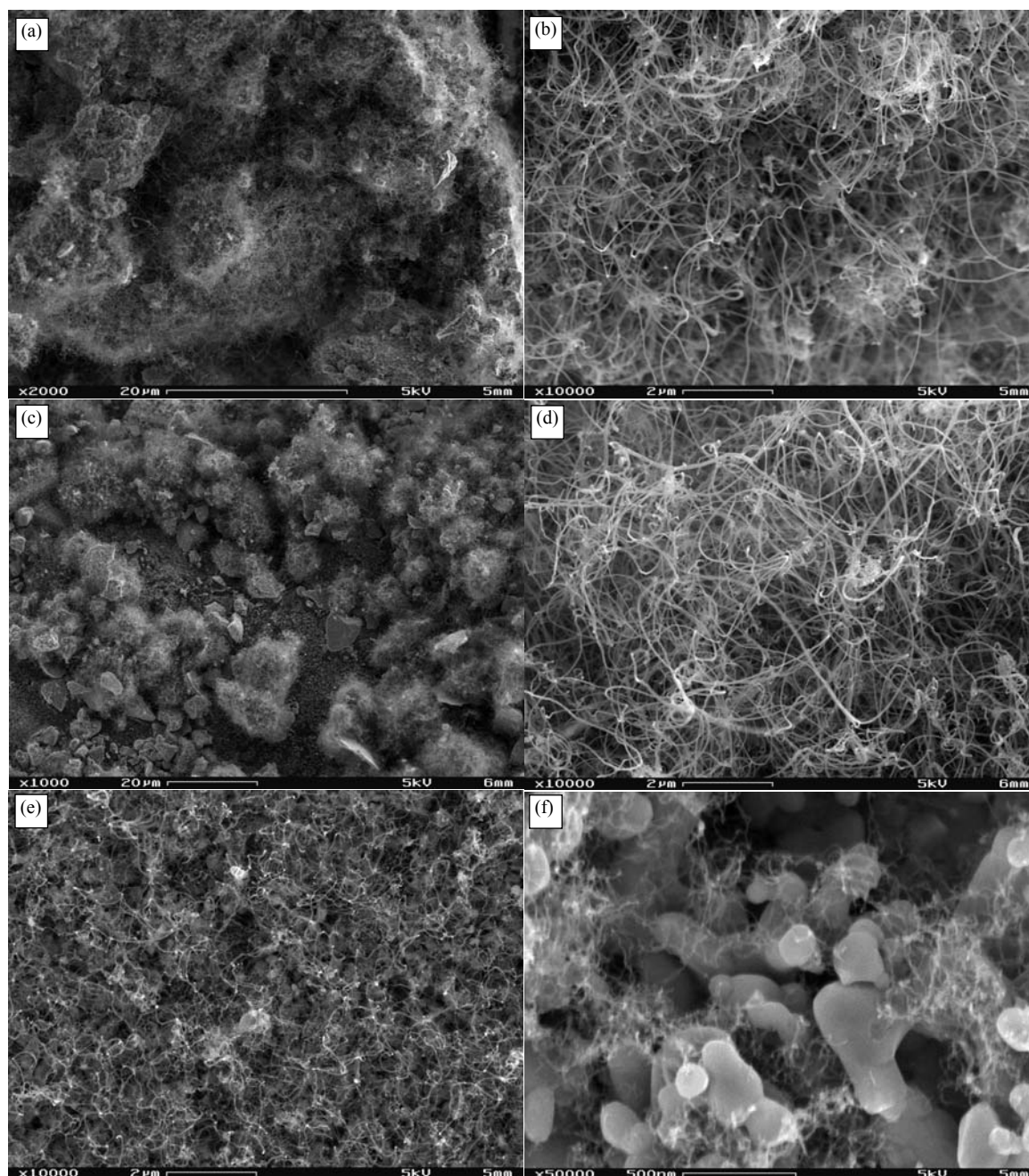
Figure 8.4 Typical FESEM images of CNTs grown from spinel solid solutions at z=6.2mm. (a) Low magnification image of CNTs from $NiAl_2O_4$. (b) High magnification image of CNTs covering a single reduced $NiAl_2O_4$ grain. (c) Low magnification image of CNTs from $CoAl_2O_4$. (d) High magnification image of CNTs covering a single reduced $CoAl_2O_4$ grain. (e) Low magnification image of CNTs from $ZnFe_2O_4$. (f) High magnification image of CNTs covering reduced $ZnFe_2O_4$ grains.

Figure 8.4 shows the typical FESEM images of CNTs grown from the spinel solid solutions. As seen in Fig. 8.4 (a) (a low magnification image of CNTs grown from $NiAl_2O_4$), a large yield of densely-packed CNTs cover all reduced grains. A closer look at the surface of a single reduced grain, as shown in Fig.8.4 (b), shows that the grain is covered uniformly and densely with CNTs arranged in long entangled bundles with outer diameters of 20-50nm and lengths of more than 10μm. Similar CNT morphologies as those from $NiAl_2O_4$ are obtained from $CoAl_2O_4$ in terms of length, diameter, and yield, as shown in Fig. 8.4 (c) (low magnification) and Fig.8.4 (d) (higher magnification), where CNTs cover the surfaces of the reduced $CoAl_2O_4$ grains. From our experimental observation, the overall yield of CNTs from $NiAl_2O_4$ is a bit higher than from $CoAl_2O_4$. The reason could be due to the poorer crystallization level of the nickel aluminate spinel. Because the only metal nanoparticles active for CNT growth are those located at the surface of the reduced grains, the active-to-inactive nanoparticle ratio could be increased using powders with a high specific surface area such as poorly crystallized oxide solid solutions[7]. The concentration of nickel nanoparticles on the surface of the reduced grains is a bit higher than that for cobalt nanoparticles, perhaps due to poorer bulk crystallization level of nickel aluminate spinel giving a higher CNT yield. However, for the solid solutions having a relatively high specific area, most of the metallic ions are located at or near the surface of the unreduced grains and can readily be reduced to the metallic states, giving rise to a very high number of metal particles. These in turn can easily coalesce at the surface of the reduced grain to form much larger particles leading to CNTs of larger diameter[19]. Moreover, upon heating during the CNT growth process, the recrystallization of poorly crystallized solid solution can provoke the entrapment of

carbon within the reduced grain to potentially deteriorate the mechanical property of the CNT-containing composites prepared from these nanocomposite powders[7]. CNTs from $ZnFe_2O_4$ are a mixture of MWNTs and SWNTs, as shown in Fig.8.4 (e), (a lower magnification FESEM image). By noting that the magnification of Fig.8.4 (e) is the same as the magnifications of Fig. 8.4 (b) and Fig. 8.4 (d), we can see that a majority of CNTs from $ZnFe_2O_4$ are much thinner than those from either $NiAl_2O_4$ or $CoAl_2O_4$, with a diameter less than 15nm, and also shorter with lengths around 2μm. Fig. 8.4 (f) shows a higher magnification FESEM of CNTs from $ZnFe_2O_4$, which mainly contains SWNTs with diameters around 5nm. CNTs from $ZnFe_2O_4$ are not only thinner and shorter than those from both $NiAl_2O_4$ and $CoAl_2O_4$, but also lower in overall yield. The reason may be attributed to the well-crystallized level of zinc ferrite spinel, as indicated in the XRD patterns. The well crystallized solid solution has a low specific surface area favoring the formation of metal particles of smaller size[20], resulting in a low but high quality yield of CNTs with smaller size and higher aspect ratio[7]. Furthermore H_2 likely increases the mobility of reduced metal nanoparticles on the surface of the solid spinel grains, causing the metal nanoparticles to coalesce into larger nanoparticles[21]. This effect may be more prominent for Ni and Co particles than for Fe particles. Since the zinc (Zn) of zinc ferrite spinel reduces faster and more easily than does the Fe[22], the formed Fe nanoparticles are likely to be smaller and less numerous. In addition, the reduced Zn evaporates easily in the CNT growth region (above 700 °C) due to its low melting point (~419 °C). The local Zn vapor could decrease the effect of the enhancing aspect of H_2 in terms of the mobility of metal particles, making the formed Fe nanoparticles less prone to coalescence. Also, the local Zn vapor could affect the precipitation and diffusion of the carbon precursors

(CH$_4$, CO and C$_2$H$_2$) over Fe catalytic nanoparticles. All these factors could cause the resulting CNTs to be thinner and shorter, along with a CNT yield that is lower compared to those from NiAl$_2$O$_4$ and CoAl$_2$O$_4$. Comparison of the FESEM images of our results with those from Peigney's group[5,6,7,8, 23] (Figure 8.5) shows that our CNT yield is obviously higher, probably due both H$_2$ and CO acting as reducing agents in our growth process instead of H$_2$ only in their process. For instance, ZnFe$_2$O$_4$ can be reduced by CO through the reaction[24]

$$ZnFe_2O_4^{(s)} + 4CO^{(g)} \rightarrow Zn^{(g)} + 2Fe^{(s)} + 4CO_2^{(g)} \qquad (8.1)$$
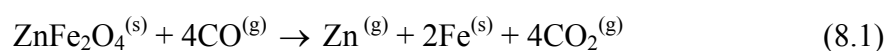
CO can also increase the catalytic activity[25], contributing to CNT growth as carbon precursor.
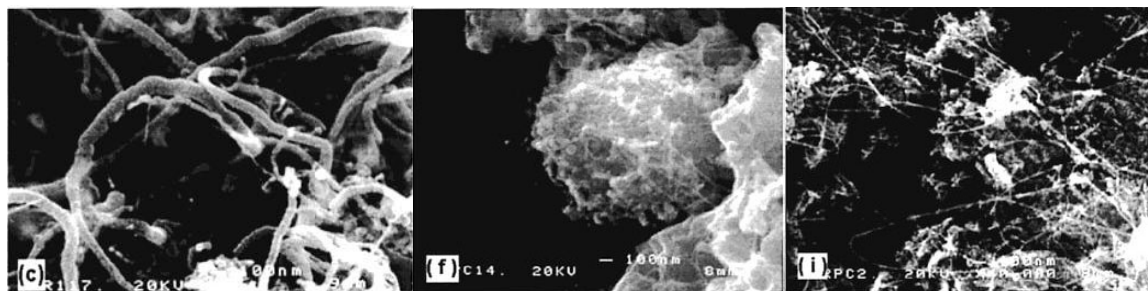
Figure 8.3 SEM images of CNTs referenced from Peigney's group paper (Figure from reference 23). CNTs formed from Mg$_{0.90}$Fe$_{0.10}$O solid solutions prepared with a urea ratio of 1 (c), 4 (i), and 8 (f) respectively.
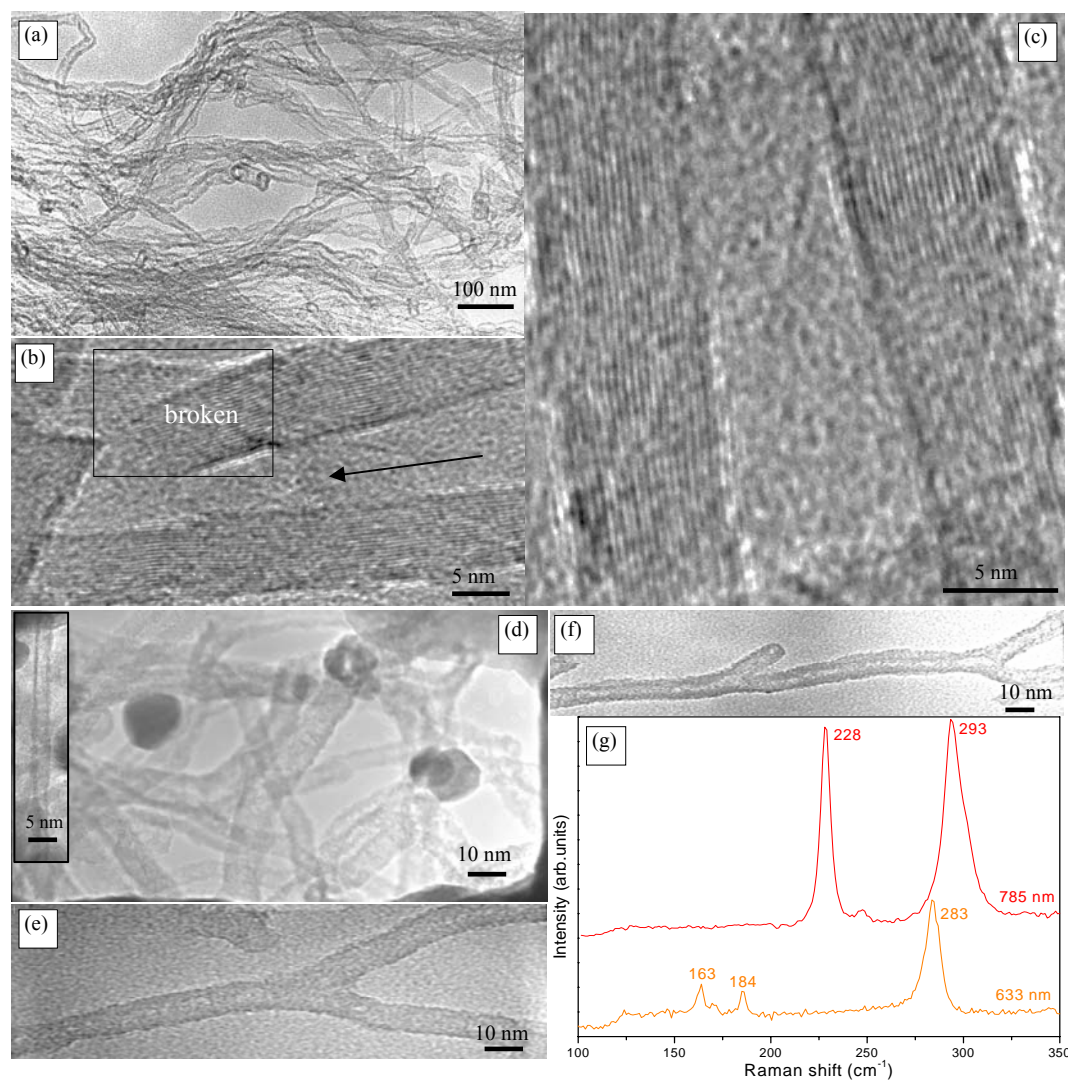
Figure 8.6 TEM images of CNTs from $NiAl_2O_4$ are taken (a-c), and (d-f) show the CNT TEM images from $ZnFe_2O_4$, (g) displays the Raman spectra of as-grown CNTs from $ZnFe_2O_4$.

The detailed structures of as-grown CNTs are studied using TEM. Fig.8.6 (a) shows CNTs grown from $NiAl_2O_4$, whose diameters range from 20-40nm. A HRTEM is taken, as in Fig.8.6 (b), showing the broken graphite layers on the CNT (as indicated by a rectangle), and the non-broken layers are parallel to the CNT core (directed by the arrow). This shows that CNTs are not nearly as strong under compression and shear stress due to their hollow structure and high aspect ratio; as such they tend to undergo

buckling and fracture when placed under compressive, torsional or bending stress.
Fig.8.6 (c) shows a HRTEM image of the CNTs from $NiAl_2O_4$ where the well-graphized walls are seen to be parallel to each other, showing the good quality of as-synthesized CNTs. As observed from FESEM images, much thinner CNTs are obtained from $ZnFe_2O_4$. This observation is confirmed by the TEM images, as in Fig. 8.6 (d), in which the outer diameters of CNTs are less than 15nm, and in the inset of Fig. 8.6 (d) that presents a SWNT with a diameter of around 3nm. Y-junction CNTs are also observed from $ZnFe_2O_4$, as shown in Fig.8.6 (e) (showing a single Y junction), and in Fig. 8.6 (f) (where multiple Y junctions are shown). These Y shaped topologies have been extensively studied due to their application as intratube heterojunction nanoelectronic devices[26,27]. The asymmetry in the *I-V* curve around zero bias found at the Y junction suggests that Y-junction nanotubes may be of use in this direction[28]. Also, the Y-junction nanotubes are expected to reinforce composites better than straight ones[29]. As discussed in Chapter 7, the formation of Y-shaped CNTs results from the insertion of non-hexagonal rings (pentagons and heptagons) in the hexagonal network in the region where the branches are joined together. A model of a Y-shaped CNT is shown in Figure 8.7[30].
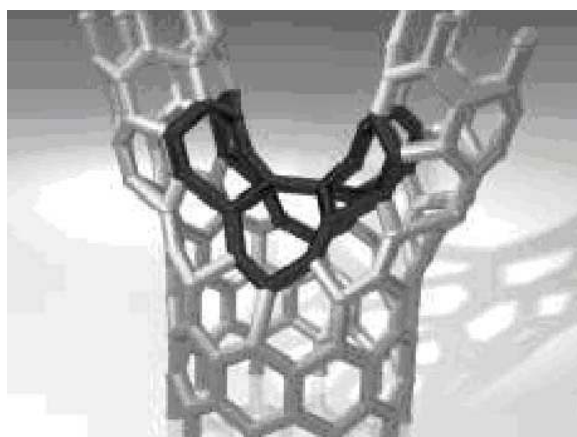
Figure 8.7 a model of Y-shaped CNT, where the dark black rings are pentagons and heptagons introduced into the hexagon network at the junction (Figure from reference 30).

The presence of SWNTs from $ZnFe_2O_4$ is also confirmed by evaluating the as-grown CNTs using Raman Spectroscopy (performed on a Renishaw System 1000 micro-Raman spectrometer) excited at two laser wavelengths: 633nm and 785nm. As shown in Fig. 8.6 (g), two Radial Breathing Modes (RBM) frequencies are collected corresponding to the two excitations. From these, the typical SWNT diameters can then be calculated to be 0.87nm, 1.34nm, 1.52nm, 0.84nm, and 1.08nm by using the empirical relationship $d = 248/\lambda$, where $d(nm)$ indicates the nanotube diameter[31, 32]. These calculated diameters correspond to the RBM peak positions λ (cm^{-1})=283, 184, 163 (from 633nm excitation), 293 and 228 (from 785nm excitation), respectively.
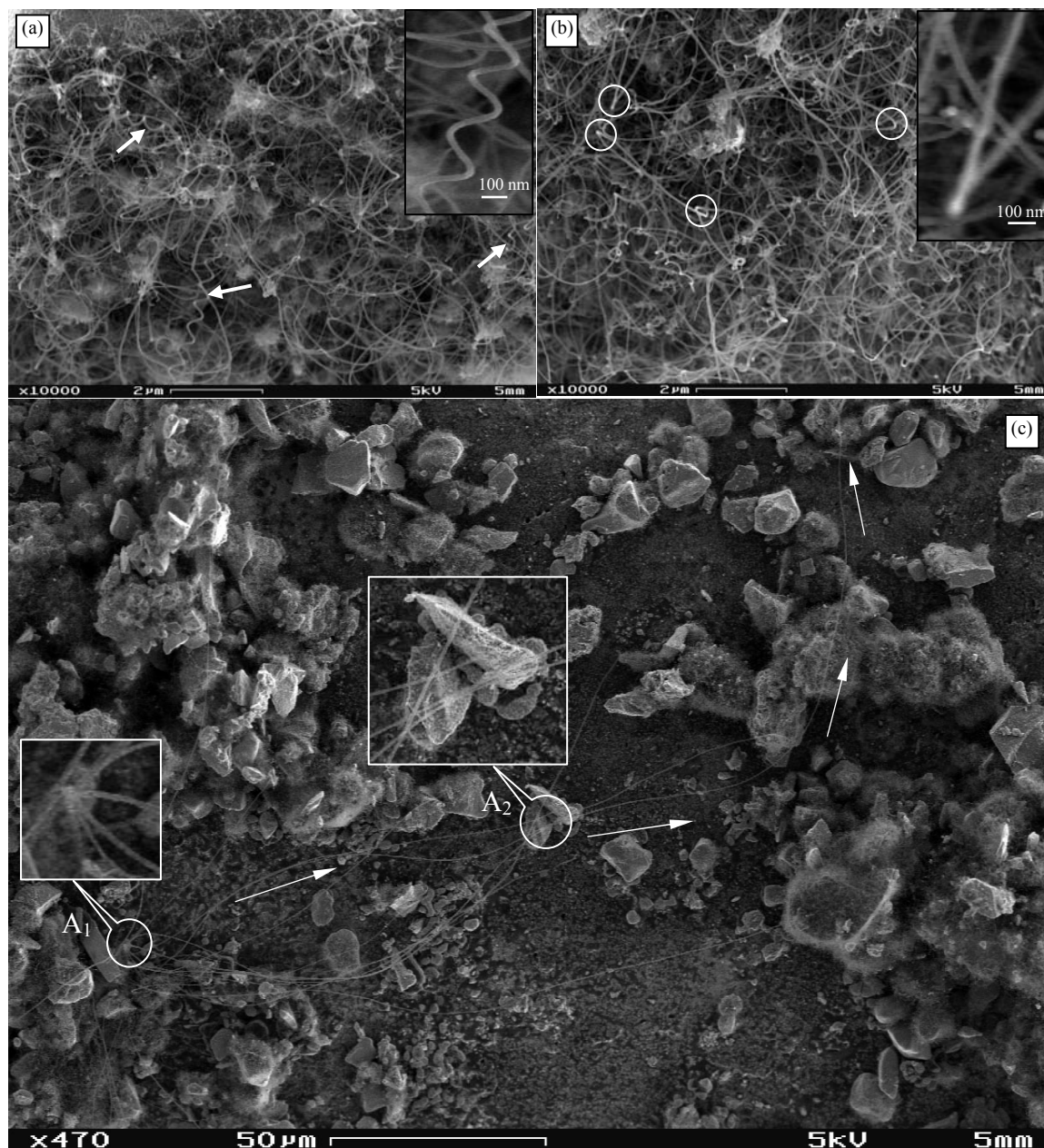
Figure 8.8 Special-structured CNTs grown from spinel solid solutions. (a) Typical regularly coiled CNTs from $CoAl_2O_4$. (b) Typical TC-type CNTs from $NiAl_2O_4$. (c) Ultra-long CNTs from $NiAl_2O_4$.

In CNTs grown from $NiAl_2O_4$ and $CoAl_2O_4$, we also observe many spring-like regularly coiled carbon nanotubes (CCNTs), as indicated by the arrows in Fig. 8.8 (a). The inset in Fig. 8.8 (a) shows an enlarged image of one segment of a typical CCNT. This special structure has unique properties and could be used for many applications such as novel devices and sensors[35], nanoelectromechanical systems (NEMS)[35], microwave adsorption materials [33], and elastic filling in composites[33]. We also observe the thermocouple (TC)-like nanotubes from $NiAl_2O_4$ and $CoAl_2O_4$, as circled in Fig. 8.8 (b). The inset in Fig. 8.8 (b) shows the enlarged image of the junction (bend) of TC nanotube where the bending angle almost reaches 180°. The bending angle could follow a simple topological relation[34]. These structures are produced due to the difference in carbon diffusion rates on the crystallographic faces of the catalytic particles[35,36], as discussed in Chapter 7. The pentagon carbon ring cause a hexagonal network curve inward creating a surface with positive curvature while a heptagonal carbon ring is needed to make the hexagonal network curve outward forming a negative curvature[37]. Both pentagons (P) and heptagons (H) are required to accommodate the change of surface curvature, making it possible to create any geometrical surface theoretically[38,39]. If a pair of P-H carbon rings is formed during the CNT growth, the tube will be forced to turn (Figure 8.9 (a))[39]. Another turn is introduced if a second pair of P-H carbon rings is created. As more P-H carbon rings build up, a node with a sharp total twist angle (e.g. TC-like CNT in this work) is formed[40]. If the orientation of P-H pairs rotates along the CNT body during the growth, a helical or coiling structure will be formed[41,42] (Fig. 8.9 (b) and Fig. 8.8 (a)). The periodicity (L) and coiling diameter (D) are determined by the twist angle and the distance between the adjacent P-H pairs[39] (Fig. 8.9(b)). The fluctuation in the creation

rates of P-H pair resulting from the change in the local growth conditions during the CNT growth can produce a complex shape, which is likely to be the reason that the carbon structures are very versatile[39].
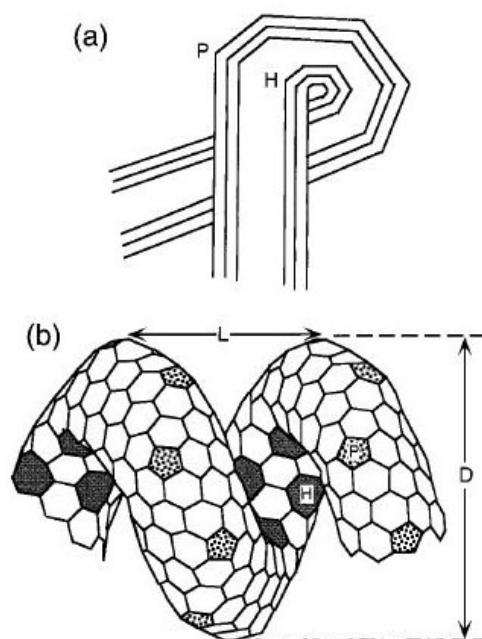
Figure 8.9 (a) Formation of a node along the body of a carbon nanotube as a result of introducing the paired pentagon (P) and heptagon (H) carbon rings. The node is formed if the density of the P-H pairs is high and the interpair distance is short. (b) Formation of a helical carbon nanotube by twisting the orientations of the P-H pairs along the body of the nanotube. A coil structure is formed if the twisting angle and interpair distance are kept constant (Figure from reference 39).

Additionally, we obtain ultra long CNTs and carbon nanofibers (CNFs) from $NiAl_2O_4$, having a diameter of less than 200nm and a length up to more than 200μm long, as shown in Fig. 8.8 (c) (the longest one followed by arrows). These filamentous carbons seem to originate from very fine sized nickel aluminate grain, while some filaments rest on other grains in the elongation process, as indicated by callouts A_1 and A_2 respectively in Fig. 8.8 (c). Low grain sizes have a high specific surface area that produces more metal nanoparticles on the surface of reduced grains, and low size grains also cause the

preferable segregation of NiO. The presence of NiO causes the reduction of the nickel aluminate solution at lower temperature[5] due to the lower reduction temperature of NiO(~400 ^{o}C)[43,44] compared to the relatively high reduction temperature (~790 ^{o}C) of $NiAl_2O_4$[45]. The Ni ions in the NiO are also much easier to be reduced than those Ni ions incorporated in the crystalline lattice of $NiAl_2O_4$[43]. Therefore, a large amount of nickel catalyst nanoparticles could be formed on a fine reduced grain in a very short time and coalesce more easily leading to the formation of very long CNTs and CNFs of large diameter. This view has been advanced by Ivanov *et al*[46], where the longest tubes are also the thickest.

8.3.2 Effects of axial locations on CNT growth

Our flame is characterized by large characteristic thermal and chemical gradients in the axial direction that are advantageous for investigating CNT growth conditions within a single flame due to the large parameter space of conditions. However, this could result in the uniformity of CNTs in the axial direction in terms of yield, diameter, and purity. Spinel solid solutions are tested at different axial z locations in the flame. No filamentous carbons (only amorphous carbons) are observed above z=6.6mm, corresponding to the fuel side where the local gas-phase temperature is around 1350K. This is reasonably in line with the observation reported by Peigney[8], who observed only some CNTs at temperatures close to 1070°C (1340K), despite increasing concentrations of carbon precursors such as CO and C_2H_2. Again, this is likely due to deactivation of the catalysts at higher temperatures. Figure 8.10 shows FESEM images of MWNTs grown from $NiAl_2O_4$ solid solutions tested at three different axial z locations in the flame where the gas-phase temperatures range from 1300K to 1000K with decreasing axial height. As can

be seen in Figs.8.10 (a-c), there appears to be a slight difference in CNT diameters and lengths, but there are obvious differences in the yields. Although the Ni nanoparticles reduced from solid solutions are active at these temperatures, the yield in Fig. 8.10 (b) is the highest. This is may be because increasing the reduction temperature increases the reduction yield and thus favors the formation of surface metal particles to produce more CNTs[8]. The yield decrease in Fig. 8.10 (a) could mainly be due to the deactivation of a portion of formed Ni nanoparticles at a relatively higher temperature than in Fig.8.10 (b), whereas the decreased CNT yield in Fig.8.10 (c) is primarily attributed to the lower formation rate of Ni nanoparticles reduced from the solid solutions at lower temperatures. Below z= 5.8mm in the flame, where the local gas-phase temperatures are around 950K, CNTs are no longer observed, despite sufficient concentrations of CO and CH_4 in the flame. This corresponds to lack of nanoparticle formation at these temperatures, consistent with the required temperature (usually above $600^{o}C$) for catalytic methods[6]. It is also in reasonable agreement with Hernadi's report that no carbon materials are deposited at 700 ^{o}C using methane as precursor[47]. The CNT growth temperature range in our experiment is found to be similar to the temperatures used in CVD[5,6,7,8,11,28,29,48]. Note from Fig.8.3 (b) that TC-measured temperatures for the substrate and gas-phase temperatures are approximately the same in the region of CNT formation. This means that there is no temperature gradient between the substrate and the gas-phase during CNT growth. Similar trends are found for $CoAl_2O_4$ and $ZnFe_2O_4$ solid solutions.
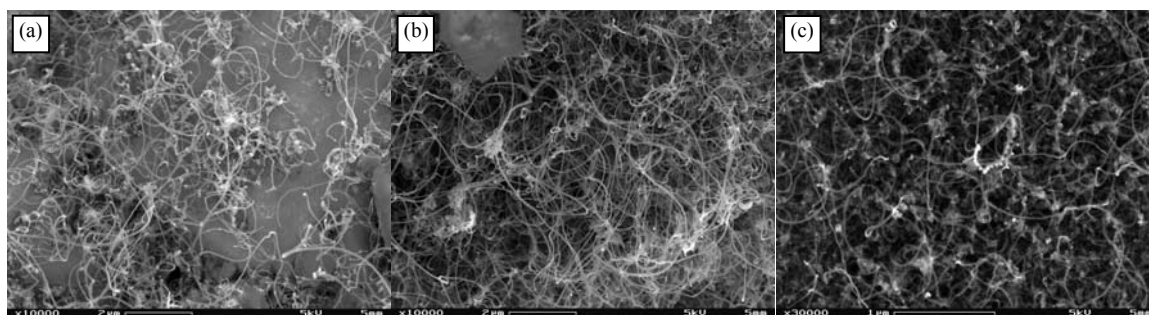
Figure 8.10 FESEM images of CNTs grown from NiAl$_2$O$_4$ at different axial z locations. (a) z=6.4mm. (b) z=6.2mm. (c) z=5.8mm.

8.3.3 Effects of H$_2$ on CNT growth
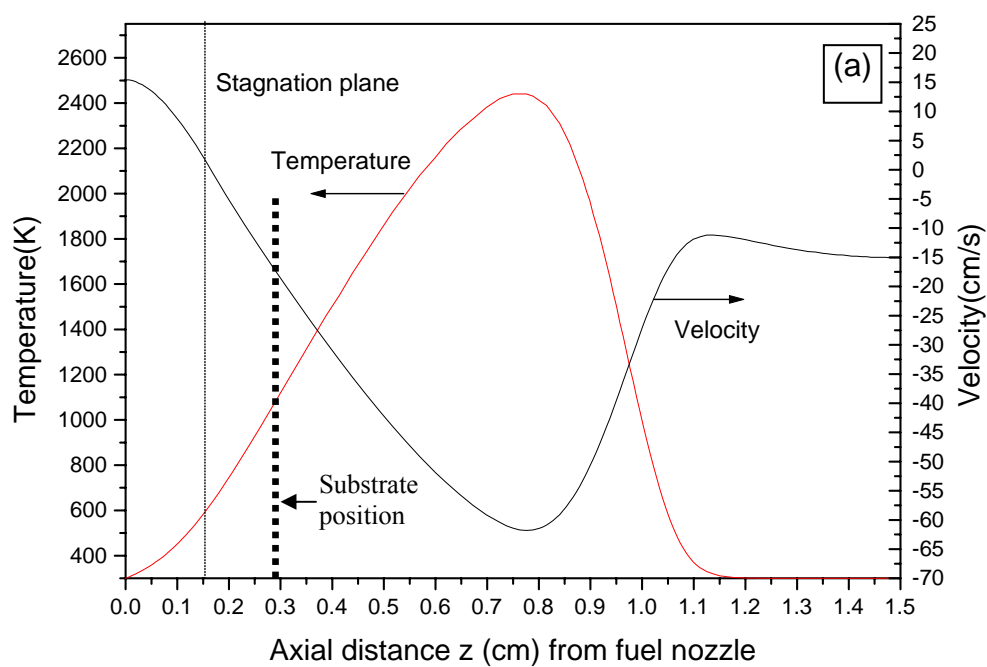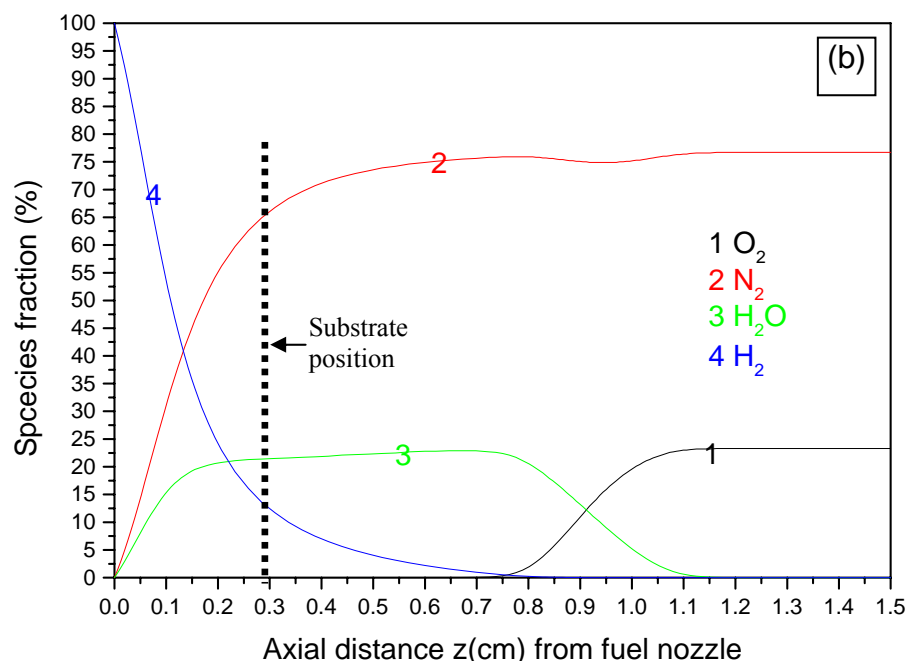
Figure 8.11 (a) the temperature profile and velocity distribution along the axial z direction with the stagnation plane marked, and (b) the profiles of major species of a counter-flow diffusion flame with 100%H_2 versus air.

Additionally, we have investigated a two-step growth process composed of H_2 reduction of spinel metal-oxide powders in a pure H_2 counter-flow flame, followed by CNT growth from these H_2-reduced powders in a pure methane counter-flow flame. Figure 8.11 shows a computed flame structure of the pure H_2 CDF, along with the examined position marked.

Figure 8.12 gives the CNTs grown from the two-step growth, where the $NiAl_2O_4$ powders are reduced for 2 minutes at ~1100K in the pure H_2 flame. Then the CNTs are produced from these reduced powders for 10 minutes at ~1100K in the pure methane flame. The results (Fig.8.12) show no obvious differences from the CNTs obtained without the first independent step of H_2 reduction in terms of CNT yield, diameter, and length. These could be explained by the inevitable appearance of H_2 resulting from the

methane pyrolysis in the pure methane flame, as seen in Fig. 8.3(b). As such, using CO flame would be better in isolating nanoparticle and CNT formation routes, where nanoparticle size and formation is controlled in a H_2 flame, and CNT growth is controlled in a CO flame without H_2 presence.
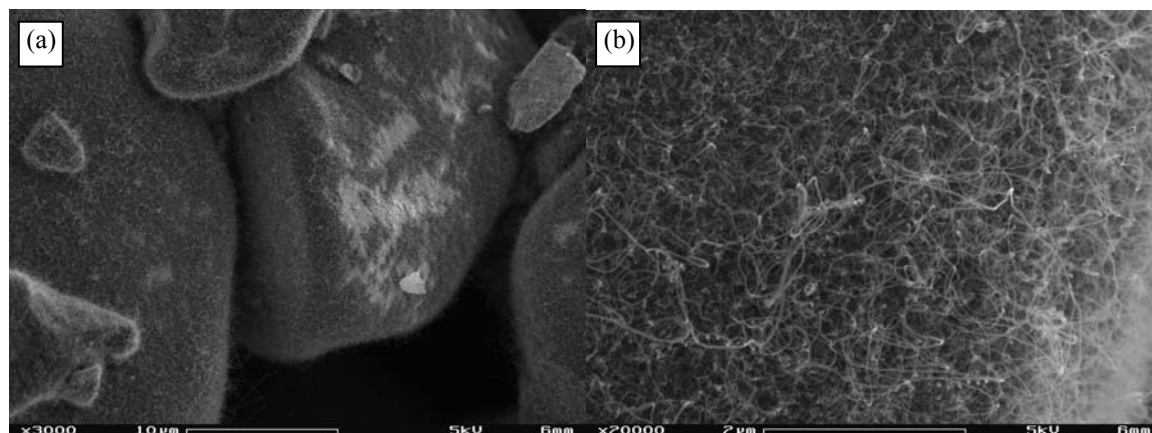
Figure 8.12 FESEM images of CNTs obtained by two-step growth. (a) low magnification showing reduced $NiAl_2O_4$ grains covered with a layer of CNTs and (b) higher magnification depicting the CNTs dispersing on the surface of a single grain.

8.4 Concluding remarks

MWNTs and SWNTs are synthesized catalytically through decomposition of carbon precursors (e.g. CH_4, CO and C_2H_2) over catalyst nanoparticles (i.e. Ni, Co and Fe) *in-situ* reduced from spinel solid solutions (i.e. $NiAl_2O_4$, $CoAl_2O_4$ and $ZnFe_2O_4$) in a methane/air CDFs. The spinels are prepared by co-precipitation method, and the production process of CNTs can be a continuous and energy-efficient process under one atmospheric pressure. CNT growth activities are investigated as functions of spinel solid solution composition, local gas-phase temperatures, C-related species concentrations, and sampling positions. CNTs grown from $ZnFe_2O_4$ are found to be a mixture of MWNTs

and SWNTs with ~ 30% SWNT content. Special-structured CNTs such as regularly coiled CNTs, large bending CNTs, and Y-junction CNTs are observed. Without CNT extractions, these as-grown CNT-containing nanocomposites can be further used to prepare dense composites, for which their mechanical and electric properties could be quite interesting.

Reference:

[1] J.-F. Colomer, G. Bister, I. Willems, Z. Konya, A. Fonseca, G. Van Tendeloo, J. B.Nagy, Synthesis of single-wall carbon nanotubes by catalytic decompostion of hydracarbon, *Chem. Commun*.1999.1343-1344.

[2] J.-F. Colomer , C. Stephan , S. Lefrant , G. Van Tendeloo , I. Willems , Z. Ko′nya , A. Fonseca , Ch. Laurent , J. B.Nagy, Large-scale synthesis of single-wall carbon nanotubes by catalytic chemical vapor deposition CCVD/method, Chemical Physics Letters, 317 (2000):83–89

[3] Á. Kukovecz, Z. Kónya, N. Nagaraju, I. Willems, A. Tamási, A. Fonseca, J. B. Nagy and I. Kiricsi, Catalytic synthesis of carbon nanotubes over Co, Fe and Ni containing conventional and sol-gel silica-aluminas, Phys. Chem. Chem. Phys., 2000, 2:3071-3076

[4] P. Coquay, Ch. Laurent , A. Peigney, O. Quénard, E. DeGrave and R.E. Vandenberghe, From ceramic–matrix nanocomposites to the synthesis of carbon nanotubes, Hyperfine Interactions 130: 275–299, 2000.

[5] Bacsa RR, Laurent C, Peigney A, Vaugien T, Flahaut E, Bacsa WS, et al. (Mg,Co)O solid-solution precursor for the large-scale synthesis of carbon nanotubes by catalytic chemical vapor deposition. J Am Ceram Soc 2002; 85(11):2666-69.

[6] Flahaut E, Peigney A, Laurent C, Rousset A. Synthesis of single-walled carbon nanotube-Co-MgO composite powders and extraction of the nanotubes. J Mater Chem 2000; 10:249-252.

[7] Laurent C, Peigney A, Rousset A. Synthesis of carbon nanotube-Fe-Al2O3 nanocomposite powder by selective reduction of different Al1.8Fe0.2O3 solid solutions. J Mater Chem 1998; 8(5):1263-1272.

[8] Peigney A, Coquay P, Flahaut E, Vandenberghe RE, , Laurent C. A study of the formation of single- and double-walled carbon nanotubes by a CVD method. J Phys Chem B 2001; 105:9699-9710.

[9] R.R. Bacsa , Ch. Laurent , A. Peigney, W.S. Bacsa , Th. Vaugien ,A. Rousset, High specific surface area carbon nanotubes from catalytic chemical vapor deposition process, Chemical Physics Letters 323(2000):566–571

[10] E. Flahaut , Ch. Laurent, A. Peigney, Catalytic CVD synthesis of double and triple-walled carbon nanotubes by the control of the catalyst preparation, Carbon 43 (2005) 375–383

[11] Laurent C, Peigney A, Dumortier O, Rousset A. Carbon nanotubes-Fe-Alumina nanocomposites, Part II: microstructure and mechanical properties of the hot-pressed composites. Journal of the European Ceramic Society 1998; 18:2005-2013.

[12] A. Peigney, E. Flahaut, Ch. Laurent, F. Chastel, A. Rousset, Aligned carbon nanotubes in ceramic-matrix nanocomposites prepared by high-temperature extrusion, Chemical Physics Letters, 352 (2002) 20–25

[13] Flahaut E, Peigney A, Laurent C, Marlière, Chastel F, Rousset A. Carbon nanotube-metal-oxide nanocomposites: microstructure, electrical conductivity and mechanical properties. Acta Mater 2000; 48:3803-3812.

[14] Lee F.T., and Hayes P., Mechanism of the reduction of zinc ferrites in H2/N2 gas mixtures, *Mineral processing and extractive metallurgy review*, 28(2): 127-157, 2007

[15] Kobayashi M., Shirai H., and Nunokawa M., Elucidation of sulfidation mechanism of zinc ferrite in a resuctive gas enrironment by in situ x-Ray diffraction analysis and Mossbauer spectroscopy, Ind. Eng. Chem. Res., 39:1934-1943, 2000

[16]Devaux X, Laurent C, Brieu M, Rousset A. Iron-alumina interface in ceramic matrix nanocomposites. Journal of alloys and compounds, 1992; 188: 179-181.

[17]Lee FT. Reduction mechanisms and behaviour of zinc ferrite—Part 2: ZnFe2O4 solid solutions. Trans instn min metall (sect C: mineral process extr metall) 2001; 110(3): 123-132.

[18]Baker RT. Catalytic growth of carbon filaments. Carbon 1989; 27:315-23.

[19]Devaux X, Laurent C, Rousset A. Chemical synthsis of metal nanoparticles dispersed in alumina. Nanostruct Mater1993; 2:339-346.

[20]Laurent C, Blaszczyk C, Brieu M, Rousset A. Elaboration, microstructure and oxidation behavior of metal-alumina and metal-chromia nanocomposite powders. Nanostructured materials 1995; 6:317-320.

[21]Haug K, Zhang Z, John D, Walters FC, Zehner MD, Plummer EW. Effects of hydrogen in Ni (100) summonolayer homoepitaxy. Physical review B 1997; 55(16): R10233-R10236

[22]Lee FT. Reduction mechanisms and behavior of zinc ferrite- Part 1: pure ZnFe2O4. Trans instn min metall (sect C: mineral process extr metall) 2001; 110: 14-24.

[23]Coquay P., Peigney A., Grave E.D., Vandenberghe R.E., and Laurent C., Carbon nanotubes by a CVD method. Part II: Formation of nanotubes from (Mg, Fe)O Catalysts, *J.Phys.Chem. B*, 106:13199-13210, 2002

[24]Lee F.T., Reduction mechanisms and behaviour of zinc ferrite-part I: pure ZnFe2O4, *Trans. Instn. Min. Metall. (Sect. C: Mineral Process. Extr. Metall.)*, 110:C14-C24, 2001

[25]Jongsomjit B. Cobalt-support compound formation in alumina-supported cobalt catalysts. Pittsburgh PA USA, University of Pittsburgh, PhD thesis, 2002.

[26]Chico L, Benedict LX, Louie SG, Cohen ML. Quantum conductance of carbon nanotubes with defects. Phys Rev B 1996; 54(4): 2600-2606.

[27]Chico L, Crespi VH, Benedict LX, Louie SG, Cohen ML. Pure carbon nanoscale devices: nanotube heterojunctions. Phys Rev Lett 1996; 76(6): 971-974.

[28]Satishkumar BC, Thomas PJ, Govindaraj A, Rao CNR. Y-junction carbon nanotubes. Applied Physics Letters 2000; 77(16): 2530-2532.

[29]Li WZ, Wen JG, Ren ZF. Straight carbon nanotube Y junctions, Applied Physics Letters 2001; 79(12): 1879-1881.

[30]A. Latge, R. B. Muniz, and D. Grimm. Brazilian Journal of Physics, vol. 34, no. 2B, June, 2004

[31]Saito R, Dresselhaus G and Dresselhaus M S. Trigonal warping effect of carbon nanotubes. Phys. Rev. B 2000; 61:2981-2990.

[32]Jorio A, Saito R, Hafner J H, Lieber C M, Hunter M, McClure T, Dresselhaus G and Dresselhaus M S. Structural (n, m) Determination of Isolated Single-Wall Carbon Nanotubes by Resonant Raman Scattering. Phys Rev. Lett. 2001. 86:1118-1121.

[33]Liu Y, Shen Z. Preparation of carbon microcoils and nanocoils using activated carbon nanotubes as catalyst support. Carbon 2005; 43:1574-1577.

[34]Han J, Anantram MP, Jaffe RL, Kong J, Dai H. Observation and modeling of single-wall carbon nanotube bend junctions. Physical Review B, 1998; 57(23): 14983-14989.

[35]Szabó A, Fonseca A, Nagy JB, Lambin P, Biró LP. Structural origin of coiling in coiled carbon nanotubes. Carbon 2005; 43:1628-1633.

[36]Haug K, Zhang Z, John D, Walters FC, Zehner MD, Plummer EW. Effects of hydrogen in Ni (100) summonolayer homoepitaxy. Physical review B 1997; 55(16): R10233-R10236

[37]Iijima, S.; Ichihashi, T.; Ando, Y. Nature 1992, 356, 776.

[38]Oh sawa, E.; Yoshida, M.; Fujita, M. MRS Bulletin XIX 33-36 (November, 1994).

[39]Gao R., Wang Z.L., and Fan S., Kinetically controlled growth of helical and zigzag shapes of carbon nanotubes, *J. Phys. Chem. B*, 104:1227-1234, 2000

[40]Kang, Z. C.; Wang, Z. L. Philos. Mag. 1996, B73, 905.

[41]Ihara, S.; Itoh, S. Carbon 1995, 33, 931.

[42]Settton, R.; Setton, N. Carbon 1997, 33, 497.

[43]Shan W, Luo M, Ying P, Shen W, Li C. Reduction property and catalytic activity of Ce1-XNiXO2 mixed oxide catalysts for CH4 oxidation. Applied Catalysis A: General 2003; 246:1-9.

[44]Zhang X, Liu J, Jing Y, Xie Y. Support effects on the catalytic behavior of NiO/Al2O3 for oxidative dehydrogenation of ethane to ethylene. Appl Catal A: Gen 2003; 240: 143-150.

[45]Nga NK, Chi DK. Synthesis, characterization and catalytic activity of CoAl2O4 and NiAl2O4 spinel-type oxides for NOx selective reduction. Adv in tech of mat and mat proc J (ATM) 2004; 6(2): 336-343.

[46]Ivanov V, Fonseca A, Nagy JB, Lucas A, Lambin P, Bernaerts D, Zhang XB.Catalytic production and purification of nanotubules having fullerene-scale diameters. Carbon 1995; 33(12): 1727-1738.

[47]Hernadi K, Fonseca A, Nagy JB, Bernaerts D, Lucas AA. Fe-catalyszed carbon nanotube formation. Carbon 1996; 34(10): 1249-1257.

[48]Unalan HE, Chhowalla M. Investigation of single-walled carbon nanotube growth parameters using alcohol catalytic chemical vapor deposition. Nanotechnology 2005; 16:2153-2163.

Chapter 9

Nanostructured ZnO Materials from Inverse Diffusion Flames

9.1 Introduction

In previous Chapters, CNTs were grown off of catalytic substrates in the carbon rich region of the flames. In this chapter, we demonstrate the growth of metal-oxides directly from the base-metal substrate. Zinc, a low-melting-point metal, is examined as substrate in producing ZnO nanowires. Several techniques for the fabrication of one-dimensional ZnO nanowires have been explored using different starting materials, e.g. zinc metal powder[1,2,3,4,5,6,7,8,9], ZnO powder[10,11,12,13,14,15,16], and metal organic precursor[17,18,19]. The vapor pressure of zinc is sufficiently high to grow nanowires at low temperatures. Lyu and coworkers[5,6] synthesized well-aligned single-crystalline ZnO nanowires on NiO-nanoparticle deposited Al_2O_3 substrates situated 3-5mm above metal zinc powder in a tube furnace flowing Ar at 450°C for 1hr. Nanowires of uniform 55-nm diameter and up to 2.6-μm length grew in the c-axis direction. Higher temperatures (and carbon assistance) are needed when starting with ZnO. Dang *et al*.[8] heated Zn powder at 550°C for 30min in a quartz tube by flowing 20% O_2 and 80% Ar to produce ZnO nanowires on the surface of the original powder. The single-crystalline nanowires had diameters of 20-60 nm and lengths of tens of microns, but had 2 different growth directions, i.e. [001] and [210]. Higher temperatures (and carbon assistance) are needed when starting with ZnO. Huang et al.[10] grew ZnO nanowires on Au-coated silicon substrates placed downstream

of a mixture of ZnO and graphite powders heated to 900-925°C under a flow of Ar for 5-30min. Depending on the catalytic Au-layer thickness, nanowire diameters ranged from 50-200nm and up to 50μm long, with [0001] preferential growth direction. Banerjee *et al.*[15] heated ZnO and graphite powders at 900-1100°C in an airflow under 0.1 to 10 torr, and nanowires grew downstream on graphite flakes (700-900°C). The nanowires, with growth direction [0001], ranged from 30-100nm and lengths 2-15μm, with samples collected closer to the source being longer with smaller diameter. Metalorganic vapor phase epitaxy (MOVPE) can produce nanorods if the temperature is low; higher temperature results in flat epilayer growth[18]. Park et al.[17] reported low-pressure MOVPE growth of ZnO nanorods on Al_2O_3 substrates at temperatures between 400-500°C, using diethylzinc (DEZn) with O_2 and Ar. Vertically well-aligned nanorods of uniform diameter of ~25nm and lengths of 800nm grew along the c-axis direction in 1hr.

As shown above, ZnO growth can be based on various growth mechanisms, i.e. vaporliquid-solid (VLS) (catalytic and self-catalytic) and vapor-solid (VS), which may even occur simultaneously due to the low melting temperature and high vapor pressure of zinc (and its suboxides), perhaps explaining the various morphologies often exhibited by ZnO, and the need to define conditions carefully in order to isolate, control, and optimize nanowire growth. Moreover, processing can be complex involving graphite (or carbon nanotube) powders[10,11,12,13,14,15], multiple steps[2,3,16,19], catalysts[1,3,10,13], nanoparticle seeding[2,5,6], and low pressure systems[7,11,13,14,15,16,17,18,19], as well as long processing times. In this Chapter, a robust flame synthesis method is employed to grow single-crystalline nanowires with uniform diameters, with growth rates of microns/min, without any pretreatment or catalysts, in open environments, and directly on zinc-plated substrates.

Diameters ranging from 25-400nm are selectable depending on local chemical species and temperature conditions.

9.2 Experiment

The raw substrate is studied by XRD using Cu-Kα radiation (λ=0.15418nm), and XRD spectrum of the raw substrate surface shows that all peaks can be indexed to zinc (PDF#040831, Figure 9.1).
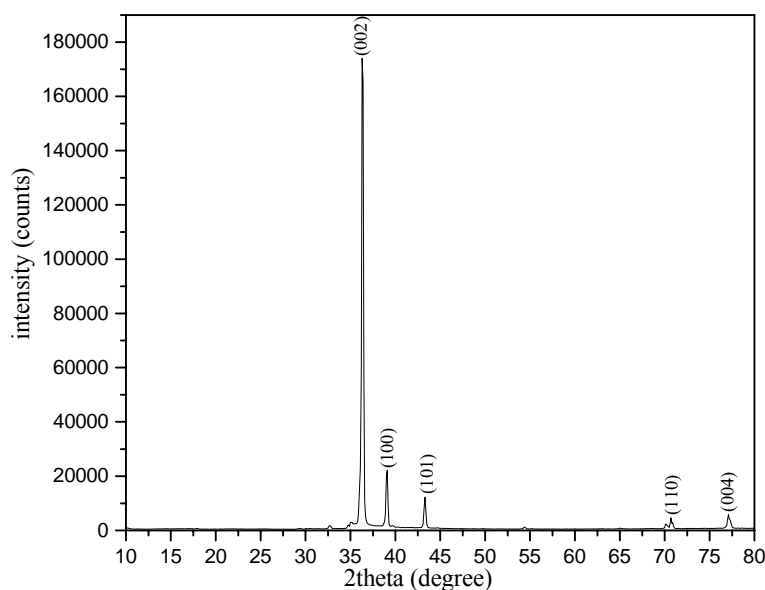
Figure 9.1 XRD pattern of the raw substrate surface

The experiments for present study are conducted in the same flame configuration (Figure 9.2) as used in Chapter 6, namely, an IDF established on a co- flow burner. SRS is employed to measure the gas-phase temperatures and concentrations of oxygen-related species (i.e., O_2, H_2O, CO) at the specific locations (r and z) where ZnO nanomaterials are produced, as illustrated in the Figure 9.3.

Zinc-galvanized steel sheets are machined into 120mm-long substrates with rectangular cross section of 1mm width and 0.5mm thickness, which are then ultrasonically cleaned. By mounting them on two-axis positioner, the substrates are then inserted radially/horizontally (r) into the flame structure at various axial positions (z), as shown in Fig. 9.2, where local temperature and gas-phase chemical species are appropriate to promote reactions leading to zinc oxide. This geometry permits facile examination of the parameter space, as well as substrate probing of the fuel side of the flame structure for nanowire growth without piercing the reaction zone and allowing oxygen leakage, thereby isolating O_2 versus H_2O reactions with Zn. The processing time in the flame is 10 minutes for each substrate
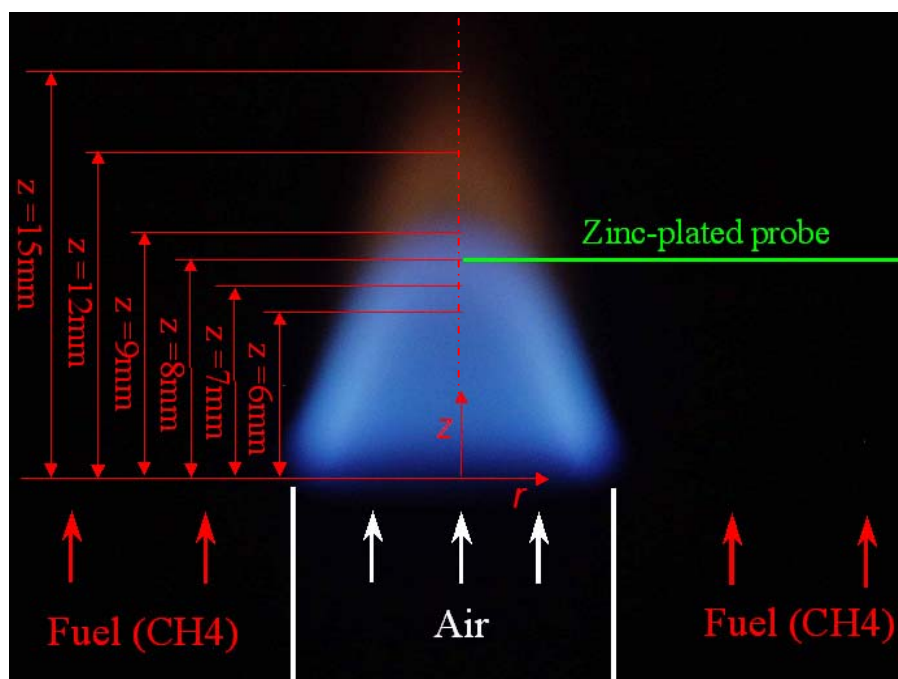
Figure 9.2 An IDF with investigated positions for ZnO nanostructure growth

The morphologies of as-grown zinc oxide nanostructures are examined using field-emission scanning electron microscopy (FESEM), with elemental analysis conducted using energy dispersive x-ray spectroscopy (EDX). Structural features of the nanomaterial are investigated using high-resolution transmission electron microscopy (HRTEM), along with selected area electron diffraction (SAED).
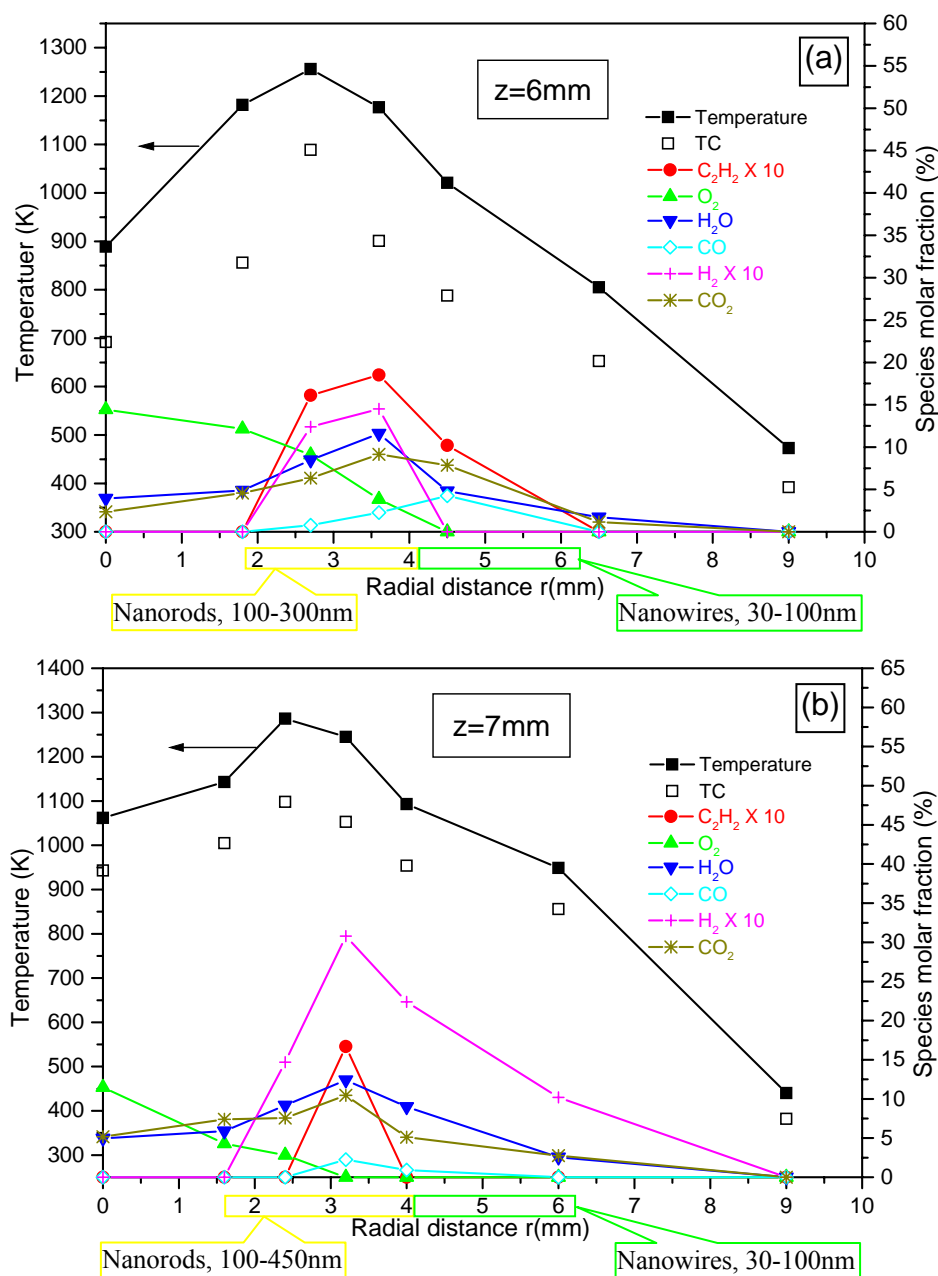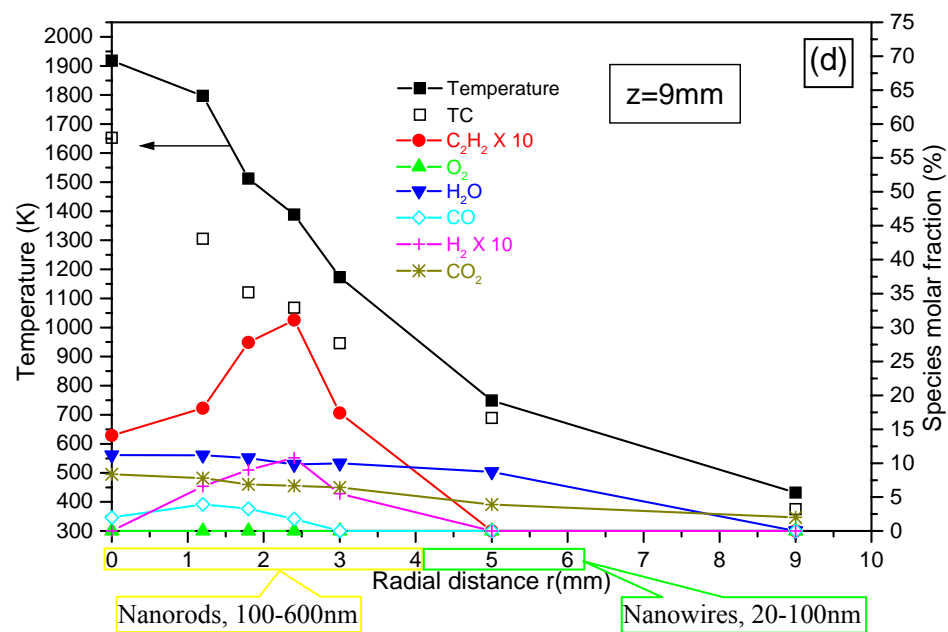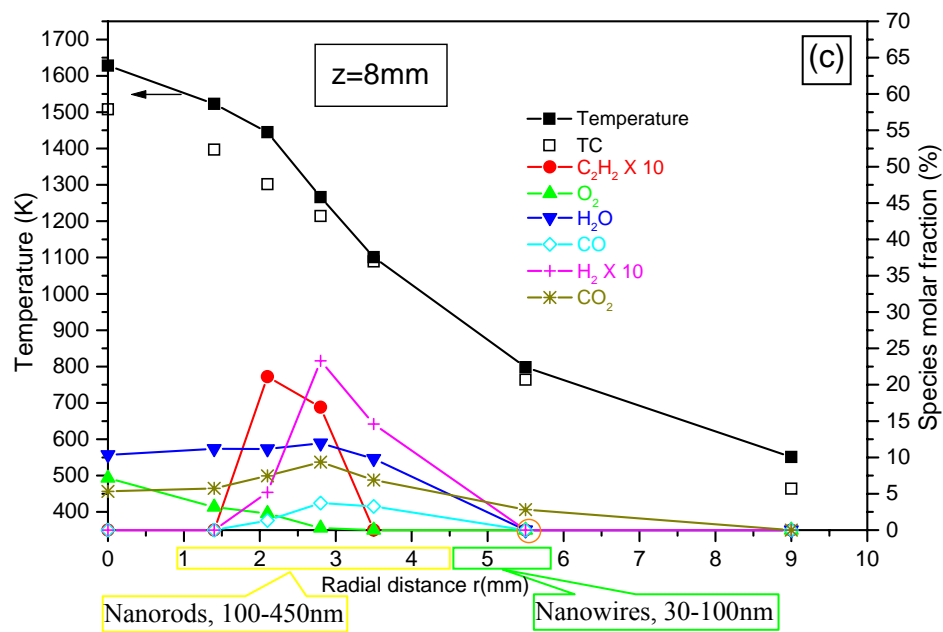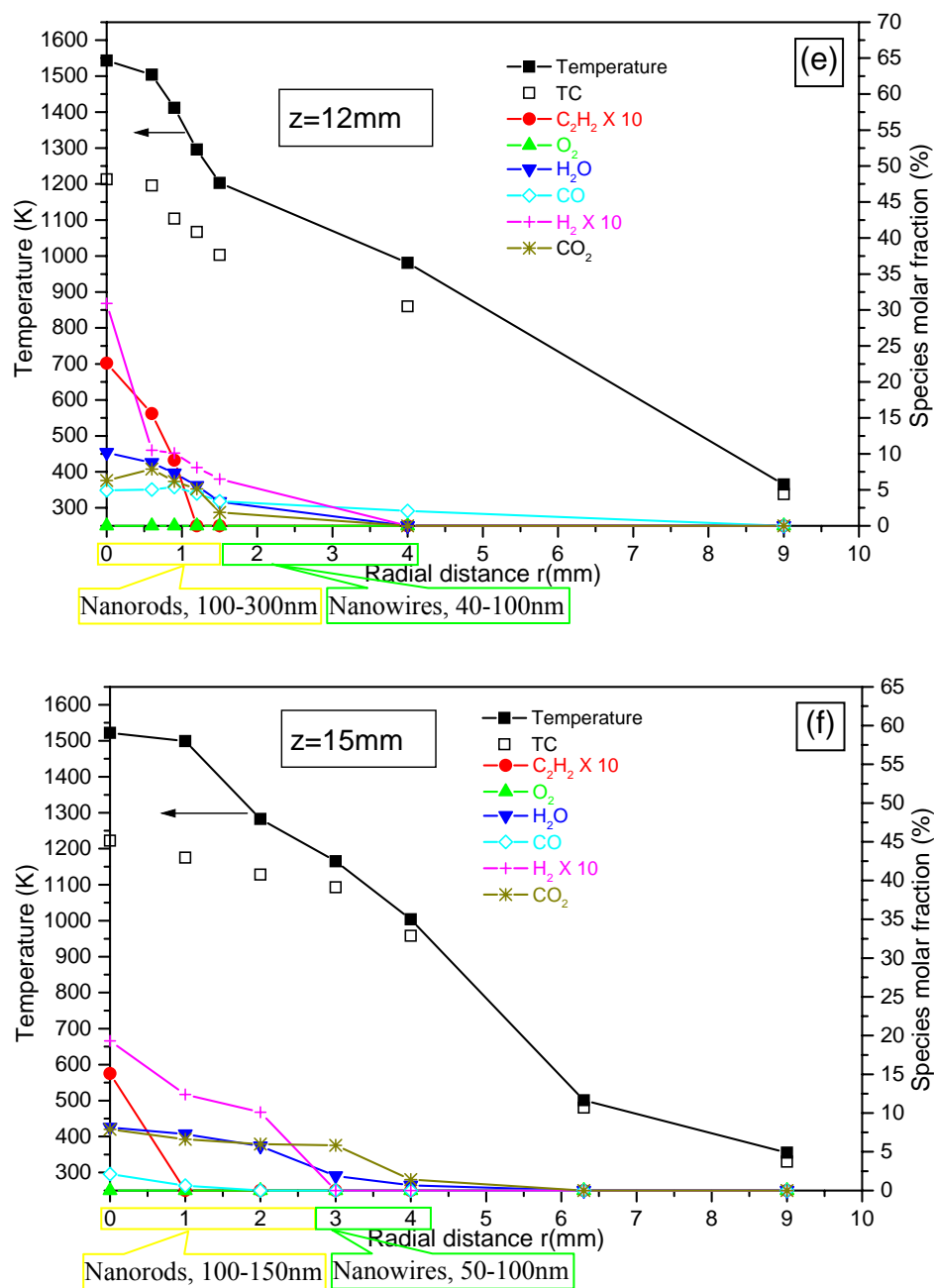
Figure 9. 3 The profiles of temperature and major species measured by SRS for the production of ZnO nanostructures, at (a) z= 6mm, (b) z=7mm, (c) z=8mm, (d) z=9mm, (e) z=12mm and (f) z=15mm, along with the temperatures measured by thermocouple (TC)

9.3 Results and Discussion

Due to the sensitivity of ZnO nanostructures to their growth conditions (e.g. temperature and growth-related chemical species), examination of various temperatures and chemical species is required to understand the growth mechanism of ZnO nanostructures and to map the relations between ZnO nanostructures/morphologies and their corresponding growth conditions in flames. IDFs favor such examination as they present large gradients of temperature and chemical species in both axial (z) and radial (r) directions. As such ZnO growth for different axial and radial positions in IDFs are investigated. We first present and discuss the results at z=8m – a characteristic axial position where a variety of ZnO nanostructures (e.g. nanowire, nanoribbon and hierarchal structure) are obtained. As evinced from Fig.9.3 (c) (z=8mm), nanowires are produced on both the fuel and oxidizer sides of the reaction zone, suggesting that the route for synthesis is not only through reactions with oxygen. In fact, there appears (as seen from Fig. 9.3 (c)) to be a threshold for oxygen concentration for the formation of nanowires, although the phenomenon may actually be coupled with H_2 presence, to be discussed later. Figure 9.4(a) shows a FESEM image of large hexagonal-cross-section nanowires growing in the [0001] direction, corresponding to the growth conditions marked on Fig.9.3(c) on the oxidizer side of the reaction zone. These as-grown nanowires are 100-400nm in diameter, with lengths of more than 10μm for a sampling duration of 10min. Nanowires of diameters <100nm (and lengths ~5μm) are grown only on the fuel side and at temperatures <1100K. The smallest nanowires are 25-40nm in diameter (e.g. Fig.9.4 (b)), and are formed at ~800K at the growth boundary for the case of Fig. 9.3(c). Similar to other works[4,6,18], there is a correspondence of larger-diameter (and hexagonal crystal

morphology) nanowires with high temperatures. Interestingly, transition from nanowire to nanoribbon formation (Fig.9.4(c)) is found sparsely near these ~30-nm nanowires, suggesting that the local nanostructured growth conditions are at a critical juncture in terms of species concentration rather than just temperature. Nonetheless, EDX spectra [Fig.9.4 (d)] for all growth regions marked on Fig.9.3(c) and shown in Fig.9.4 reveal that the nanostructures are composed of only Zn and O, in proportions indicating that the as-synthesized nanomaterials are ZnO.
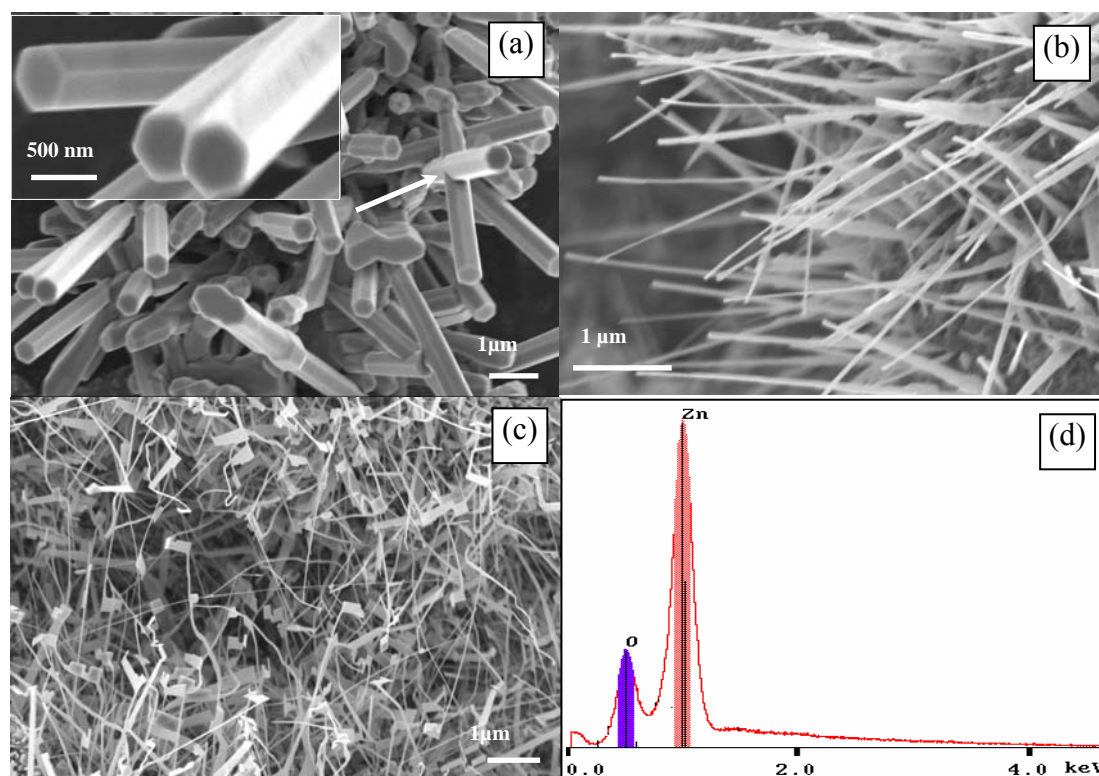
Figure 9.4 FESEM images corresponding to growth characteristics marked in Fig.9.1(c) of (a) 100-400nm diameter nanowires, where arrows show interpenetrative growth, (b) < 50nm diameter rnanowires, and (c) nanowires with transition to nanoribbons at the tips. (d) EDX spectra of as-grown nanowires.

Figure 9.5(a) presents a low magnification bright-field TEM image of a uniform 35-nm nanowire. Although nanowires reported in the literature are almost exclusively found to grow in the [0001] direction (due to the lowest surface energy of the (0002) facet[20]), Fig.9.5 (b) shows a HRTEM image, where it's zoomed inset and SAED pattern both reveal that the growth direction is [11$\bar{2}$0]. High magnification (Fig.9.5(c)) divulges that the nanowire is dislocation free and single crystalline in nature. The d-spacings calculated from the SAED pattern inset match well with d-spacings of (11$\bar{2}$0) and (10$\bar{1}$0) respectively (PDF#800075), confirming the wurzite ZnO structure. Fourier transform pattern of the HRTEM image further verifies these d-spacings, as well as the growth direction along [11$\bar{2}$0], for nanowires with diameters <<100nm.
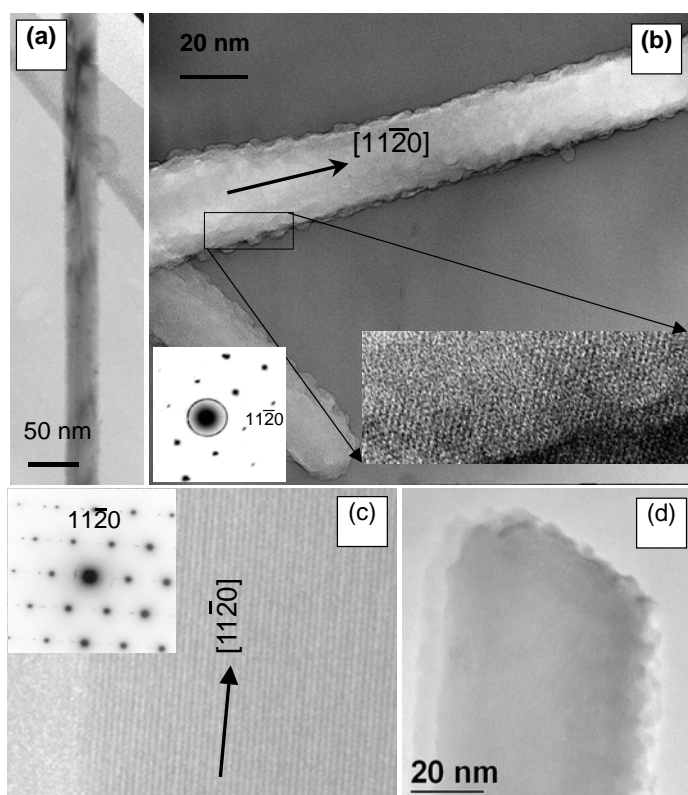
Figure 9.5 TEM images showing (a) a uniform 35-nm diameter nanowire, (b) a nanowire with [11$\bar{2}$0] growth direction, (c) lattice fringes of a nanowire, along with SAED pattern (inset), and (d) a nanowire tip.

The growth mechanism of the nanowires appears to be VS. In the VLS process, growth is promoted by a liquid-solid interface, generally identified by the presence of droplets at the nanowire tips. The morphology of a nanowire shown in Fig.9.5 (d) reveals no metal nanoparticle at its tip. Although some works, e.g. Ref. 8, have proposed a base growth "self-catalytic" VLS mechanism, the presence of interpenetrative growth of nanowires, as seen in Fig.9.4 (a), similar to that of Ref[21] 20, and the transitioning from nanowire to nanoribbon growth at the tips, as seen in Fig.9.4(c), provide further evidence for vapor phase transport and deposition.

The specific case of Fig.9.3(c) (z=8mm) shows gas-phase temperatures ranging from 800-1500K as being conducive for nanowire growth. Thermocouple measurements indicate that local substrate temperatures are 50-200K lower, as seen in Fig.9.3. The melting point of zinc is 692K, and the boiling point is 1180K. For substrate temperatures within this range, there will be a liquid layer of zinc on the substrate, along with a high Zn vapor pressure.

The exothermal reactions of condensed zinc with water vapor provides the possibility of $(ZnO)_n$ cluster formation[22]:

$$n(Zn)_{S,L} + nH_2O \rightarrow (ZnO)_n + nH_2. \quad (+219.60 \text{ kJ/mol}) \qquad (9.1)$$
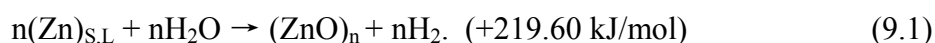
For $(Zn)_L$, small clusters should have a high mobility, allowing coagulation into nanoparticles[22], which serve to nucleate zinc oxide nanowires. For $(Zn)_S$, when the substrate temperature is below (or near) the melting point, initial nanostructural growth can occur through an epitaxial process[22]. Again, as seen in other works, the vapor pressure of zinc at temperatures slightly lower than its melting point can be enough for gas-phase growth[23]. Depending on the preferential faceting of the initial nanostructured

seeds, ensuing elongated growth along a given direction proceeds from diffusion and condensation of zinc oxide vapor as adatoms at the tip of a nanowire (although growth through a base mechanism[8,16] may co-exist). It is known that higher Zn vapor partial pressure can suppress the growth velocity of ZnO along the [0001] direction[24]. The direction of $[11\bar{2}0]$ is preferred as the growth velocity in $[11\bar{2}0]$ is faster than any other direction in the c plane owing to the lower bind energy[25]. This may help to explain the favored $[11\bar{2}0]$ growth direction of the smaller diameter nanowires, synthesized at low gas phase temperatures (~800K), versus the [0001] growth direction of the larger diameter nanowires, synthesized at high temperatures.

Zn vapor readily oxidizes in the gas phase, forming ZnO. Although Zn can react with oxygen, the experiments (see Fig.9.3 (c)) show that increased O_2 concentrations preclude nanowire formation. This effect is probably due to oxidation of the zinc substrate surface where the high- melting-point (2248K) oxide layer prevents Zn vaporization. Other works[8,15] have also reported the inhibiting effect of increased oxygen partial pressure on ZnO nanostructured growth. Nevertheless, the presence of hydrogen, which bounds the nanowire growth region shown in Fig.9.3(c), likely plays a critical factor by reducing any formed oxide layer, exposing base metal.

There exists ample water vapor (a combustion by-product) at elevated temperatures such that the endothermic gas-phase reaction,

$$\text{Zn}^{(g)} + \text{H}_2\text{O}^{(g)} \rightarrow \text{ZnO}^{(g)} + \text{H}_2^{(g)}, \tag{9.2}$$
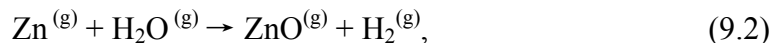
can generate ZnO vapor. Nanowires can then be formed through condensation and deposition of vapor ZnO, from a hotter gas phase to a cooler substrate, on both the oxidizer and fuel sides of the flame structure (Fig.9.3(c)). Gibbs free energies ΔG^0 for

reactions (9.1) and (9.2) are calculated (at 1 atm.) and given in Table 9.1 (all thermochemical data are from reference[26]). As can bee seen in Table 9.1, both reactions are spontaneous within the temperature range of ZnO growth.

Table 9.1 Gibbs free energies of reactions 9.1 and 9.2 within investigated growth temperature range[26]

T (K)	ΔG^0 (kJ/mol, Eq. (9.1))	ΔG^0 (kJ/mol, Eq. (9.2))
800	-66.137	-103.923
1000	-55.437	-73.072
1200	-43.033	-43.033
1400	Not available	-13.67
1600	Not available	15.113

Similar to H_2O, CO_2 (another combustion by-product) is found on both sides of the reaction zone. A heterogeneous mechanism, where Zn adsorbing on a ZnO nanowire reacts directly with CO_2, can produce ZnO growth[27]. At the same time, CO can adsorb on adsorbed Zn to form a Zn-CO species that reacts with CO_2, forming solid ZnO[27]. It is likely that this set of surface reactions dominates at low temperature (e.g. in the synthesis of the small diameter $[11\bar{2}0]$ nanowires), while the homogeneous water vapor route dominates at high temperature (e.g. in the synthesis of the larger diameter [0001] nanowires), further explaining the differences in diameter and morphology.

While temperature decreases steadily with radius in the characteristic case of Fig.9.3(c) (z=8mm), the species concentrations are not fixed and are, in fact, non-monotonic. Thus, temperature is not the only variable governing nanostructure growth morphology as a function of radial position; and the departure from the "conventional" nanowire as seen in Fig.9.4(c) is not surprising (to be discussed later). Nevertheless, other axial locations were investigated; and the results show that for the same quantitative local conditions (temperature and species), the same growth morphology is attained,

corroborating that optimal local conditions for ZnO nanowire synthesis are "universal" and likely to be translatable to other methods and geometries of gas-phase synthesis. For example, at both z=12mm and 15mm, the probed locations are in the post-flame zone where no oxygen is available (see Figs.9.3 (e) and (f)). In these regions, only nanowire structures are obtained, similar to Fig.9.4 (b). At both z=12mm and 15mm, where local conditions are ~1250K with ~3% H_2O mole fraction and ~1050K with ~1% H_2O mole fraction, respectively, nanowires of ~120 nm (Fig. 9.6 (a)) and ~40 nm (Fig. 9.6 (b)) in diameters are grown, respectively, similar to the characteristic case of Fig.9.3(c) for z=8mm.
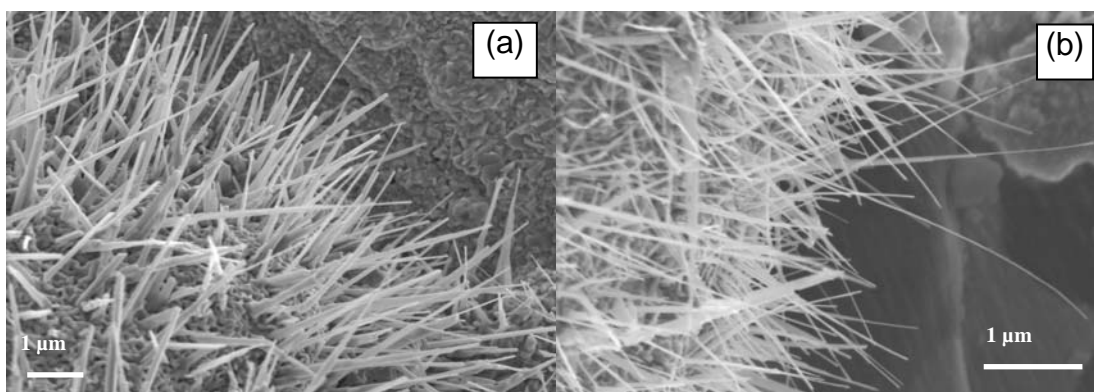
Figure 9. 6 FESEM images of ZnO nanowires produced at *z*=12mm and 15mm, (a) ~120nm, (b) ~40nm.

Morphologies related to the "basic" nanowire are often formed. At *z*=6mm, for regions of moderate-to-low temperature (~950K) and low H_2O mole fraction (<1%), hierarchical architectures of long ZnO nanowires with diameters of 30-50nm are produced (Fig.9.7 (a)). The growth of such hierarchical structures is generally considered to be based on two stages[28,29]. The first stage is the formation of the primary nanowire along its fast growth direction, and the second stage is the nucleation and epitaxial growth of secondary nanowires on the primary nanowire. A low magnification TEM of

such a hierarchy structure is shown in Figure 9.8(a), which is composed of a long trunk wire and short thin branch wires (~15nm) with a uniform cross-section. A hierarchy structure with nucleation sites (indicated by arrowheads) on the trunk is presented in Fig. 9.8(b), indicating the two-stage growth mechanism. The moderately low temperature, low H_2O concentration, and relatively high concentrations of CO_2 and CO for this synthesis condition further support the role of the aforementioned surface-reaction growth mechanism. These hierarchical nanostructures may be helpful in studies of nanostructure growth mechanism and may find applications in nanoelectronics, opto-electronics, catalyst, and displays[28].
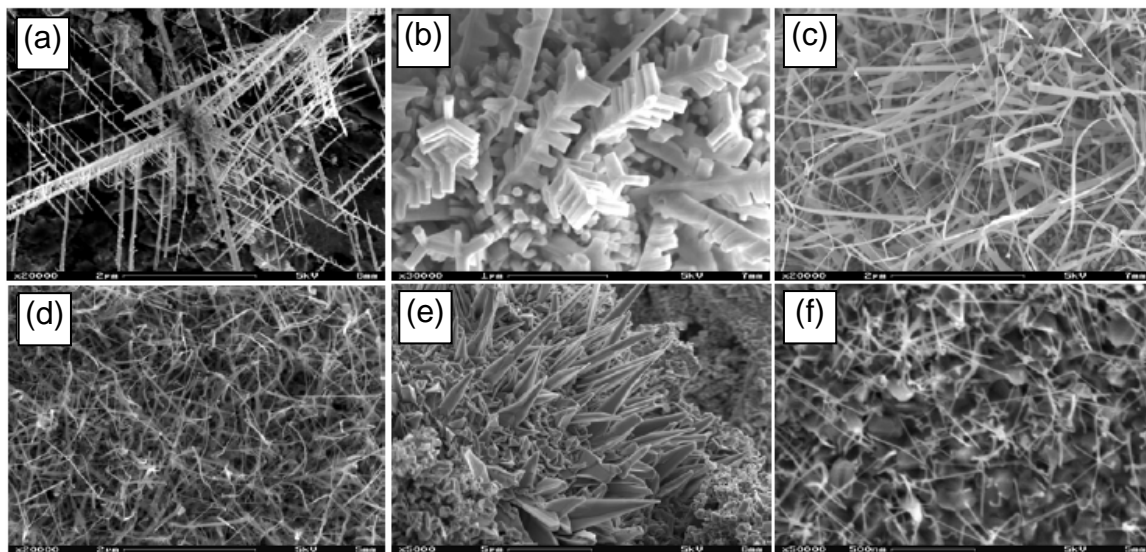
Figure 9.7 FESEM images of (a) hierarchical architectures of long nanowires, (b) hierarchical structures of short nanorods, (c) nanoribbons, (d) intermixed nanowires and nanoribbons, (e) nanocones, and (f) short nanoneedles.

At z=7mm, for regions of temperature ~1100K and H_2O mole fraction ~10%, hierarchical structures of short nanorods are obtained (Fig.9.7 (b)). The secondary nanorods exhibit hexagonal cross-section, with the gas-phase water route likely coming

into play. In the temperature range of 950-1000K and H_2O mole fraction of ~4%, nanoribbons appear as shown in Fig. 9.7(c). In comparison with the z=8mm case (Fig. 9.3(c)) for the same temperature range, where transition from nanowires to nanoribbons occurs as shown previously in Fig.9.4(c), higher H_2O concentration at the z=7mm location instead produces full nanoribbons (Fig. 9.7(c)), with widths of ~100nm and lengths up to 10μm. Figure 9.7(d) shows another morphology in the transition from nanowires to nanoribbons at the z=8mm location (complementing that of Fig.4 (c)), where very-small-width (~20nm) nanoribbons are intermixed with very-small-diameter (~10nm) nanowires.
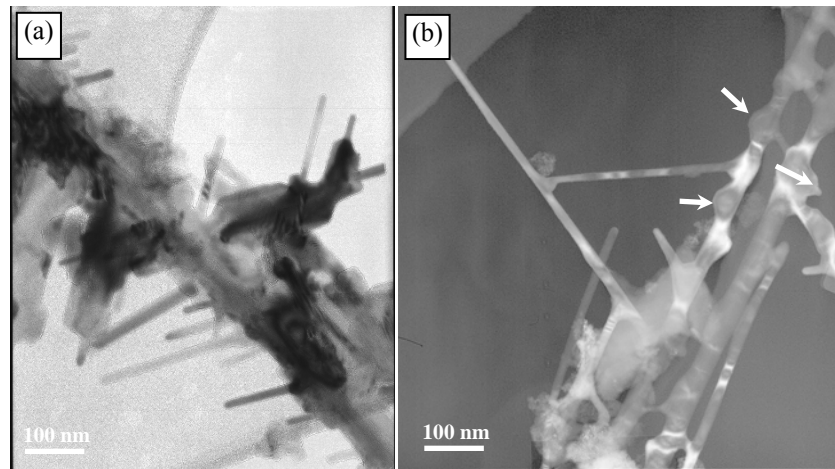
Figure 9.8 low magnification TEM images of hierarchical structures, (a) a hierarchy with a long trunk and short thin branched wires, and (b) a hierarchy with nucleation sites on the trunk.

At z=9mm, nanoribbon morphologies disappear. For regions of high gas-phase temperature (1400-1500K), substrate temperature near the 1180K, and ~9% mole fraction H_2O concentrations, nanocones (with base diameters of 600-800nm tapering into a very sharp tip) emerge (Fig. 9.7(e)). These nanocones could offer potential application as probing tips with high spatial resolution in both vertical and horizontal dimensions or

field-emission tips due to the increased field-enhancement factor[30]. The formation of this structure is probably due to the insufficient supply of ZnO vapor during the growth period, explaining the formation of the very sharp tip. For moderate temperatures, nanowires similar to Fig. 9.4(a) are found; while for low temperatures (600-700K) and H_2O mole fractions <5%, short nanoneedles (Fig. 9.7(f)) of only ~10nm diameter appear, branching from common points that are likely be ZnO/Zn liquid droplets at such low temperatures.

As the interpenetrative growth (shown by the arrowhead in Fig.9.4 (a)) indicates nanowire formation through VS mechanism, the formation of slabs (directed by arrowheads in Figure 9.9 (a)) can also show the VS mechanism. These slabs may result from depositing vapor and filling the gaps between the cross-linked rods[31]. The thickness of these slabs is roughly the same as the rod's diameter. TEM image (Fig. 9.9(b)) shows a cross-link of two nanowires.
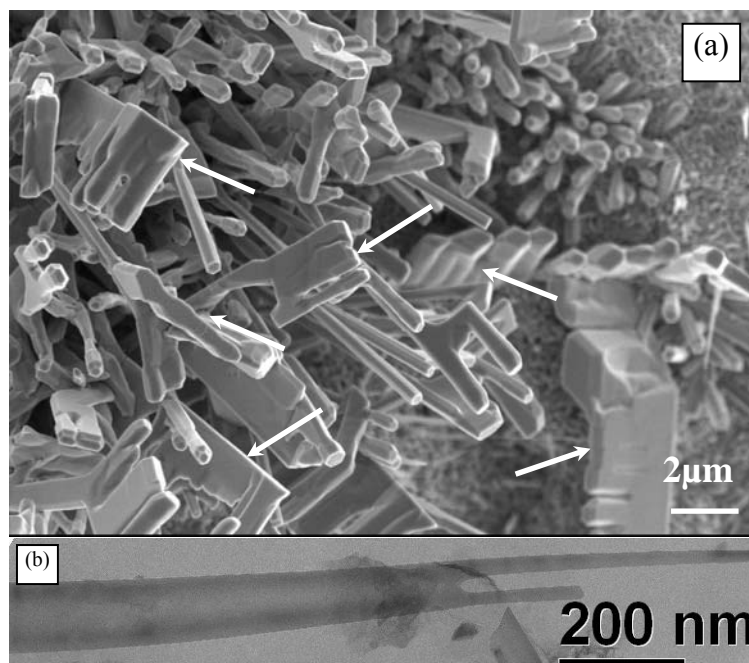
Figure 9.9 the formation of slab-shaped structures shown in (a) a FESEM image and (b) a TEM image.

The possible growth regions of different major ZnO nanostrucures (nanorods and nanowires) in our experiments are listed in Table 9.2. The nanorods here are defined as the structures with a diameter greater than 100nm, while the nanowires are defined as the structures with a diameter less than 100nm. The corresponding temperatures and growth-related chemical species in these growth regions can be obtained by referring to the SRS measurements in Fig. 9.3.

Table 9.2 Summarizes the possible growth regions of different ZnO nanostructures in our experiment.

z (mm) \ r (mm)	0	1	2	3	4	5	6
15	[	$100<d<150$		] [	$50< d< 100$	]	
12	[	$100<d<300$	] [	$40<d<100$		]	
9	[		$150<d<600$	] [$100<d<150$] [		$20<d<100$	]
8		[	$200<d<450$	] [$100<d<200$	] [$30<d<100$]		
7			[$200<d<450$] [$100<d<200$] [		$30<d<100$		]
6			[$150<d<300$] [$100<d<200$] [		$30<d<100$		]

* d stands for diameter (unit: nm)

As mentioned previously, other morphologies do indeed appear. Almost all of the diverse nanostructures for ZnO reported in the literature can be found in our system. Non-nanowire-like structures are formed, such as bicrystal[32], nanowall[33], nanosaw[34], and nanocage[35], (see Figure 9.10). These structures are small in quantity and generally present in regions with low temperature (<800K) and low H_2O concentrations (<1%) on the fuel side. Since these structures are usually obtained in small cavities on the substrate surface, the formation of these structures probably results from the very locally kinetic change in the vapor deposition induced by the turbulence flow inside the small craters. The bicrystal (Fig. 9.10(a)) is composed of two crystals forming a twin structure with a single twin boundary along the length. An enlarged view of the tip portion of a bicrystal

is presented to show the sharp boundary at the center (inset in Fig. 9.10(a)). These unusual structures offer a model system for studying charge and mass transport across/along a single planar defect[36]. Fig. 9.10 (b) depicts single-sided teethed ZnO nanosaw structures. This polar surface-induced asymmetric growth could be attributed to the self-catalysis of the Zn-terminated (0001) surface that is chemically active while the negatively charged O-terminated polar surface is chemically inert[34]. The nanostructure resembling walls is shown in Fig. 9.10 (c), and these nanowalls are connected to each other, displaying an irregular network with wall thicknesses of about 20-40 nm, with varying "pore" sizes. These nanowalls can be potentially used for photocatalysts, optoelectrics[33], energy storage or conversion and data storage and memory devices[37]. Hexagon-based polyhedral cages (Fig. 9.6 (d)) exhibit unique geometrical shapes, which could be a single crystal or a "single crystalline" textured nanostructure, and can be a potential candidate for drug delivery application[35].
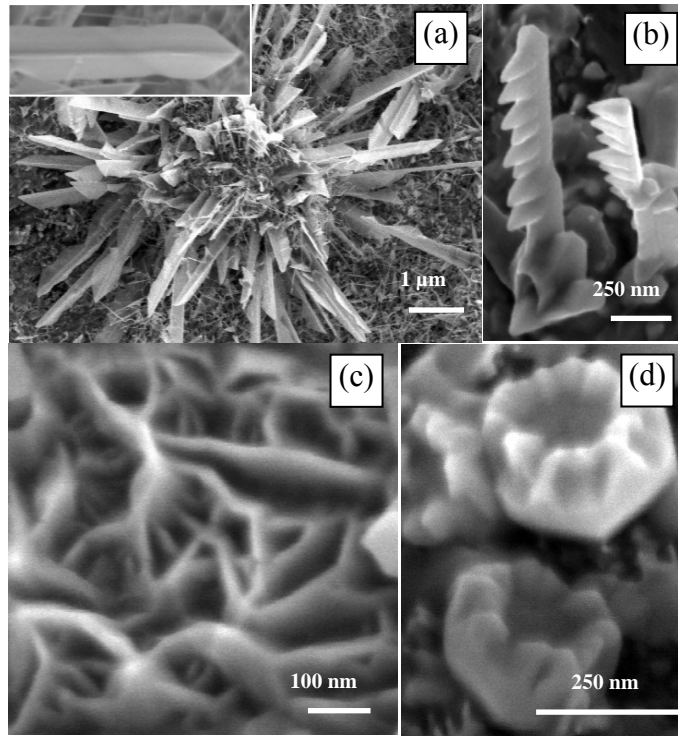
Figure 9.10 FESEM images of some ZnO nanostructures at z=8mm (also present in other axial positions), (a) bicrystals, (b) nanosaws, (c) nanowalls, and (d) nanocages

9.4 Conclusion

The synthesis of single-crystalline, ZnO nanowires grown directly on zinc-plated substrates at high rates in a flame process has been demonstrated, with the potential for large growth areas at atmospheric pressure. Only a few works, e.g. Ref.8 have reported direct growth on the starting materials (as well as multiple growth directions), with most using substrates as collectors. The liquid interface present in our system appears to inhibit well-aligned growth; however, use of templated/patterned substrates should produce such control, along with crystal growth direction. At the same time, local specification of temperature (e.g. low or high) and species (e.g. O_2, CO_2, or H_2O) can be readily tuned in

our flame system, along with substrate temperature, to achieve a desired growth characteristic.

Reference

[1] Kong, Y.C., Yu, D.P., Zhang, B., Fang, W., and Feng, S.Q., "Ultraviolet-emitting ZnO nanowires synthesized by a physical vapor deposition approach*,", Appl. Phys. Lett.*, 78(4):407 (2001).

[2] Lee, C.J., Lee, T.J., Lyu, S.C., Zhang, Y., Ruh, H., Lee, H.J., "Field emission from well-aligned zinc oxide nanowires grown at low temperature," *Appl. Phys. Lett.*, 81:3648 (2002).

[3] Wang, Y.W., Zhang, L.D., Wang, G.Z., Peng, X.S., Chu, Z.Q., and Liang, C.H., "Catalytic growth of semiconducting zinc oxide nanowires and their photoluminescence properties," *J. Cryst. Growth,* 234:171-175 (2002).

[4] Zhang, Y., Wang, N., Gao, S., He, R., Miao, S., Liu, J., Zhu, J., and Zhang, X., "A simple method to synthesize nanowires,", *Chem. Mater.*, 14:3564-3568 (2002).

[5] Lyu, S.C., Zhang, Y., Ruh, H., Lee, H.J., Shim, H.W., Suh, E.K., and Lee, C.J., "Low temperature growth and photoluminescence of well-aligned zinc oxide nanowires,", *Chem. Phys. Lett.,* 363:134-138 (2002).

[6] Lyu, S.C., Zhang, Y., Lee, C.J., Ruh, H., and Lee, H.J., "Low-temperature growth of ZnO nanowire array by a simple physical vapor-deposition method,", *Chem. Mater.*, 15:3294-3299 (2003).

[7] Tseng, Y.K., Huang, C.J., Cheng, H.M., Lin, I.N., Liu, K.S., and Chen, I.C., "Characterization and field-emission properties of needle-like zinc oxide nanowires grown vertically on conductive zinc oxide films,", *Adv. Funct. Mater.,* 13(10):811-814 (2003).

[8] Dang, H.Y., Wang, J., and Fan, S.S., "The synthesis of metal oxide nanowires by directly heating metal samples in appropriate oxygen atmospheres," Nanotechnology 14:738-741 (2003).

[9] Wang, L., Zhang, X., Zhao, S., Zhou, G., Zhou, Y., Qi, J., "Synthesis of well-aligned ZnO nanowires by simple physical vapor deposition on c-oriented ZnO thin films without catalysts or additives,", *Appl. Phys. Lett.*, 86:024108 (2005).

[10] Huang, M.H., Wu, Y., Feick, H., Tran, N., Weber, E., and Yang, P., "Catalytic growth of zinc oxide nanowires by vapor transport," Adv. Mater. 13(2):113-116 (2001).

[11] Yao, B.D., Chan, Y.F., and Wang, N., "Formation of ZnO nanostructures by a simple way of thermal evaporation," Appl. Phys. Lett. 81(4):757 (2002).

[12] Gundiah, G., Deepak, F.L., Govindaraj, A., and Rao, C.N.R., "Carbothermal synthesis of the nanostructures of Al2O3 and ZnO," *Top. Catal,.* 24:137-146 (2003).

[13] Jo, S.H., Lao, J.Y., Ren, Z.F., Farrer, R.A., Baldacchini, T., and Fourkas, J.T., "Field-emission studies on thin films of zinc oxide nanowires,", *Appl. Phys. Lett*., 83(23):4821 (2003).

[14] Xu, C.X., and Sun, X.W., "Characteristics and Growth Mechanism of ZnO Whiskers Fabricated by Vapor Phase Transport,", *Jpn. J. Appl. Phys.*, 42:4949-4952 (2003).

[15] Banerjee, D., Lao, J.Y., Wang, D.Z., Huang, J.Y., Steeves, D., Kimball, B., Ren, Z.F., "Synthesis and photoluminescence studies on ZnO nanowires," *,Nanotechnology,* 15:404-409 (2004).

[16] Hu, J.Q., Li, Q., Wong, N.B., Lee, C.S., and Lee, S.T., "Synthesis of uniform hexagonal prismatic ZnO whiskers,", *Chem. Mater.* ,14:1216-1219 (2002).

[17] Park, W.I., Kim, D.H., Jung, S.W., and Yi, G.C., Metalorganic vapor-phase epitaxial growth of vertically well-aligned ZnO nanorods, *Appl. Phys. Lett.,* 80(22):4232 (2002).

[18] Ogata, K., Maejima, K., Fujita, Sz., and Fujita, Sg., Growth mode control of ZnO toward nanorod structures or high-quality layered structures by metal-organic vapor phase epitaxy, *J. Cryst. Growth*, 248:25-30 (2003).

[19] Liu, X., Wu, X., Cao, H., and Chang, R.P.H., Growth mechanism and properties of ZnO nanorods synthesized by plasma-enhanced chemical vapor deposition, *J. Appl. Phys.*, 95(6):3141-3147 (2004).

[20] C.X.Xu and X.W.Sun , Characteristics and Growth Mechanism of ZnO Whiskers Fabricated by Vapor Phase Transport, Jpn. J. Appl. Phys., Part 1 42(8):4949-4952, 2003

[21] Yang, R., and Wang, Z.L., Interpenetrative and transverse growth process of self-catalyzed ZnO nanorods, *Solid State Commun.,* 134:741-745,2005

[22]Vostrikov, A.A., Shishkin, A.V., and Timoshenko, N.I., Synthesis of zinc oxide nanostructures during zinc oxidation by sub- and supercritical water, *Tech. Phys. Lett.,* 33:30-34, 2007

[23]Wang, Z. L., Zinc oxide nanostructures: growth, properties and applications, *J. Phys.:Condens. Mattr,* 16: R829-R858, 2004

[24]Yu Hang Leung, Aleksandra B. Djurišić, Ju Gao, Mao Hai Xie , Wai Kin Chan, Changing the shape of ZnO nanostructures by controlling Zn vapor release: from tetrapod to bone-like nanorods, Chemical physics letters,385:155-159, 2004

[25]C.X. Xu, X. W. Sun, Z.L Dong, G.P. Zhu and Y.P. Cui, Zinc oxide hexagram whiskers, Applied physics letters, 88:093101, 2006.

[26] Ihsan Barin in collaboration with Fried Sauert et al., *Thermochemical data of pure substances*, Weinheim, Federal Republic of Germany ; New York, NY, USA : VCH, c1989-

[27]Osborne, J.M., Rankin, W.J., McCarthy, D.J., and Swinbourne, D.R., The oxidation of zinc vapor in CO-CO2-N2 gas mixtures, *Metall. Mater. Trans. B*, 32B:37-45, 2001

[28]Ying Dai, Yue Zhang, Yuan Qiang Bai, Zhong Lin Wang. Bicrystalline zinc oxide nanowires. Chemical Physics Letters 2003, 375: 96-101.

[29]J. Y. Lao, J. Y. Huang, D. Z. Wang and Z. F. Ren. Hierarchical oxide nanostructure. J. Mater. Chem. 2004, 14:770-773.

[30]Won II Park, Gyu-Chul Yi, Miyoung Kim, Stephen J. Pennycook, ZnO nanoneedles grown vertically on Si substrates by non-catalytic vapor-phase epitaxy, Adv. Mater., 14(24):1841-1843, 2002

[31]JH PARK, HJ CHOI, YJ CHOI, SH SOHN, JG PARK, Ultrawide ZnO nanosheets, Journal of material chemistry, 14:35-36, 2004

[32]Ying Dai, Yue Zhang, Yuan Qiang Bai, Zhong Lin Wang. Bicrystalline zinc oxide nanowires. Chemical Physics Letters 2003, 375: 96-101.

[33]J. Y. Lao, J. Y. Huang, D. Z. Wang, Z. F. Ren, D. Steeves, B. Kimball, and W. Porter. ZnO nanowalls. Applied Physics A: Materials Science & Processing 2004. 78: 539-542.

[34]Z. L. Wang, X. Y. Kong, and J. M. Zuo. Induced growth of asymmetric nanocantilever arrays on polar surfaces. Physical Review Letters 2003, 91(18)

[35]Pu Xian Gao and Zhong Lin Wang. Mesoporous polyhedral cages and shells formed by textured self-assembly of ZnO nanocrystals. J. Am. Chem. Soc. 2003, 125:11299-11305.

[36]Ying Dai, Yue Zhang, Yuan Qiang Bai, Zhong Lin Wang. Bicrystalline zinc oxide nanowires. Chemical Physics Letters 2003, 375: 96-101.

[37]Hou T. Ng, Jun Li, Michael K. Smith, Pho Nguyen, Alan Cassell, Jie Han, M. Meyyappan. Growth of epitaxial nanowires at the junctions of nanowalls. Science 2003, 300:1249-1249

Chapter 10

ZnO Nanomaterials from Counterflow Diffusion Flames

10.1 Introduction

As shown in Chapter 9, various ZnO nanostructures can be obtained in IDFs, given the appropriate local growth conditions (e.g. temperature and growth-related chemical species). However, the large radial gradients in IDFs can result in non-uniformity of ZnO nanostructure, making it somewhat difficult to properly assess the growth conditions of specific ZnO nanostructures. To better correlate ZnO morphologies with local conditions, counter-flow diffusion flames (CDFs) with quasi-one-dimensionality are employed in this chapter, where the gradients vary mainly in the axial direction. The axial separation of fuel side and airside with respect to the reaction zone in CDFs also makes it easy to evaluate the effects of H_2O versus O_2 in the synthesis of ZnO nanostructures. Another motivation of adopting CDFs is to see if the obtained relations between ZnO nanostructures and their corresponding local conditions in IDFs can be translatable to another configuration of synthesis. Conditions for ZnO nanstructures in a flame environment could be established that may be directly applicable as specific operating conditions for other flame configurations, as well be reference conditions for other methods of synthesis.

10.2 Experiments and computations

The CDF experiment setup used in this chapter is as shown in Fig. 4.4 and Fig. 7.1(a). To be convenient for discussions, the flame structure determined computationally and experimentally (by SRS) is plotted again in Fig. 10.1, along with the actual flame with schematic insertion of substrates on the both sides of flame (Fig.10.1 (a)). The actual probed axial positions are marked in Fig. 10.1(b) and listed in Table 10.1 along with the growth conditions at each position.
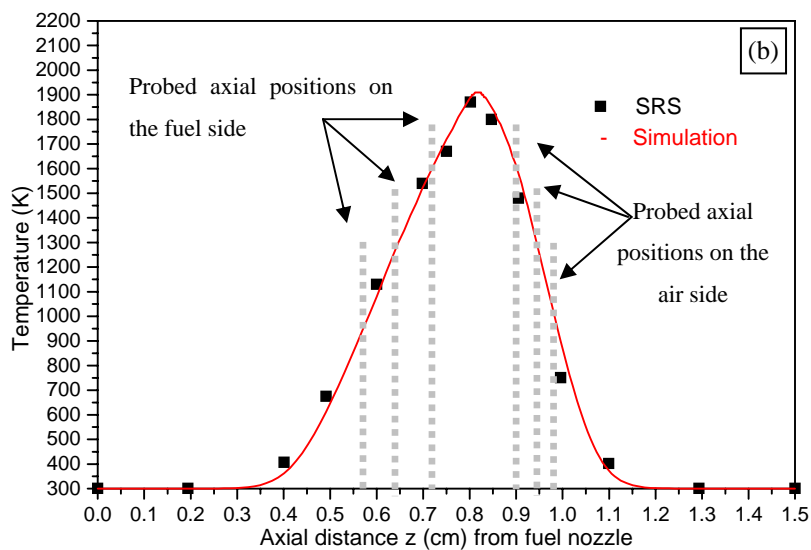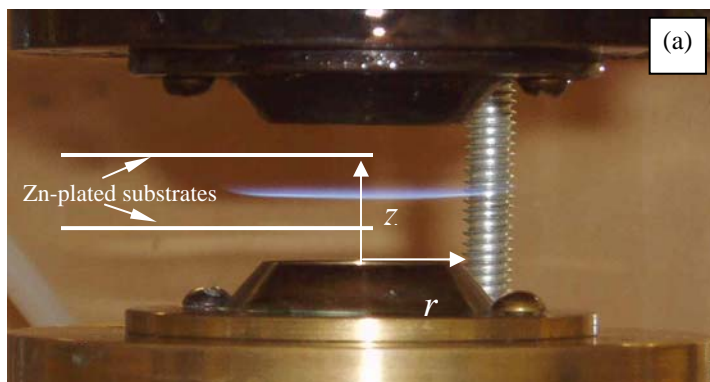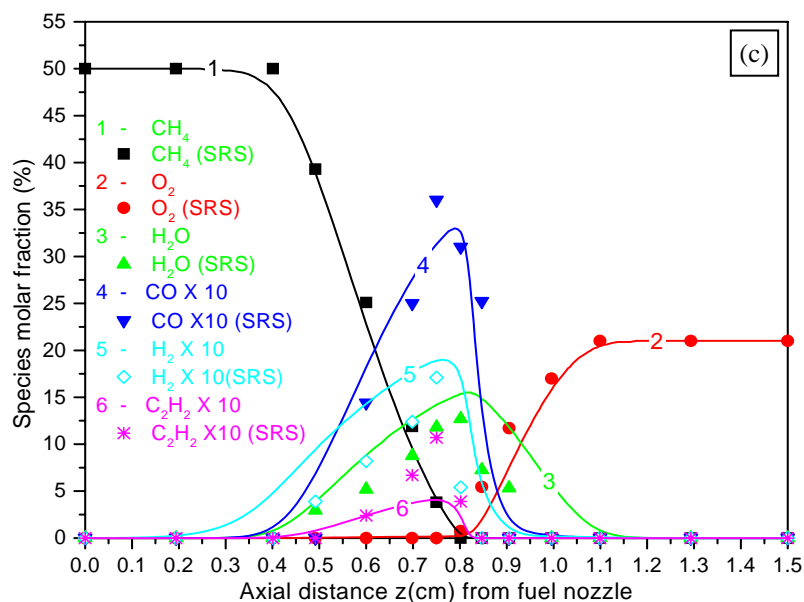
Figure 10.1. Flame structure with 50%CH$_4$ measured by SRS and compared with simulations, (a) an actual CDF with substrates inserted, (b) temperature profile along the axial z direction and the probed positions, and (b) the molar fractions of major species along the axial *z* direction.

10.3 Results and discussions

To perform comparisons between IDFs and CDFs, six characteristic axial (*z*) positions in CDFs are examined, three of which are located on the airside and another 3 on the fuel side (Table 10.1). The growth conditions (e.g. temperature, water vapor/oxygen concentration) for ZnO nanostructures at these positions are similar to those in IDFs where ZnO nanowires with diameters of ~450nm, ~150nm, less than 100nm respectively are produced on the fuel side and ZnO nanowires of ~500nm and ~200nm along with micro-sized ZnO islands/chunks respectively are obtained on the airside. Correspondingly, similar ZnO nanostructures are expected at these positions in CDFs.

Table 10.1 the axial positions investigated in CDFs

	Axial position z (mm)	T (K)	O_2 (mole fraction %)	H_2O (mole fraction %)
Fuel side	5.7	1000	0	8
	6.4	1300	0	10
	7.2	1600	0	13
Airside	9	1600	6	12
	9.4	1300	10	10
	9.8	1000	13	8

Figure 10.2 shows the various structures obtained at z=9mm (Table 10.1). Nanorods with a diameter of around 450nm are shown in Fig. 10.2(a), displaying uniform hexagonal cross-section along the growth direction, similar to the nanorods obtained in IDFs (Fig. 9.4(a)). "Welded" joints of nanorods are observed as in Fig. 10.2(b), which might be formed by a sintering process at the high local temperature[1]. Fig. 10.2(c) gives nanorods with a sharp tip (similar to the structures in Fig 9.7 (e) in IDFs) might result from the local decrease in supply of ZnO vapor as more source materials are consumed[2]. Fig. 10.2(d) shows so-called "nanonails"[3,4] that display a gradually decreasing cross section from the top to bottom of the structure. The growth of nanonails is likely due to better absorption of incoming ZnO vapor at the top than at the bottom due to their large packing density[4]. Nanorods with sharp tips arranged into flower-like patterns are shown

in Fig. 10. 2(e). The nanorods grow out of the substrate radiatively at different angles (with respect to the substrate) to develop into flower patterns. Many ZnO nuclei formed at the early stages are likely to aggregate together, with a number of nanorods growing from them to form the flower-like pattern[5]. Although these nanorods with a sharp tip do not seem to exhibit hexagonal cross section, they are likely comprised of hexagonal facets[4]. Complicated structures are developed by multiple growths of nanorods as in Fig. 10.2(f), where the structure resembles a bunch of grapes. Fig 10.2 (g) gives a slab shape structure formed by subsequent filling of the gaps among the nanorods, showing similarity with the structures formed in IDFs (Fig. 9.9 (a)). Tetrapod-shaped structures, as shown in Fig. 10.2(h), are comprised of four rod-shaped arms formed at tetrahedral angles from a central core[6]. These four arms have hexagonal cross section nanorods with uniform diameter and length. It is generally proposed that the presence of a tetrahedral zinc blende core nucleate the growth of four cylindrical arms[7]. Fig. 10.2 (i) displays some defective hexagonal nanorods, as indicated by arrowheads. These defects imply the vapor-solid growth mechanism of ZnO nanomaterials in flames.

Although these nanorods at z=9mm can be self-assembled into different structures and exhibit different morphologies, most of them range from 300nm to 500 nm in diameter and have symmetrical hexagonal facets, indicating a strong preferred orientation along the c -axis of ZnO[5], corresponding to those structures produced in IDFs for similar growth conditions (temperature between ~1500K and ~1600K, O_2 ranging from 5% to 7 % while H_2O from 9% to 11%) .
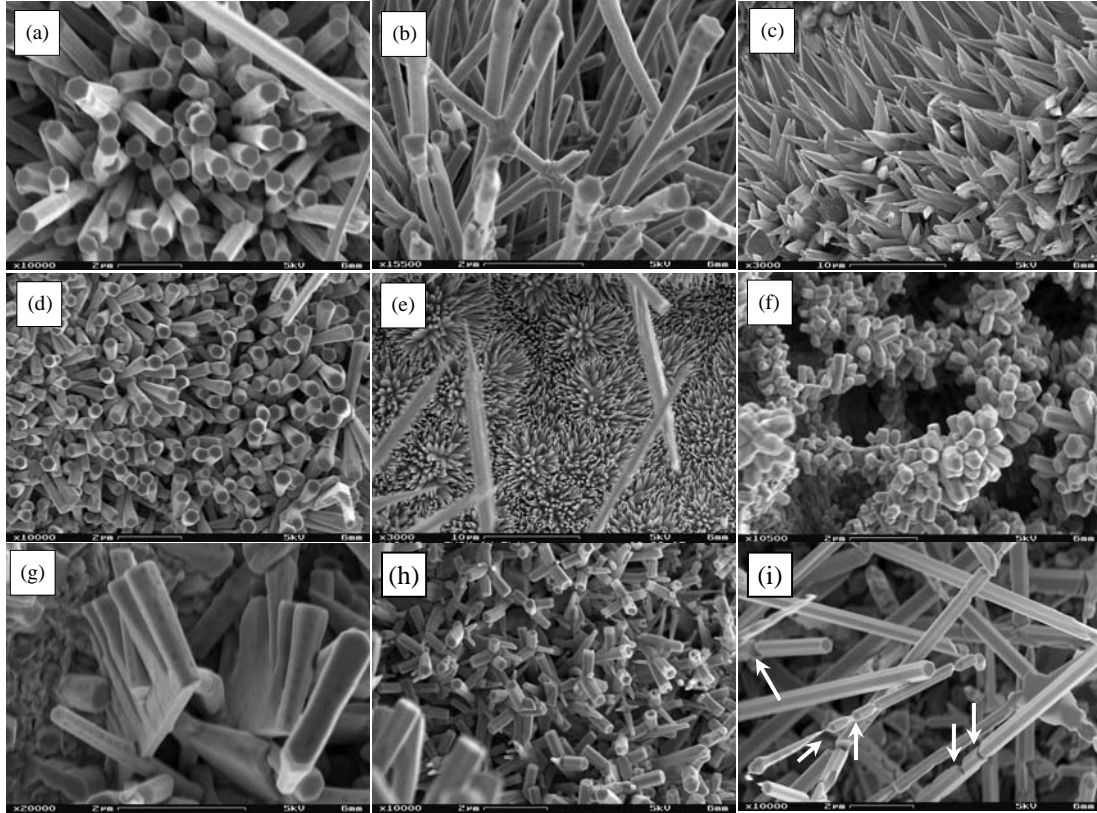
Figure 10.2 FESEM images of nanomaterials from the axial position on the oxidizer side where T=~1600K.

The structures and morphologies shown in Figs. 10.2(c), (e), (f) and (h) are generally sprout from small craters on the substrate surface. Compared to the size of nanomaterial, the growth condition changes (e.g. vapor deposition rate) induced by these craters are large enough to change the structures and morphologies of as-grown nanomaterials, as manifested in IDFs (Fig.9.10).
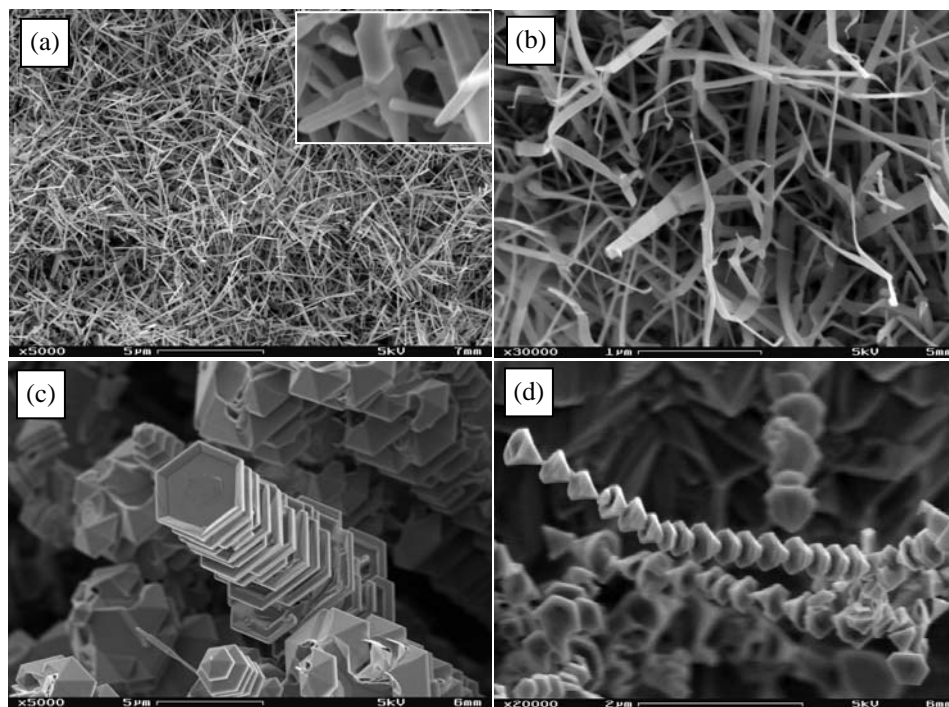
Figure 10.3 FESEM images of nanomaterials from the axial position on the oxidizer side where T=~1300K. (a) Nanorods, (b) nanoribbons, (c) tower-like structure, (b) chain-like structure.

Another axial position (z=9.4) on the oxidizer side is examined (Table 10.1). Figure 10.3 displays some FESEM images of as-observed ZnO nanomaterials at this position. The majority of ZnO nanomaterials are nanorods ranging from 100nm-200nm in diameter. As shown in Fig.10.3 (a), the inset shows a high-magnification image of nanorods displaying clearly hexagonal facets. The correspondence of nanostructures and growth conditions at this position is reasonably in agreement with that obtained in IDFs where nanorods of ~100nm to ~200nm in diameters are produced in the region whrere temperature is between ~1200K and ~1300K, O_2 is from 8% to 12 %, and H_2O is from 7% to 11%. Radially away from the flame centerline, a small quantity of ZnO nanoribbons (Fig.10.3 (b)) is found to be intermixed with nanowires (~20nm in

diameter).   These nanoribbons on average are 50nm wide, but are uniform in thickness at ~10nm.   In contrast to the nanoribbons observed only on the fuel side in IDF in Chapter 9, these nanoribbons grow on the oxidizer side.   The reason could be associated with the much lower O_2 concentration (estimated less than 1%) and lower temperature (<900K) in this case, favoring the nanoribbon growth.   These nanoribbons are observed away from the flame center and close to the outside N_2 co-flow, diluting the local O_2 through diffusion and further cooling the local substrate surface through convection. Tower-like structures are observed in Fig. 10.3(c), and these structures consist of many individual hexagonal plates piled up layer upon layer[8].   The individual hexagonal plates have a diagonal length of ~3μm and a thickness of about 200nm.   By the same token, chain-like structures shown in Fig. 10.3(d) are composed of many ZnO sharp cones connected to one another.   Each cone is characterized an obvious hexagonal bottom with a sharp tip.

ZnO nanomaterials at an axial position (z=9.8mm) with a lower temperature (Table 10.1) are also probed to study the effects of oxygen.   At this position, the main products are the micro-sized columns (Fig. 10.4(a)).   These columns show irregular hexagonal cross sections and are at least 10μm in diameter. They are also observed in IDFs where temperature ranges from ~950K to ~1100K, and O_2 from ~13% to ~15%.   Such columns are probably nucleated from big Zn droplets.   A small amount of nanosheets with a thickness of ~50nm and various shapes are observed radially away from the flame centerline.   These nanosheets can roll up to form pipes, and can also connect to each

other to form channels. From the environment of ZnO nanoribbons and nanosheets in IDFs, we suspect in CDFs that the local growth condition for nanosheets is similar to the growth condition for nanoribbons.
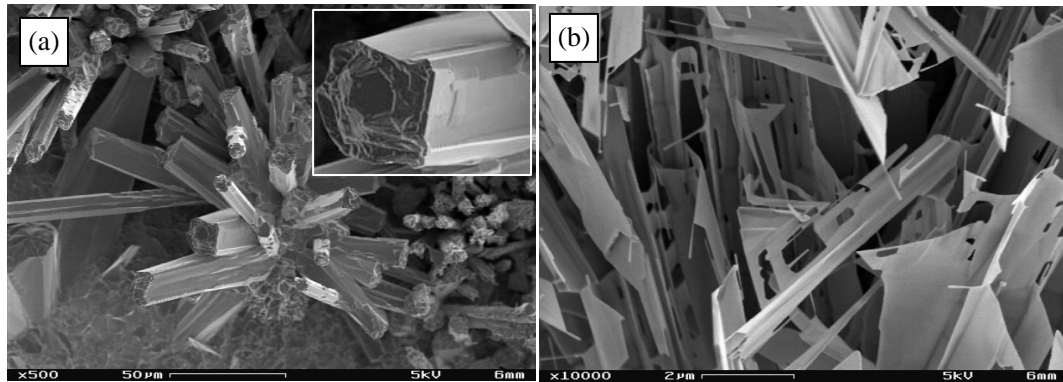
Figure 10.4 FESEM images of nanomaterials from the axial position on the oxidizer side where T=~1000K. (a) Microsized columns/chunks, (b) nansheets.

The fuel side of CDF is investigated to study the effects of H_2O on ZnO growth, since O_2 does not exist on the fuel side while H_2O does (Fig.10.1 (c)). Another necessity for exploring the fuel side of the CDF is to compare it to the growth conditions of ZnO on the fuel side of the IDF. To match the temperatures probed on the airside of CDF, three axial positions on the fuel side are examined (Table 10.1). Figure 10.5 shows the nanostructures obtained from these positions. As expected, perfect hexagonal nanorods are observed at T=~1600K (z=7.2 mm, Table 10.1)) with uniform diameter of ~450nm (Fig. 10.5(a)), which is in agreement with the results for IDFs where ~500 nm diameter nanorods are produced on the fuel side with temperature ~1600K and H_2O as ~12%. By comparing the growth conditions at this position (z=7.2mm) with those at position

z=9mm on the airside where the temperature are the same (Table 10.1), it seems that the temperature plays a key role in determining the ZnO nanostructure in high temperature zone as the ZnO nanorods at both positions are almost the same (in terms of diameter) despite the difference in O_2 concentration (Fig. 10.2 (a) and Fig. 10.5(a)). Nanorods produced at T=~1300K (z=6.4mm) have an average diameter of ~150nm and a length up to 30μm (Fig. 10.5(b)), showing similarity to the results in IDFs where nanorods with a diameters of ~200nm correspond to a growth condition with temperature be ~1300K and H_2O be 12% on the fuel side. Fig. 10.5(c) (z=5.7mm) shows thin nanowires ranging from ~30nm to ~100 nm in diameter. Most of them have a diameter of ~50nm and up to tens of micrometers long, displaying consistency with the results in IDFs where similar ZnO nanowires (~40nm-~100nm in diameter) grow for approximately the same conditions on the fuel side (temperature as ~1000K-~1100K and H_2O as ~8%-~10%). Away from the flame centerline at this position, a very small quantity of nanoribbons is observed (Fig. 10.5(d)). These nanoribbons are ~150nm wide and ~25nm thick, and can be up to several tens of micrometers in length, the same as produced in IDFs under similar condition (temperature<1000K and H_2O as ~2%).
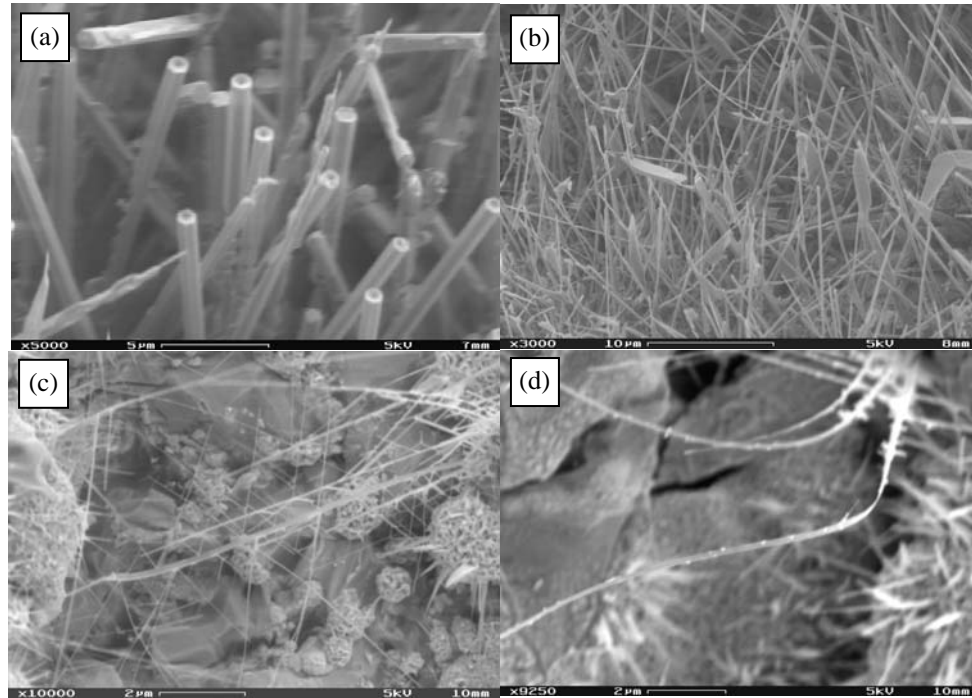
Figure 10.5 ZnO nanomaterials from the fuel side. (a) T=~1600K, (b) T=~1300K, (c) and (d) T=~1000K.

In theory, the same morphology of ZnO nanomaterials are supposed to be produced across the radial direction at an axial position on both the oxidizer and fuel sides of CDFs. However, our results show that to some extent, different morphologies and structures appear along the radial directions of the axial positions. For example, at T=1600K (z=9.0mm) on the oxidizer side, although major products are nanorods with a hexagonal cross section (Fig. 10.2), there is some quantity of tetrapod structures and nanorods with a sharp tip. Beside the aforementioned effects resulting from an uneven substrate surface, other parameters may play roles. CDFs are considered to be quasi one-dimensional flame structures, but they are not truly one-dimensional since there is a radial velocity and radial velocity gradient, along with non-radial experimental boundary

condition. The radial velocity and its gradient could affect the distribution of temperature and species along the radial direction of an axial position. In addition, the insertion of substrates into the flame can exert some disturbances to the flow field, further causing certain changes of the flame structure. The growth condition changes induced by all these factors may be enough to change the structures and morphologies of as-prepared ZnO nanomaterials, since they are very sensitive to the local growth environment. Wang *et al*[9] reported in their experiment that the temperature, vapor flow, and the availability of the Zn-O vapor could affect the morphologies of as-prepared ZnO structures. The work by Hu *et al*[8] concluded that ZnO morphologies are closely related with the reaction temperature, oxygen partial pressure and the flow rate. Gao *et al*[10] also mentioned that the local temperature and surface diffusion rate have an influence on ZnO nanostructures. Nevertheless, the uniformity of ZnO nanomaterials in CDFs is reasonably acceptable, namely, one structure/morphology constituting the major product (~70% by volume) harvested at an axial position. At the same time, we notice that the above-mentioned changes in the radial direction seem to not be strong enough to influence the CNT growth from CDFs, as reported in Chapters 7 and 8, with reasonably uniform CNTs harvested along the probe in terms of diameter, yield and alignment. The sensitivity of ZnO nanostructures to the slight radial gradient might be due to the liquid layer and the Marangoni effect. As discussed in Chapter 9, a liquid Zn layer may exist on the substrate surface due to the low melting point of Zn (692K). The surface tension of this liquid layer is temperature dependent and would decrease with increasing

temperature[11]. Thus a surface tension gradient would be created on the liquid layer resulting from the presence of the actual temperature gradient along the radial direction in CDFs (due to experimental conditions). Such a gradient in surface tension will naturally cause the liquid to flow away from regions of low surface tension, as a liquid with a high surface tension pulls more strongly on the surrounding liquid than one with a low surface tension[12]. This effect (a mechanism of mass transfer) is called Marangoni effect. This Marangoni effect probably affects the local nucleation of ZnO nanostructures, the preferential faceting of nanostructures, the local reaction of Zn with H_2O, and the absorption of ZnO vapor, resulting in the different nanoturtures and morphologies of final as-grown ZnO, along the radial length of the probe.

By comparing to the IDFs, some similar conclusions can be drawn. On the oxidizer side where oxygen content is ~above 15%, no nanosized materials, but instead microsized ZnO islands/columns/chunks, are produced (Fig. 10. 4(a)), though the temperature (~1000K) may be favorable for thick ZnO nanorod growth. The diameter of nanorods/wires increases with increasing temperature. Higher growth temperatures will favor formation of ZnO nanowires/rods with larger diameters, and a higher growth temperature is also beneficial to the synthesis of ZnO nanowires/rods possessing perfect hexagonal crystal morphology. The relations of ZnO nanostructures and their local growth environments are also similar between IDFs and CDFs, as discussed previously at each investigated axial position. These conclusions should play a guiding role in the synthesis of ZnO nanomaterials from flame environments.
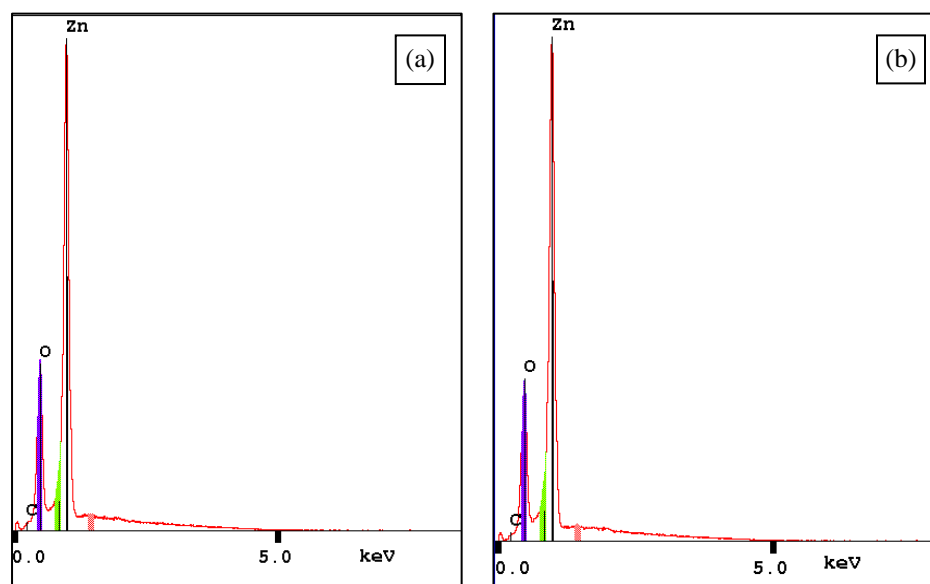
Figure 10. 6 EDXS spectra of as-produced ZnO nanomaterials from CDFs. (a) on the oxidizer side, and (b) on the fuel side.

Concerning growth mechanisms, the same mechanisms are proposed as discussed for the IDFs. The as-produced ZnO nanomaterials are analyzed using EDXS to identify their elemental compositions. Figure 10.6 displays two representative EDXS spectra, one collected from the oxidizer side (Fig. 10.6(a)) and another from the fuel side (Fig. 10.6(b)). These spectra contain elemental oxygen and elemental zinc only, indicating the as-prepared materials are ZnO.
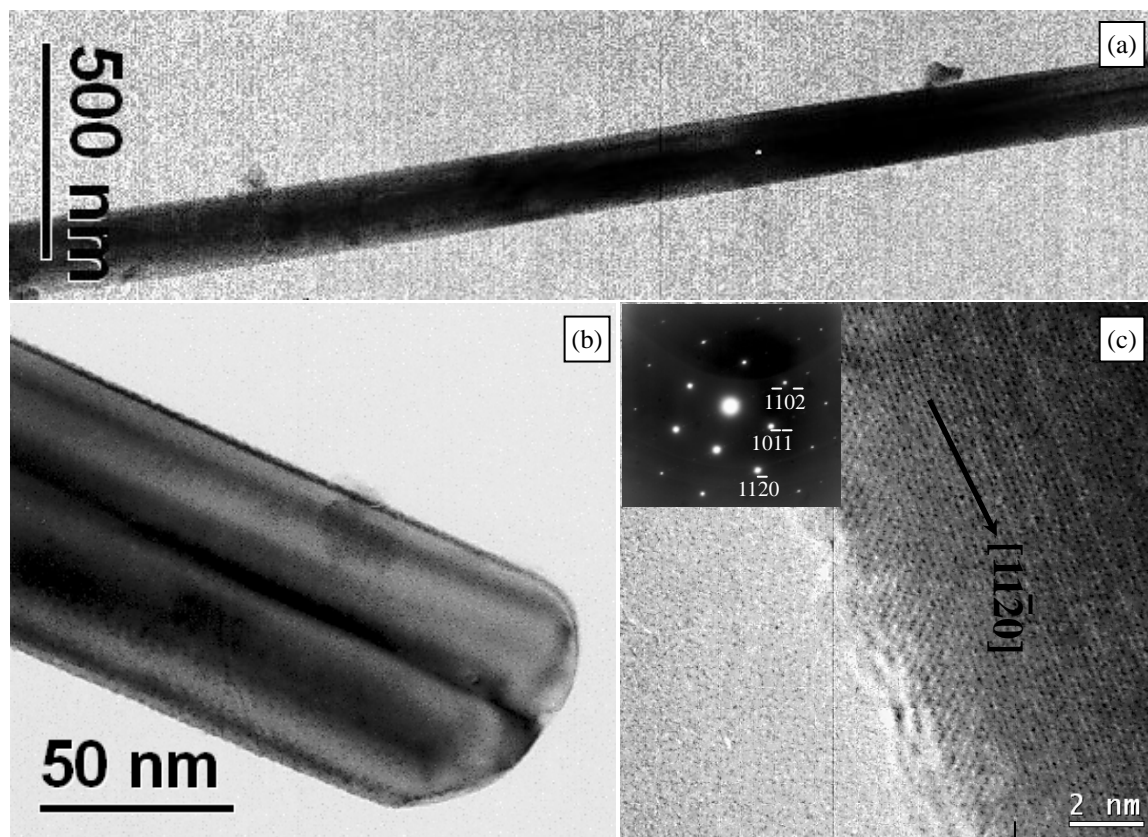
Figure 10.7 TEM images of ZnO nanorods/wires from the fuel side of CDF. (a) A nanorod with a diameter of ~150 nm, (b) the tip of a nanowire of ~70nm in diameter, and (c) the HRTEM of (b) along with its SAED.

As seen from FESEM images, the majority of ZnO nanorods produced on the oxidizer side exhibit hexagonal facets suggesting they grow along the [0001] direction, whereas the ZnO nanorods/wires grown from the fuel side often have different growth directions, as examined in IDFs in Chapter 9. For comparison, we focus on characterizing the ZnO nanorods/nanowires from the fuel side of CDFs by using TEM and HRTEM. Figure 10.7 describes TEM and HRTEM images of nanorods/wires prepared from the fuel side, along with its SAED pattern. A low magnification TEM

image of a rod-shape structure is shown in Fig. 10.7(a). This nanorod is around 150nm in diameter with a uniform cross section along its growth direction. Fig. 10.7(b) shows the tip of a nanowire with a diameter of ~70nm, suggesting vapor-solid growth. A HRTEM image of the edge of this nanowire tip is depicted in Fig. 10.7(c). The inset in Fig.10.7(c) is a corresponding SAED from which the growth direction of the nanowires is determined to be along $[11\bar{2}0]$. This growth direction is surprisingly the same as the growth direction $[11\bar{2}0]$ of ZnO nanowires observed from the fuel side of IDFs. This agreement further shows that despite different flame configurations with inherently different gradients, similar local growth environments result in similarly structured ZnO nanomaterials. The correspondence might also apply to other 1D nanomaterials synthesis via the flame route as well.

10.4 Conclusions

In this chapter, ZnO nanostructures fabricated in CDFs are demonstrated, and parametric studies are performed. The agreements between IDFs and CDFs are acceptable in terms of ZnO nanostructure morphology, with the corresponding growth conditions almost identical.

Reference

[1]P. X. Gao, C. S. Lao, W. L. Hughes, Z.L. Wang, Three-dimensional interconnected nanowire networks of ZnO, Chemcial Physics Letters, 408:174-178, 2005

[2]Pu Xian Gao and Zhong L. Wang, Nanopropeller arrays of zinc oxide, Applied physics letters, 84(15):2883-2885, 2004

[3]Z.L. Wang, Zinc oxide nanostructures: growth, properties and applications, J. Phys.: Condens. Matter 16 (2004) R829–R858

[4]J. Y. Lao, J. Y. Huang, D. Z. Wang, and Z. F. Ren, ZnO Nanobridges and Nanonails, Nano letters, 3(2): 235-238, 2003

[5]W. Bai, K. Yu, Q. Zhang, F. Xu, D. Peng, and Z. Zhu, Large-scale synthesis of ZnO flower-like and brush pen-like nanostructures by a hydrothermal decomposition route, Materials Letters, 61:3469-3472, 2007

[6]Y. Dai, Y. Zhang, and Z. L. Wang, The octa-twin tetraleg ZnO nanostructures, Solid State Communications, 126(11): 629-633, 2003

[7]Marcus C. Newton, and Paul A. Warburton, ZnO tetrapod nanocrystals, Materialstoday, 10(5):50-54, 2007

[8]P.A. Hu, Y. Q. Liu, L. Fu, X.B. Wang, D.B. Zhu, Controllable morphologies of ZnO nanocrystals: nanowire attracted nanosheets, nanocartridges and hexagonal nanotowers, Applied Physics A, 80:35-38, 2005

[9]Feifei Wang, Li Cao, Anlian Pan, Ruibin Liu, Xiao Wang, Xing Zhu, Shiquan Wang, and Bingsuo Zou, Synthesis of Tower-like ZnO structures and visible photoluminescence origins of varied-shaped ZnO nanostructures, J. Phys. Chem, C, 111:7655-7660, 2007

[10]P.X Gao, and Z.L Wang, Applied physics letters, 84:2883, 2007

[11]Moore, Walter J. (1962). *Physical Chemistry*, 3rd ed.. Prentice Hall.

[12]http://en.wikipedia.org/wiki/Marangoni_effect

Chapter 11

Tungsten Oxide Nanowires from Counterflow Diffusion Flames

11.1 Introduction

In this chapter, we examine the synthesis of tungsten oxide (WO_x) nanowires from tungsten (W) substrates that have a much higher melting temperature (3695K) than Zn. As such, the substrate remains in the solid phase, and the Marangoni effect does not take place for WO_x synthesis, which can occur for ZnO synthesis resulting in non-uniformity of ZnO nanostructures as reported in Chapter 11. The unique properties and associated applications of WO_x nanowires (as reviewed in Chapter 2) motivate us to explore this material.

Gu *et al*[1] obtained tungsten oxide nanowires on tungsten tips, pre-treated with electrochemical etching, by heating them to 700ºC in argon flow. The nanowires had diameters of 10-30nm and an average length of 0.3μm after 10min. Later, Li *et al*[2] grew quasi-aligned single-crystalline $W_{18}O_{49}$ nanotubes and naowires by heating tungsten foils as targets (1000-1050ºC) and using a Ta wafer (650ºC) as substrate at low pressures (0.2-10torr). After 2 hours, the nanowires were 20-100nm in diameter and < 3μm long. Qi *et al*[3] obtained potassium-doped tungsten oxide nanowires by heating a tungsten plate (625-650ºC) covered with a layer of potassium halide salts for 2 hours. The heavily-doped wires had diameters of ~400nm and average lengths of 10μm. Liu *et al*[4] heated a thin tungsten filament (1400ºC) in a vacuum chamber with some air leakage (oxygen partial

pressure $\sim 2.7 \times 10^{-5}$ torr) for 48 hours to grow undoped/doped tungsten oxide nanowires. The wires were found standing straight and clean on the filament, being $\sim$30nm in diameter and up to a few tens of microns long. Wang *et al*[5] synthesized dense and well-crystallized monoclinic $W_{18}O_{49}$ (010) nanowires with diameters of 10$\sim$20nm and lengths of 0.15-0.2μm in 1h from annealing (680ºC) and then oxidizing in O_2 (450ºC) WC_x films.

As can be seen above, processing can be complex, involving pretreatment[1], catalysts[3], and vacuum systems[2,4], while still characterized by low single-nanowire growth rates and low total yield densities. Consequently, studies on nanoscale WO_x materials and their applications are presently limited due to lack of easy processes for high- rate, yield, purity, and orientation synthesis of such materials. The growth of tungsten oxide nanowires over large areas remains especially challenging. In this chapter, CDFs are employed to grow well-aligned, single-crystal nanowires with diameters ranging from 20-50nm, coverage density of 10^9-10^{10}cm^{-2}, and growth rates of microns per minute, without any pretreatment and in open environments. The method is also robust in that the combustion process inherently provides for (i) an elevated enthalpy source to evaporate the metal substrate atoms, (ii) the gas-phase chemical species (e.g. oxidizer, water vapor, hydrogen) to produce the requisite oxide, and (iii) a favorable temperature gradient for growth of the nanowires.

11.2 Experiments

The CDF used in this chapter is the same as the Flame #1 in Chapter 7. Its computed flame structure is re-plotted in Figure 11.1, along with the substrate position marked. An actual flame with the schematic insertion of tungsten substrate into it is also given in Fig.

11.1(a) for convenience. A tungsten wire substrate (99.95% purity, 0.5mm diameter), without any pre-treatment, is inserted radially into the flame structure at the axial position z = 0.88cm (Fig.11.1), where the temperature and oxygen supply are sufficient to promote reactions leading to tungsten oxide. The morphology of as-grown tungsten oxide nanowires is examined using FESEM. Elemental analysis is conducted using EDXS attached to FESEM. Structural features of the nanomaterial are investigated using HRTEM, along with SAED.
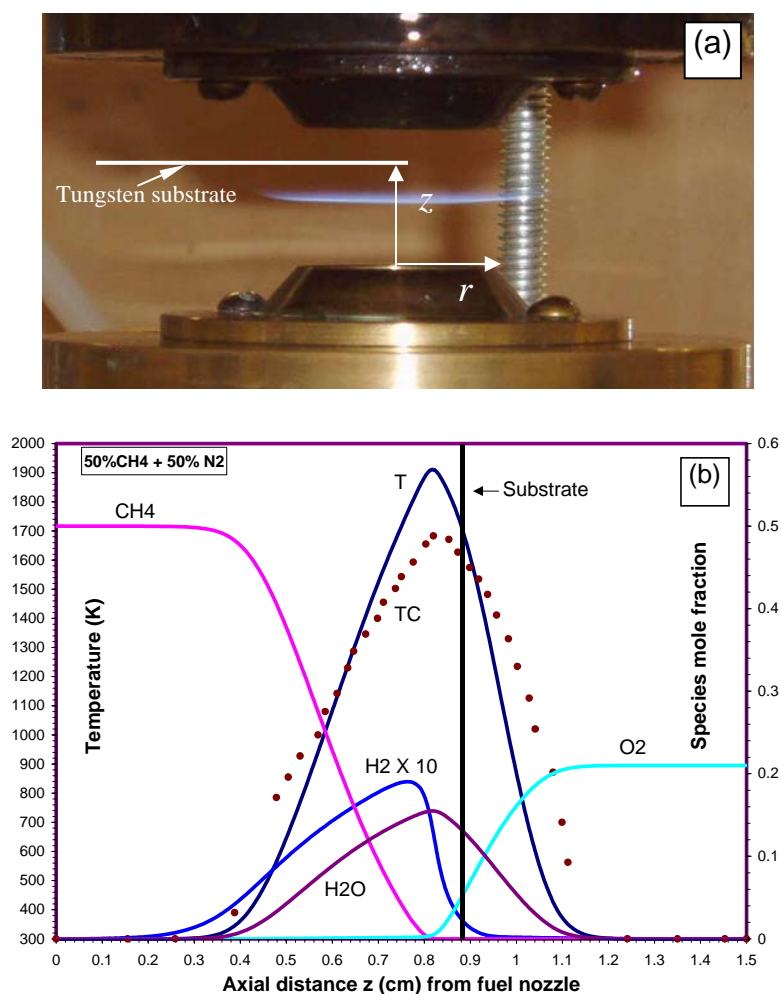
Figure 11.1 Gas-phase flame structure of CDF. Tungsten substrate position is marked.

11.3 Results and discussions

Figure 11.2(a) shows a low magnification FESEM image of a dense yield of nanomaterials grown directly on a tungsten substrate. A magnified image of a top view (Fig.11.2(b)) shows vertically-oriented nanowires. A side view (Fig.11.2(c)) reveals individual nanowires, as well as those grouped in small bundles. The as-grown nanowires have diameters of 20-50nm, with lengths of more than 10µm for a sampling duration of 10 minutes.
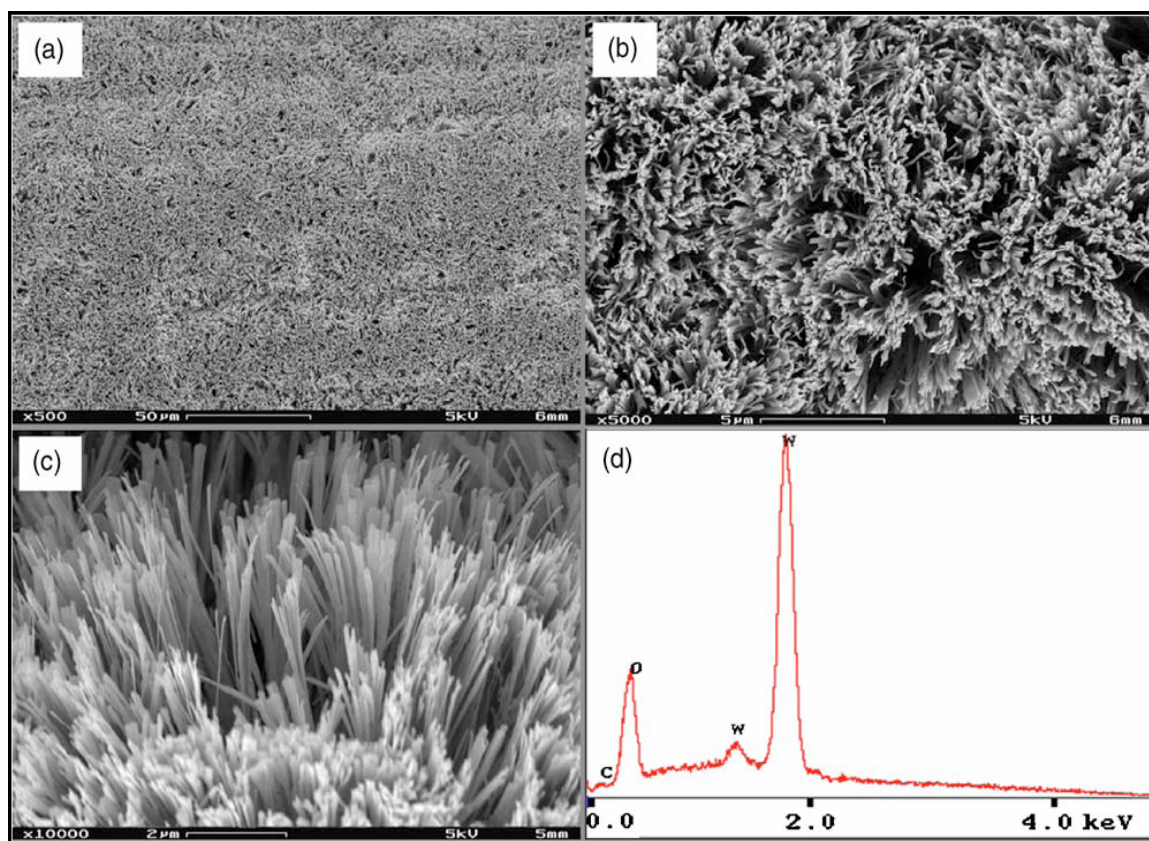
Figure 11.2 (a) Low magnification FESEM image of as-grown tungsten oxide nanowires showing high density of yield. (b) Typical FESEM image of nanowires from a magnified top view. (c) Typical FESEM image of nanowires from a side-view. (d) EDXS spectra of as-grown nanowires.

EDXS mappings for different growth regions of various sizes, from 10µm × 10µm to single nanowires, are essentially the same with no discernable differences. The EDXS spectra, Fig.11.2 (d), show that the nanowires are composed of W and O, along with negligible amounts of C. The presence of C results most likely from deposition of C on the nanowires from carbon-containing species that diffuse from the reaction zone during processing. Nevertheless, the findings indicate that the as-synthesized materials are nanosized tungsten oxide wires.
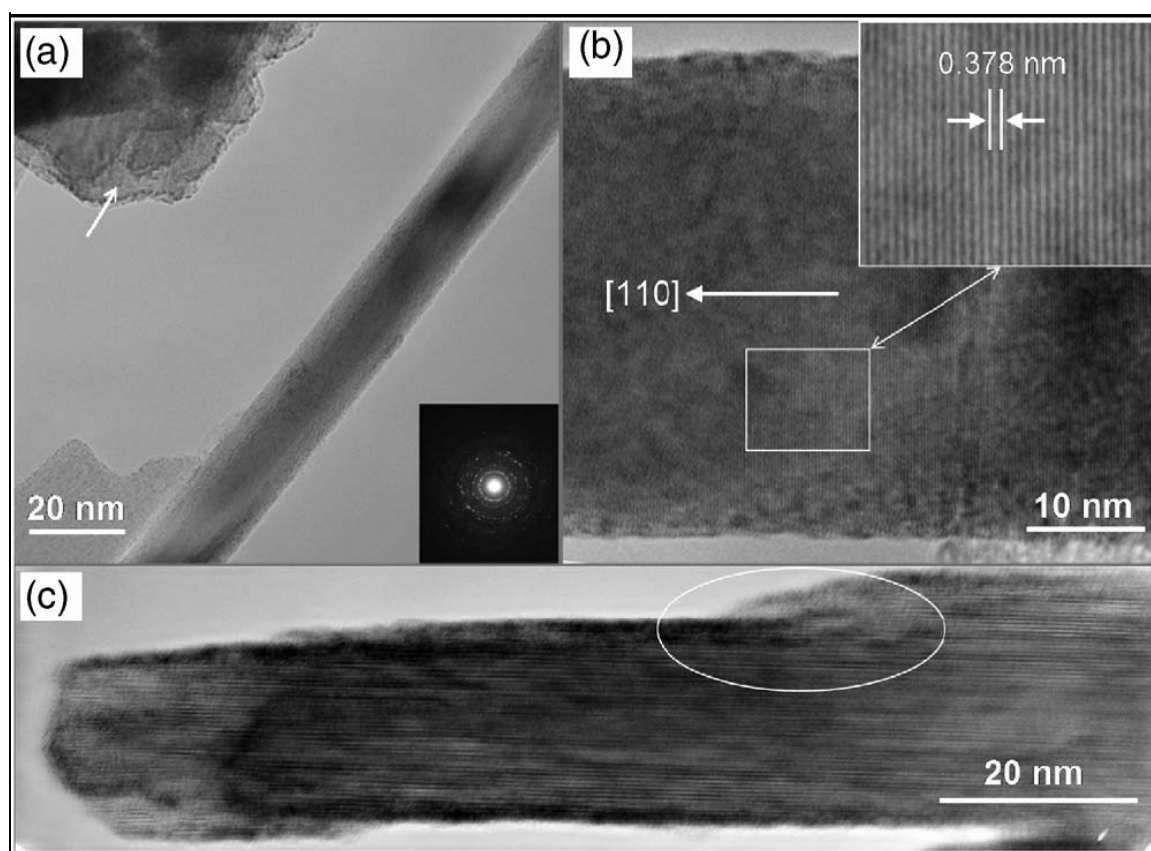
Figure 11.3 (a) TEM image showing a 20nm nanowire and platelets, along with the selected area electron diffraction pattern (inset). (b) HRTEM image of a single tungsten oxide nanowire, along with lattice-plane spacing (inset). (c) HRTEM of a nanowire tip, with ledge growth suggesting VS mechanism.

Tungsten oxide can exhibit different crystal structures, such as cubic and monoclinic WO_3, tetragonal $WO_{2.9}$, and monoclinic $W_{18}O_{49}$. Figure 11.3(a) presents a low magnification bright-field TEM image of a 20nm nanowire. Nanocrystallized tungsten oxide platelets (as indicated by the arrow) which come off the surfaces of bundled nanowires during TEM sample preparation can also be observed. The inset in Fig.11.3 (a) is a SAED pattern from the tungsten oxide nanowire and platelets. The indexed SAED pattern with the first three highest intensities of 3.779Å, 3.126Å and 2.67Å match very well with the tetragonal phase of $WO_{2.9}$ with lattice constants of $a = 5.3$Å, $b = 5.3$Å, and $c = 3.83$Å (PDF card #18-1417). These d-spacings correspond to {110}, {101}, and {200}, respectively.

HRTEM imaging of a typical flame-grown nanowire is shown in Fig.11.3 (b), revealing its dislocation-free, single-crystalline nature. Analysis of the two-dimensional Fourier transform pattern of the TEM image gives an average spacing for the lattice planes of 3.78Å, which corresponds to the reflections from d-spacings of (110) planes of the tetragonal $WO_{2.9}$ phase. Thus, these as-grown single crystalline nanowires have preferable growth along the [110] direction, as indicated in Fig.11.3 (b).

The mechanism of formation of these nanowires appears to be by vapor-solid (VS) growth. In the vapor-liquid-solid (VLS) process, the growth is promoted by a liquid-solid interface, generally marked by the presence of droplets at the tips of the nanowires. The morphology of a nanowire is shown in Fig.11.3(c), evincing no metal nanoparticle at its tip. The TEM image further reveals thickening by a ledge-growth mechanism, which is additional evidence for vapor-phase transport and deposition.

Figure 11.1 shows that the gas-phase temperature at the substrate is ~1720K, with the tungsten-substrate temperature estimated to be ~1600K, which is sufficiently high to evaporate tungsten/oxygen species. With available oxygen at the probe location, as displayed in Fig.11.1, conditions are then favorable for evaporated tungsten/oxygen species to react with oxygen to form tungsten oxide. At the same time, oxygen can react with the tungsten substrate to form tungsten oxide, which may then evaporate due to its low melting temperature (~1870K). In fact, formation of vapor-phase tungsten oxide species can be quite spontaneous, e.g.[6]

$$W^{(s)} + O_2{}^{(g)} \rightarrow WO_2{}^{(g)}, \; \Delta G = -40.08 \text{kJ/mol} \cdot \text{K} \; (1723\text{K}). \tag{11.1}$$
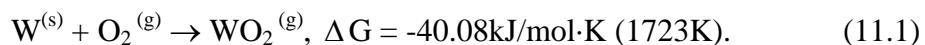
Initial formation of tungsten oxide nanoparticles on the surface of the substrate serves to nucleate the tungsten oxide nanowires. Subsequent elongated growth along the [110] direction results from preferential diffusion and condensation of tungsten oxide vapor as adatoms at the tip of a nanowire.

With solid phase WO_2 readily transformed into WO_3, i.e.[6]

$$WO_2{}^{(s)} + \tfrac{1}{2}O_2{}^{(g)} \rightarrow WO_3{}^{(s)}, \; \Delta G = -108.24 \text{kJ/mol} \cdot \text{K} \; (1273\text{K}), \tag{11.2}$$
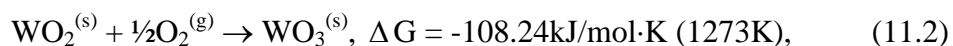
we hypothesize that, given the elevated temperature in the probe region (near the tungsten oxide decomposition temperature of ~1720K), decomposition of solid-phase WO_3 results in the formation of the final $WO_{2.9}$ tetragonal phase. The positive temperature gradient extending outward from the (cooler) substrate surface into the (hotter) surrounding gas likely promotes the vertical orientation of the nanowires.

The high growth rates that are observed in the flame process are due to favorable local conditions allowing for various mechanisms to occur simultaneously. The presence of water vapor (a combustion by-product) at the probe location (Fig.11.1) may further

enhance the nanowire growth process. Water vapor can not only form tungsten oxide, e.g.[7]:

$$W^{(s)} + 3H_2O^{(g)} \rightarrow WO_3^{(s)} + 3H_2^{(g)}, \tag{11.3}$$
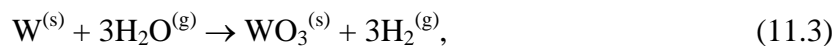
but it can also increase the rates of tungsten oxide evaporation and hydrate species formation, e.g.[8]:

$$WO_3^{(s)} + H_2O^{(g)} \rightarrow WO_2(OH)_2^{(g)}. \tag{11.4}$$
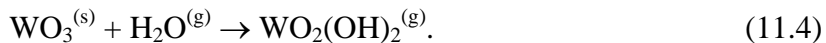
In addition, the elevated temperatures and radical species, e.g. OH and H, innate in the flame permit nanowire growth without substrate pretreatment or external catalysts. Gu *et al*[1] observed that a clean and unoxidized tungsten surface was necessary for tungsten oxide nanowire growth. However, similar to Liu *et al*[4], we grow tungsten oxide nanowires with high quality, orientation, and purity from oxidized surfaces. Other works have found that H_2 reduction[1] prior to heat treatment is necessary to grow nanowires on tungsten substrates. Again, this is not necessary in our experiments. As can be seen in Fig.11.1, small concentrations of H_2 are inherently present at the probe location, which, in combination with the elevated temperatures, can aid in initial nanoparticle formation. Finally, the high characteristic temperature in the flame process induces nanowire growth without the help of catalysts. External catalysts are needed to produce tungsten oxide nanowires in the temperature range of 873-973K[1,3,7], while neither catalyst nor pretreatment of substrate is necessary in the temperature range of 1073-1873K[2,4,9,10,11,12,13].

11.4 Results at other axial positions on the oxidizer side

Additional axial positions on the oxidizer side are examined in order to investigate possible affecting parameters. Figure 11.3 displays some FESEM images of tungsten oxide nanowires collected from an axial position (z=9.1mm) on the oxidizer side, where the gas-phase temperature is about 1500K (substrate ~1400K) and O_2 and H_2O are ~8% and ~11% respectively. Compared to the results at z=8.8mm, the length and diameter of nanowires are almost the same. But the overall yield is found to decrease, simply resulting from the reduced WO_x vapor due to the lower temperature. As shown in Fig. 11.3(a), the substrate surface is populated with flower-shaped patterns that are composed of radiatively emanating nanowires. Fig.11.3 (b) depicts a zoomed-in pattern of nanowires. Many WO_x nuclei formed at the early staged are likely to aggregate together, with nanowires growing from these aggregated nucleation sites to form a flower-like pattern, similar to the formation of flower-like ZnO nanorods in Chapter 10 (Fig.10.2 (e)). Radially away from the flame center at this position, a small quantity of scattered nanowires is observed to spread over the substrate surface, as illustrated in Fig. 11.3(c).
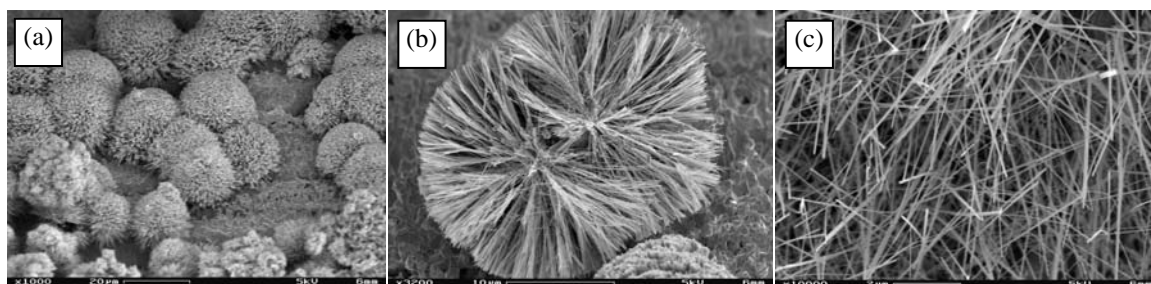
Figure 11.3 Tungsten oxide nanowires collected from where temperature is ~1500K. (a) nanowires form to flower-shaped patterns, (b) A pattern with nanowires parallel to the substrate, (c) mat of nanowires.

At axial position (z=9.6), the temperature is around 1100K and O_2 and H_2O are ~13% and ~8%, respectively. As seen from Fig. 11.4, the yield is significantly decreased. Very few nanowire clusters are found on the substrate surface, as seen from Fig. 11.4(a). An interesting ribbon-shaped tungsten oxide nanostructure is displayed in Fig. 11.4(b), which is ~20nm in thickness, with width ~5μm and length ~80μm. The end section of this nanoribbon (as marked in Fig. 11.4(b)) is magnified in Fig. 11.4(c). The formation of this ribbon could be explained as vapor-solid filling of the gaps between parallel nanowires, with the thickness of this ribbon shown to be equal to the diameter of thin nanowires, similar to the ZnO slabs in Chapter 10 (Fig.10.2 (g)). Such ultrathin sheets are of interest in terms of properties and applications. It is worth the additional effort to study the formation of such ultrathin ribbons with larger areas. Compared to other positions (z=8.8mm and 9.1mm), the diameters of the nanowire are still almost the same. The decrease in yield at this axial position again results from the lesser supply of tungsten suboxide species vapor at these relatively lower temperatures, due to the high melting temperature of tungsten. It can be concluded that the yield of tungsten oxide nanomaterials decreases with the decreaseing flame temperatures on the oxidizer side, despite increasing O_2 concentrations.
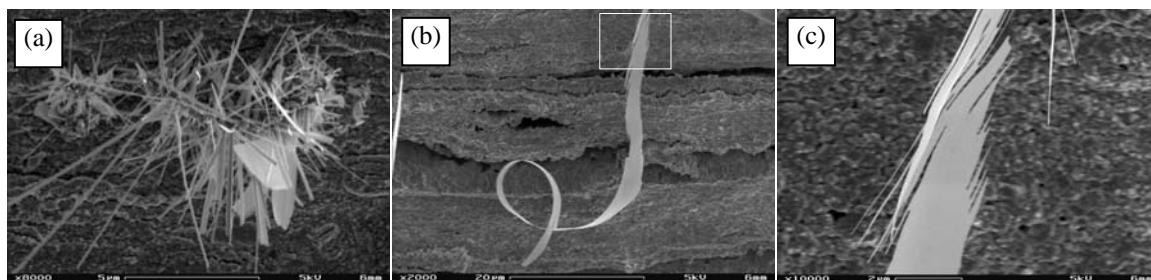
Figure 11.4 Tungsten oxide nanomaterials collected from where temperature is ~1100K, (a) nanowires form to tree-like structure, (b) A nanoribbon, (c) Enlarged end section of the nanoribbon showing its formation mechanism.

11.5 Results from the fuel side

Unlike the oxidizer side, more carbon-containing species occur on the fuel side where growth of CNTs is usually explored. Tungsten carbide nanocrystals (for example, nanowires and nanorods) have been fabricated by a number of techniques such as thermal annealing[14], and pyrolysis of W-containing compound[15]. As such, tungsten carbide nanomaterials are expected to be made on the fuel side of the CDFs in our experiments due to the disappearance of O_2. By inserting the tungsten substrates into the positions on the fuel side where the temperatures are the same as those at positions on the oxidizer side (Fig. 11.1), namely, ~1720K, ~1500K, and ~1100K respectively, tungsten-based nanowires are produced, as shown in Fig. 11.5.
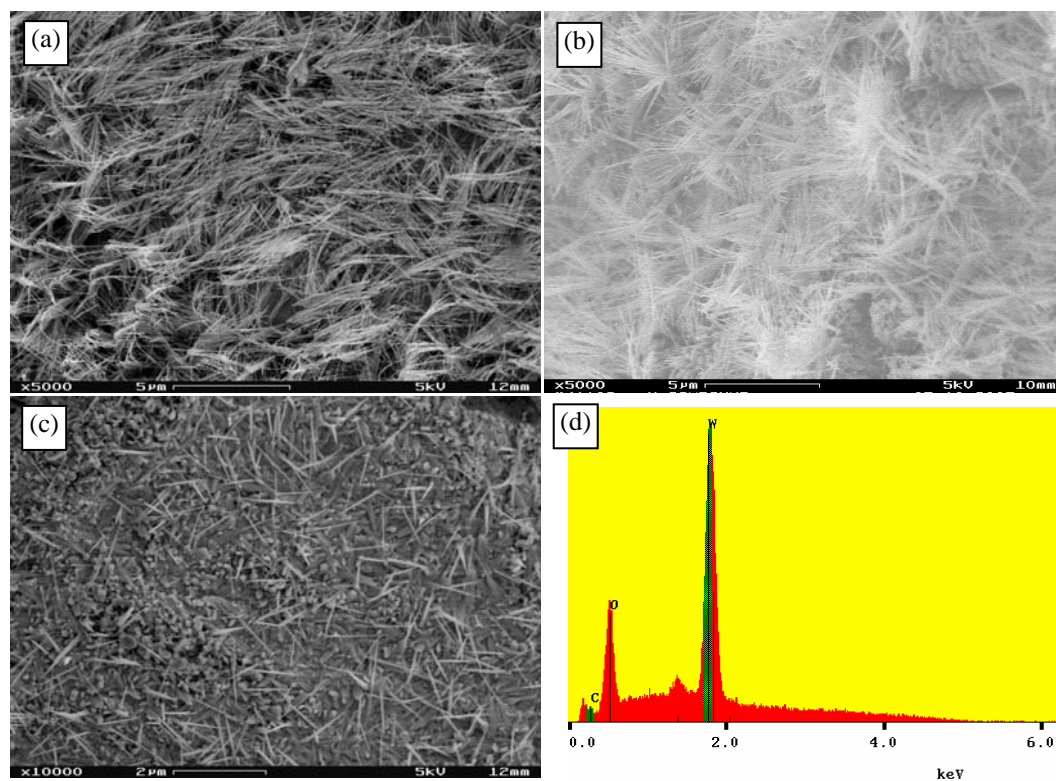
Figure 11.5 Tungsten oxide nanowires from the fuel side of CDF at temperatures of (a) ~1720K, (b) ~1500K, and (c) ~1100K, (d) a representative EDX spectrum of as-produced materials.

All these materials are examined using EDXS, with the spectra basically the same. A representative spectrum is given in Fig. 11.5(d) where W and O elements are identified along with some C, indicating that these nanowires are actually tungsten oxide instead of tungsten carbide. In fact, no differences can be seen between this spectrum and the EDX spectrum collected from the oxidizer side (Fig. 11.2(d)).

The presence of oxide nanowires on the fuel side is likely attributed to the reaction of H_2O with tungsten (Equation (11.3), $W^{(s)} + 3H_2O^{(g)} \rightarrow WO_3^{(s)} + 3H_2^{(g)}$) on the fuel side. The preference of tungsten oxide formation over tungsten carbide formation may be due to tungsten oxide having a lower free energy than tungsten carbide at high temperatures. In other words, it is more spontaneous to produce tungsten oxide than to produce tungsten carbide. Tungsten carbide can be produced through the following reactions[16]

$$W^{(g)} + C^{(g)} \rightarrow WC^{(g)} \qquad (11.5)$$

or/and

$$W^{(g)} + CH_4^{(g)} \rightarrow WC^{(g)} + 2H_2^{(g)} \qquad (11.6)$$
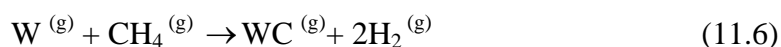
The Gibbs free energies of reaction for these reactions (Equations (11.3), (11.5) and (11.6)) are calculated (at 1 atm) and listed in Table 11.1 (all thermochemical data are from Ref.17[17], and tungsten in Equation (11.3) is taken as gas state).

Table 11.1 Gibbs free energies of reaction of Equations (3), (5) and (6) within investigated growth temperature range (thermochemical data from reference 17)

T (K)	ΔG^0 (kJ/mol, Eq. (3))	ΔG^0 (kJ/mol, Eq. (5))	ΔG^0 (kJ/mol, Eq. (6))
800	-762.365	-1366.84	-772.341
1000	-714.668	-1305.621	-764.505
1200	-672.264	-1243.921	-756.595
1400	-628.658	-1181.902	-748.489
1600	-585.694	-1119.677	-740.199
1800	-556.097	-1057.371	-731.774

From Table 11.1, however, we find that the Gibbs free energies for these three reactions (i.e. Eqs. (11.3), (11.5), and (11.6)) are all favorable in their forward reactions in producing tungsten oxide and tungsten carbide. As such the lack of tungsten carbide formation for the temperatures examined on the fuel side is likely due to highly different kinetic rates, which can not be readily assessed using an equilibrium thermodynamic analysis. An aspect controlling the kinetic rates is the activation energy, which we suspect is much greater for the reactions (11.5) and (11.6). This hypothesis is supported by other works, where tungsten carbide formation is reported only at higher temperatures (>1673K) under hydrogen environment using pure tungsten as reactant[17,18,19,20,21]. For this reason, due to our lower temperatures, tungsten oxide rather than tungsten carbide is preferably obtained. Nonetheless, more study is needed.

At a temperature of ~1720K (same temperature as on the oxidizer-side synthesis), as shown in Fig.11.5 (a), nanowires with a lower degree of vertical alignment and a lower yield are obtained, compared to nanowires produced on the oxidizer side (Fig. 11.2). The lower yield probably results from lack of availability of O_2 on the fuel side, as the H_2O concentrations on both sides are almost same (~13% on the oxidizer side and ~14% on the fuel side). With the melting temperature of tungsten too high for W vapor to be present, gaseous tungsten/oxygen species for much is critical. As such, Eqs. 11.1 and

11.2 are probably more important than Eq. 11.3 in forming WO_x subspecies necessary for nanowire growth. The lower degree of vertical alignment suggests that besides the temperature gradient (from the cooler substrate to the hotter gas phase) mentioned previously, some other factors could also contribute to this alignment, such as the spatial crowding effect[11]. A high density of nucleation sites on the surface leads to a crowding effect where vertically aligned growth of nanowires can occur when wires support one another during the growth. The yield at a temperature of ~1500K (Fig. 11.5(b)) is lower than the yield at a temperature of ~1720 K (Fig. 11.5(a)). It is also lower than the yield from the same temperature on the oxidizer side (Fig.11.3 (a)). The same observation applies to the yield at temperature of ~1100K (Fig. 11.5(c)). The diameters of all the nanowires, however, are not obviously different. These results suggest that both temperature and availability of O_2 are key factors governing nanowire yield as lower temperatures where direct formation of WO_x subspecies is reduced.

11.6 Preliminary results of effects of application of electric fields

As electric fields can affect CNT growth, application of electric fields may also affect the growth of tungsten oxide nanowires. As expected, applied external electric fields dramatically change the morphologies of as-synthesized nanowires, as depicted in Fig. 11.6, where the bias voltages applied are +10V, -5V, and -10V, respectively. Layers of tungsten oxide are stripped off the substrate, where nanowires grow from both sides of those pieces to form double sided comb structures (Fig. 11.6 (a) and (b)) and double-sided saw shapes (Fig. 11.6 (c)). Again, these morphologies appear based on the unit nanowires, where vapor-solid has filled in the gaps. These morphologies might result

from some interaction of applied electric fields with the flame-induced ion cloud around the substrate, and further investigation is needed.
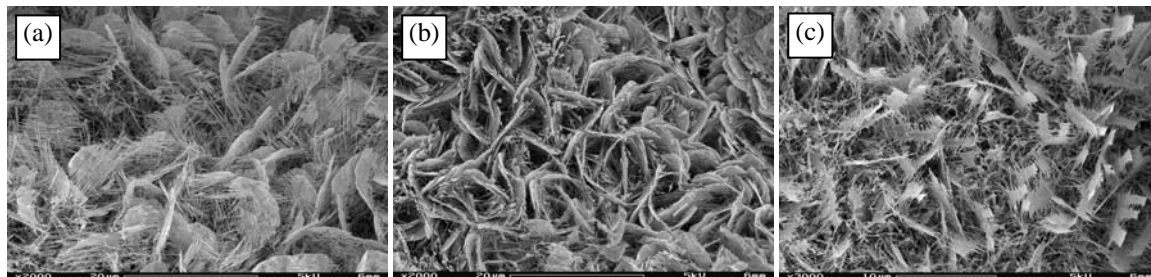
Figure 11.6 Effects of electric fields on tungsten oxide nanowires investigated at temperature of ~1720K on the oxidizer side, (a) +10V, (b) –5V, and (c) –10V.

11.7 Conclusions

In summary, we demonstrate the synthesis of vertically aligned, single-crystalline, tetragonal $WO_{2.9}$ nanowires grown directly from tungsten substrates at high rates in a flame process. The growth mechanism appears to be vapor-solid based, with key parameters being the radical species present, oxidizer and water vapor concentrations, substrate temperature, and gas-phase temperature. Systematic variation of these parameters is readily achieved in our flame technique, which would be very time-consuming and tedious in other heat-treatment and CVD methods. Effects of applied electric fields are preliminarily probed. Finally, our technique is promising for large-scale applications due to its simplicity, scalability, and economy.

References

[1] G. Gu, B. Zheng, W. Q. Han, S. Roth, and J. Liu, Nano Lett. **2**, 849 (2002)

[2] Y. Li, Y. Bando, and D. Golberg, Adv. Mater. **15**, 1294 (2003).

[3] H. Qi, C. Wang, and J. Liu, Adv. Mater. **15**, 411 (2003).

[4] K. Liu, D. T. Foord, and L. Scipioni, Nanotech. **16**, 10 (2005).

[5] S.-J. Wang, C.-H. Chen, R.-M. Ko, Y.-C. Kuo, C.-H. Wong, K.-M. Uang, T.-M. Chen, and B.-W. Liou, Appl. Phys. Lett. **86**, 263103 (2005).

[6]S. Vaddiraju, H. Chandrasekaran, and M. K. Sunkara, J. Am. Chem. Soc. **125**, 10792 (2003).

[7]K. Hong, W. Yiu, H. Wu, J. Gao, and M. Xie, Nanotech. **16**, 1608 (2005).

[8]M. Gillet, R. Delamare, and E. Gillet, Eur. Phys. J. D **34**, 291 (2005).

[9]Y. Q. Zhu, W. Hu, W. K. Hsu, M. Terrones, N. Grobert, J. P. Hare, H. W. Kroto, D. R. M. Walton, and H. Terrones, Chem. Phys. Lett. **309**, 327 (1999).

[10]Y.B. Li, Y. Bando, D. Golberg, K. Kurashima, Chem. Phys. Lett. 367, 214 (2003).

[11]S. Vaddiraju, H. Chandrasekaran, and M. K. Sunkara, J. Am. Chem. Soc. 125, 10792 (2003)

[12]J. Liu, Y. Zhao, and Z. Zhang, J. Phys.: Condens. Matter **15**, L453 (2003).

[13]Y. Z. Jin, Y. Q. Zhu, R. L. D. Whitby, N. Yao, R. Ma, P. C. P. Watts, H. W. Kroto, and R. M. Walton, J. Phys. Chem. B 108, 15572 (2004).

[14]Shui-JinnWang, Chao-Hsuing Chen, Shu-Cheng Chang,Chin-HongWong, Kai-Ming Uang, Tron-Min Chen, Rong-Ming Ko and Bor-Wien Liou, On the thermal annealing conditions for self-synthesis of tungsten carbide nanowires from WCx films, Nanotechnology: 16 (2005) 273–277

[15]Sangaraju Shanmugam, David S. Jacob, and Aharon Gedanken, Solid State Synthesis of Tungsten Carbide Nanorods and Nanoplatelets by a Single-Step Pyrolysis, The journal of physical chemistry B: letters, 2005, 109, 19056-19059

[16] Hudson M.J., Peckett J.W., and Harris P.J.F., Low-temperature sol-gel preparation of ordered nnaoparticles of tungsten carbide/oxide, *Ind. Eng. Chem. Res.,* 44:5575-5578, 2005

[17] Ihsan Barin in collaboration with Fried Sauert et al., *Thermochemical data of pure substances*, Weinheim, Federal Republic of Germany ; New York, NY, USA : VCH, c1989-

[18]J.-M. Giraudon, P. Devassine, J.-F. Lamonier, L. Delannoy, L. Leclercq, and G. Leclercq, Synthesis of Tungsten Carbides by Temperature-Programmed Reaction with CH4`H2 Mixtures. Influence of the CH4 and Hydrogen Content in the Carburizing Mixture, *Journal of Solid State Chemistry,* 154: 412-426, 2000

[19]Sangaraju Shanmugam, David S. Jacob, and Aharon Gedanken, Solid State Synthesis of Tungsten Carbide Nanorods and Nanoplatelets by a Single-Step Pyrolysis, *J. Phys. Chem. B,* 109(41): 19056-19059, 2005

[20] G. M. Wang, S. J. Campbell, A. Calka, W. A. Kaczmarek, Synthesis and structural evolution of tungsten carbide prepared by ball milling, *Journal of Materials Science*, 32:1461–1467,1997

[21]L. E. Toth, Transition metal carbides and nitrides, Academic Press, New York, p. 13, 1971

Chapter 12
Concluding Remarks

12.1 Reviews of results and conclusions

In recent years, one-dimensional (1D) nanostrucutres, such as tubes, rods, wires, and ribbons, have been extensively explored due to their many unique properties and their potential applications in electronics, photonics, and biological processes. Although various approaches have been developed to fabricate 1D nanostructures, flame synthesis offers many advantages, such as energy-efficiency, large parameter space, high growth rate, process controllability, processing continuity, and promising scalability. Flames provide the local conditions, i.e. temperature and chemical species, which can be conducive for CNT and metal-oxide nanowire growth. Moreover, well-defined flame configurations allow for the probing of fundamental controlling mechanisms (e.g. using laser-based spectroscopy), which are difficult to realize in many other current methods of synthesis.

In this work, the fundamental growth of 1D nanostructures in strategic flame configurations is investigated. Specifically, the investigated 1D nanostructures include CNTs and metal-oxide nanowires (i.e. ZnO, $WO_{2.9}$, Fe_2O_3/Fe_3O_4, CuO/Cu_2O). The probed flame configurations consist of premixed flames (PFs), normal diffusion flames (NDFs), inverse diffusion flames (IDFs), and counter-flow diffusion flames (CDFs). Methane is chosen as the primary fuel due to its well-known chemical kinetics, relative

non-sootiness, and potential cost-effectiveness (e.g. natural gas). Emphasis is placed on using IDFs and CDFs for the production of CNTs and nanowires.

The 1-D CDF, characterized ideally by gradients only in the axial direction, permits simulation involving detailed chemistry (e.g. GRI-Mech 1.2[1]) and transport, which can be verified by gas-phase spontaneous Raman spectroscopy (SRS). A radially inserted probe substrate defines a single local growth condition. As such, by designing a flame structure through simulation and then by investigating the local conditions for materials synthesis, a CDF provides facile examination of the appropriate parameter space.

The IDF, featuring a large parameter space due to its 2-D axi-symmetric geometry, can be especially advantageous in synthesizing CNTs. Post-flame species are largely comprised of pyrolysis vapors that have not passed through the oxidation zone. As a reult, soot formation processes, which compete with CNT formation routes and contaminate metal-oxide nanowires, are more effectively separated from oxidation processes in IDFs, which also tend to soot less than NDFs. Furthermore, the carbon-related growth species generated in IDFs can be much greater in concentration than that practically achieved in PFs, which should enhance the yield of CNTs. By using diffusion flames (burning stoichiometrically), flame-speed and cellular stabilization problems related to premixed flames are avoided. The flame structures of IDFs are measured by SRS at specific locations of CNT and ZnO growth.

Temperatures are also measured using a 125 µm Pt/Pt–10%Rh thermocouple (S-type) coated with silica to assess the actual substrate temperatures, which are expected to differ

from gas-phase temperatures due to radiative effects and conductive losses along the probe lengths.

In general, transition metals (e.g. Ni, Co, and Fe) and their alloys have been used as catalysts for CNT growth. Bimetallic catalysts, such as alloys, generally exhibit a decrease in their melting temperature and an increase in their carbon solubility as compared to single metals[2], and are known to increase the yield of CNTs[3]. The growth and properties of CNTs strongly depend on the properties of the catalysts, namely nanoparticle size, catalyst film thickness, and catalyst composition. In this work, different catalytic substrates are investigated, including different metal-alloy substrates (i.e., Fe, Fe/Cr, Ni/Cu, Ni/Ti, Ni/Cr, Ni/Cr/Fe). The requisite catalytic nanoparticles are formed dominantly through the substrate surface breakup induced by the lattice mismatch between the metal and the surface-formed carbide, with various morphologies of MWNTs grown. Vertically well-aligned MWNTs with uniform diameters are obtained using Ni/Cr/Fe and Ni/Ti alloys as substrates. Special-structured CNTs such as regularly coiled CNTs, large bending CNTs and Y-junction CNTs are observed. We observe that Ni-containing alloys generally produce a higher yield and smaller diameter of CNTs, likely due to its relatively low carbon solubility and rapid carbon diffusivity.

Catalytic nanoparticles are also produced *in situ* by reducing metal-oxide solid solutions (e.g. by local H_2 found in the flame structure), which allows for spatially-distinct and size-limited metal nanoparticles to form on the substrate surface. Solid metal-oxide spinel solutions with different transition metal ions (i.e. $NiAl_2O_4,$

$CoAl_2O_4$ and $ZnFe_2O_4$) are examined, and large quantities of CNTs are produced. Yield from $ZnFe_2O_4$ is found to be lower than those from $NiAl_2O_4$ and $CoAl_2O_4$, which could be attributed to the difficulty in reducing the solution to form Fe nanoparticles. For the same reasons perhaps, CNTs produced from $ZnFe_2O_4$ are found to contain at least 30% SWNTs.

CO, C_2H_2, and C_2 are identified as the main carbon precursors to CNT synthesis. It is found that CO is more active than C_2H_2. In particular, the effects of acetylene addition are examined. Acetylene is often necessary for metal-catalyzed CNT growth since C_2 species readily undergo dissociative adsorption. Concurrently, however, the molecular path towards soot formation requires C_2 species, most notably acetylene (C_2H_2), which is essential to the formation of the first aromatic ring, benzene, enabling subsequent polycyclic aromatic hydrocarbon (PAH) growth. PAHs can then form soot particles adulterating the yield. Moreover, PAHs can deactivate the metal-catalyst species. However, our result shows that the addition of C_2H_2 enhances the vertical alignment of CNTs from Nr/Fe/Cr alloy in CDFs, along with imposing a negative voltage bias to a floating point substrate. In addition, H_2 is generally present, which prolongs the life of the catalysts, despite competition between etching of sp^2 carbon by H atoms and deposition of sp^2 carbon by hydrocarbon intermediates.

The effects of other parameters on CNT growth are also studied, which mainly include the local gas-phase temperatures and voltages bias applied to the substrates. High temperature generally increases the CNT yield, but up to a point, where higher

temperatures result in decreased yield, likely due to deactivation or evaporation of catalytic nanoparticles. The temperature range for CNT growth in our system is observed to be between 900-1300K, which is in good agreement with those using the CVD method. The lower yield at low temperature results from the lack of catalytic nanoparticle formation. Our results show that applied voltage bias on the substrate is conducive to aligning CNTs, as well as enhancing their growth rates as compared to grounded conditions.

To the best of our knowledge, this work represents some of the first work on the flame synthesis of 1D metal-oxide nanostructures. The flame synthesis of zinc oxide nanostructures and tungsten oxide nanowires are focused in this work.

Single-crystalline ZnO nanowires are grown directly on zinc-plated steel substrates (characterized by a low melting point) at high rates (microns/minute) with no catalysts. The growth of the nanostructures is very sensitive to local gas-phase chemical species concentrations (i.e. O_2, H_2, CO_2, H_2O) and temperature (800-1500K). Larger-diameter (>100nm) hexagonal-cross-section nanowires, with [0001] growth direction, are produced at higher temperatures; while smaller-diameter (25-40 nm) nanowires, with [11$\bar{2}$0] growth direction, are produced at lower temperatures, and only on the fuel side of the reaction zone (with no oxygen present). H_2O appears to be the main route for synthesis. Nanoribbons and other nanowire-based morphologies are also found and discussed. The sensitivity of ZnO nanostructure morphology to radial position on the substrate (despite small gradients which do not affect CNT morphology) likely results

from the presence of a liquid layer on the substrate surface subject to Marangoni forces.

Aligned single-crystal tungsten oxide nanowires are grown directly from tungsten substrates (characterized by a high melting point) at high rates. The nanowires have diameters of 20-50nm, lengths $> 10\mu m$, coverage density of 10^9-$10^{10} cm^{-2}$, and growth rates $> 1\mu m/min$. Growth occurs by the vapor-solid mechanism, with local gas-phase temperature (~1720K) and chemical species (O_2, H_2O, and H_2) strategically specified at the substrate for self-synthesis. Although nanowires are grown on both sides of the reaction zone for the same temperature, indicating the role of H_2O in synthesis, the yield on the fuel side is very small, signifying the importance of O_2. Voltage bias is shown to dramatically change the morphologies of the as-synthesized WO_x nanowires. Some exploratory results relating to the synthesis of nanowires of iron oxide and copper oxide are presented and discussed in Appendix 1. It is found that the substrate is hotter than the gas phase for in the synthesis of these materials, suggesting a purely surface chemistry route for synthesis.

By determining local *in-situ* temperature and gas-phase chemical-species concentrations corresponding to given 1D nanostructure morphologies and growth rates, not only are fundamental mechanisms revealed, but flame-configuration-independent conditions are also established, which should be directly applicable as specific operating conditions for other gas-phase synthesis methods. In this work, the local growth conditions for CNTs are compared between IDFs and CDFs, and the same comparison is also done for ZnO. We find that local conditions for CNT and ZnO growth and

morphology can be reasonably transferred between different flame configurations. For example, vertically well-aligned CNTs can be grown on Ni/Cr/Fe alloy substrates in both IDFs and CDFs, where the local conditions match reasonably (temperature difference within 50K, and difference of growth-related species concentrations within 0.1% in mole fraction). ZnO nanowires with a diameter of ~50nm are collected on the fuel sides in both IDFs and CDFs where the temperature is ~1000K and H_2O is ~9% in mole fraction. If carefully extracted, universal synthesis conditions may be obtained that can be acceptably independent of the specific flame configuration.

12.2 Suggestions for future work

Vertically-aligned CNTs are produced, but a more quantitative method is needed to evaluate the alignment. That is, how can we characterize the alignment quantitatively in terms of its properties and applications? This quantitative analysis might be done by measuring such properties as electron tunneling density and monitoring the performance of CNT based gas sensors.

Reducing oxide solid solutions in the flames provides a way to produce CNTs of high yield, as well as to form CNTs based nanocomposites. Further studies on the $ZnFe_2O$ solid solution are worthwhile as this solution can produce SWNTs and MWNTs with less wall numbers. The effect of degree of crystallinity of the spinels should be investigated.

CNTs with remarkable alignment and high yield are fabricated from Ni/Ti alloy, as reported for CDFs in Chapter 7. These MWNTs have much thinner diameter; however

they grow from fissures on the substrate rather than covering most of the surface area of the substrate. Additional research is needed to examine the reasons for this phenomenon.

Application of external electric fields to substrates is shown to change the as-produced CNT morphologies and to enhance the CNT yields, particularly oin improving their vertical alignment as demonstrated in Chapters 6 (IDF) and 7 (CDF). Both negative and positive bias voltage is found to support aligned growth.   The exact driving force behind this effect needs to be investigated further.

As reported, ZnO can engender a family of different nanostructures.   Different ZnO nanostructures can be grown in a single experiment, resulting from the gradients of local growth conditions such as temperature and gas phase species, which at the same time also make it difficult to manipulate these materials.   Therefore, uniformity of nanostructures is required for up-scaled production.

Preliminary investigation of external electric fields on morphologies of tungsten nanowires has been conducted, but more research is advised.   Initial results show that nanowires of iron oxide and copper oxide can be readily fabricated from CDFs.   The same parametric studies carried out for ZnO are needed for these systems.   Finally, besides the growth of 1D nanostructures from flames, further investigation of their properties is recommended.   The measurement and exploration of electronic and photonic properties of as-prepared nanomaterials *in-situ*, can help to better direct the growth of these nanostructures and their direct inclusion into devices.

Reference

[1] Frenklach M., Wang H., Goldenberg, M., et al. Gas Research Institute Topical Report No. 95/0058,November 1, 1995.

[2] Arana, C.P., Puri, I.K., and Sen, S., Catalyst influence on the flame synthesis of aligned carbon nanotubes and nanofibers, *Proc. Combust. Inst.,* 30: 2553–2560, 2005

[3] Moisala A., Nasibulin A.G., and Kauppinen E.I., The role of metal nanoparticles in the catalytic production of single-walled carbon nanotubes-a review, *J. Physics: Cond. Mat.,* 15: S3011–S3035, 2003

Appendix 1

Some Preliminary Results of Nanowires of Iron Oxide and Copper Oxide from CDFs

1. Preliminary results of nanowires of iron oxide

Iron oxides are widely used as semiconductor, recording material and photocatalyst[1]. Nanoscaled magnetic ferrites (Fe_3O_4) are of particular interest due to their size and chemical compatibility with biological tissues and their unique combination of electronic and magnetic properties. Plenty of current research is focused on developing ferrite nanoparticles for ultrahigh density memory storage and advanced communications devices[2]. On the basis of experiments, one-dimensitional nanostructured ferrites are expected to exhibit many properties unlike those of particles of the same phase[2]. Recent research has shown that the high aspect ratio of magnetic ferrite nanowires can produce a larger magnetic moment than that observed in particles of the same volume, providing significant benefits in numerous applications. Hematite (α-Fe_2O_3), the most stable iron oxide under ambient conditions, has received considerable attention as a solar energy conversion material due to its excellent properties, such as a small band gap (2.1 eV), high resistivity to corrosion, and low cost[3]. One-dimensional nanostructures of magnetic ferrite, hematite, and $\varepsilon - Fe_2O_3$ also provide ideal theoretical systems for fundamental studies of electron spin and magnetic behavior of materials near quantum levels[2].

In this section, iron oxide nanowires are prepared from CDFs with 50%CH_4/50%N_2 reacting with air at atmospheric pressure. The process for growing iron oxide nanowires

is similar to those for zinc oxide and tungsten oxide (Chapters 10 and 11). An ultrasonic-cleaned pure iron substrate (melting point: 1811K) with diameter of ~0.8mm is inserted into the flame on the oxidizer side where the gas-phase temperature is around 1000K (z=9.8mm, substrate temperature: ~1100K) and the concentrations of O_2, H_2O, and CO are about 14%, 7%, and 0.4% respectively. The experimental duration is 10 minutes. The as-produced materials are scanned post-experiment using FESEM. Appendix 1.1 shows FESEM images of iron oxide nanomaterials. Thin nanowires of ~20nm in diameter are intermixed with thick nanorods of around 100nm in diameter as shown in Appendix 1.1(a). Ribbon/leaf shaped nanomaterials[4] are also observed as shown in Appendix 1.1(b). One chemical pathway for the formation of iron oxide is as follows

$$4Fe^{(s)} + 3O_2^{(g)} \rightarrow 2Fe_2O_3^{(s)} \qquad \text{(Appendix 1.1)}$$
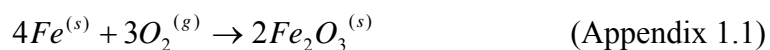
As seen, the gas-phase temperature (~1000K) at this position is much lower than the melting point of iron (1811K). As such the vapor pressure of iron is very low at such low temperature[4] (e.g. iron vapor pressure is 5.5 x 10^{-3} Pa at 1489K[5]) and Fe evaporation followed by condensation process will be negligible[3]. The 1D growth of iron nanostructures, therefore, seems, inexplicable by the vapor-liquid-solid (VLS) and vapor-solid (VS) mechanisms. The former is unlikely due to the fact that no spherical particles have been found at the tips of the nanowires, and the latter is ruled out due to either the very low vapor pressure of iron[3,4] and the higher substrate temperature (~1100K versus the gas-phase ~1000K, resulting from radiation from the flame above as seen in Fig.11.1). These discussions are supported by observations in Refs 3 and 4 where iron nanowires were fabricated on pure iron substrate (99.96 wt% of Fe) at temperatures of 813K-923K in an oxygen-containing environment (i.e. O_2 and H_2)[3,6] and nanobelts and

nanowires of iron oxide were produced by flowing O_2 over pure iron foil (99.9% purity) in a temperature range of 673K $-$1073K[4]. At such low temperatures, the iron oxide nanostructures might be formed through the tip-growth mechanism proposed by Takagi et al[7], which states the growth occurs by diffusion of iron atoms or ions from the base to the tip of the nanowire where they react with oxygen from mixture gases. There are two possible processes of supplying iron atoms for iron oxide nanostructures growth: (1) surface diffusion along the sides of the nanostructures, and (2) internal diffusion along planar defects (e.g. twin and stacking fault) up the axis of the nanostructures[3,8,9,10]. But at this point, we cannot tell their phases, namely Fe_3O_4, α-Fe_2O_3, or $\varepsilon - Fe_2O_3$, and further studies are needed.
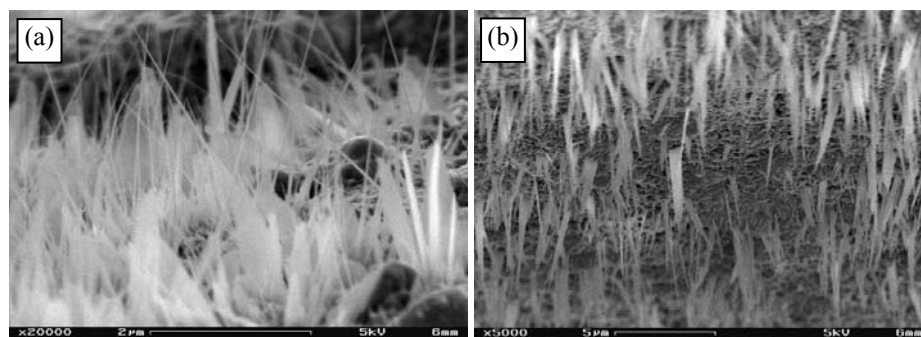
Appendix 1.1 FESEM images of (a) nanowires and nanorods, and (b) nanoribbons of iron oxide.

2. Some results of nanowires and nanoribbons of copper oxide

Copper oxide is a p-type semiconductor and is useful for the preparation of organic catalysts, and more recently, gas sensors[11]. Cuprous oxide (Cu_2O) is a nonstoichiometric p-type semiconductor with a band gap of 2.0 eV and has been proposed as a photocatalytic material for splitting water into H_2 and O_2 via visible light irradiation[12].

CuO is a p-type semiconductor with a band gap of 1.2 eV commonly studied for its photoconductive properties[13].

Nanomaterials of copper oxide synthesized via flames are demonstrated here. CDFs with 50%CH_4 diluted by 50%N_2 are used to conduct the experiments. After pure copper substrate (melting point: 1358K) with a diameter of ~1mm are cleaned ultrasonically, they are inserted into the flame on the oxidizer side (z=9.9mm) where the gas-phase temperature is around 900K (substrate temperature: ~1000K) and the concentrations of O_2, H_2O, and CO are about 15%, 5%, and 0.3% respectively. The experimental duration is 10 minutes, and then the as-produced materials are examined using FESEM.
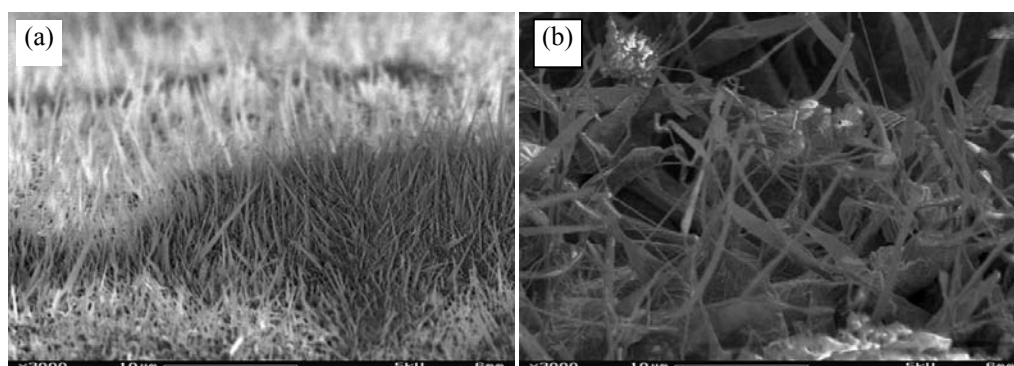
Appendix 1.2 FESEM images of copper oxide nanomaterials. (a) nanorods , (b) nano-ribbons, rods and wires

Some preliminary results are shown in Appendix 1.2. Nanorods with a diameter of about 100nm are given in Appendix 1.2(a). A mixture of thin nanowires, nanorods and nanoribbons are shown in Appendix 1.2(b). Similar to the iron-oxide case, the substrate is hotter than the gas phase, suggesting that the condensation mechanism is unlikely. Again, a heterogeneous route may be controlling. Because these results are preliminary, more work is required to examine their phases and crystallinity.

Reference

[1] Fu Y., Chen J., Zhang H., Synthesis of Fe2O3 nanowires by oxidation of iron, *Chemical Physics Letters*, 350:491, 2001

[2] Morber, J. R., Ding, Y., Haluska, M. S., Li, Y., Liu, J. P., Wang, Z. L., and Snyder, R. L., PLD-Assisted VLS Growth of Aligned Ferrite Nanorods, Nanowires, and Nanobelts Synthesis, and Properties, *J. Phys. Chem. B,* 110:21672, 2006

[3] Fu Y.Y., Wang R.M., Xu J., Chen J., Yan Y., Narlikar A.V., Zhang H., Synthesis of large arrays of aligned a-Fe2O3 nanowires, *Chemical Physics Letters*, 379:373, 2003

[4] Xiaogang Wen, Suhua Wang, Yong Ding, Zhong Lin Wang, and Shihe Yang, Controlled Growth of Large-Area, Uniform, Vertically Aligned Arrays of r-Fe2O3 Nanobelts and Nanowires, J. Phys. Chem. B 2005, 109, 215-220

[5] Kulikov I S 1986 Termodinamika Oksidov (Thermodynamics of Oxides) (Moscow: Metallurgija) p 344

[6] Yunyi Fu, Jing Chen, Han Zhang, Synthesis of Fe2O3 nanowires by oxidation of iron, Chemical Physics Letters 350 (2001) 491–494

[7] Takagi, R. *J. Phys. Soc. Jpn*. 1957, 12, 1212.

[8] G. Pfefferkorn, *Naturwissenschaften* 40 (1953) 551

[9] D.A. Voss, E.P. Butler, T.E. Mitchell, *Metall. Trans. A* 13 (1982) 929.

[10] R.L. Tallman, E.A. Gulbransen*, Nature* 218 (1968) 1046,and references therein.

[11] Wang W., Zhan Y. and Wang G., One-step, solid-state reaction to the synthesis of copper oxide nanorods in the presence of a suitable surfactant, *Chem. Commun.,* 727–728, 2001

[12] Oh J., Tak Y. and Lee J., Electrodeposition of Cu2O nanowires using nanoporous alumina template, *Electrochemical and Solid-State Letters*, 7(3): C27, 2004

[13] Wang W., Varghese O.K., Ruan C., Paulose M. and Grimes C.A., Synthesis of CuO and Cu2O crystalline nanowires using Cu(OH)2 nanowire templates, *J. Mater. Res.,* 18(12): 2756, 2003

Appendix 2. Reaction mechanism in GRI-Mech 1.2

Rate coefficient in the form $K_f = AT^\beta \exp(-E/RT)$ (units are moles, cubic centimeters, seconds, Kelvins and calories per mole)

	Reactions	A	β	E
1.	2O+M<=>O2+M	1.200E+17	-1.000	0.00
	Enhanced third-body efficiencies:			
	H2/ 2.40/ H2O/15.40/ CH4/ 2.00/			
	CO/ 1.75/ CO2/ 3.60/ C2H6/ 3.00/			
	AR/ 0.83/			
2.	O+H+M<=>OH+M	5.000E+17	-1.000	0.00
	Enhanced third-body efficiencies:			
	H2/2.00/ H2O/6.00/ CH4/2.00/			
	CO/1.50/ CO2/2.00/ C2H6/3.00/			
	AR/0.70/			
3.	O+H2<=>H+OH	5.000E+04	2.670	6290.00
4.	O+HO2<=>OH+O2	2.000E+13	0.000	0.00
5.	O+H2O2<=>OH+HO2	9.630E+06	2.000	4000.00
6.	O+CH<=>H+CO	5.700E+13	0.000	0.00
7.	O+CH2<=>H+HCO	8.000E+13	0.000	0.00
8.	O+CH2(S)<=>H2+CO	1.500E+13	0.000	0.00
9.	O+CH2(S)<=>H+HCO	1.500E+13	0.000	0.00
10.	O+CH3<=>H+CH2O	8.430E+13	0.000	0.00
11.	O+CH4<=>OH+CH3	1.020E+09	1.500	8600.00
12.	O+CO+M<=>CO2+M	6.020E+14	0.000	3000.00
	Enhanced third-body efficiencies:			
	H2/2.00/ O2/6.00/ H2O/6.00/			
	CH4/2.00/ CO/1.50/ CO2/3.50/			
	C2H6/3.00/ AR/0.50/			
13.	O+HCO<=>OH+CO	3.000E+13	0.000	0.00
14.	O+HCO<=>H+CO2	3.000E+13	0.000	0.00
15.	O+CH2O<=>OH+HCO	3.900E+13	0.000	3540.00
16.	O+CH2OH<=>OH+CH2O	1.000E+13	0.000	0.00
17.	O+CH3O<=>OH+CH2O	1.000E+13	0.000	0.00
18.	O+CH3OH<=>OH+CH2OH	3.880E+05	2.500	3100.00
19.	O+CH3OH<=>OH+CH3O	1.300E+05	2.500	5000.00
20.	O+C2H<=>CH+CO	5.000E+13	0.000	0.00
21.	O+C2H2<=>H+HCCO	1.020E+07	2.000	1900.00
22.	O+C2H2<=>OH+C2H	4.600E+19	-1.410	28950.00
23.	O+C2H2<=>CO+CH2	1.020E+07	2.000	1900.00
24.	O+C2H3<=>H+CH2CO	3.000E+13	0.000	0.00
25.	O+C2H4<=>CH3+HCO	1.920E+07	1.830	220.00
26.	O+C2H5<=>CH3+CH2O	1.320E+14	0.000	0.00
27.	O+C2H6<=>OH+C2H5	8.980E+07	1.920	5690.00
28.	O+HCCO<=>H+2CO	1.000E+14	0.000	0.00
29.	O+CH2CO<=>OH+HCCO	1.000E+13	0.000	8000.00
30.	O+CH2CO<=>CH2+CO2	1.750E+12	0.000	1350.00
31.	O2+CO<=>O+CO2	2.500E+12	0.000	47800.00
32.	O2+CH2O<=>HO2+HCO	1.000E+14	0.000	40000.00
33.	H+O2+M<=>HO2+M	2.800E+18	-0.860	0.00
	Enhanced third-body efficiencies:			
	O2/0.00/ H2O/0.00/ CO/0.75/			
	CO2/1.50/ C2H6/1.50/ N2/0.00/			
	AR/0.00/			

	Reactions	A	β	E
34.	H+2O2<=>HO2+O2	3.000E+20	-1.720	0.00
35.	H+O2+H2O<=>HO2+H2O	9.380E+18	-0.760	0.00
36.	H+O2+N2<=>HO2+N2	3.750E+20	-1.720	0.00
37.	H+O2+AR<=>HO2+AR	7.000E+17	-0.800	0.00
38.	H+O2<=>O+OH	8.300E+13	0.000	14413.00
39.	2H+M<=>H2+M	1.000E+18	-1.000	0.00
	Enhanced third-body efficiencies:			
	H2/0.00/ H2O/0.00/ CH4/2.00/			
	CO2/0.00/ C2H6/3.00/ AR/0.63/			
40.	2H+H2<=>2H2	9.000E+16	-0.600	0.00
41.	2H+H2O<=>H2+H2O	6.000E+19	-1.250	0.00
42.	2H+CO2<=>H2+CO2	5.500E+20	-2.000	0.00
43.	H+OH+M<=>H2O+M	2.200E+22	-2.000	0.00
	Enhanced third-body efficiencies:			
	H2/0.73/ H2O/3.65/ CH4/2.00/			
	C2H6/3.00/ AR/0.38/			
44.	H+HO2<=>O+H2O	3.970E+12	0.000	671.00
45.	H+HO2<=>O2+H2	2.800E+13	0.000	1068.00
46.	H+HO2<=>2OH	1.340E+14	0.000	635.00
47.	H+H2O2<=>HO2+H2	1.210E+07	2.000	5200.00
48.	H+H2O2<=>OH+H2O	1.000E+13	0.000	3600.00
49.	H+CH<=>C+H2	1.100E+14	0.000	0.00
50.	H+CH2(+M)<=>CH3(+M)	2.500E+16	-0.800	0.00
	Low pressure limit:	3.200E+27	-3.140	1230.00
	Troe parameters: a =0.6800,			
	T^{***} =78.00, T^{*} =1995.00, T^{**} =5590.00			
	Enhanced third-body efficiencies:			
	H2/2.00/ H2O/6.00/ CH4/2.00/			
	CO/1.50/ CO2/2.00/ C2H6/3.00/			
	AR/0.70/			
51.	H+CH2(S)<=>CH+H2	3.000E+13	0.000	0.00
52.	H+CH3(+M)<=>CH4(+M)	1.270E+16	-0.630	383.00
	Low pressure limit:	2.477E+33	-4.760	2440.00
	Troe parameters: a = 0.7830,			
	T^{***} =74.00, T^{*} =2941.00, T^{**} =6964.00			
	Enhanced third-body efficiencies:			
	H2/2.00/ H2O/6.00/ CH4/2.00/			
	CO/1.50/ CO2/2.00/ C2H6/3.00/			
	AR/0.70/			
53.	H+CH4<=>CH3+H2	6.600E+08	1.620	10840.00
54.	H+HCO(+M)<=>CH2O(+M)	1.090E+12	0.480	-260.00
	Low pressure limit:	1.350E+24	-2.570	1425.00
	Troe parameters: a = 0.7824,			
	T^{***} =271.00, T^{*} = 2755.00, T^{**} =6570.00			
	Enhanced third-body efficiencies:			
	H2/2.00/ H2O/6.00/ CH4/2.00/			
	CO/1.50/ CO2/2.00/ C2H6/3.00/			
	AR/0.70/			
55.	H+HCO<=>H2+CO	7.340E+13	0.000	0.00
56.	H+CH2O(+M)<=>CH2OH(+M)	5.400E+11	0.454	3600.00
	Low pressure limit:	1.270E+32	-4.820	6530.00
	Troe parameters: a = 0.7187,			

Reactions	A	β	E
$T^{***}=103.00, T^{*}=1291.00, T^{**}=4160.00$			
Enhanced third-body efficiencies:			
H2/2.00/ H2O/6.00/ CH4/2.00/			
CO/1.50/ CO2/2.00/ C2H6/3.00/			
57. H+CH2O(+M)<=>CH3O(+M)	5.400E+11	0.454	2600.00
Low pressure limit:	2.200E+30	−4.800	5560.00
Troe parameters: $a=0.7580,$			
$T^{***}=94.00, T^{*}=1555.00, T^{**}=4200.00$			
Enhanced third-body efficiencies:			
H2/2.00/ H2O/6.00/ CH4/2.00/			
CO/1.50/ CO2/2.00/ C2H6/3.00/			
58. H+CH2O<=>HCO+H2	2.300E+10	1.050	3275.00
59. H+CH2OH(+M)<=>CH3OH(+M)	1.800E+13	0.000	0.00
Low pressure limit:	3.000E+31	−4.800	3300.00
Troe parameters: $a=0.7679,$			
$T^{***}=338.00, T^{*}=1812.00, T^{**}=5081.00$			
Enhanced third-body efficiencies:			
H2/2.00/ H2O/6.00/ CH4/2.00/			
CO/1.50/ CO2/2.00/ C2H6/3.00/			
60. H+CH2OH<=>H2+CH2O	2.000E+13	0.000	0.00
61. H+CH2OH<=>OH+CH3	1.200E+13	0.000	0.00
62. H+CH2OH<=>CH2(S)+H2O	6.000E+12	0.000	0.00
63. H+CH3O(+M)<=>CH3OH(+M)	5.000E+13	0.000	0.00
Low pressure limit:	8.600E+28	−4.000	3025.00
Troe parameters: $a=0.8902,$			
$T^{***}=144.00, T^{*}=2838.00, T^{**}=45569.00$			
Enhanced third-body efficiencies:			
H2/2.00/ H2O/6.00/ CH4/2.00/			
CO/1.50/ CO2/2.00/ C2H6/3.00/			
64. H+CH3O<=>H+CH2OH	3.400E+06	1.600	0.00
65. H+CH3O<=>H2+CH2O	2.000E+13	0.000	0.00
66. H+CH3O<=>OH+CH3	3.200E+13	0.000	0.00
67. H+CH3O<=>CH2(S)+H2O	1.600E+13	0.000	0.00
68. H+CH3OH<=>CH2OH+H2	1.700E+07	2.100	4870.00
69. H+CH3OH<=>CH3O+H2	4.200E+06	2.100	4870.00
70. H+C2H(+M)<=>C2H2(+M)	1.000E+17	−1.000	0.00
Low pressure limit:	3.750E+33	−4.800	1900.00
Troe parameters: $a=0.6464,$			
$T^{***}=132.00, T^{*}=1315.00, T^{**}=5566.00$			
Enhanced third-body efficiencies:			
H2/2.00/ H2O/6.00/ CH4/2.00/			
CO/1.50/ CO2/2.00/ C2H6/3.00/			
AR/0.70/			
71. H+C2H2(+M)<=>C2H3(+M)	5.600E+12	0.000	2400.00
Low pressure limit:	3.800E+40	−7.270	7220.00
Troe parameters: $a=0.7507,$			
$T^{***}=98.50, T^{*}=1302.00, T^{**}=4167.00$			
Enhanced third-body efficiencies:			
H2/2.00/ H2O/6.00/ CH4/2.00/			
CO/1.50/ CO2/2.00/ C2H6/3.00/			
AR/0.70/			

Appendix 1 (continued)

	Reactions	A	β	E
72.	H+C2H3(+M)<=>C2H4(+M)	6.080E+12	0.270	280.00
	Low pressure limit:	1.400E+30	-3.860	3320.00
	Troe parameters: $a = 0.7820,$			
	$T^{***} = 207.50, T^{*} = 2663.00, T^{**} = 6095.00$			
	Enhanced third-body efficiencies:			
	H2/2.00/ H2O/6.00/ CH4/2.00/			
	CO/1.50/ CO2/2.00/ C2H6/3.00/			
	AR/0.70/			
73.	H+C2H3<=>H2+C2H2	3.000E+13	0.000	0.00
74.	H+C2H4(+M)<=>C2H5(+M)	1.080E+12	0.454	1820.00
	Low pressure limit:	1.200E+42	-7.620	6970.00
	Troe parameters: $a = 0.9753,$			
	$T^{***} = 210.00, \ T^{*} = 984.00, T^{**} = 4374.00$			
	Enhanced third-body efficiencies:			
	H2/2.00/ H2O/6.00/ CH4/2.00/			
	CO/1.50/ CO2/2.00/ C2H6/3.00/			
	AR/0.70/			
75.	H+C2H4<=>C2H3+H2	1.325E+06	2.530	12240.00
76.	H+C2H5(+M)<=>C2H6(+M)	5.210E+17	-0.990	1580.00
	Low pressure limit:	1.990E+41	-7.080	6685.00
	Troe parameters: $a = 0.8422,$			
	$T^{***} = 125.00, T^{*} = 2219.00, T^{**} = 6882.00$			
	Enhanced third-body efficiencies:			
	H2/2.00/ H2O/6.00/ CH4/2.00/			
	CO/1.50/ CO2/2.00/ C2H6/3.00/			
	AR/0.70/			
77.	H+C2H5<=>H2+C2H4	2.000E+12	0.000	0.00
78.	H+C2H6<=>C2H5+H2	1.150E+08	1.900	7530.00
79.	H+HCCO<=>CH2(S)+CO	1.000E+14	0.000	0.00
80.	H+CH2CO<=>HCCO+H2	5.000E+13	0.000	8000.00
81.	H+CH2CO<=>CH3+CO	1.130E+13	0.000	3428.00
82.	H+HCCOH<=>H+CH2CO	1.000E+13	0.000	0.00
83.	H2+CO(+M)<=>CH2O(+M)	4.300E+07	1.500	79600.00
	Low pressure limit:	5.070E+27	-3.420	84350.00
	Troe parameters: $a = 0.9320,$			
	$T^{***} = 197.00, T^{*} = 1540.00, T^{**} = 10300.00$			
	Enhanced third-body efficiencies:			
	H2/2.00/ H2O/6.00/ CH4/2.00/			
	CO/1.50/ CO2/2.00/ C2H6/3.00/			
	AR/0.70/			
84.	OH+H2<=>H+H2O	2.160E+08	1.510	3430.00
85.	2OH(+M)<=>H2O2(+M)	7.400E+13	-0.370	0.00
	Low pressure limit:	2.300E+18	-0.900	-1700.00
	Troe parameters: $a = 0.7346,$			
	$T^{***} = 94.00, T^{*} = 1756.00, T^{**} = 5182.00$			
	Enhanced third-body efficiencies:			
	H2/2.00/ H2O/6.00/ CH4/2.00/			
	CO/1.50/ CO2/2.00/ C2H6/3.00/			
	AR/0.70/			
86.	2OH<=>O+H2O	3.570E+04	2.400	-2110.00
87.	OH+HO2<=>O2+H2O	2.900E+13	0.000	-500.00

	Reactions	A	β	E
88.	OH+H2O2<=>HO2+H2O	1.750E+12	0.000	320.00
	DUPLICATE			
89.	OH+H2O2<=>HO2+H2O	5.800E+14	0.000	9560.00
	DUPLICATE			
90.	OH+C<=>H+CO	5.000E+13	0.000	0.00
91.	OH+CH<=>H+HCO	3.000E+13	0.000	0.00
92.	OH+CH2<=>H+CH2O	2.000E+13	0.000	0.00
93.	OH+CH2<=>CH+H2O	1.130E+07	2.000	3000.00
94.	OH+CH2(S)<=>H+CH2O	3.000E+13	0.000	0.00
95.	OH+CH3(+M)<=>CH3OH(+M)	6.300E+13	0.000	0.00
	Low pressure limit:	2.700E+38	-6.300	3100.00

Troe parameters: $a = 0.2105,$

$T^{***} = 83.50, T^{*} = 5398.00, T^{**} = 8370.00$

Enhanced third-body efficiencies:
H2/2.00/ H2O/6.00/ CH4/2.00/
CO/1.50/ CO2/2.00/ C2H6/3.00/

96.	OH+CH3<=>CH2+H2O	5.600E+07	1.600	5420.00
97.	OH+CH3<=>CH2(S)+H2O	2.501E+13	0.000	0.00
98.	OH+CH4<=>CH3+H2O	1.000E+08	1.600	3120.00
99.	OH+CO<=>H+CO2	4.760E+07	1.228	70.00
100.	OH+HCO<=>H2O+CO	5.000E+13	0.000	0.00
101.	OH+CH2O<=>HCO+H2O	3.430E+09	1.180	-447.00
102.	OH+CH2OH<=>H2O+CH2O	5.000E+12	0.000	0.00
103.	OH+CH3O<=>H2O+CH2O	5.000E+12	0.000	0.00
104.	OH+CH3OH<=>CH2OH+H2O	1.440E+06	2.000	-840.00
105.	OH+CH3OH<=>CH3O+H2O	6.300E+06	2.000	1500.00
106.	OH+C2H<=>H+HCCO	2.000E+13	0.000	0.00
107.	OH+C2H2<=>H+CH2CO	2.180E-04	4.500	-1000.00
108.	OH+C2H2<=>H+HCCOH	5.040E+05	2.300	13500.00
109.	OH+C2H2<=>C2H+H2O	3.370E+07	2.000	14000.00
110.	OH+C2H2<=>CH3+CO	4.830E-04	4.000	-2000.00
111.	OH+C2H3<=>H2O+C2H2	5.000E+12	0.000	0.00
112.	OH+C2H4<=>C2H3+H2O	3.600E+06	2.000	2500.00
113.	OH+C2H6<=>C2H5+H2O	3.540E+06	2.120	870.00
114.	OH+CH2CO<=>HCCO+H2O	7.500E+12	0.000	2000.00
115.	2HO2<=>O2+H2O2	1.300E+11	0.000	-1630.00
	DUPLICATE			
116.	2HO2<=>O2+H2O2	4.200E+14	0.000	12000.00
	DUPLICATE			
117.	HO2+CH2<=>OH+CH2O	2.000E+13	0.000	0.00
118.	HO2+CH3<=>O2+CH4	1.000E+12	0.000	0.00
119.	HO2+CH3<=>OH+CH3O	2.000E+13	0.000	0.00
120.	HO2+CO<=>OH+CO2	1.500E+14	0.000	23600.00
121.	HO2+CH2O<=>HCO+H2O2	1.000E+12	0.000	8000.00
122.	C+O2<=>O+CO	5.800E+13	0.000	576.00
123.	C+CH2<=>H+C2H	5.000E+13	0.000	0.00
124.	C+CH3<=>H+C2H2	5.000E+13	0.000	0.00
125.	CH+O2<=>O+HCO	3.300E+13	0.000	0.00
126.	CH+H2<=>H+CH2	1.107E+08	1.790	1670.00
127.	CH+H2O<=>H+CH2O	5.710E+12	0.000	-755.00
128.	CH+CH2<=>H+C2H2	4.000E+13	0.000	0.00
129.	CH+CH3<=>H+C2H3	3.000E+13	0.000	0.00
130.	CH+CH4<=>H+C2H4	6.000E+13	0.000	0.00

Appendix 1 (continued)

	Reactions	A	β	E
131.	CH+CO(+M)<=>HCCO(+M)	5.000E+13	0.000	0.00
	Low pressure limit:	2.690E+28	−3.740	1936.00
	Troe parameters: $a=0.5757$,			
	$T^{***}=237.00, T^{*}=1652.00, T^{**}=5069.00$			
	Enhanced third-body efficiencies:			
	H2/2.00/ H2O/6.00/ CH4/2.00/			
	CO/1.50/ CO2/2.00/ C2H6/3.00/			
	AR/0.70/			
132.	CH+CO2<=>HCO+CO	3.400E+12	0.000	690.00
133.	CH+CH2O<=>H+CH2CO	9.460E+13	0.000	−515.00
134.	CH+HCCO<=>CO+C2H2	5.000E+13	0.000	0.00
135.	CH2+O2<=>OH+HCO	1.320E+13	0.000	1500.00
136.	CH2+H2<=>H+CH3	5.000E+05	2.000	7230.00
137.	2CH2<=>H2+C2H2	3.200E+13	0.000	0.00
138.	CH2+CH3<=>H+C2H4	4.000E+13	0.000	0.00
139.	CH2+CH4<=>2CH3	2.460E+06	2.000	8270.00
140.	CH2+CO(+M)<=>CH2CO(+M)	8.100E+11	0.500	4510.00
	Low pressure limit:	2.690E+33	−5.110	7095.00
	Troe parameters: $a=0.5907$,			
	$T^{***}=275.00, T^{*}=1226.00, T^{**}=5185.00$			
	Enhanced third-body efficiencies:			
	H2/2.00/ H2O/6.00/ CH4/2.00/			
	CO/1.50/ CO2/2.00/ C2H6/3.00/			
	AR/0.70/			
141.	CH2+HCCO<=>C2H3+CO	3.000E+13	0.000	0.00
142.	CH2(S)+N2<=>CH2+N2	1.500E+13	0.000	600.00
143.	CH2(S)+AR<=>CH2+AR	9.000E+12	0.000	600.00
144.	CH2(S)+O2<=>H+OH+CO	2.800E+13	0.000	0.00
145.	CH2(S)+O2<=>CO+H2O	1.200E+13	0.000	0.00
146.	CH2(S)+H2<=>CH3+H	7.000E+13	0.000	0.00
147.	CH2(S)+H2O(+M)<=>CH3OH(+M)	2.000E+13	0.000	0.00
	Low pressure limit:	2.700E+38	−6.300	3100.00
	Troe parameters: $a=0.1507$,			
	$T^{***}=134.00, T^{*}=2383.00, T^{**}=7265.00$			
	Enhanced third-body efficiencies:			
	H2/2.00/ H2O/6.00/ CH4/2.00/			
	CO/1.50/ CO2/2.00/ C2H6/3.00/			
148.	CH2(S)+H2O<=>CH2+H2O	3.000E+13	0.000	0.00
149.	CH2(S)+CH3<=>H+C2H4	1.200E+13	0.000	−570.00
150.	CH2(S)+CH4<=>2CH3	1.600E+13	0.000	−570.00
151.	CH2(S)+CO<=>CH2+CO	9.000E+12	0.000	0.00
152.	CH2(S)+CO2<=>CH2+CO2	7.000E+12	0.000	0.00
153.	CH2(S)+CO2<=>CO+CH2O	1.400E+13	0.000	0.00
154.	CH2(S)+C2H6<=>CH3+C2H5	4.000E+13	0.000	−550.00
155.	CH3+O2<=>O+CH3O	2.675E+13	0.000	28800.00
156.	CH3+O2<=>OH+CH2O	3.600E+10	0.000	8940.00
157.	CH3+H2O2<=>HO2+CH4	2.450E+04	2.470	5180.00
158.	2CH3(+M)<=>C2H6(+M)	2.120E+16	−0.970	620.00
	Low pressure limit:	1.770E+50	−9.670	6220.00
	Troe parameters: $a=0.5325$,			
	$T^{***}=151.00, T^{*}=1038.00, T^{**}=4970.00$			
	Enhanced third-body efficiencies:			

Appendix 1 (continued)

Reaction	A	β	E
H2/2.00/ H2O/6.00/ CH4/2.00/			
CO/1.50/ CO2/2.00/ C2H6/3.00/			
AR/0.70/			
159. 2CH3<=>H+C2H5	4.990E+12	0.100	10600.00
160. CH3+HCO<=>CH4+CO	2.648E+13	0.000	0.00
161. CH3+CH2O<=>HCO+CH4	3.320E+03	2.810	5860.00
162. CH3+CH3OH<=>CH2OH+CH4	3.000E+07	1.500	9940.00
163. CH3+CH3OH<=>CH3O+CH4	1.000E+07	1.500	9940.00
164. CH3+C2H4<=>C2H3+CH4	2.270E+05	2.000	9200.00
165. CH3+C2H6<=>C2H5+CH4	6.140E+06	1.740	10450.00
166. HCO+H2O<=>H+CO+H2O	2.244E+18	-1.000	17000.00
167. HCO+M<=>H+CO+M	1.870E+17	-1.000	17000.00
Enhanced third-body efficiencies:			
H2/2.00/ H2O/0.00/ CH4/2.00/			
CO/1.50/ CO2/2.00/ C2H6/3.00/			
168. HCO+O2<=>HO2+CO	7.600E+12	0.000	400.00
169. CH2OH+O2<=>HO2+CH2O	1.800E+13	0.000	900.00
170. CH3O+O2<=>HO2+CH2O	4.280E-13	7.600	-3530.00
171. C2H+O2<=>HCO+CO	5.000E+13	0.000	1500.00
172. C2H+H2<=>H+C2H2	4.070E+05	2.400	200.00
173. C2H3+O2<=>HCO+CH2O	3.980E+12	0.000	-240.00
174. C2H4(+M)<=>H2+C2H2(+M)	8.000E+12	0.440	88770.00
Low pressure limit:	7.000E+50	-9.310	99860.00
Troe parameters: $a = 0.7345$,			

$T^{***} = 80.00, T^{*} = 1035.00, T^{**} = 5417.00$

Enhanced third-body efficiencies:			
H2/2.00/ H2O/6.00/ CH4/2.00/			
CO/1.50/ CO2/2.00/ C2H6/3.00/			
AR/0.70/			
175. C2H5+O2<=>HO2+C2H4	8.400E+11	0.000	3875.00
176. HCCO+O2<=>OH+2CO	1.600E+12	0.000	854.00
177. 2HCCO<=>2CO+C2H2	1.000E+13	0.000	0.00
178. CHA+O2=>CH+O2	2.40E+12	0.5	0.
179. C2H+O2=>CHA+CO2	4.50E+15	0.00	25083.61
180. C2+OH=>CHA+CO	3.61E+11	0.00	0.
181. C2+H2<=>C2H+H	4.00E+05	2.4	1000.
182. C2+O2<=>CO+CO	5.00E+13	0.00	0.

Curriculum Vita

Fusheng Xu

Education

Ph.D. Mechanical and Aerospace Engineering, October 2007
Rutgers University, Piscataway, NJ

M.S. Mechanical and Electronic Engineering, June 1999
Petroleum University, Beijing, China

Associate Degree, Mechanical Engineering, June 1994
Nanjing College of Communication and Transportation, Nanjing, China

Experience

2002-2007, Graduate Assistant, in Mechanical Engineering, Rutgers University, USA

1999-2002, Software Engineer, IT Center of SINOpec Engineering Inc., Beijing, China

1996-1999, Graduate Assistant, in Mechanical Engineering, Petroleum University, Beijing, China

1994-1996, Assistant Mechanical Engineer, Technology Section of Transportation Vehicles Factory of Changzhou, Jiangshu, China,

Publications

Xu, F**.**, Liu, X., and Tse, S.D., "Synthesis of Carbon Nanotubes on Metal Alloy Substrates with Voltage Bias in Methane Inverse Diffusion Flames," *Carbon,* **44**(3): 570-577 (2006)

Xu, F., Tse, S.D., Al-Sharab, J.F., and Kear, B.H., "Flame Synthesis of Aligned Tungsten Oxide Nanowires," *Applied Physics Letters,* **88**: 243115 (2006)

Xu, F., Zhao, H., and Tse, S.D., "Carbon Nanotube Synthesis on Catalytic Metal Alloys in Methane/Air Counterflow Diffusion Flames", *Proceedings of the Combustion Institute,* **31**(2): 1839-1847 (2006)

Xu, F**.,** Liu, X., Tse, S.D., Cosandey, F., and Kear, B.H., "Flame Synthesis of Zinc Oxide Nanowires on Zinc-Plated Substrates," accepted to *Chemical Physics Letters*, (2007).

Xu, F**.**, Sun, G., Kear, B.H., and Tse, S.D., "Catalytic Flame Synthesis of Carbon Nanotubes on Metal-Oxide spinels," to be submitted (2007)

Xu, F., Tse, S.D., Kear, B.H., and Cosandey, F., " Flame Synthesis of Zinc Oxide Nanorods, Ribbons, and Cones in Counter-flow Flames," to be submitted (2007)